Development of a Proof of Concept Low Temperature Superfluid Magnetic Pump with Applications

By

Amir E. Jahromi

A dissertation in partial fulfillment of

the requirements for the degree of

Doctor of Philosophy

(Mechanical Engineering)

at the

UNIVERSITY OF WISCONSIN – MADISON

2015

Date of final oral examination: 12/10/2015

The dissertation is approved by the following members of the Final Oral Committee (alphabetically):

Roxann L. Engelstad, Professor, Mechanical Engineering
Franklin K. Miller, Assistant Professor, Mechanical Engineering
Gregory F. Nellis, Professor, Mechanical Engineering
John M. Pfotenhauer, Professor, Mechanical Engineering
Peter T. Timbie, Professor, Physics

Development of a Proof of Concept Low Temperature Superfluid Magnetic Pump with Applications

Under the supervision of Professors Franklin K. Miller and Greg F. Nellis
at the University of Wisconsin – Madison

Abstract

State of the art particle and photon detectors such as Transition Edge Sensors (TES) and Microwave Kinetic Inductance Detectors (MKID) use large arrays of sensors or detectors for space science missions. As the size of these space science detectors increases, future astrophysics missions will require sub-Kelvin coolers over larger areas. This leads to not only increased cooling power requirements, but also a requirement for distributed sub-Kelvin cooling. Development of a proof of concept Superfluid Magnetic Pump is discussed in this work. This novel low temperature, no moving part pump can replace the existing bellows-piston driven ^{4}He or ^{3}He-^{4}He mixture compressor/circulators used in various sub Kelvin refrigeration systems such as dilution, Superfluid pulse tube, or active magnetic regenerative refrigerators. Due to its superior thermal transport properties this pump can also be used as a simple circulator of sub-Lambda ^{4}He to distribute cooling over large surface areas. The pump discussed in this work was experimentally shown to produce a maximum flow rate of 440 mg/s (averaged over cycle), 665 mg/s (peak) and produced a maximum pressure difference of 2323 Pascal. This pump worked in an "ideal" thermodynamic state: The experimental results matched with the theoretical values predicted by a computer model. Pump curves were developed to map the performance of this pump. This successful demonstration will enable this novel pump to be put to test in suitable sub Kelvin refrigeration systems. Numerical modeling of an Active Magnetic Regenerative Refrigerator (AMRR) that uses the Superfluid Magnetic Pump (SMP) to circulate liquid ^{3}He-^{4}He through a magnetic regenerator is presented as a potential application of such a pump.

Approved:

Asst. Professor Franklin K. Miller
Department of Mechanical Engineering
University of Wisconsin-Madison

Professor Greg F. Nellis
Department of Mechanical Engineering
University of Wisconsin-Madison

Acknowledgments

This work is dedicated to:

My dearest Cyrus, You are my world, you are my everything. I can't wait to see what great things the future holds for you.

My dearest Casper, You will be forever missed young man thank you for teaching me so many lessons in life…

First and foremost I would like to thank my family, in particular my father, my mother, my grandmother, and my wife for all their encouragement dedication and support. Without your dedication and help achieving this level would've not been even remotely possible so thank you all for your continual support. Special thanks goes to my wife, Amanda for all her patience, due diligence, and support in these very difficult few last months. Thank you to my lovely sons, Cyrus and Casper for giving meaning to my life and existence. Finally thanks to my uncle.

Second, special thanks goes to my advisors, Prof. Franklin Miller and Prof. Greg Nellis. I am forever grateful for all your support, all your technical advice, and your patience through my entire graduate school education. You two are among the most intelligent group of people whom I had the pleasure to work with. I have learnt a tremendous amount from you. Franklin, thank you so much for all your guidance and your understanding of my situation at various stages of my graduate school career. I loved working with you. Thank you for teaching me all the interesting physics stuff involved in low temperature physics. And thank you for your friendship and your patience. You got me where I am, and I am forever grateful for that. Greg, thank you so much again for your trust in me and for coming to my rescue when I needed financial support for the continuation of the project. Thank you so much for giving me the opportunity to serve as your teaching assistant and for teaching me so much in the field. Finally thank you a millions times for teaching me how to write! You two are just awesome…

Many thanks to Prof. John Pfotenhauer. I am also grateful to all your kindness and your extreme support throughout my graduate education. You have also contributed significantly to my success. It has been an honor and a privilege to work for you. I thoroughly enjoyed many of our fine conversations whether be on the topic of engineering, physics, or life in general. You are an outstanding professor and a truly kind one! Thank you so much for everything you taught and provided for me. Thanks for having me as your TA for ME 370, it was an awesome experience.

Many thanks also goes to Prof. Roxann Engelstad. Roxy has been a fine example and role model of how a professor and an effective leader should be in academia. I absolutely loved taking your class, it was one of the best courses I have ever taken here at UW-Madison. I learnt so much from you. You are a truly wonderful professor who is extremely intelligent, hardworking, and dedicated to her students. It is no surprise that all your students love you and your work ethic! You are an amazing role model and I aspire to reach your level.

Prof. Peter Timbie, thank you so much for accepting my invitation to be on my PhD committee. I very much enjoyed our conversations on the topic of low temperature physics. Thank you so much for kindly showing your awesome lab and for sharing your great work with me. I hope we continue to work together when I start my job at NASA – Goddard.

There is a long list of individuals that I would like to thank here. Thank you so much for your friendship, support, and encouragement to: Jake Leachman, Harrison Skye, Amanda Pertzborn, Michael Cheadle, Jacob Brenner, Bryant Mueller, Diego Fonseca (my Amigo! I have so much respect for you, I am proud of you brother), Fritz S. (my partner in crime!), Christian H., Evan Sheehan (finish up soon!), Eric Alar (get back to school!), Brian Leyde (Second partner in crime), Nathan Hartung (thanks for your help friend), Jack H. (my political partner), Matt Kuntz (thank for all your help, you’re awesome!), Anna, Amy V., Liz B., Rachael, Avi Friedman, Joe

Shinners, Rogelio Rosas, Brad Moore, Cameron Gilanshah, Cooper H., Jake Kilbane, MEhrdad Arjmand (thanks for being with me in the hardest times brother), Nate Haggerty, Soenke T., Tyler W. , and Wenjie Z.

I would also like to thank all my colleagues at NASA-Goddard Space Flight Center: Ed Canavan, Jim Tuttle, Dan Sullivan, John Francis, Mark Kimball, Peter Shirron, Rob Boyle, Hudson DeLee, Eric Silk, Donald Wegel, Mike D., Shuvo Mustafi, Rick Letmate, Tom Hait, Stuart, and Kim. I am looking forward to working with all of you.

Gratefully acknowledged financial support for this project was provided by Robert M. Boltz Wisconsin distinguished graduate fellowship, Klaus and Jean Timmerhaus scholarship, Wisconsin Alumni Research Foundation fellowship, and University of Wisconsin's distinguished dissertation completion fellowship. Also thanks to NASA-Goddard's Space Flight Center for providing interesting and challenging projects throughout the PHD program and during tour of duty to GSFC.

Table of Contents

Abstract i
Acknowledgments iii
Table of Contents vi
List of Figures x
List of Tables xiv
Nomenclature xv
1. Introduction and Literature Review 1
1.1. Introduction 1
1.2. A novel Superfluid Magnetic Pump (SMP) 2
1.2.1. AMRR: An application of the SMP 3
1.3. Motivation for sub-Kelvin coolers in space science missions 5
1.3.1. Demand for future generation detector coolers 7
1.4. Overview of refrigerators for space science missions 8
1.5. Current state of the art near Kelvin and sub Kelvin coolers for space science use 10
1.5.1. ^{3}He sorption coolers 11
1.5.2. Adiabatic Demagnetization Refrigerators 13
1.5.3. Dilution Refrigerators 15
1.5.4. Comparison of refrigerators 15
1.6. NASA's requirements for future sub Kelvin coolers 17
1.7. Primary advantages of SMP driven coolers 18
1.7.1. Active Magnetic Regenerative Refrigerators (AMRR) 18
1.7.2. Superfluid Pulse Tube Refrigerators (SPTR) 19
1.7.3. Cold Cycle Dilution Refrigerators (CCDR) 20
1.8. Research objectives 22
1.9. Thesis outline 22
1.10. References 23
2. Preliminary concepts 26
2.1. Introduction 26
2.2. Helium 26
2.2.1. Pure ^{4}He 26

2.2.2. Pure ^{3}He 38
2.2.3. ^{3}He-^{4}He mixtures 40
2.3. Magneto-caloric effect 49
2.3.1. Paramagnetic materials for low temperature magnetic refrigeration 51
2.3.2. GGG properties and suitability 53
2.4. References 56
3. Review of the low temperature facility and equipment 58
3.1. Introduction 58
3.2. Low temperature facility 58
3.3. Measurement and other lab equipment 61
3.4. References 66
4. Modeling of the SMP 67
4.1. Introduction 67
4.2. Qualitative description of the SMP's operation during one cycle 68
4.3. Assumptions required for the SMP modeling 69
4.3.1. Eddy currents in the canister body 69
4.3.2. Superfluid turbulence in the superleak 71
4.3.3. Entropy generation due to pressure drop and heat transfer in the bed 72
4.3.4. Entropy generation within the GGG particles 76
4.3.5. Summary of assumptions 77
4.4. Ideal cycle; a simple model 78
4.4.1. Process I-II (Adiabatic Magnetization) 80
4.4.2. Process II-III (Isothermal Magnetization) 81
4.4.3. Process III-IV (Adiabatic Demagnetization) 82
4.4.4. Process IV-I (Isothermal Demagnetization) 83
4.5. Model predictions and results 84
4.6. References 87
5. Numerical model of an AMRR system: an application of the SMP 88
5.1. Introduction 88
5.2. System description 89
5.3. Cycle operation 90
5.3.1. No-Flow Demagnetization (NFD) 91

5.3.2. Flow Demagnetization (FD) 91
5.3.3. No-Flow Magnetization (NFM): 92
5.3.4. Flow Magnetization (FM): 92
5.4. Numerical model 93
5.4.1. Cold Heat Exchanger (CHX) 95
5.4.2. 1st order AMRR model 98
5.4.3. Numerical regenerator model: 1-D transient 99
5.4.4. SMP 106
5.4.5. Hot Heat Exchanger (HHX) 109
5.5. Potential system losses and limitations 110
5.6. Summary of results 110
5.7. References 111
6. Construction and assembly 113
6.1. Introduction 113
6.2. Superconducting magnets 113
6.2.1. Niobium-Titanium (Nb-Ti) superconducting wire 115
6.2.2. Axial magnetic field of a solenoid 117
6.2.3. Hoop stress 118
6.2.4. Heat generation due to eddy currents in mandrel 119
6.2.5. A.C. losses 120
6.2.6. Maximum temperature rise in mandrel 122
6.2.7. Summary of model parameters 122
6.2.8. Superconducting magnet construction 123
6.3. GGG canisters 130
6.4. Superleak 135
6.5. Superfluid shut-off valve 139
6.6. Venturi flow meter 142
6.7. Differential Pressure gauge 143
6.8. References 147
7. Experimental results 148
7.1. SMP experiment design 148
7.2. SMP experiment procedure 152

7.3. Preparatory steps towards the SMP experiment 159
7.3.1. Pre-checks 159
7.3.2. Preparation 160
7.4. SMP experimental results 162
7.4.1. General trend 164
7.4.2. Temperature amplitude vs. ramp rate 169
7.4.3. Canister temperatures vs. base temperature 169
7.5. SMP experiment data analysis 170
7.5.1. Proof of flow in the SMP circuit 170
7.5.2. Mass flow rate produced by the SMP 172
7.5.3. Mass flow rate versus ramp rate 178
7.5.4. Pump curves for the SMP 181
7.5.5. SMP's energy efficiency 183
7.6. Summary of results 184
7.7. References 185
8. Conclusions and future work 186
8.1. Summary/conclusions 186
8.2. Future work 189
8.2.1. Second canister and superconducting magnet 190
8.2.2. ^{3}He-^{4}He test 190
8.2.3. AMRR, SPTR, and CCDR 191
Appendix 193
Appendix A 193
Appendix B 199
Estimating the CHX requirement 199
EES code for 1st order AMRR model 202
EES code for Regenerator model 204
EES code for the SMP model 218

List of Figures

Figure 1. Schematic of the Superfluid Magnetic Pump (SMP) 3
Figure 2. Schematic of the tandem AMRR system (LHS: Left Hand Side, RHS: Right Hand Side) 5
Figure 3. A simple diagram of a bolometer. 6
Figure 4. Simulation of an event in an ideal calorimeter. (Enss 2005) 7
Figure 5. Image of the JWST (on the left) and SST (on the right) NASA-GSFC. 9
Figure 6. Different cooling approaches as a function of base temperature (data taken from Rando 2013). 9
Figure 7. Cooling power as a function of operating temperature for some proven systems. (Shirron 2008) 11
Figure 8. Schematic of the SPTR (Jahromi 2014). 20
Figure 9. Overview schematic of the CCDR that uses SMPs as its compressor. (Mueller 2012) 21
Figure 10. Temperature-Pressure diagram for ^{4}He (Van Sciver 2012) 27
Figure 11. Mass concentration as a function of reduced temperature below the lambda line. 29
Figure 12. Specific heat Vs. Temperature for ^{4}He (Van Sciver 2012) 31
Figure 13. Entropy per mole of ^{4}He [J/mol-K] at temperatures below the lambda point at atm pressure 32
Figure 14. Viscosity of He II as measured by oscillating disk (Van Sciver 2012). 34
Figure 15. He II critical velocity (Van Sciver 2012) 35
Figure 16. Fountain effect (Thermo-mechanical effect). 37
Figure 17. Temperature vs. pressure phase diagram for ^{3}He (Vollhardt 2013) 39
Figure 18. Phase diagram for ^{3}He-^{4}He mixtures (a) 3-D surface plot (b) T-x diagram projected along saturated pressure surface (Chaudhry 2009) 42
Figure 19. Osmotic pressure of ^{3}He-^{4}He mixture 43
Figure 20. Lines of constant ^{4}He chemical potential on a T-x plane at zero pressure (Chaudhry 2009) 44
Figure 21. Ebner and Edwards Gedanken apparatus, note that the Control Volumes are fixed and not moving with pistons, dashed box (big CV), dot-dashed box (small CV) 45
Figure 22. A paramagnetic material under two conditions: with applied magnetic field and without magnetic field (Jahromi 2011) 51
Figure 23. The heat capacity constant, α vs. ordering temperature T_0 for Gd compounds (Barclay 1981) 53
Figure 24. Temperature of GGG as a function of specific entropy at various constant external applied magnetic fields 54
Figure 25. Specific heat of GGG as a function of temperature at various constant external applied magnetic fields 55
Figure 26. An overall schematic of our 1 Kelvin facility (Helium is traced by numbers, Components are labeled by letters, HX: Heat Exchange(r)); *A*: PT-410 Cryomech cryocooler equipped with vibration isolator, *B*: Cryocooler's 1st stage HX, *C*:1st stage HX platform and shield assembly connected to *B* via heat straps [16], *D*: 2nd stage HX, *E*: 2nd stage HX platform

and shield assembly connected to *D* via heat straps, *F*: Superfluid film killer, *G*: Capillary (fixed J-T valve), *H*:Copper 1 Kelvin pot, *I*: 1Kelvin plate, *J*: evacuated exhaust line, *K*: bellows, *L*: Vacuum isolation valve, *M*: SogeVac SV 25-B rotary vane vacuum pump, *N*: Dewar, *O*: Helium reservoir equipped with a 2 stage pressure regulator. 59
Figure 27. An image of the low temperature facility 61
Figure 28. Cryocon model 44 temperature controller 62
Figure 29. Keithley source meter model 2440 63
Figure 30. Keithley multimeter model 2700 with multiplexer card 63
Figure 31. Capacitance bridge GenRad 1615-A 64
Figure 32. EG&G model 5210 Lock in amplifier 64
Figure 33. Gorman star winder machine 65
Figure 34. Thermal diffusive time constant for GGG vs applied magnetic field 77
Figure 35. Qualitative plots of temperature and applied magnetic field vs. time in an ideal SMP cycle (a) shows purely isothermal SMP cycle, (e) shows purely adiabatic SMP cycle, and (b) through (d) show combinations of the limits in the SMP operation 79
Figure 36. Mass displacement as a function of T_{high} for various values of T_{low} in the SMP 85
Figure 37. Pump power versus T_{high} for various values of T_{low} . The trend for maximum power is shown by the dashed line. 86
Figure 38. A simplified schematic of the AMRR discussed in this chapter. LHS denotes Left Hand Side and RHS denotes Right Hand Side 89
Figure 39. Schematic diagram of the four processes in the AMRR during one cycle operation of the system. Consider Left Hand Side of the system: A) No Flow Demagnetization B) Flow Demagnetization C) No Flow Magnetization D) Flow Magnetization 93
Figure 40. A flowchart diagram of the AMRR model 94
Figure 41. A schematic of the CHX 98
Figure 42. A diagram representing the numerical grid technique used in the AMRR model 101
Figure 43. Temperature profile as a function of axial location through the NFD process. 103
Figure 44. Temperature profile as a function of axial location through the FD process. 104
Figure 45. Temperature profile as a function of axial location through the NFM process..... 105
Figure 46. Temperature profile as a function of axial location through the FM process. 106
Figure 47. SMP process for one cycle operation of the AMRR 107
Figure 48. Number of moles of ^{3}He remaining in the canister through the SMP's operation.... 109
Figure 49. Processes involved in the design of a superconducting magnet. 114
Figure 50. Critical current density of two commercial low temperature superconductors as a function of magnetic field and temperature (Ekin 2006). 116
Figure 51. Cross sectional view of a typical multi filamentary superconducting wire with a resistance network shown along the length of the wire. 117
Figure 52. Applied magnetic field as a function of axial location. 123
Figure 53. Image of the mandrel after machining operation is complete. 124
Figure 54. Wire spool configuration (wire is highlighted for enhanced visual effect). 126
Figure 55. An image taken at a random time during the winding process. 126
Figure 56. Demonstration of protection vs. normal operation circuit. 128
Figure 57. Potted diode pocket. NOTE: *CTD-A521 is white, see excerpt at end of section.... 129

Figure 58. An image of the finished products. 130
Figure 59. An image of the custom made crushing apparatus. 132
Figure 60. A flowchart of the crushing procedure. 133
Figure 61. Schematic of the canister lid. 134
Figure 62. Suspender mechanism for the canisters. 135
Figure 63. An image of the finished canisters. Right image is the premade canister and left canister is the one constructed for this work. 135
Figure 64. An exploded view of the superleak assembly. 136
Figure 65. A semi-sectional view of the superleak assembly. 138
Figure 66. An image of the finished product. 139
Figure 67. Schematic of the SS-4BW-TW valve used to seal against superfluid helium (Swagelok 2015) 140
Figure 68. An image of the superfluid shut-off valve along with a representing schematic. 141
Figure 69. A drawing and image of the venturi flowmeter. 143
Figure 70. Diagram of the dielectric insensitive differential pressure transducer (Talbot 1998) 144
Figure 71. Pressure transducer, finished product. 145
Figure 72. Change in capacitance as a function of differential pressure for the pressure gauge. 146
Figure 73. A diagram of the SMP experimental setup. 150
Figure 74. Phasor diagram representing the balancing procedure for the capacitance bridge. Dotted line shows the path to balancing the bridge. 161
Figure 75. Experimental data for SMP experiment at base temperature of 1.44 K 166
Figure 76. Experimental data for SMP experiment at base temperature of 1.61 K 167
Figure 77. Experimental data for SMP experiment at base temperature of 1.76 K 168
Figure 78. Temperature of the active canister vs. time during a capped experiment. 171
Figure 79. Temperature of the active canister vs. time above the lambda point. 172
Figure 80. Mass flow rate vs. time for the SMP experiment at base temperature of 1.44 K 175
Figure 81. Mass flow rate vs. time for the SMP experiment at base temperature of 1.61 K 176
Figure 82. Mass flow rate vs. time for the SMP experiment at base temperature of 1.76 K 177
Figure 83. Mass flow rate produced by the SMP as a function of superconducting magnet ramp rates for three base temperatures. Note: error bars are very small. 178
Figure 84. Mass flow rate produced by the SMP as a function of base temperature for three ramp rates. 180
Figure 85. SMP pump curve at a base temperature of 1.44 K 182
Figure 86. SMP pump curve at a base temperature of 1.61 K 182
Figure 87. SMP pump curve at a base temperature of 1.76 K 183
Figure 88. Energy efficiency of the SMP as a function of ramp rate at three base temperatures. 184
Figure 0-1 Magnetic field a distance h above the center of a single circular loop carrying current *I* 194
Figure 0-2 A tightly wound solenoid with *n* turns per unit length, magnetic field is calculated along the axis of the solenoid at arbitrary points 195
Figure 0-3 Differential segment of the solenoid 196

Figure 0-4 Diagram of solenoid in two situations (a) the point along the axis of the solenoid is within the solenoid (b) the point along the axis is outside the solenoid 197

List of Tables

Table 1. Advantages and disadvantages of selected sub Kelvin coolers for space science applications info taken from (Clark 2005) 17
Table 2. Some facts on ^{4}He (Keller 1969) *Evaluated at atm pressure 27
Table 3. Some facts about ^{3}He (Van Sciver 2012) *Evaluated at atm pressure 40
Table 4. Some properties required for a good paramagnetic material (Barclay 1981) 52
Table 5. List of some major components in the low temperature facility 60
Table 6. List of measurement and other lab equipment 66
Table 7. Assumptions made for the model of an ideal SMP cycle 78
Table 8. Initial and boundary condition for NFD process. 103
Table 9. Initial and boundary conditions for the FD process. 104
Table 10. Initial and boundary conditions for the NFM process. 105
Table 11. Initial and boundary conditions for the FM process. 106
Table 12. Initial and Boundary conditions for the SMP. 108
Table 13. Summary of the AMRR model results 111
Table 14. Design parameters for the SMP superconducting magnet. 123
Table 15. List of experimental runs for SMP. *Denotes runs not discussed in this subsection for consistency. 163
Table 16. Summary of SMP experimental results 185

Nomenclature

$\vec{A}$	Area element vector
A_λ	Gorter-Mellink constant, 1150 (m-s/kg)
A_c	Cross sectional area (m^2)
A_s	Surface area (m^2)
b	Internal intrinsic magnetic field (0.481 Tesla for GGG)
B	Applied magnetic field (Tesla)
B_0	Constant used in Kim and Anderson model, refer to J_{c0}
c	Specific heat capacitance (J/kg-K)
c	Specific molar density
C	Capacitance (F)
C	Number of distinguishable chemical species
d	Diameter (m)
d_p	Particle diameter
D_h	Hydraulic diameter
$\vec{E}$	Electrical Field vector
E	Energy (J) or (eV)
f	Darcy friction factor
f	He II conductivity function
F	Force (N)
F	Number of intensive internal property
g	Landé-g factor (2 for GGG)
g	Parameter used in conductivity function
G	Mass flux
h	Heat transfer coefficient (W/m^2-K)
h_k	Kapitza conductance (W/m^2-K)
H	Height (m)

i	Specific enthalpy
I	Current (A)
J	Current density (A/m^2)
J	Quantum spin number (7/2 for GGG)
J_{c0}	Kim and Anderson constant $J_c(B)=J_{c0}.B_0/(B+B_0)$
k	Boltzmann's constant
k_{eff}	Effective thermal conductivity (W/m-K)
k_f	Fluid thermal conductivity (W/m-K)
K_r	Constant 3×10^{-6} (cm^{n+1})
$\vec{l}$	Loop element vector
L	Inductance
L	Length
$\dot{m}$	Mass flow rate (kg/s)
n	number of moles
Nu	Nusselt number
$\dot{N}$	Molar flow rate (mol/s)
P	Pressure (Pa)
P	Pump power (W)
Pr	Prandtl number
q	Heat flux (W/m^2)
Q	Total heat (J)
$\dot{Q}$	Heat transfer rate (W)
$\dot{Q}'$	Heat transfer rate per nit length (W/m)
r	Radius (m)
R	Gas constant
Re	Reynolds number
s	specific entropy (J/kg-K)
S	Total entropy (J/K)

t	Reduced temperature T/T_λ
t	Time (s)
th	thickness (m)
T	Temperature (K)
T_b	Interface temperature (K)
T_{base}	Base temperature (K)
u	Specific internal energy (J/kg)
U	Total internal energy (J)
v	Velocity (m/s)
$\bar{v}$	Mean velocity (m/s)
V	Molar specific volume of ^{3}He (27.58×10^{-6} m^3/mol)
V	Electrical potential (Volt)
$\mathcal{V}$	Total volume (m^3)
$\dot{W}$	Rate of work (W)
x	^{3}He concentration
x	Location (m)

Greek symbols

α	Lattice heat capacity constant
α	Heat transfer area per unit length (1/m)
α	Thermal diffusivity (m^2/s)
β	Bohr-Magneton, 9.274×10^{-24} (J/Tesla)
χ	Magnetic susceptibility
Δ	Change in value
η_{FEP}	Fountain effect pump efficiency
ε	Porosity
λ	Lambda point (2.17 K)
λ_{SC}	Fraction of superconductor in wire
Π	Number of phases

ρ	Density (kg/m^3)
ρ_{el}	Electrical resistivity (ohm-m)
τ_{diff}	Diffusive time constant (s)
μ	Viscosity (Pa-s)
μ	Chemical potential
μ_0	Permeability of free space, $4\pi \times 10^{-7}$ (N/A^2)
ν	Molar specific volume (mol/m^3)
ω	Tortuosity
φ	Magnetic flux
σ_θ	Hoop stress (Pa)
ζ	Conductivity ratio k_f/k_{solid}

Superscripts

0	Pure element
3	Helium-3
4	Helium-4
i	Time step
j	Location step
os	Osmotic
SS	Stainless Steel

Subscripts

I, II, III, IV	States
a	inner radius (m)
b	Outer radius (m)
eff	Effective
gen	Generated
int	Intermediate
max	Maximum value

min	Minimum value
n	Normal component of He II
s	Superfluid component of He II
sc	Superfluid critical
th	thickness

Acronyms

AMRR	Active Magnetic Regenerative Refrigerator
CCDR	Cold Cycle Dilution Refrigerator
CHX	Cold Heat Exchanger
FD	Flow Demagnetization
FM	Flow Magnetization
GGG	Gadolinium Gallium Garnet ($Gd_3Ga_5O_{12}$)
LHS	Left Hand Side
NbTi	Niobium-Titanium
Nb_3Sn	Niobium Tin
NFD	No Flow Demagnetization
NFM	No Flow Magnetization
RHS	Right Hand Side
SMP	Superfluid Magnetic Pump
SPTR	Superfluid Pulse Tube Refrigerator

1. Introduction and Literature Review

1.1. Introduction

Development of a novel non-moving part and near thermodynamically reversible Superfluid Magnetic Pump (SMP) is discussed in this work. Traditional fluid based sub Kelvin refrigeration systems use bellows-piston compressors to drive the working fluid in systems such as the dilution, superfluid pulse tube, and active magnetic regenerative refrigerators. These refrigerators are free of any mechanical moving parts except for the compressors. The SMP will provide the advantage of replacing the last remaining moving parts in traditional sub Kelvin coolers, hence making them reliable, efficient, and more compact in future orbital systems. The SMP will also enable continuous operation of such refrigeration systems due to its tandem operation capability, allowing the working fluid to reciprocate during one cycle operation. Current state of the art coolers for space science use are Adiabatic Demagnetization Refrigerators (ADR). Although free of any mechanical moving parts, the superconducting magnet's proximity to sensitive detectors pose a real issue for ADR systems. The SMP provides the great advantage of being able to operate remotely from these sensitive detectors. Systems that use the SMP as their compressor are very likely to not depend on the use of heat switches which pose another issue for current space science missions. The objective of this chapter is to briefly familiarize the reader with the SMP and a novel AMRR system as an application. It proceeds with a brief literature review describing various state of the art technologies and compares them to an AMRR that uses the SMP as its displacer. The general objectives of this research are presented at the end of this chapter.

1.2. A novel Superfluid Magnetic Pump (SMP)

Figure 1 shows a schematic of the SMP discussed in this work. The SMP can be thought of as an enhanced, reliable, and nearly thermodynamically reversible version of traditional Thermo-Mechanical Pumps (TMP). The SMP provides many advantages over the TMPs that are discussed later in this chapter. The SMP has no mechanical moving parts and it consists of a bed packed with a suitable paramagnetic material for use between 1 and 2 K with void space for the working fluid (^{4}He or a mixture of ^{3}He-^{4}He). A superconducting magnetic coil surrounds the bed. Changing the current in the coil changes the magnetic field and therefore the temperature of the paramagnetic material due to the magneto-caloric effect. Because the fluid in the pump body is in good thermal contact with the paramagnetic material its temperature tracks that of the paramagnetic material. As the magnetic field increases the magnetic entropy in the paramagnetic material decreases causing the thermal entropy of the material and the fluid to increase resulting in an increase in temperature. When the field is reversed the magnetic entropy in the paramagnetic material increases causing the temperature of the material and fluid to decrease. This process is nearly reversible because the entropy used to increase the fluid temperature during the high-pressure part of the pump cycle comes from the magnetic entropy of the paramagnetic material and can be returned to the material when the magnetic field is reduced. This eliminates the need for the thermal link to the precooling stage and the need to lift all of the generated entropy that would result from a heater in a traditional TMP. This new type of pump is nearly thermodynamically reversible in its theoretical limit.

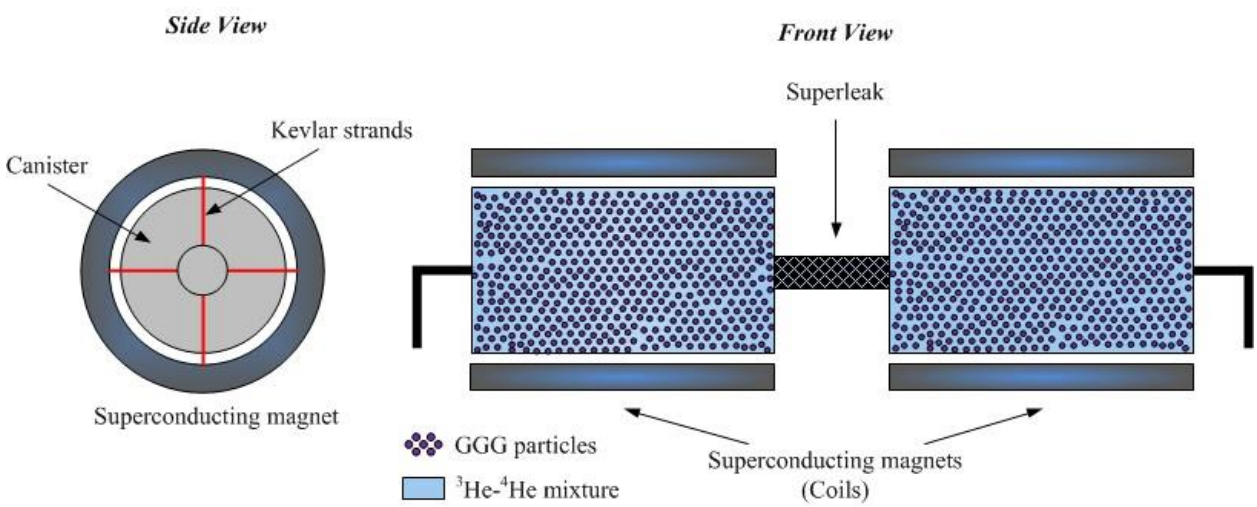

Figure 1. Schematic of the Superfluid Magnetic Pump (SMP)

1.2.1. AMRR: An application of the SMP

Magnetic refrigeration is a technique that utilizes the magneto-caloric effect in a paramagnetic material. The smaller goal of this research is to predict the performance of a proof of concept non-moving part sub Kelvin magnetic refrigeration system that can provide 600 µW of cooling power at 750 mK and reject heat to a platform at 1.57 K using the SMP discussed in this work. The objective of this subsection is to provide a brief overview of the system setup and operation.

Figure 2 shows a schematic of the AMRR discussed in this work. It is a tandem system, meaning it is two refrigeration systems that operate half cycle out of phase from each other. It consists of a displacer, two regenerators, two hot heat exchangers, and one cold heat exchanger. The AMRR uses a liquid mixture of ^{3}He-^{4}He that moves through finely crushed Gadolinium Gallium Garnet (GGG) in the regenerator beds during one cycle of operation. This liquid mixture will be referred to as the “fluid” and the GGG as the “refrigerant”.

One cycle of operation of the AMRR begins with the demagnetization of the Left Hand Side (LHS) regenerator's refrigerant from peak field while fluid is stagnant throughout the entire system. This demagnetization reduces the refrigerant's temperature, which in turn causes the warmer surrounding fluid to deposit its heat into the refrigerant. Demagnetization continues until the bottom of the LHS regenerator reaches the target low temperature. At this time the LHS displacer begins pushing fluid out through the entire system in a counter clockwise direction. The LHS regenerator's refrigerant is further demagnetized while fluid travels downward until it runs out of field. Note that the field change was controlled in such a way to keep the bottom temperature below the target low temperature so fluid is removing heat from the cold heat exchanger throughout this process. The displacer stops moving fluid at the end of the demagnetization process. Magnetization of the LHS regenerator's refrigerant begins while fluid is stagnant until the temperature throughout the regenerator is increased. The displacer begins pushing fluid through the system in a clockwise direction. Magnetization of the LHS regenerator continues, allowing the refrigerant to reject its heat into the cooler surrounding fluid. The fluid must exit the top of the regenerator at a temperature warmer than the hot heat exchanger allowing the fluid to reject the energy at the hot heat exchanger. The magnetization continues until peak field is reached at which point the system returns to the beginning of the cycle.

One of the key features of this AMRR is the displacer technology. This proof of concept cooler can also demonstrate this unique displacer technology in a refrigeration system, which will enable other coolers at even lower temperatures, such as the dilution, pulse tube superfluid, and combination-Continuous Adiabatic Demagnetization refrigeration (CADR) systems to be free of any moving parts. The motivation behind using such coolers as an application of the SMP is presented next.

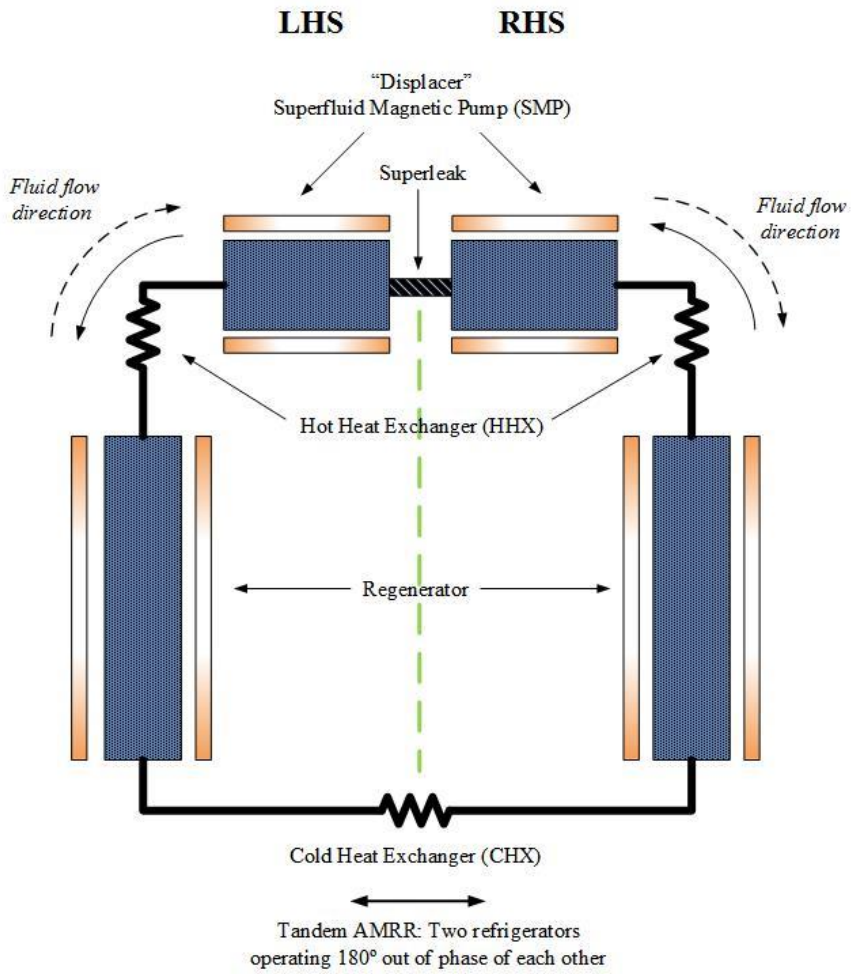

Figure 2. Schematic of the tandem AMRR system (LHS: Left Hand Side, RHS: Right Hand Side)

1.3. Motivation for sub-Kelvin coolers in space science missions

Sub Kelvin cooling is required for many of the most sensitive detectors used in space science applications. These detectors can be used to investigate some of the most important cosmological questions such as the existence and nature of dark matter, dark energy, quasi-particles, star formations, etc. There are several reasons that these detectors must be cooled to extremely low temperatures to achieve the best resolution. An example of a simple detector, a microcalorimeter, is depicted in Figure 3. It contains only three parts: An absorber or thermal mass that absorbs the incident power and thermalizes the energy, a perfectly coupled thermometer that

measures the temperature increase (spike) in the absorber, and a weak thermal link to a heat sink that returns to the absorber temperature to some defined value in the absence of a signal.

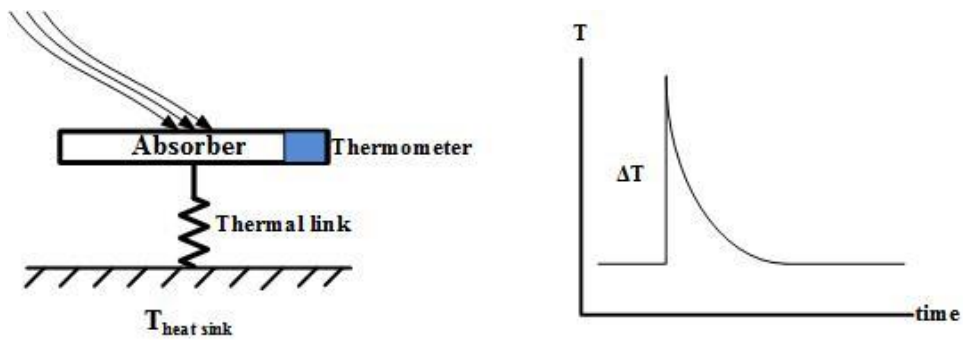

Figure 3. A simple diagram of a bolometer.

The most important reason for sub Kelvin cooling in these detectors is to minimize the noise to signal ratio in order to be able to make accurate measurement of the incident energy. Figure 4 shows an example of just signal and signal + noise received by a bolometer of the type shown in Figure 3. Many sources of noise are inherently present in thermal systems so the goal is to identify and minimize these sources of noise, which include Thermodynamic Fluctuation Noise (TFN), Thermometer Johnson-Nyquist noise, Load resistor Johnson noise, Amplifier noise, and Photon background noise. For a Transition Edge Sensor (TES), a type of detector where superconducting transition temperature is exploited for measurement purposes, all of these sources of noise give rise to the following relation between energy resolution ΔE and operational temperature T of a detector (Cabrera 1998):

$$\Delta E \simeq 2.35\sqrt{4\,k\,T\,E_{max}} \qquad (1)$$

where k is Boltzmann's constant, and E_{max} is the maximum incident energy that a detector will experience.

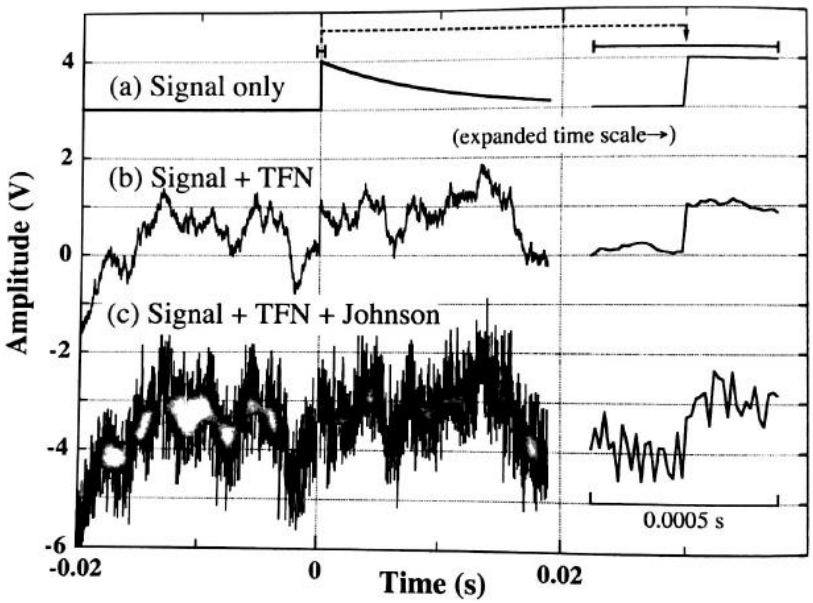

Figure 4. Simulation of an event in an ideal calorimeter. (Enss 2005)

By now it is apparent that the lower the operational temperature of the detector, the smaller the energy levels that can be resolved. For example if the maximum incident energy of photon is 10 keV then the minimum energy resolved is 3.8 eV at 780 mK as opposed to 7.2 eV at 2.7 K.

1.3.1. Demand for future generation detector coolers

The ideal astrophysics detection technology would have a large observational field of view, very fine spatial and spectral resolution, a very large effective measurement area, and the ability to handle bright sources with precision timing. As a result of this, demand has significantly grown for larger arrays of detectors in space science applications. Thus development of more powerful coolers with a capability to efficiently distribute cooling over these large arrays is essential. For example, a modest cooling power of less than 1 μW at 60 mK was sufficient for the small (6 x 6)

detector arrays used in early instruments using X-ray microcalorimeters (Kelley 1999). However, recent rapid advances in arraying and multiplexing technologies such as those discussed by Noroozian et. al. (2013) are generating a need for higher cooling powers (5-10μW) and lower temperatures (less than 30 mK). Another significant requirement for future detectors is the development of coolers with high thermal stability at ultra-low temperatures. For example Microwave Kinetic Inductance Detectors (MKIDs) require extremely stable ultra-low temperature background in the highest sensitivity applications. The development of more powerful coolers with a more stable ultra-low temperature that is in line with NASA's requirements for future missions is essential to fulfill the demands of the astrophysics community. A review of the past, current, and future space science coolers is provided in the following sections.

1.4. Overview of refrigerators for space science missions

Various refrigeration techniques exist for space science applications. When designing a low temperature system it is most efficient to use multiple stages of cooling for improved thermodynamic efficiency and to utilize optimal cooling techniques for the various temperature ranges. These techniques are mainly divided into two sub-categories: passive cooling and active cooling. Passive cooling is predominantly used as the first stage cooler in the form of radiators (providing the highest heat sink temperature). Radiators take advantage of the biggest heat sink in the universe, deep space, to expel the heat generated in the lower stages of a cooling system via thermal radiation. Examples of this technique used in a mission are the James Webb Space Telescope (JWST) and Spitzer Space Telescope (SST) as shown in Figure 5. The other type of passive cooling is stored cryogen cooling, which can provide lower temperatures than radiators.

Samples are kept at low temperatures by expelling the parasitic heat into a stored cryogen vessel which results in the gradual boil-off of the stored cryogen. Active coolers are either single shot or cyclic. Different types of active coolers exist, such as mechanical coolers (pulse tube and Stirling), Dilution, CADR, Sorption, JT, and Normal-Insulator-Superconducting (NIS). Figure 6 provides an overview of the different cooling approaches as a function of base temperature (data taken from Rando 2013, self-compiled).

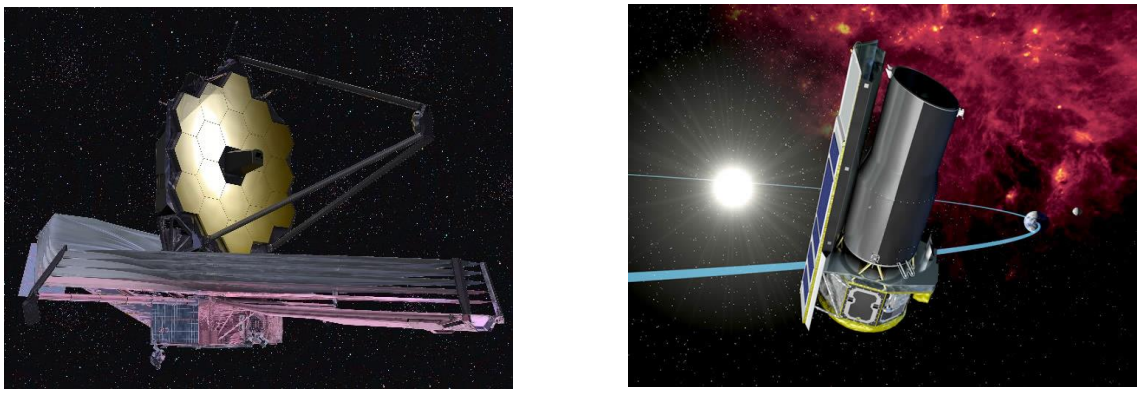

Figure 5. Image of the JWST (on the left) and SST (on the right) NASA-GSFC.

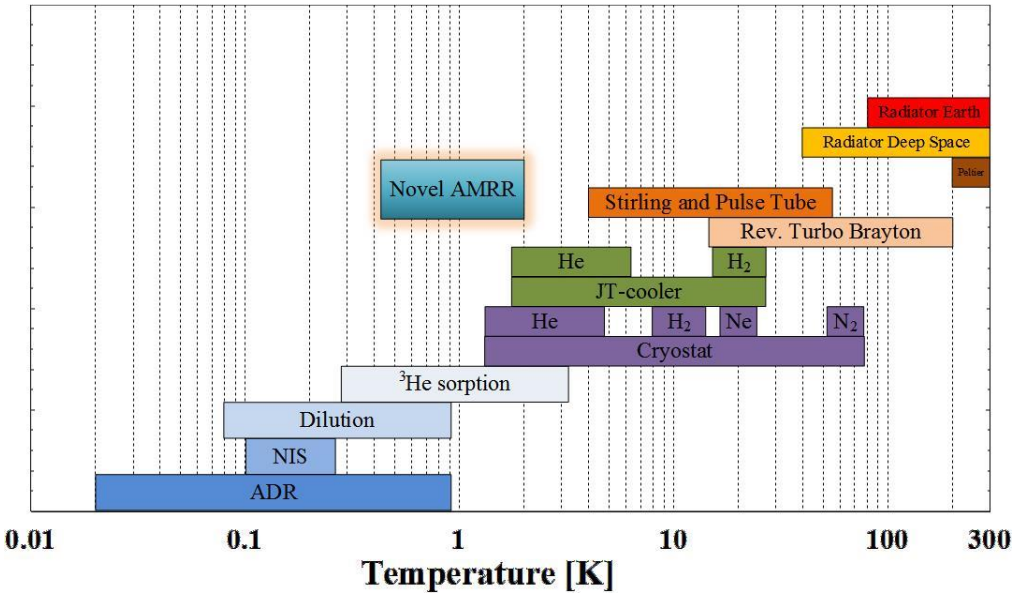

Figure 6. Different cooling approaches as a function of base temperature (data taken from Rando 2013).

1.5. Current state of the art near Kelvin and sub Kelvin coolers for space science use

As discussed earlier, the trend for future missions is to use progressively larger detector arrays, with a correspondingly larger heat lift requirement. Future missions will implement 1000+ pixel arrays and current efforts in the cooler technology are rapidly underway to meet minimum requirements of future detectors. A number of methods exist for cooling to temperatures below 1 K such as: solid state coolers (i.e. ADR and NIS), and fluid based systems (i.e. ^{3}He sorption and dilution refrigerators). Both types have advantages and disadvantages. For example, they vary considerably in their cooling capacities, operating temperature range, heat sink temperature range, and requirements for inclusion with various detector and instrument components. In some cases, they are viable over only part of the necessary temperature range between detector and heat sink, and therefore must be used as part of a larger cooling chain.

One of the major challenges and constraints on the design is the heat sink to which the sub Kelvin cooler needs to reject its heat. The majority of the sub Kelvin coolers were initially coupled to a superfluid helium bath. These baths generally provided a base temperature of 1 K as the heat sink. Rapid helium boil-off, inadvertent superleaks, stratification issues, and complex designs were among chief reasons that these types of heat sinks were abandoned. Mechanical coolers (i.e. pulse tube refrigerators) replaced the superfluid baths as the heat sink. However mechanical moving parts and vibration inducing mechanisms from the hot side of these type coolers introduced a new challenge for space science cooling. The community has shifted toward using solid state systems and multi-staging ADRs to replace the mechanical coolers. Figure 7 shows a graph of demonstrated cooling power in space as a function of operating temperature for some sub Kelvin

coolers. The goal of this section is to give a brief overview of state of the art sub Kelvin cooler technologies and identifying each one's capabilities, advantages and disadvantages.

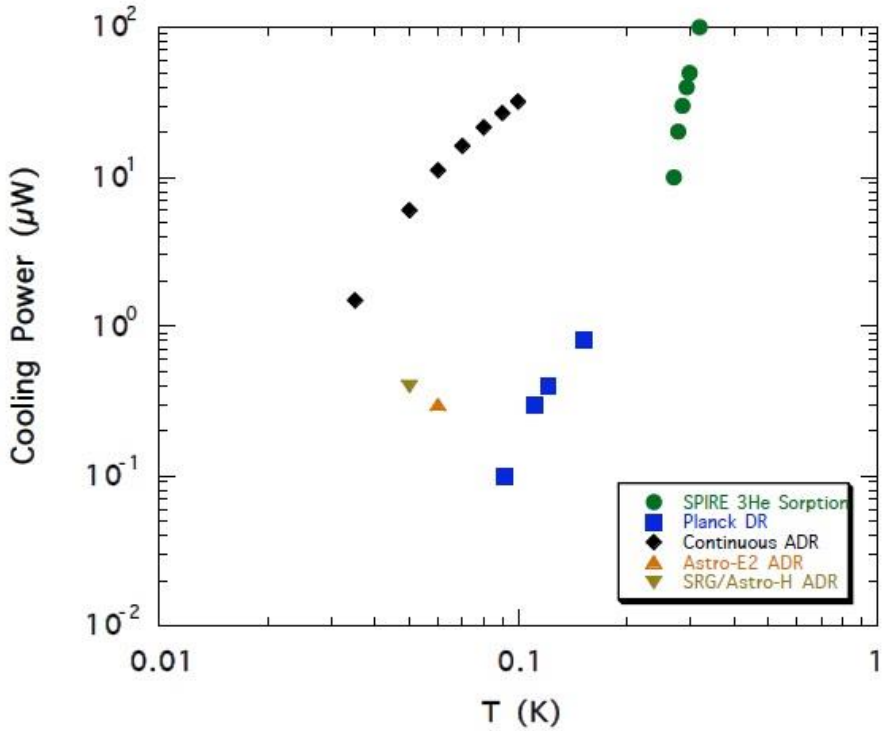

Figure 7. Cooling power as a function of operating temperature for some proven systems. (Shirron 2008)

1.5.1. ^{3}He sorption coolers

Sorption refrigerators use a sorption pump to evaporate liquid from an evaporator to produce cooling. Within the sorption pump is a material that has a large surface area. This large surface area correlates to a large binding energy for ^{3}He, so when the material is cold ^{3}He is strongly attracted to its surface and a very low vapor pressure above the material results. The pumping action follows from this low vapor pressure, and drives large-scale evaporation of liquid from the evaporator. The remaining liquid is cooled until the evaporation rate balances the heat load. This balance point is, in principle, variable through adjustments in the material or surface

area. In practice, however, helium requires a very large surface area relative to the amount of helium that can be fully adsorbed. In order to maintain a low equilibrium pressure throughout the pumping phase, the helium should take up only a fraction of an atomic layer on the getter surfaces. As a result of this constraint, the evaporator is typically operated near or moderately below the limiting temperature (300 mK for ^{3}He and 1 K for ^{4}He refrigerators). Heaters coupled to the evaporator can stabilize the base temperature, while long-term control is achieved through regulation of the sorption pump temperature. Minimizing parasitic heat loads through careful design or through the use of multiple stages and ensuring a low impedance pumping path has produced ultimate temperatures of 200 mK or slightly lower (Bhatia 2000).

During the hold time of the refrigerator, liquid is evaporated as heat is absorbed. Once the liquid is depleted, the ^{3}He gas must be desorbed and re-condensed by warming and recycling the sorption pump. If using charcoal as the material, as is typical, the temperature must be raised to about 50 K to desorb the gas (Duband 2008). In ground-based coolers, this can be done in a condenser anchored to the heat sink, from which the liquid can drip back into the evaporator. Coolers in space science missions will need to re-condense within the evaporator itself. This is accomplished by designing the evaporator so that the liquid will be sure to make thermal contact and be properly confined through surface tension. During the condensation phase, the evaporator is thermally connected to the heat sink with a heat switch. This same heat switch provides thermal isolation during the cool down and operational phase. Typically, the heat sink will be 2.5 K or lower. While it could be as warm as 3.2 K – the critical point of ^{3}He – this would produce considerable waste heat, since the pump would need to be sufficiently heated to raise the helium pressure above the critical value. The lower typical temperature reduces the power needed as well as the amount of helium that must be evaporated to cool to the operating point. The amount of

liquid helium remaining once the operating point has been reached, as well as the detector heat load are the determining factors in a sorption pump's hold time. During operation, waste heat is produced from the heat of adsorption in the pump. During recycling, the heat of condensation of the ^{3}He charge, the heat required to operate the heat switch, and the heat required to warm the sorption bed all contribute to waste heat as well. For the Herschel cooler, operating at 277 mK with a 10 μW load, the total heat rejected is 23 mW into the superfluid helium at ~1.5 K. As seen from this data, the sorption refrigerator is not very efficient (~1.5% of Carnot) (Shirron 2009); in fact this is one of the primary disadvantages of this type of refrigerator.

1.5.2. Adiabatic Demagnetization Refrigerators

A typical single-shot ADR consists of a paramagnetic material in a capsule (often called a "salt pill"), a heat switch, and a superconducting magnet. During magnetization, the salt pill is thermally connected to a heat sink via the heat switch. This heat sink also thermally isolates the salt pill after reaching peak field. Subsequent demagnetization then causes the salt pill to cool to its operating temperature. This point will be reached with some magnetic field remaining, depending on starting and ending temperatures and the peak field. This allows regulating the temperature – with no waste heat input – as the salt pill absorbs heat both from the load (detectors or other experiment components) and parasitic sources. As heat is absorbed, the field is continually reduced until it reaches zero. At this point, the ADR must then be recycled. For space missions, the hold time requirement is typically 24 hours, followed by a recycling period of no more than 1 hour.

While the magneto-caloric effect can be used over a very wide range of high and low temperatures, there are practical limitations for a single stage device. One significant limitation is that the magnetic field applied must be roughly proportional to the heat sink temperature (1 T for

a 1 K sink, and 4 T for a 4 K sink for operation at 100 mK) for a single stage ADR to reach very low temperature (Serlemitsos 1998). At present, high field to current ratio magnet technology is limited to NbTi, and practically limited to heat sinks at 5 K or lower and fields of 4 T or lower. Typical single-stage ADRs that operate at 50 mK requires a heat sinks to be approximately 2 K (Shirron 2014). With colder heat sinks, temperatures as low as 20 mK are readily achievable. However, ADRs are easily adaptable to multi-stage configurations which also provide size and mass benefits. As an example, the single-stage ADR on Astro-E2 operating at 60 mK used 920 g of ferric ammonium alum refrigerant, a 2 T NbTi magnet and a 1.3 K superfluid helium bath as a heat sink. Its net (detector) cooling power was 0.3 microwatts, and the total mass was 15 kg (Kelley 2007).

The Astro-H cooler uses a redundant heat sink: one operating at liquid helium temperature and another utilizing the Joule-Thomson (JT) effect at ~2 K. This two stage cooler uses two distinct refrigerants. The higher stage is gadolinium lithium fluoride (GLF) with a magnet operating at 3 T, while the lower stage uses chrome potassium alum with a magnet operating at 2 T. The lowest stage is capable of removing 0.4 μW at a temperature of 50 mK, and the total mass of the system is 8 kg (Mitsuda 2008).

ADR systems have a few disadvantages, one of which they share with the sorption cooler: significant heating can come from operation of the heat switches, especially active gas-gap switches. Hysteresis losses can contribute to significant loss of efficiency in these systems as well. Another disadvantage is the need for current leads for the magnets – on the order of a few amps – but recent development in high temperature superconductor materials allow these currents to be introduced to low temperatures with minimal impact on the thermal design.

1.5.3. Dilution Refrigerators

Dilution refrigerators (DRs) were developed in the 1960s and quickly became the standard laboratory sub-Kelvin cooling. In comparison to other techniques (principally ADR and ^{3}He sorption), DRs operated continuously, had very large cooling power, and could reach temperatures of a few mK. Dilution refrigerators heavily rely on gravity for phase separation, hence, successful demonstration of DRs in microgravity conditions has proven difficult.

The Planck mission, however, developed an open-cycle DR that has achieved cooling to 100 mK (Triqueneaux 2006). The system feeds gaseous ^{3}He and ^{4}He from external storage tanks, condenses them at 4.5 K with a sequence of radiative and Joule-Thomson (JT) coolers, and pre-cools the individual streams to 1.6 K with a JT cooler which uses the exiting ^{3}He-^{4}He mixture as its expansion fluid. The two streams are further pre-cooled in counterflow heat exchangers with the exiting mixture.

The mixing of the two streams is an endothermic process. Because the ^{4}He flow must be cooled by the dilution process, the net cooling is much less than that for a conventional DR cycle where ideally only ^{3}He is circulated. Utilizing careful minimization of parasitic heat loads, the 100 nW cooling power is sufficient to cool the bolometers to 100 mK. The external tanks contain enough ^{3}He and ^{4}He to achieve a short lifetime of 2 years. The pre-cooling requirement from auxiliary cryocoolers for the dilution unit is 2 mW at 4.5 K (Shirron 2009). Like sorption coolers, this results in a low overall efficiency, less than 1% of Carnot. To improve on this performance, plans are underway to convert the operation to a closed-cycle. This will potentially increase the cooling power into the range of 1 μW at 50 mK, and eventually remove the lifetime limitation.

1.5.4. Comparison of refrigerators

An overview of major sub Kelvin cooler technologies, and challenges associated with each method was presented in previous sections. Among biggest challenges are relatively short recycling time, use of heat switches such as gas gap, low efficiency, high mass, and potentially low reliability. However each technology offers a unique application to certain temperature range and/or cooling powers that enables them to be combined to produce a more efficient, lower mass cooler overall. For example the high cooling power of ^{3}He sorption coolers allow it to be coupled to a lower stage, more efficient cooler such as ADRs. The ^{3}He is capable of providing high cooling power at 300 mK to help lower stage ADRs provide cooling at 50 mK. Table 1 provides a summary of advantages and disadvantages associated with each type of sub Kelvin cooler. NIS coolers were not discussed previously and are not commonly used, however they are included in this table for completeness.

Type	Power/Cooling Temp range	Advantages	Disadvantages
^{3}He sorption	10 µW at 300 mK	Light weight	Reliance on heat switch
			High temp recycling
		Simple mechanism	Issues with gettering
Single-shot ADR	200 nW to 1 µW at 50 mK	Long hold times	Low temperature span
		Simplest	Reliance on heat switch
		Solid state	Excessive Heat due to Eddy current
		Demonstrated	Field close to detectors
Multi-stage ADR	5-10µW at 50 mK	Higher cooling power	Heavy reliance on heat switch
		Solid state	
		Demonstrated	

		Higher heat sink T	Field close to detectors
Dilution	100 µW at 100 mK	Extremely powerful	Phase separation
		Continuous	
		Higher heat sink T	
NIS*	40-80 nW at 200 mK	Simple	Low power
		Reliable	Micro scale
		Direct detector pixel integration	High parasitic heat

Table 1. Advantages and disadvantages of selected sub Kelvin coolers for space science applications info taken from (Clark 2005)

1.6. NASA's requirements for future sub Kelvin coolers

NASA Goddard Space Flight Center (GSFC) has recently published requirements for various technologies used in future space science missions. Among them are requirements for future sub Kelvin coolers that must be met by 2025 (CorTech MATRIX 2013). These requirements are listed here:

- Combination of coolers must yield cold temperatures well below 1 K with powers of 100's of µW.
- Combination of coolers are preferred to operate from 4 K down to 100 mK with a continuous heat lift of 10 µW.
- Design must be compact and light weight (typically below 5 kg).

- Coolers must be free of mechanical moving parts for low induced vibrations to sensitive instruments.
- Coolers must meet minimum compatibility requirements for integration with far-IR telescopes in the next decade.
- Coolers must be able to distribute cooling over large areas for either detection technology or shielding.
- Coolers must be able to operate reliably in micro gravity conditions.

1.7. Primary advantages of SMP driven coolers

As noted earlier, the SMP is free of any moving mechanical parts. It eliminates the need for a gas gap or mechanical heat switch and it will enable relevant sub Kelvin refrigeration systems to operate continuously and reliably. It has the capability of distributing cooling over large surface areas. The advantages of using an SMP in various types of sub Kelvin coolers are listed and discussed in the next three sub sections. The AMRR, SPTR, and CCDR are discussed as primary examples of systems that could benefit from using the SMP as their compressor/circulator.

1.7.1. Active Magnetic Regenerative Refrigerators (AMRR)

The AMRR system discussed in this work is uniquely positioned to satisfy NASA's requirements for future sub Kelvin coolers. The cooler is free of any moving parts, will be able to provide relatively high cooling powers at low temperatures, will be able to efficiently remove heat from large arrays of detectors, and will significantly reduce the presence of applied magnetic field in the vicinity of detectors that would otherwise introduce an adverse effect on the measurements.

An AMRR could significantly reduce several risk factors on future Gamma, infrared, and X-ray Astrophysics missions and enhance the capabilities of NASA-GSFC Cryogenics and Fluids branch. An AMRR system is relatively easy to understand and study, hence making this system a suitable first choice for demonstrating the potentials of an SMP in a sub Kelvin refrigerator. A successful demonstration of this technology will lead to significant development of other types of related refrigeration systems using the novel circulator in the proposed AMRR. An AMRR of this type is well suited to be used in combination with other sub-Kelvin coolers, enabling high heat lifts at warmer stages of very-low temperature ADRs.

1.7.2. Superfluid Pulse Tube Refrigerators (SPTR)

The magnetically driven superfluid pulse tube refrigerator (SPTR) could be a viable option for sub Kelvin cooling of space science detectors. The refrigerator requires no moving parts and an analysis published by Jahromi and Miller (2014) shows that the SPTR can provide cooling to temperature below 200 mK while rejecting heat at 1.6 K.

A schematic of the SPTR is shown in Figure 8. The refrigerator consists of a near reversible SMP module, two warm heat exchangers, a recuperative heat exchanger, two cold heat exchangers, two pulse tubes and an orifice. This machine actually consists of two superfluid pulse tubes running 180 degrees out of phase. The flow from one machine exchanges heat with flow from the other in the recuperator. This technique is used because most solid regenerator materials do not have significant heat capacity compared to the helium working fluid at temperatures below 1 K and therefore conventional regenerators are impractical. The SPTR is different from the previous superfluid Stirling cycle machines such as those demonstrated by Swift and Kotsubo (1991) Brisson and Watanabe (1996) and Phillips et. al. (2003) because a magnetic fountain effect pump replaces the warm end pistons, eliminating all moving mechanical parts.

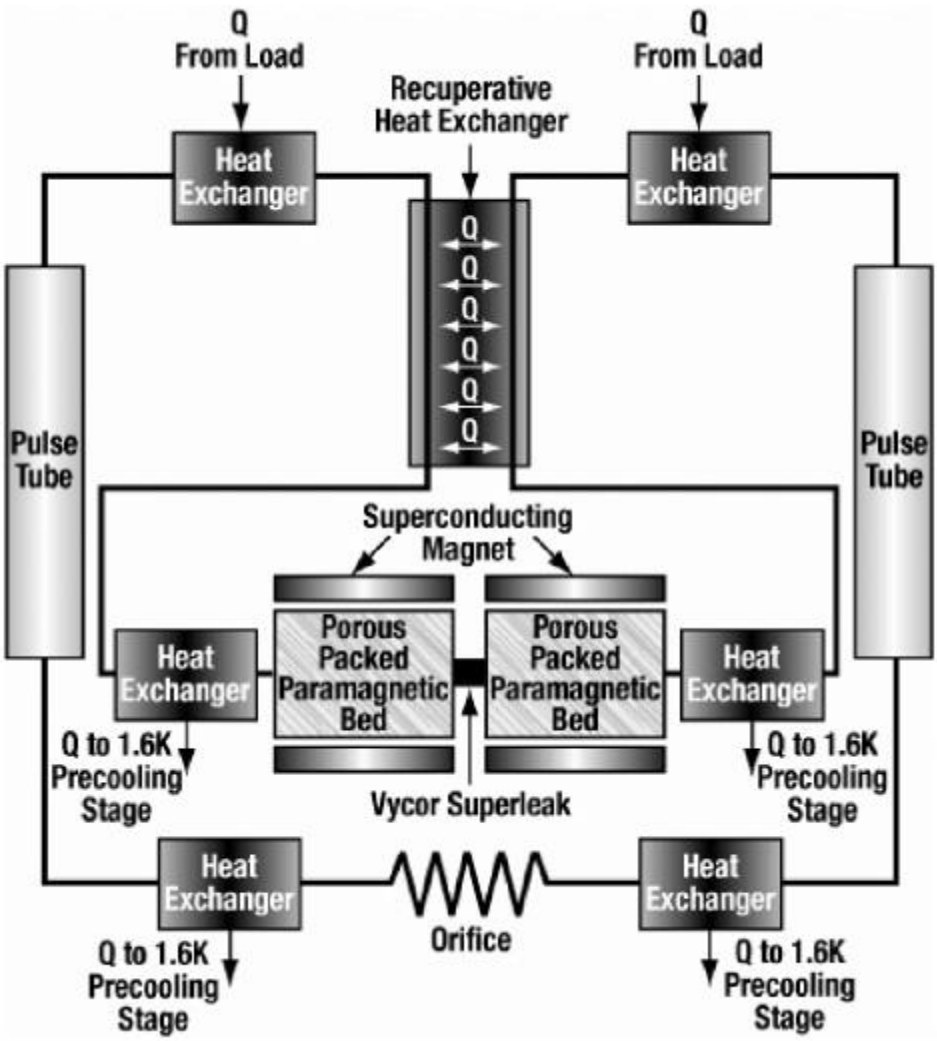

Figure 8. Schematic of the SPTR (Jahromi 2014).

1.7.3. Cold Cycle Dilution Refrigerators (CCDR)

One existing method for attaining sub-Kelvin temperatures is helium dilution refrigeration – a continuous cooling cycle relying on the endothermic mixing of two helium isotopes, ^{3}He-^{4}He, that occurs at temperatures less than 860 mK. A proposed modified version of the traditional helium dilution cycle, termed the *cold-cycle* ^{3}He-^{4}He dilution refrigerator, shown in Figure 9 attempts to overcome limitations of the existing cycle by replacing and altering several key

components, chief among them the novel SMP, in an effort to improve the thermodynamics and reliability of the machine. Recent simulations estimate that 80 μW of cooling capacity can be achieved at a temperature of 100 mK, while a minimum temperature of about 50 mK is attainable at no cooling load (Mueller 2012).

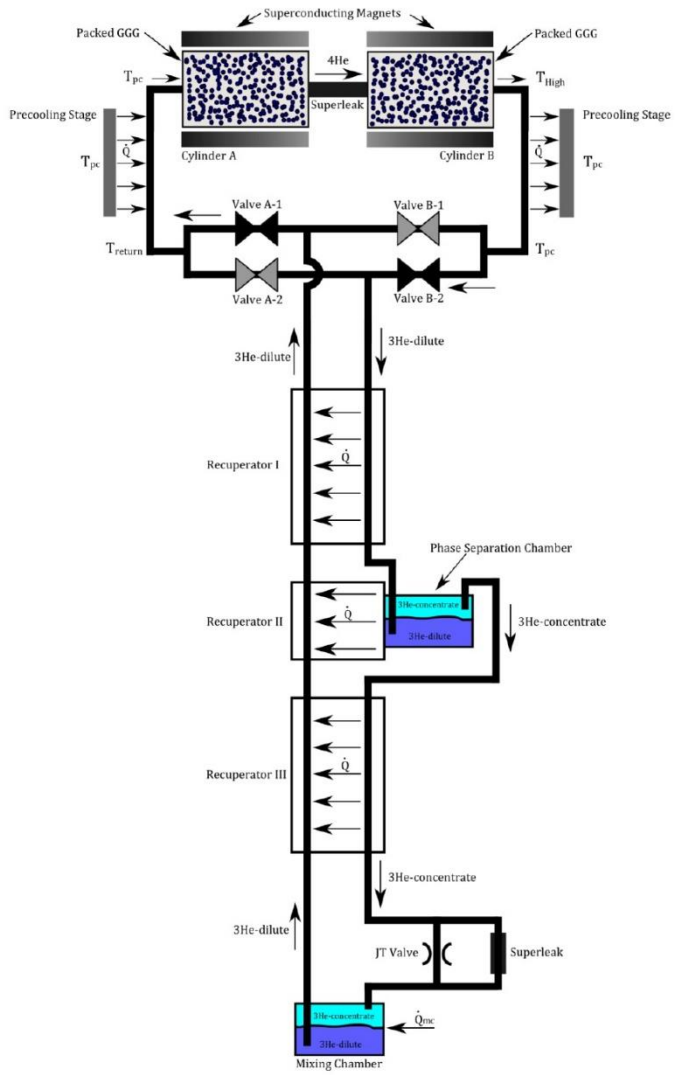

Figure 9. Overview schematic of the CCDR that uses SMPs as its compressor. (Mueller 2012)

1.8. Research objectives

The primary objective of this research is to develop and experimentally verify a proof of concept SMP with pure ^{4}He, collect data of power input versus temperature and to measure the mass flow rate produced by this pump under different run conditions as well as developing a pump curve that maps the performance of the proof of concept SMP. As a secondary objective the author attempts to model and simulate the performance of a proof of concept ^{3}He-^{4}He AMRR that is capable of removing 600 μW of heat at 750 mK and reject its heat to a platform at 1.57 K using the novel SMP that is experimentally verified by this work. A 1 K temperature platform previously developed at UW-Madison will act as the heat sink for this AMRR (Jahromi 2011). A numerical model of the regenerators was developed that carries out a transient simulation of the components in the cycle during one cycle of operation. This model has the capability to predict the cooling power, molar flow rate of mixture, required temperature of the heat sink as well as the heat rejection power of the system.

The key technology discussed in this work is the non-moving part displacer. This displacer has great potential to be used in various other sub Kelvin refrigeration systems, providing reliable, long lasting, and efficient systems that can be used in future space science missions. Therefore, successful demonstration of the displacer will create many opportunities for new and improved sub Kelvin refrigeration systems.

1.9. Thesis outline

The purpose of the remainder of this document is to show the process that has been used to develop the experimental model of the SMP, and the AMRR, design and construction of the SMP as well as test setup and results from this test. Chapter 2 gives a brief introduction to the

fundamental properties of various concepts used in the SMP and AMRR that serves as a primer to understanding the model and design of the system. Chapter 3 provides a brief introduction to the low temperature facility and equipment that is used to experimentally test the SMP. Chapter 4 provides a detailed discussion of one cycle operation of the SMP along with a simple model of an ideal system of this type. A numerical model of an AMRR as an example of a system that can benefit from the use of the SMP is discussed in chapter 5. Construction and assembly of the SMP apparatus along with the test set up is detailed in chapter 6. This includes a discussion of special techniques used in low temperature experiments that resulted in the ultimate success of the SMP test. Chapter 7 provides the experimental results of the SMP. An analysis and discussion of the trends observed in the experimental results is provided in this chapter as well. Finally the main document concludes by providing future work suggestions in chapter 8. A list of pertinent materials such lengthy derivations, and programming codes is provided as an Appendix to this document.

1.10. References

Bhatia, R. S., et al. "A three-stage helium sorption refrigerator for cooling of infrared detectors to 280 mK." Cryogenics 40.11 (2000): 685-691.

Cabrera, B. and Clarke, R. M. and Colling, P. and Miller, A. J. and Nam, S. and Romani, R. W., Applied Physics Letters, 73, 735-737 (1998), DOI:http://dx.doi.org/10.1063/1.121984

Clark, A. M., et al. "Cooling of bulk material by electron-tunneling refrigerators." Applied Physics Letters 86.17 (2005): 173508.

CorTech Matrix, NASA-Goddard Space Flight Center Internal publications (2013)

Duband, L., et al. "Herschel flight models sorption coolers." Cryogenics 48.3 (2008): 95-105.

Enss, Christian, ed. *Cryogenic particle detection*. Vol. 99. Springer, 2005.

Jahromi, A. E., Master's thesis, University of Wisconsin – Madison, 2011.

Jahromi, Amir E., and Franklin K. Miller. "A sub-Kelvin superfluid pulse tube refrigerator driven by paramagnetic fountain effect pump." *Cryogenics* 62 (2014): 202-205.

Kelley, R., et al. "Toward a 2-eV microcalorimeter x-ray spectrometer for Constellation-X." *SPIE's International Symposium on Optical Science, Engineering, and Instrumentation*. International Society for Optics and Photonics, 1999.

Kelley, Richard L., et al. "The Suzaku high resolution X-ray spectrometer." Publications of the Astronomical Society of Japan 59.sp1 (2007): S77-S112.

Kotsubo, V., and G. W. Swift. "Superfluid Stirling-cycle refrigeration below 1 Kelvin." *Journal of Low Temperature Physics* 83.3-4 (1991): 217-224.

Mitsuda, Kazuhisa, et al. "The X-ray microcalorimeter on the NeXT mission." SPIE Astronomical Telescopes+ Instrumentation. International Society for Optics and Photonics, 2008.

Mueller, B. E., Master's thesis, University of Wisconsin – Madison, 2012.

Noroozian, Omid, et al. "High-resolution gamma-ray spectroscopy with a microwave-multiplexed transition-edge sensor array." Applied Physics Letters 103.20 (2013): 202602.

Phillips C, Brisson JG, Preliminary experimental results using a three-stage superfluid stirling refrigerator. In: cryocoolers 12: Proceedings of the 12th international cryocoolers conference; 2003. p. 681–86

Rando, Nicola. "Cryogenics in space." *Observing Photons in Space*. Springer New York, 2013. 639-655.

Serlemitsos, A. T., M. SanSebastian, and E. S. Kunes. "Final design of the XRS/Astro-E ADR." Advances in cryogenic engineering. Springer US, 1998. 957-963.

Shirron, Peter. "Cryogenic Technology for CMB-Pol: Sub-Kelvin Cooling." *Proc. Technology Development for a CMB Probe of Inflation, Boulder CO http://cmbpol. uchicago. edu* (2008).

Shirron, Peter, et al. "Cooling system for the soft x-ray spectrometer (SXS) onboard ASTRO-H." *SPIE Astronomical Telescopes+ Instrumentation*. International Society for Optics and Photonics, 2009.

Shirron, Peter J. "Applications of the magnetocaloric effect in single-stage, multi-stage and continuous adiabatic demagnetization refrigerators."*Cryogenics* (2014).

Triqueneaux, S., et al. "Design and performance of the dilution cooler system for the Planck mission." Cryogenics 46.4 (2006): 288-297.

Watanabe, A., G. W. Swift, and J. G. Brisson. "Measurements with a recuperative superfluid Stirling refrigerator." *Advances in cryogenic engineering*. Springer US, 1996. 1527-1533.

Mark V. Zagarola., and Chen, Weibo, "Development of a Low-Temperature AMRR for Space Applications." (2011).

2. Preliminary concepts

2.1. Introduction

The objective of this chapter is to present fundamental properties of pure ^{3}He, ^{4}He, and ^{3}He-^{4}He mixtures along with a brief introduction to the magneto-caloric effect and thermodynamic state properties of Gadolinium Gallium Garnet (GGG). These fundamental discussions will act as a foundation for future chapters.

2.2. Helium

Helium is a colorless, odorless, non-toxic, monatomic element. Due to its weak intermolecular potential, helium has the lowest critical temperature and boiling point among all the elements. It has two protons, two electrons, but in its stable form, it may have either one or two neutrons; corresponding to the ^{3}He, and ^{4}He isotopes respectively. Out of all of the helium that is found naturally on earth, only 0.000137% is ^{3}He and the rest is the more prevalent isotope of helium, ^{4}He. Both isotopes exhibit markedly bizarre behaviors at low temperatures, which make them unique from the rest of the elements in the periodic table. It is necessary for the reader to become familiar with these unusual properties of helium before it is possible to understand a refrigeration system that utilizes ^{3}He-^{4}He mixtures as its working fluid. Elemental properties of each isotope are separately presented in this section followed by a description of ^{3}He-^{4}He mixtures.

2.2.1. Pure ^{4}He

^{4}He is a light, colorless, and odorless gas at room temperature that occurs naturally due to the radioactive decay of elements within the Earth's crust, mainly Thorium and Uranium. Because it can easily escape the atmosphere, ^{4}He is obtained almost exclusively from natural gas wells

where it can be found in concentrations of up to 7 percent (Enss 2005). ^{4}He has the lowest critical point of the common cryogenic liquids, at 5.2 K and 2.3 atm; this can be observed on its pressure-temperature phase diagram which is shown in Figure 10. A remarkable property of ^{4}He is immediately seen from this figure; it does not have a triple point. Helium is the only element that does not solidify under its own vapor pressure. In fact, a pressure greater than 25 atmosphere must be exerted on its liquid phase at temperatures near zero Kelvin in order to form solid helium. This characteristic of helium makes it the only cryogenic fluid capable of producing sub-Kelvin temperatures using various thermodynamic refrigeration cycles. Some facts about ^{4}He are listed in Table 2.

Boiling point*	**4.215 K**
Triple point	**Does not exist**
Lambda point*	**2.172 K**
Critical Temperature	**5.2 K**
Critical Pressure	**2.26 atm**

Table 2. Some facts on ^{4}He (Keller 1969) *Evaluated at atm pressure

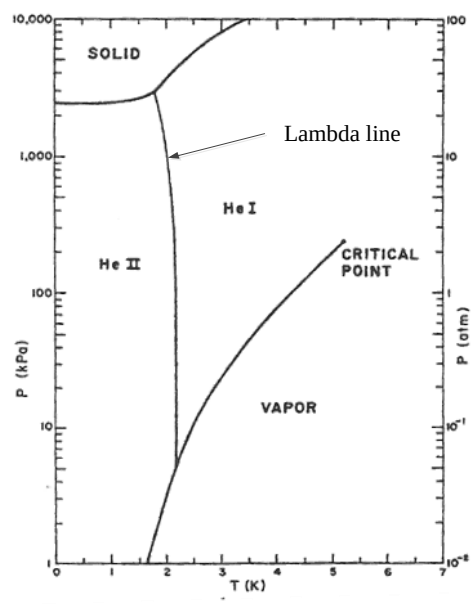

Figure 10. Temperature-Pressure diagram for ^{4}He (Van Sciver 2012)

2.2.1.1. He I and He II

^{4}He, when liquefied, remains a normal fluid until its temperature is decreased to a transition temperature that is known as the lambda point (and labeled the lambda line in Figure 10) at which point helium undergoes a phase transition. The lambda line obtains its name from its resemblance to the Greek letter lambda when tracing the specific heat versus temperature plot of helium in the transitional region (Van Sciver 2012). Liquid ^{4}He above the lambda line is known as He I or the "warmer liquid helium"; He I is regarded as a normal fluid because it behaves as a Newtonian fluid. There is no specific volume change or latent heat associated with the lambda transition.

The term He II or the "cooler liquid helium" is used for liquid ^{4}He when it is subcooled to temperatures below the lambda line. He II does not behave as a Newtonian fluid and demonstrates some remarkably odd properties due to quantum effects. Kapitsa reported that there is no measurable resistance to flow when he studied the flow of He II through small capillaries. This fact implies that He II has no viscosity. As a result, Kapitsa coined the term "superfluid" to describe He II. Later, other experiments done by Keesom and Meyer demonstrated the existence of a viscous drag in He II during an oscillating disk experiment. The contradicting results of the two experiments, one showing He II as an inviscid and the other suggesting that it has viscosity, led to the development of the two fluid model by Landau and Tisza.

2.2.1.2. Landau's two fluid model for He II

Liquid ^{4}He exists in two different phases: He I, the normal fluid, and He II, superfluid and normal helium at temperatures lower than the lambda point. The two phases are separated by the lambda line. At either end of this line, ^{4}He has two lambda points: a lower lambda point, which is the intersection of the vapor pressure curve with the lambda line and an upper lambda point, which

is the intersection of the solid phase line and the lambda line. The lower lambda point is 2.172 K at 5 kPa and the upper lambda point is 1.763 K at approximately 30 MPa. Once subcooled to temperatures below the lambda line, normal liquid ^{4}He does not undergo an abrupt transition to a superfluid, but rather the transition is gradual. As the temperature is decreased further below the lambda line, more and more normal fluid becomes superfluid. At 1 K, 98.7% of the fluid has transitioned to superfluid. It is now apparent that superfluid and normal helium coexist at temperatures below the lambda point, this fact is used to define the term He II whereas superfluid is one of the two components present in He II. This phenomenon is depicted in Figure 11, which shows the ratio of each fluid component as a function of temperature. The normal to superfluid ^{4}He composition can be predicted using the following relationship (Van Sciver 2012):

$$\frac{\rho_n}{\rho} = \left(\frac{T}{T_\lambda}\right)^{5.6} \quad for \;\; T \le T_\lambda \tag{2}$$

where ρ_n is the density for the normal component, ρ is the total density of the fluid, T is the temperature, and T_λ is the lambda point as a function of pressure.

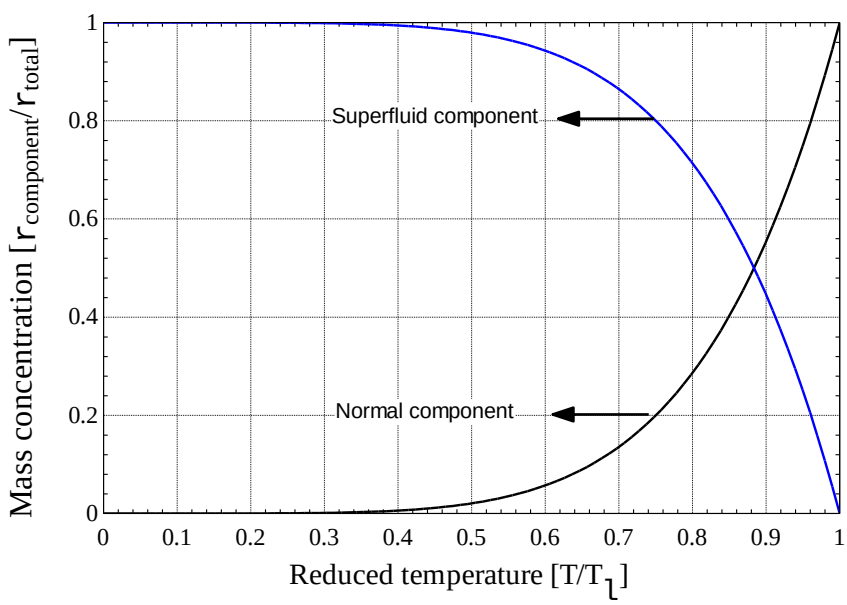

Figure 11. Mass concentration as a function of reduced temperature below the lambda line.

The specific heat of liquid ^{4}He varies unlike any other fluid. As shown in Figure 12, the specific heat capacity of liquid helium increases to a large value as the temperature approaches the lambda point. Also, the thermal conductivity of liquid ^{4}He behaves in a unique manner. Above the lambda point, the thermal conductivity decreases as the temperature is decreased. This behavior is consistent with that of a gas obtained from kinetic theory. However, below the lambda point, the heat transport properties of He II become quite interesting. When a container filled with He I is being pumped on in order to reduce the liquid ^{4}He pressure and therefore the temperature, one can observe nucleate boiling as a result of a temperature gradient in the bulk fluid. As the temperature is decreased through the lambda point, the violent bubbling suddenly stops and the liquid becomes stable; however, the boiling process has not stopped. In fact, boiling and evaporation continues even when ^{4}He is subcooled below the lambda point. Due to an incredibly large thermal conductivity there is no temperature gradient within the body of the fluid and therefore there is no chance for a bubble to form and float in the main body of the liquid because of natural convection. However, evaporation continues in a small region confined to the top of the fluid. This is because any heat added to the body of the fluid rapidly travels to the free surface where vaporization takes place. The thermal conductivity of He II is orders of magnitude higher than the thermal conductivity of copper at room temperature; the apparent thermal conductivity of superfluid helium can be as large as 100 kW/m-K in wide channels and open containers, hence another reason for the name “superfluid”.

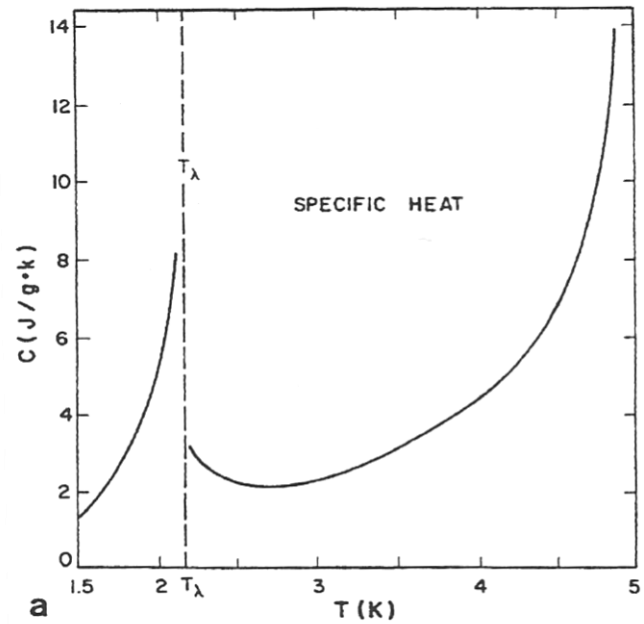

Figure 12. Specific heat Vs. Temperature for ^{4}He (Van Sciver 2012)

2.2.1.3. Thermal properties of He II

He II exists in a condensed liquid state, therefore it has non-negligible interparticle interactions. Thermodynamically, this liquid behaves differently from other conventional liquids. The superfluid component of He II is in its ground state, (in quantum mechanics ground state refers to the lowest energy level a particle can possess corresponding to the 1st mode) therefore has zero entropy. These unique properties of He II are quantified in this section.

A simple empirical relation for the entropy per mole of the ^{4}He in the He II regime is (Miller 2001):

$$s_4^0 = 4BT^3 + A\left(\frac{\Delta_1}{T} + \frac{3}{2}\right)\sqrt{T}e^{-\Delta_1/T} + C\left(\frac{\Delta_2}{T^2}\right)e^{-\Delta_2/T} \qquad (3)$$

where A,B,C, Δ_1 , and Δ_2 are constants: 23.2 J/mol-K$^{3/2}$, 6.75 x 10^{-3} J/mol-K^4, 500 J/mol, 8.65 K, and 15.7 K respectively. Superscript *0* denotes pure substance, and subscript *4* is used to denote ^{4}He in order to distinguish between ^{3}He and ^{4}He as will be discussed later in this chapter. Note that Eq. (3) is, in fact the entropy of the normal component in the He II region, the superfluid component has to entropy. Figure 13 shows a plot of entropy per mole of ^{4}He for temperatures below the lambda point. A comparison between Figure 11 and Figure 13 exhibits a striking similarity; The entropy diminishes as more and more normal component are demoted to the superfluid state as temperature is decreased below the lambda point. Also Note that specific entropy experiences a discontinuity of slope around the lambda point (not shown in the plot) and it is only a function of temperature and a weak function of pressure in the He II regime.

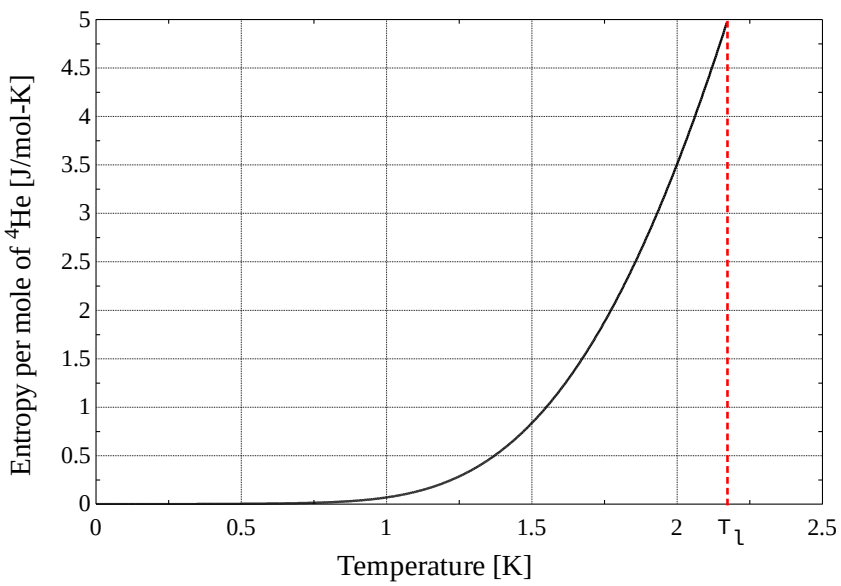

Figure 13. Entropy per mole of ^{4}He [J/mol-K] at temperatures below the lambda point at atm pressure

Liquid He II is incompressible, therefore a simple relation for the internal energy per mole of ^{4}He in the He II regime can be found from the entropy according to:

$$u_4^0 = \int T\left(\frac{\partial s}{\partial T}\right)dT = 3BT^4 + A\left(\frac{\Delta_1}{T} + \frac{1}{2}\right)T^{3/2}e^{-\Delta_1/T} + C\left(\frac{\Delta_2}{T} - 1\right)e^{-\Delta_2/T} \quad (4)$$

The enthalpy per mole of ^{4}He in the He II regime is found by applying the definition of enthalpy:

$$i_4^0 = u_4^0 + pV \quad (5)$$

where p is the pressure, and V is the molar volume of ^{4}He (27.58 x 10^{-6} m^3/mol).

2.2.1.4. Transport properties of He II

The superfluid component of ^{4}He shows no resistance to flow and has zero viscosity. Because the superfluid component has no viscosity, it can move around in the bulk liquid unimpeded which makes it an excellent thermal conductor. The viscosity and thermal conductivity of He II are quantified in this section.

There are two methods available to measure the viscosity of a fluid; Poiseuille's method and the damping provided to an oscillating disk. Using the former method, two vessels each at a different pressure are connected via capillaries of small diameter and the flow rate of liquid is measured between the two vessels. Using the latter method, a disk is caused to rotationally oscillate in the bulk liquid and the damping is measured. These two methods yield identical results for the viscosity in ordinary liquids but not for He II. Experiments have measured zero viscosity for He II using Poiseuille's method (this zero viscosity is due to the superfluid component and not the normal component). However, experiments have shown a finite value for the viscosity of He II when measured using the oscillating disk method due to the presence of the normal component in the He II. This occurs because of a phenomenon known as "Gorter-Mellink mutual friction", a result of quantum superfluid turbulence induced due to excessive shearing in the normal component of He II. The result is shown in Figure 14.

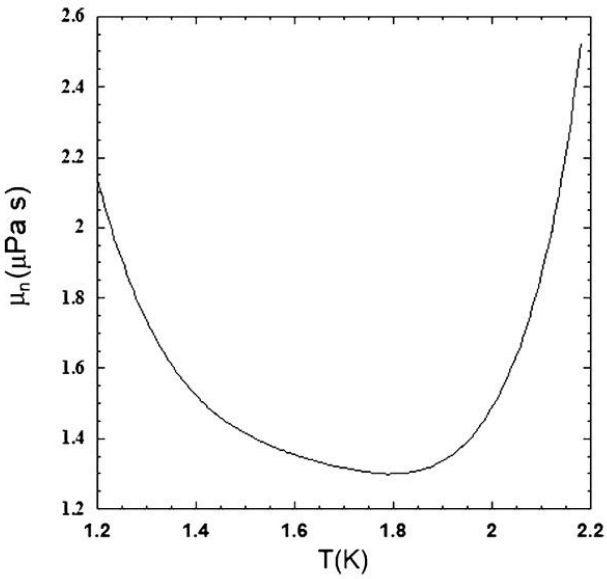

Figure 14. Viscosity of He II as measured by oscillating disk (Van Sciver 2012).

In the absence of any motion, He II has an inherently large thermal conductivity due to the unimpeded motion of the superfluid component in the bulk liquid. Any temperature gradient in stationary He II is counteracted by the rapid motion of the superfluid component. The effective value of thermal conductivity in this case can be as high as 100 kW/m-K. This is three orders of magnitude greater than for the maximum value exhibited by very pure copper.

Unfortunately, a precise formulation for the thermal conductivity of He II in laminar flow is not well established. However, the thermal conductivity for He II undergoing turbulent flow is available. In He II flow, a transition from laminar to turbulent flow occurs once the flow velocity becomes larger than the critical velocity, v_{sc}, which is either approximated in terms of classical mechanics or estimated based on the concept of quantized vortices, a subject of turbulence in quantum mechanics. Above this critical velocity, viscosity becomes non-negligible and thermal conductivity is reduced by the lack of unimpeded motion of the superfluid component within the

body of the fluid. The critical velocity in He II is a function of channel diameter as shown in Figure 15.

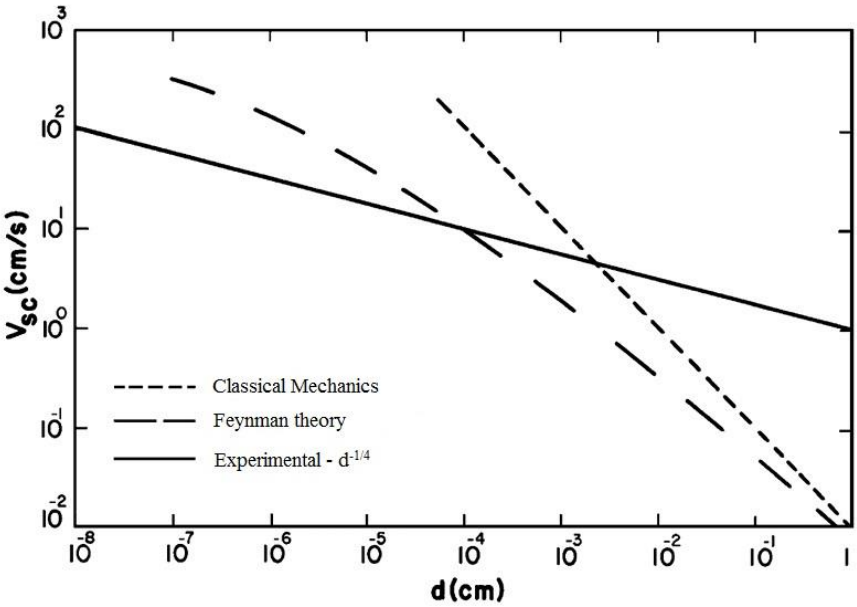

Figure 15. He II critical velocity (Van Sciver 2012)

Three data lines are shown for the critical velocity He II in Figure 15. In terms of classical mechanics, the critical velocity of He II is estimated based on a critical Reynolds number criterion determined by the normal fluid component according to (Van Sciver 2012):

$$\mathrm{Re}(v_n) = \frac{d\ \rho\ v_n}{\mu_n} \approx 1200 \tag{6}$$

where d, ρ, v, and μ are the hydraulic diameter of the channel, density, velocity, and viscosity respectively. Subscript n denotes the normal component within He II. The Feynman data line is obtained through studying quantum mechanical vortices (which is beyond the subject of this work). The last data line is found experimentally, and is found to scale with $d^{-1/4}$, where d is the diameter of the channel.

Van Sciver (2012) reports an analytical expression for He II's thermal conductivity in the turbulent regime. The function f is defined below (in units of W^3/m^5-K):

$$f^{-1}(T,p) = g(T_\lambda)[t^{5.7}(1-t^{5.7})]^3 \tag{7}$$

where $g(T_\lambda)=\rho^2 s_\lambda^4 T_\lambda^3 / A_\lambda$, $t=T/T_\lambda$, ρ is the density of He II, s_λ=1559 J/kg-K, A_λ is approximately 1150 m-s/kg. The effective thermal conductivity for He II is defined using the function f and the heat flux:

$$k_{eff} = \frac{f^{-1}(T,P)}{q^2} \tag{8}$$

where q is the heat flux in units of W/m^2. For example, for a heat flux of 10 kW/m^2 at 1 atm, and 1.95 K, the effective thermal conductivity of He II is 120 kW/m-K.

2.2.1.5. Fountain effect in He II

One of He II's remarkable properties is that a pressure rise purely due to the fountain effect is only a function of temperature. Consider the experimental setup shown in Figure 16. An inner vessel is placed in a large vessel; both vessels contain He II and both have the same initial liquid level. The bottom of the inner vessel is equipped with a porous plug material (a superleak) and a heater. The porous plug only allows superfluid helium to flow through it. The heater is turned on and heat is applied to the He II in the inner vessel. The applied heat causes the temperature and consequently the pressure of the liquid to rise. This rise in pressure in the inner vessel displaces He II from the top of the inner vessel which is why this effect is referred to as the fountain effect. Only the superfluid component of He II rushes into the inner vessel through the porous plug to replenish the displaced He II. An expression for the fountain pressure between two vessels each containing He II and connected by a superleak in a closed configuration is (Miller 2001):

$$P_f = \frac{1}{V}\left[BT^4 + AT^{3/2}e^{-\Delta_1/T} + Ce^{-\Delta_2/T}\right]\Bigg|_{T_2}^{T_1} \qquad (9)$$

where the constants were defined previously, T_1 and T_2 are the temperature of the fluid inside and outside the smaller container in Figure 16 respectively. The application of the fountain effect becomes important in the discussion of the SMP. Eq. (9) states that a temperature difference across a superleak connecting two vessels filled with He-II corresponds to a pressure difference. The pressure loss through the non-superleak ports of the vessels in a closed loop can be used to estimate the temperature difference needed to maintain a flow of He II from one vessel to the other via the superleak.

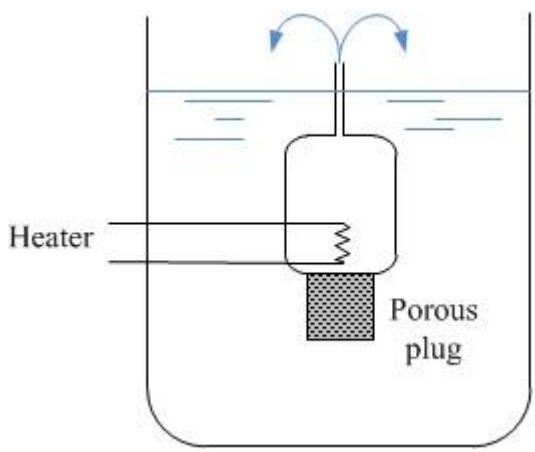

Figure 16. Fountain effect (Thermo-mechanical effect).

2.2.1.6. Rollin film

During an experiment in 1922, Kammerlingh Onnes discovered a flow of He II on surfaces above the liquid ^{4}He level. He interpreted this flow in terms of an evaporation and condensation mechanism. This interpretation was later found to be incorrect. In 1937, Simon and Rollin were able to interpret this film flow phenomenon based on the He II-two fluid model. Superfluid ^{4}He forms a mobile film above its liquid surface and it spontaneously creeps up the walls of a container

holding helium II. This phenomenon is known as the Rollin film theory. Empirical relationships have been established that relate the film thickness f_{th} to the height H above the helium surface (Van Sciver 2012):

$$f_{th} = \frac{K_R}{H^n}[cm] \tag{10}$$

where $K_R = 3\text{x}10^{-6}$ [cm^{n+1}] and n is a number between 0.3 and 0.45. For example, for a height of 1 cm above the liquid helium II level in a container, the film thickness would be 30 nm or 80 atomic layers. The thickness of the film can be reduced by introducing restrictions in the path of the flow or by reducing the diameter of the tubing or channels at the top of such vessels because the film flow is directly proportional to the ratio of the cross sectional areas in the direction of the Rollin film. This restriction is called the superfluid film killer. As will be discussed later in the construction of the system, these superfluid film killers are needed to minimize the back flow of helium when condensing ^{4}He in the system.

2.2.2. Pure ^{3}He

Like ^{4}He, ^{3}He is colorless, odorless, and a stable isotope of helium. Its abundance is only 0.000137% of the helium naturally found on earth. ^{3}He can also be obtained by radioactive (beta) decay of tritium. Every 1 liter of helium at Standard Temperature and Pressure condition (defined to be 293.15 K and 101325 Pa) yields 124 mg of ^{3}He. The price of ^{3}He in the 1950's was exceedingly high, $100 per cc STP. Thanks to its supply through radioactive decay, the price of this isotope had fallen to $0.135 per cc STP by 1966 (Keller 1969). In recent years however, there has been a rapid increase in demand for ^{3}He coupled with a reduction in supply due to a slowdown in the nuclear industry research. As a result, the price of ^{3}He has risen to $0.685 per cc STP for

DOE approved supplies and $3.284 per cc STP in free market as of the time of this writing (2015). NASA is currently debating sending manned missions to the moon in order to excavate ^{3}He because the moon has a relative abundant supply of this isotope (50 ppb of moon regolith is ^{3}He).

A temperature-pressure phase diagram for ^{3}He is shown in Figure 17. As can be seen from this plot, the critical point of ^{3}He is much lower than the critical point of the more common isotope of helium. This is due to the low binding energy of ^{3}He. Like ^{4}He, ^{3}He does not have a triple point. However, unlike ^{4}He, ^{3}He has a non-zero magnetic moment due to its unpaired nuclear spin. This magnetic moment is responsible for a large spin entropy in ^{3}He which suppresses superfluid transition temperature to 2.6 mK. Another startling property of this isotope is that it can exist in two different phases of a superfluid state. Phase B superfluid can be thought of being analogous to superfluid ^{4}He. Phase A superfluid differs in that its superfluid properties are further stabilized in the presence of a magnetic field. A pressure greater than 34 atm at temperatures near zero Kelvin must be exerted on liquid ^{3}He to solidify it. Some properties of ^{3}He are listed in Table 3.

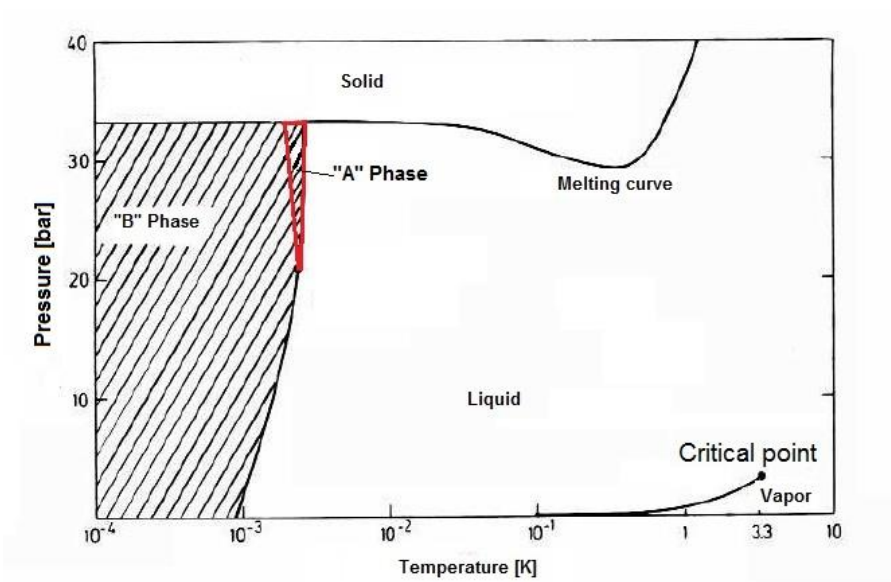

Figure 17. Temperature vs. pressure phase diagram for ^{3}He (Vollhardt 2013)

Boiling point*	**3.191 K**
Triple point	**Does not exist**
Density at 0 Kelvin*	**82.3 kg/m^3**
Critical Temperature	**3.324 K**
Critical Pressure	**115 kPa**
Thermal cond. at 3.2 K	**20 mW/m-K**

Table 3. Some facts about ^{3}He (Van Sciver 2012) *Evaluated at atm pressure

2.2.3. ^{3}He-^{4}He mixtures

Thermodynamically, ^{3}He and ^{4}He mixtures have markedly different properties than either of the pure components at low temperatures. This is because the ^{3}He atom obeys Fermi-Dirac statistics owing to its half integer quantum spin (an intrinsic form of angular momentum for elementary particles that has no analogy in classical mechanics). In contrast, the ^{4}He atom obeys Bose-Einstein statistics owing to its integer quantum spin. Thermodynamic properties of ^{3}He-^{4}He mixtures are described in this section. Some methods for calculating flow properties are simplified and presented; these are used extensively to develop the AMRR model presented in this work.

The number of intensive internal properties needed to fix the state of a non-reacting thermodynamic system F, is given by (Klein-Nellis 2012):

$$F = C - \prod + 2 \tag{11}$$

where C is the number of distinguishable chemical species in the system and $\prod$ is the number of phases that are present (i.e., solid, liquid, or vapor). In the case of a binary mixture like ^{3}He-^{4}He, three internal intensive properties are needed to thermodynamically fix the state of the mixture. These three properties are typically taken to be the temperature, pressure, and molar concentration, defined by:

$$x = \frac{n_3}{n_3 + n_4} \tag{12}$$

where n is the number of moles and subscripts 3 and 4 denote ^{3}He, and ^{4}He respectively. Figure 18 (a) shows the phase diagram for ^{3}He-^{4}He mixtures as a function of T, P, and x. Figure 18 (b) shows the projection of the three dimensional plot onto the saturated pressure surface shown in Figure 18 (a) on a T-x diagram. Notice how the ^{4}He superfluid transition temperature (i.e., the lambda line) is suppressed at higher concentrations as long as the concentration stays below 0.67. In the absence of ^{3}He, the lambda point matches that of pure ^{4}He at 2.171 K and the lambda point decreases to 0.9 K at x = 0.67. Three different regimes are immediately distinguished in Figure 18. The region above the lambda surface and the concentrated phase surface is called the He-I region. In this region, the entire mixture is in the normal state (i.e., it contains no superfluid component) and is usually not of much interest to low temperature applications. The region below the lambda surface and above the dilute phase surface is called the He-II region. This is the region of interest for this work. There are three components present in this region; a normal ^{3}He, a normal ^{4}He, and a superfluid ^{4}He component. The region below the dilute phase surface and the concentrated phase surface is called the two-phase region. The entropy of cooling associated with ^{3}He atoms' going from a ^{3}He rich phase (the concentrated phase line) to a dilute solution of ^{3}He in ^{4}He (the dilute phase line) can be exploited to provide cooling at very low temperatures and is the basis for dilution refrigerator operation. The tricritical line is formed by the intersection of all three regions discussed above. The tricritical point on the T-x saturated pressure plot occurs at x = 0.67 and T = 0.867 K.

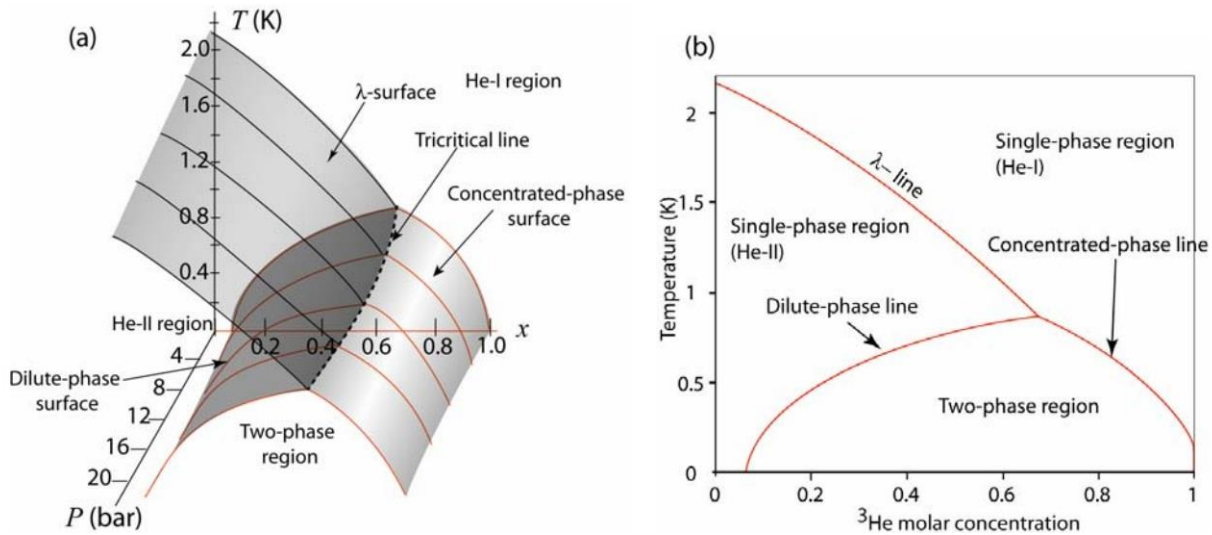

Figure 18. Phase diagram for ^{3}He-^{4}He mixtures (a) 3-D surface plot (b) T-x diagram projected along saturated pressure surface (Chaudhry 2009)

The objective of the rest of this section is to present a simplified model of some properties of ^{3}He-^{4}He mixtures that is useful for heat exchanger modeling. In addition, methods for first and second law analysis of systems using a mixture of ^{3}He-^{4}He are discussed. Consider the system shown in Figure 19 consisting of two vessels connected by a superleak. The role of the superleak is to allow superfluid ^{4}He to flow but block the normal component flow. The vessel on the left is filled with a mixture of ^{3}He-^{4}He, while the one on the right is filled with pure ^{4}He. At equilibrium, the pressure in the right vessel is less than the one on the left by an amount known as the osmotic pressure (Chaudhry 2009):

$$P^{os}(p,T,x) = \frac{\mu_4^0(p,T) - \mu_4(p,T,x)}{v_4^0(p,T)} \tag{13}$$

where μ_4^0 is the chemical potential of pure ^{4}He, μ_4 is the chemical potential of the mixture per mole of ^{4}He (^{4}He chemical potential), and v_4^0 is the molar volume of pure ^{4}He. Eq. (13) has important

implications; the osmotic pressure requires that the ^{4}He chemical potential on both sides of the superleak to be the same ($\mu_4(P, T, x)=\mu_4^0(P-P^{os}, T)$). Also, the osmotic pressure is directly related to the mixture ^{4}He chemical potential. As x increases, μ_4 decreases, and the osmotic pressure increases.

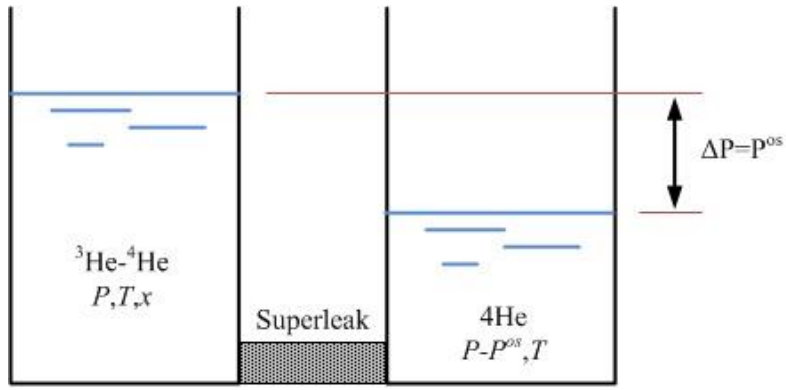

Figure 19. Osmotic pressure of ^{3}He-^{4}He mixture

In a flowing He-II mixture, normal ^{3}He is viscously interlocked with the normal component of ^{4}He. However, the superfluid component of ^{4}He moves independently from the normal components because it has no viscosity. The superfluid ^{4}He will flow freely in order to maintain constant ^{4}He chemical potential throughout the system. Therefore, in the analysis of ideal heat exchangers, both pressure and ^{4}He chemical potential are modeled as being constant in the direction of flow. Figure 20 shows a T-x plot of ^{3}He-^{4}He mixtures with lines of constant ^{4}He chemical potential at zero pressure (saturated pressure is approximated as zero pressure) shown.

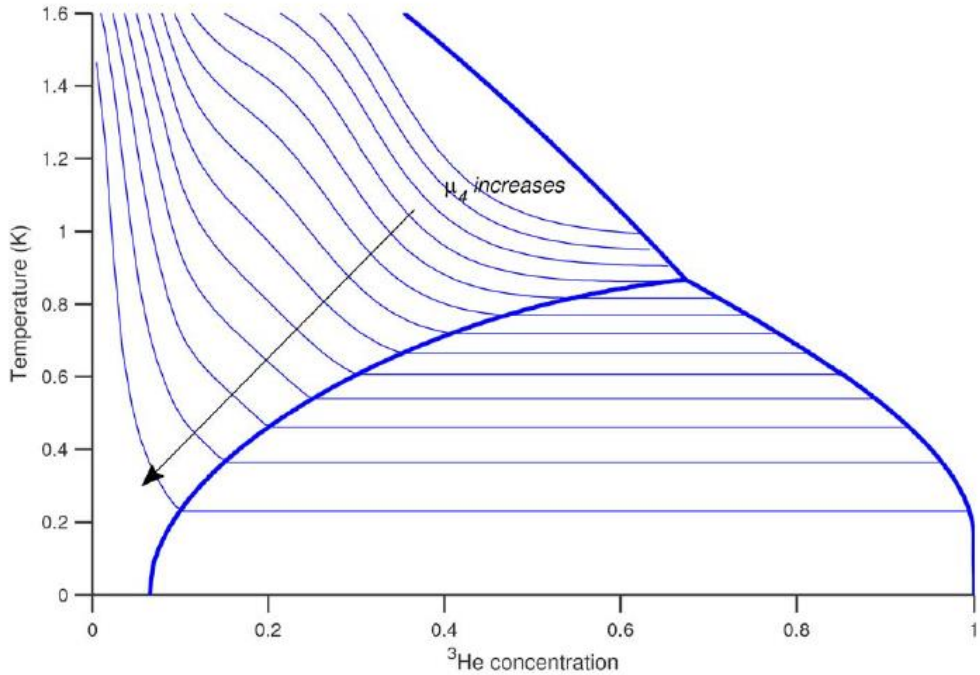

Figure 20. Lines of constant ^{4}He chemical potential on a T-x plane at zero pressure (Chaudhry 2009)

As it will become apparent in later chapters, the number of moles of each isotope of helium must be calculated separately when applying an energy balance on various parts of the AMRR. One example is the analysis of a heat exchanger. These type calculations become easier by decomposing the effective enthalpic flow into two enthalpic flows that correspond to each of the helium isotopes in a flowing mixture of ^{3}He-^{4}He. The effective enthalpy flow term is easily evaluated in He-I region since the motion of ^{3}He and ^{4}He are viscously interlocked due to the absence of any superfluid in this region. In contrast and as noted earlier, in He-II region, the superfluid component moves at a different velocity from that of the normal components. This fact implies an effective enthalpy flow that consists of two separate terms. The derivation presented below is a restatement of the work presented by Miller et. al. (2001), Ebner et. al. (1971), and Chaudhry (2009).

The effective enthalpy flow in the He-II region can be derived by considering the Gedanken apparatus shown in Figure 21. A mixture of ^{3}He-^{4}He enters the system control volume that is indicated by the control volume shown with a dashed box in the diagram (big CV). This flow is split between two cylinders; the top cylinder has no form of restrictions and contains the same temperature, pressure and molar concentration of mixture that enters the control volume. The bottom cylinder is equipped with a superleak, only superfluid ^{4}He flows through the bottom cylinder. This cylinder is maintained at the same temperature as the entering mixture by exchanging heat with a thermal reservoir and it only contains pure ^{4}He at a pressure P-P^{os}.

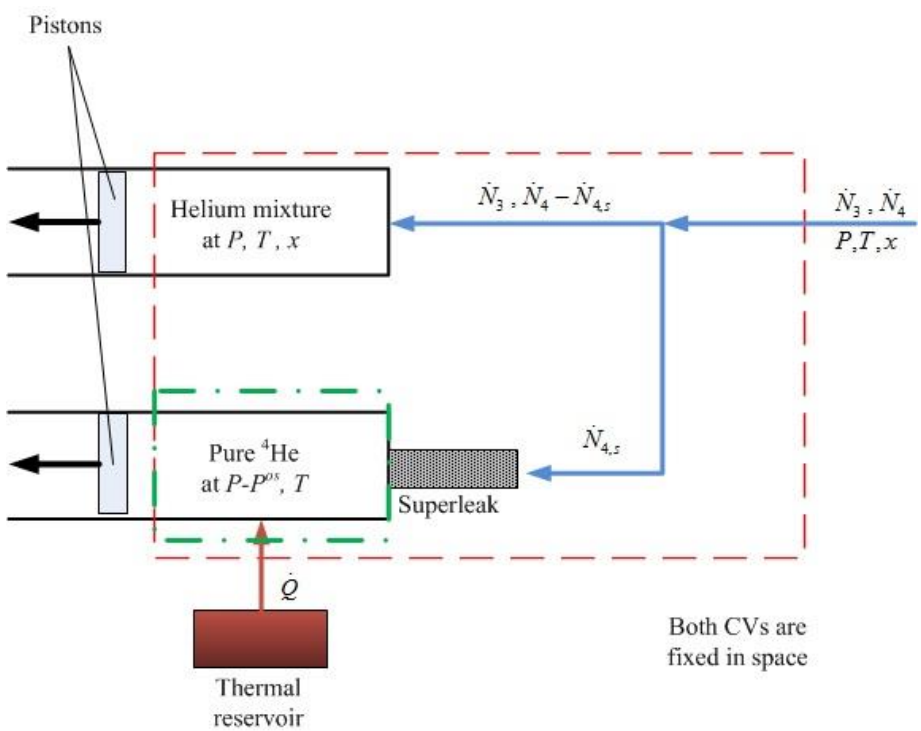

Figure 21. Ebner and Edwards Gedanken apparatus, note that the Control Volumes are fixed and not moving with pistons, dashed box (big CV), dot-dashed box (small CV)

The flow into the top cylinder is the bulk flow of an incompressible fluid where the superfluid and normal velocities are the same. Therefore, the ratio of the molar flow rates must equal the ratio of the local molar concentrations of the components:

$$\frac{\dot{N}_3}{\dot{N}_4 - \dot{N}_{4,s}} = \frac{n_3}{n_4} = \frac{x}{1-x} \tag{14}$$

The user selected a known value for $\dot{N}_4$ molar flow rate prior to the experiment. In order to keep the concertation ratio the same throughout the process in the mixture piston/cylinder the molar flow rate $\dot{N}_{4,s}$ is adjusted using the superfluid piston to ensure that the flow rates into the top cylinder obey Eq.(14).

Applying the general form of the first law to the big CV shown in Figure 21 yields:

$$\frac{dE}{dt} = \dot{Q} - \dot{W} + \sum_{\#\ ports} \dot{N}\ i \tag{15}$$

where E is the total energy, t is time, $\dot{Q}$ is the rate of heat transfer into the control volume, $\dot{W}$ is the rate of work done by the system, $\dot{N}$ is the total molar flow rate into the control volume, and i is the enthalpy of the mixture per mole of the mixture. The heat transfer rate into the bottom cylinder is evaluated by applying the general form of the second law to the control volume shown with a dot-dashed box (small CV) in Figure 21:

$$\frac{dS}{dt} = \sum_i \frac{\dot{Q}_i}{T_i} + \sum_{\#\ ports} \dot{N}s + \dot{S}_{gen} \tag{16}$$

where S is the total entropy in the control volume, $\dot{Q}_i$ is the rate of the ith heat transfer into the control volume, T_i is the temperature of the control surface where the ith heat transfer occurs, s is the molar specific entropy and $\dot{S}_{gen}$ is the rate of entropy production in the control volume. The

processes occurring in both cylinders are slow and assumed to be reversible; therefore, the entropy generation term is neglected. The only molar flow into the bottom cylinder is through the superleak and the specific entropy of the superfluid entering the control volume is zero. The time derivative of the total entropy in the control volume is the molar flow rate times the specific entropy of pure ^{4}He because the specific entropy in the small CV shown does not change in time (*T*, *P*, and *x* are all fixed). Therefore, the generalized second law relation of Eq. (16) reduces to:

$$\frac{\dot{Q}}{T} = \dot{N}_{4,s} s_4^0(P - P^{os}, T) \quad \Rightarrow \dot{Q} = T\ \dot{N}_{4,s} s_4^0(P - P^{os}, T) \tag{17}$$

There is no work done by either the big or the small CV shown in Figure 21 because they are fixed in space. In addition, the system is at steady state therefore the time derivative of the total energy is zero. There are three molar flow rates entering the big CV; the total mixture flow rate entering the control volume $\dot{N}_{total}$, the superfluid molar flow rate leaving the control volume $\dot{N}_{4,s}$, and the total molar flow rate minus the superfluid molar flow rate leaving the control volume $\dot{N}_3 + \dot{N}_4 - \dot{N}_{4,s}$, as labeled in Figure 21. A first law balance on the big CV yields:

$$0 = \underbrace{\dot{N}_{4,s} T s_4^0(P - P^{os}, T)}_{\dot{Q}} + \dot{N}_{total}\ i_{flow} - (\dot{N}_3 + \dot{N}_4 - \dot{N}_{4,s})\ i(P, T, x) - \dot{N}_{4,s}\ i_4^0(P - P^{os}, T) \tag{18}$$

the chemical potential of pure ^{4}He is defined according to:

$$\mu_4^0 = i_4^0 - T s_4^0 \tag{19}$$

Substituting Eq. (19) into (18) yields:

$$\dot{N}_{total}\ i_{flow} = (\dot{N}_3 + \dot{N}_4 - \dot{N}_{4,s})\ i(P, T, x) + \dot{N}_{4,s} \mu_4^0(P - P^{os}, T) \tag{20}$$

As described previously, the chemical potential of ^{4}He on both sides of the superleak in the bottom cylinder must be the same:

$$\mu_4(P,T,x) = \mu_4^0(P - P^{os}, T) \tag{21}$$

therefore, Eq. (21) is re-written as:

$$\dot{N}_{total}\ i_{flow} = (\dot{N}_3 + \dot{N}_4 - \dot{N}_{4,s})\ i(P,T,x) + \dot{N}_{4,s}\mu_4(P,T,x) \tag{22}$$

solving for x in Eq.(14) and mathematically manipulating and substituting x into Eq. (22) yields:

$$\dot{N}_{total}\ i_{flow} = \frac{\dot{N}_3}{x}\ i(P,T,x) + \left(\dot{N}_3 + \dot{N}_4 - \frac{\dot{N}_3}{x}\right)\mu_4(P,T,x) \tag{23}$$

Eq. (23) is re-written as:

$$\dot{N}_{total}\ i_{flow} = \dot{N}_3\left[\frac{i(P,T,x)}{x} + \frac{x-1}{x}\mu_4(P,T,x)\right] + \dot{N}_4\mu_4(P,T,x) \tag{24}$$

The osmotic enthalpy is defined according to:

$$i^{os} = \frac{i - (1-x)\mu_4}{x} \tag{25}$$

Using this definition of osmotic enthalpy in Eq. (24) yields the final result for the enthalpic flow of a ^{3}He-^{4}He mixture in the He-II region:

$$\boxed{\dot{N}_{total}\ i_{flow} = \dot{N}_3\ i^{os}(P,T,x) + \dot{N}_4\mu_4(P,T,x)} \tag{26}$$

For completeness, the same analysis can be applied to derive a form of the second law for flowing ^{3}He-^{4}He mixtures in the He-II region by substituting the heat transfer rate and molar flow rates previously found into Eq. (16):

$$\dot{N}_{total}s_{flow} = -\underbrace{\dot{N}_{4,s}s_4^0(P - P^{os}, T)}_{\frac{\dot{Q}}{T}} + (\dot{N}_3 + \dot{N}_4 - \dot{N}_{4,s})s(P,T,x) + \dot{N}_{4,s}s_4^0(P - P^{os}, T) \tag{27}$$

Eq. (27) simplifies to:

$$\dot{N}_{total}s_{flow} = (\dot{N}_3 + \dot{N}_4 - \dot{N}_{4,s})s(P,T,x) \tag{28}$$

the definition of x is used in Eq. (28) to arrive at the final result for the entropy flow of a mixture of ^{3}He-^{4}He in the He-II region:

$$\boxed{\dot{N}_{total} s_{flow} = \dot{N}_3 \frac{s(P,T,x)}{x} = \dot{N}_3 s_{3,He}} \tag{29}$$

where $s_{3,He}$ is the mixture entropy per mole of ^{3}He and is equal to the mixture entropy per mole of mixture, s, divided by x, the moles of ^{3}He per mole of mixture. This concludes the analysis of enthalpic and entropy flows of ^{3}He-^{4}He mixtures in the He-II region. All thermodynamic properties (s, g, u, i, v, and μ) used in this work are data tabulated and programmed in MATLAB by Chaudhry (2009) and presented in his PhD dissertation at MIT.

2.3. Magneto-caloric effect

The magneto-caloric effect or adiabatic temperature change is defined as the heating or cooling of a paramagnetic material due to the application of a magnetic field. The magneto-caloric effect was first discovered by Warburg in 1881. This phenomenon was later explained by Debye and Giauque. They also proposed the first practical application of the magneto-caloric effect: adiabatic magnetization for reaching temperatures lower than the boiling point of liquid helium, which was the lowest achievable temperature at the time.

The magnetic ions in a paramagnetic material can be thought of as springs: work is done on the ions in a paramagnetic material during the magnetization process, analogous to the work done on a spring in order to compress it. Similarly, during the demagnetization process the magnetic ions in a paramagnetic material do work on their surroundings, analogous to a compressed spring that does work once released from the compressed state.

The entropy of a paramagnetic material can be considered as a sum of two contributions: the entropy due to magnetic ordering ($S_{magnetic}$) and the entropy due to the temperature of the material ($S_{thermal}$). Figure 22 shows a paramagnetic material under two different conditions. On the left side of this figure no external magnetic field is applied to the paramagnetic salt (B=0), thus the magnetic ions are in their natural random orientation. The temperature and total entropy of the material at state 1 are T_1 and S_1, respectively. On the right side of the same figure an external magnetic field has been applied to the paramagnetic material ($B \neq 0$); therefore some of the magnetic ions are aligned to the externally applied magnetic field. The temperature and total entropy of the material at state 2 are T_2 and S_2, respectively. The process of moving from state 1 and state 2 could be either an adiabatic or an isothermal process, or somewhere between these limits. Entropy is related to the disorder or randomness within a system. Entropy is higher for a more disordered system. Thus if the process is adiabatic then the magnetic component of entropy must have decreased at state 2 compared to state 1. In order to preserve the total entropy of the system, the thermal component of entropy must have increased by the same amount that the magnetic entropy decreased. This implies that the temperature of the paramagnetic material at state 2 must be higher than state 1 during an adiabatic process. However the situation is different for an isothermal process. During an isothermal process the magnetic component of entropy decreases but the thermal component of entropy remains the same. Therefore, the total entropy of the paramagnetic salt must have decreased from state 2 compared to state 1 which implies that energy must be transferred by heat from the salt.

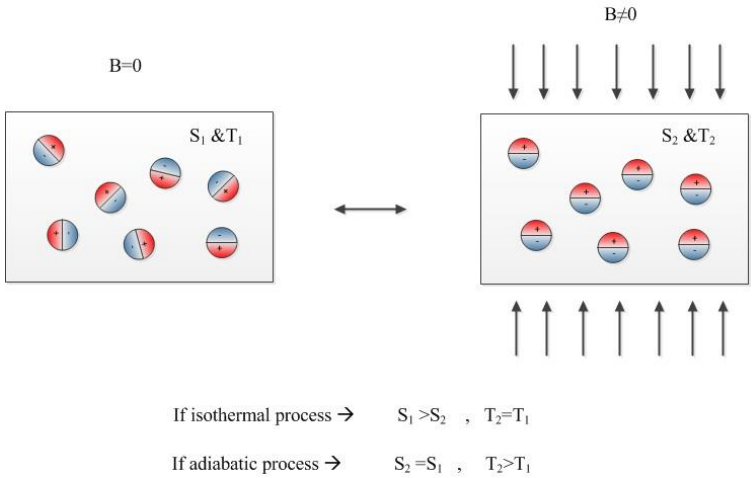

Figure 22. A paramagnetic material under two conditions: with applied magnetic field and without magnetic field (Jahromi 2011)

The equivalence of this statement to the thermodynamics of a compressible substance is evident. An adiabatic magnetization of a paramagnetic material is analogous to an adiabatic compression of an ideal gas: the pressure increases and because the process is adiabatic the temperature must increase. An isothermal magnetization of a paramagnetic material is analogous to the isothermal compression of an ideal gas: the pressure is increased and heat must be removed to keep the temperature constant thus the entropy must decrease. Thermodynamic properties of the paramagnetic material used for the AMRR in this work, Gadolinium Gallium Garnet ($Gd_3Ga_5O_{12}$ or GGG), along with a justification of its use are described in the next two sections.

2.3.1. Paramagnetic materials for low temperature magnetic refrigeration

Various paramagnetic materials are used for low temperature refrigeration applications. The suitability of these materials are determined based on their cost as well as their thermal, transport, chemical, physical, and mechanical properties. A list of the properties required by a good paramagnetic material is listed in Table 4. One of the most important criteria for the selection of a suitable paramagnetic material are low lattice and electronic heat capacity so that there is a

minimum of internal heat load as the material is magnetized or demagnetized. Another requirement is a low ordering temperature, which is defined as the temperature below which the magnetic contribution of entropy becomes appreciable relative to the thermal contribution of entropy (Barclay 1981).

A relation for the lattice heat capacity is given by Barclay (1981):

$$C = \alpha R T^3 \tag{30}$$

where α is the lattice heat capacity constant, R is the gas constant, and T is the absolute temperature. Figure 23 shows a plot of α versus the ordering temperature, T_0. The ideal material is located towards the left bottom corner of this plot. As can be seen, the best material for low temperature applications in the range of 0.4 to 1.2 K, is GGG ($Gd_3Ga_5O_{12}$); this is the material chosen in this work and the subject of next section.

Category	Property
Thermal	Low lattice and electronic heat capacity
Magnetic	Low ordering temperature
Transport	High thermal conductivity
Mechanical	Easy to fabricate for use in porous beds
Mechanical	Resistance to mechanical erosion (i.e magnetic dust)
Chemical	Resistance to short term degradation (i.e oxidation)
Chemical	Small volume per gram of ion

Table 4. Some properties required for a good paramagnetic material (Barclay 1981)

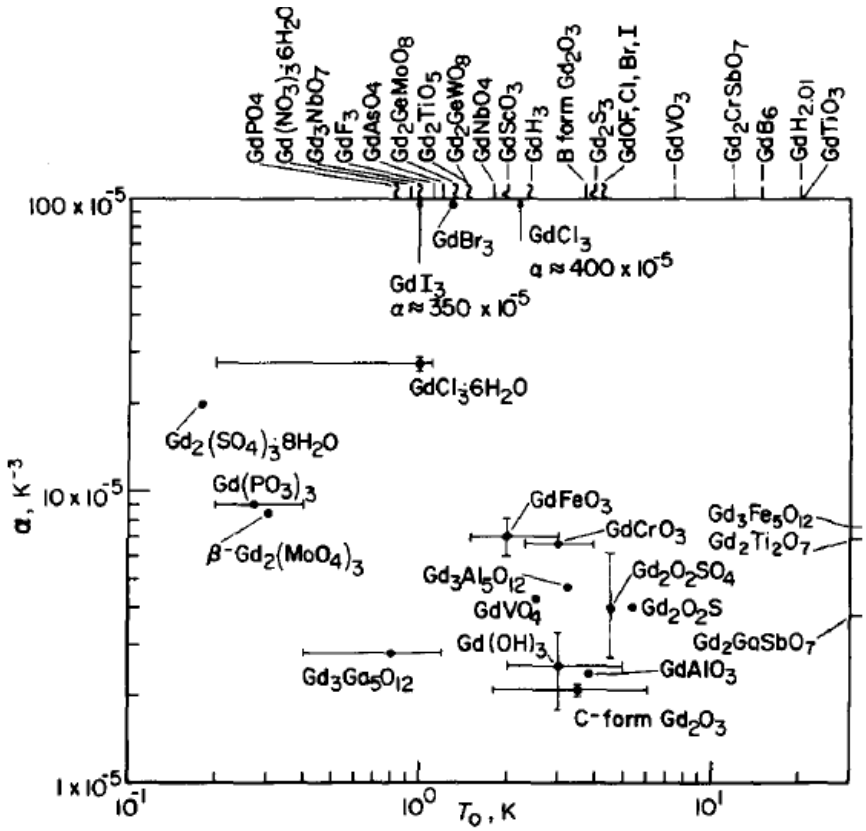

Figure 23. The heat capacity constant, α vs. ordering temperature T_0 for Gd compounds (Barclay 1981)

2.3.2. GGG properties and suitability

GGG offers excellent thermal and transport properties in the temperature range of 0.4 to ~2 K. The availability of this material also makes it suitable for use in the AMP and AMRR system described in this work. A general equation of state for all paramagnetic salts at low temperatures is expressed by Lounasmaa (1974). Just like any other paramagnetic material, GGG's entropy consists of a magnetic and a thermal component. The specific entropy of GGG (J/mol-K) as a function of temperature (*T*) and externally applied magnetic field (*B*) is:

$$s(T,B) = R\left[\frac{\chi}{2J}\coth\left(\frac{\chi}{2J}\right) - \frac{(2J+1)\chi}{2J}\coth\left(\frac{(2J+1)\chi}{2J}\right) + \ln\left(\frac{\sinh\left(\frac{(2J+1)\chi}{2J}\right)}{\sinh\left(\frac{\chi}{2J}\right)}\right)\right] \quad (31)$$

where R is the gas constant (8.314 J/K-mol), J is the spin quantum number (7/2 for GGG), and χ is the magnetic susceptibility, a positive number for paramagnets defined as:

$$\chi = \frac{\beta\, J\, g}{k\, T} \sqrt{b^2 + B^2} \quad (32)$$

where β is the Bohr magneton constant (9.274×10^{-24} J/Tesla), g is the Landé-g factor or dimensionless magnetic moment (2 for GGG), k is the Boltzmann's constant (1.381×10^{-23} J/K), b is the intrinsic internal magnetic field (0.481 Tesla for GGG). Figure 24 shows a plot of specific entropy of GGG as a function of temperature at various constant externally applied magnetic fields.

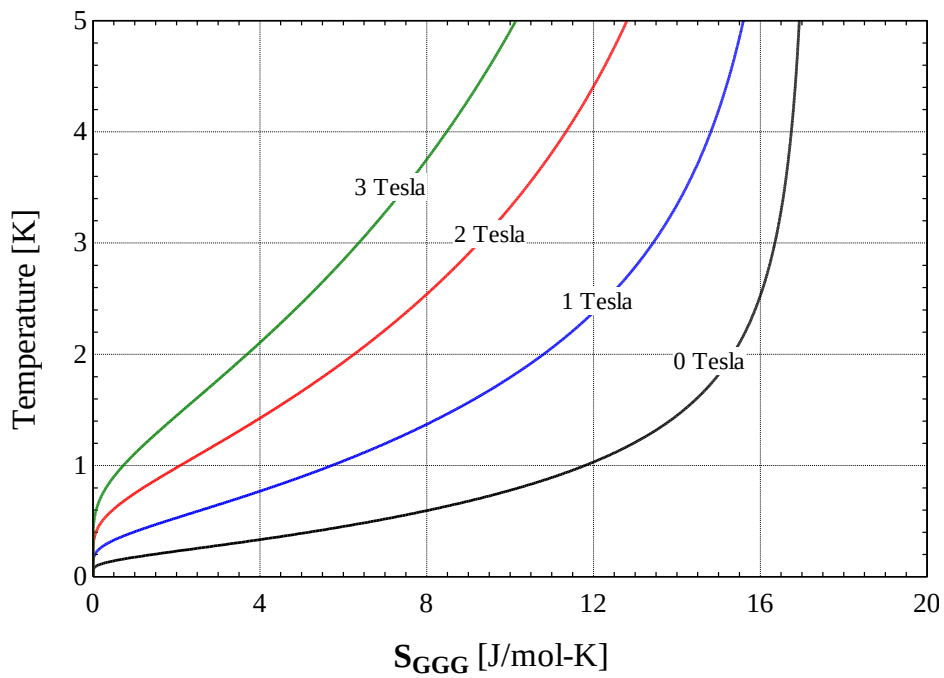

Figure 24. Temperature of GGG as a function of specific entropy at various constant external applied magnetic fields

Figure 24 shows that the entropy of GGG at 1 K in the absence of any externally applied magnetic field is 12 J/mol-K. If an external magnetic field of 2 Tesla is applied to the GGG during an

adiabatic process, then the temperature of the GGG must increase to 4.411 K. Therefore the adiabatic temperature change of GGG during this adiabatic magnetization is 3.411 K.

The specific heat capacity of GGG (incompressible, pressure is constant) as a function of temperature and applied magnetic field is (Mosely 2009):

$$C(T,B) = R\frac{-\chi}{2J}\left[(2J+1)^2\frac{\frac{\chi}{2J}}{\sinh^2\left((2J+1)\frac{\chi}{2J}\right)} - \frac{\frac{\chi}{2J}}{\sinh^2\left(\frac{\chi}{2J}\right)}\right] \tag{33}$$

Figure 25 shows the specific heat capacity of GGG (J/mol-K) as a function of temperature at various applied magnetic fields.

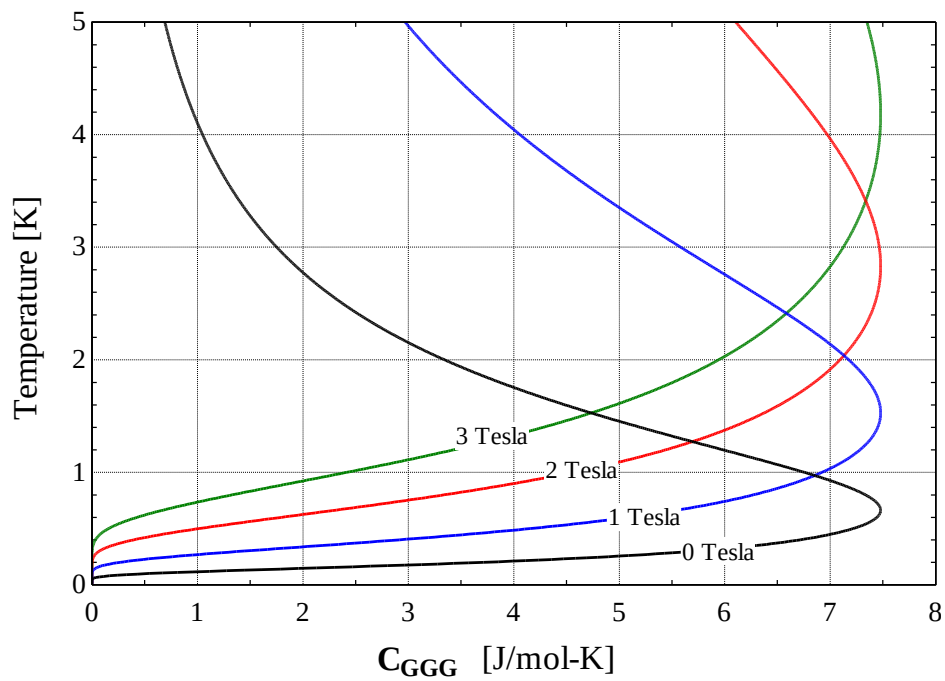

Figure 25. Specific heat of GGG as a function of temperature at various constant external applied magnetic fields

2.4. References

Barclay, J. A., and W. A. Steyert. Materials for magnetic refrigeration between 2 and 20 K. No. LA-8746-MS. Los Alamos Scientific Lab., NM (USA), 1981.

Chaudhry, G., PhD dissertation, Massachusettes Institute of Technology, 2009

Department of Energy, private communication 2013

Ebner, C., and David O. Edwards. "The low temperature thermodynamic properties of superfluid solutions of 3 He in 4 He." Physics Reports 2.2 (1971): 77-154.

Enss, Christian, ed. Cryogenic particle detection. Vol. 99. Springer, 2005.

Jahromi, A. E., Master's thesis, University of Wisconsin – Madison, 2011.

Keller, William E. Helium-3 and helium-4. Plenum Press, 1969.

Lounasmaa, Olli V., O. V. Louasmaa, and O. V. Lounasmaa. Experimental principles and methods below 1 K. Vol. 8. London: Academic Press, 1974.

Miller, F. K., and Brisson, J. G., "A simple method for the analysis of sub-Kelvin refrigerators that use a dilute superfluid 3He-4He mixture as a working fluid," Cryogenics, Vol. 41 (2001), pp. 311-318.

Moseley, Harvey. Benford, Dominic. Harvey Moseley, and Jonas Zmuidzinas. "Direct detectors for the Einstein inflation probe." Journal of Physics: Conference Series. Vol. 155. No. 1. IOP Publishing, 2009.

Nellis, G. F., Klein S. A., Thermodynamics, Cambridge University Press, 2011

Van Sciver, Steven W. Helium cryogenics. Springer Science & Business Media, 2012.

Vollhardt, Dieter, and Peter Wolfle. The superfluid phases of Helium 3. Courier Corporation, 2013.

3. Review of the low temperature facility and equipment

3.1. Introduction

The objective of this chapter is to briefly familiarize the reader with the lab equipment and facility that was either developed as part of the author's master's thesis work or during this work. This facility serves as a foundation for the SMP experiment and can be potentially used for future sub Kelvin experiments. A list of major equipment, instruments, and measurement equipment and their specifications are provided in this chapter.

3.2. Low temperature facility

The author had been responsible for modeling, design, construction and assembly of majority of the low temperature facility. This low temperature facility can be thought of as two refrigerators: A two stage commercial Cryocooler that uses a closed refrigeration cycle and a custom-built 1 K pot (a refrigerator that provides a nominal low temperature of 1 Kelvin) that works as an open cycle. These two refrigerators have different fluid circuits that are independent from one another. The Cryocooler system prepares the 1 K pot to achieve sufficiently low temperatures, thus the cryocooler must run properly before running the 1 K pot.

The cryocooler used in this facility is a Cryomech pulse tube model 410. This cryocooler has two heat exchangers, one operating at temperatures around 40 K (30 W) and the other at 4 K (1 W), hence a "two stage cryocooler". The advantage of using a pulse tube as opposed to traditional cryocoolers is extremely low levels of vibrations in the system due to the lack of any mechanical moving parts in the cold side of the system. The specific cryocooler used in this work was custom built to include an electrical isolator (a dielectric flange) that connects the remote

valve to the flex hose, eliminating inadvertent electrical noise propagation into the Dewar. The latter two features are extremely vital to the successful run of near or sub Kelvin experiments.

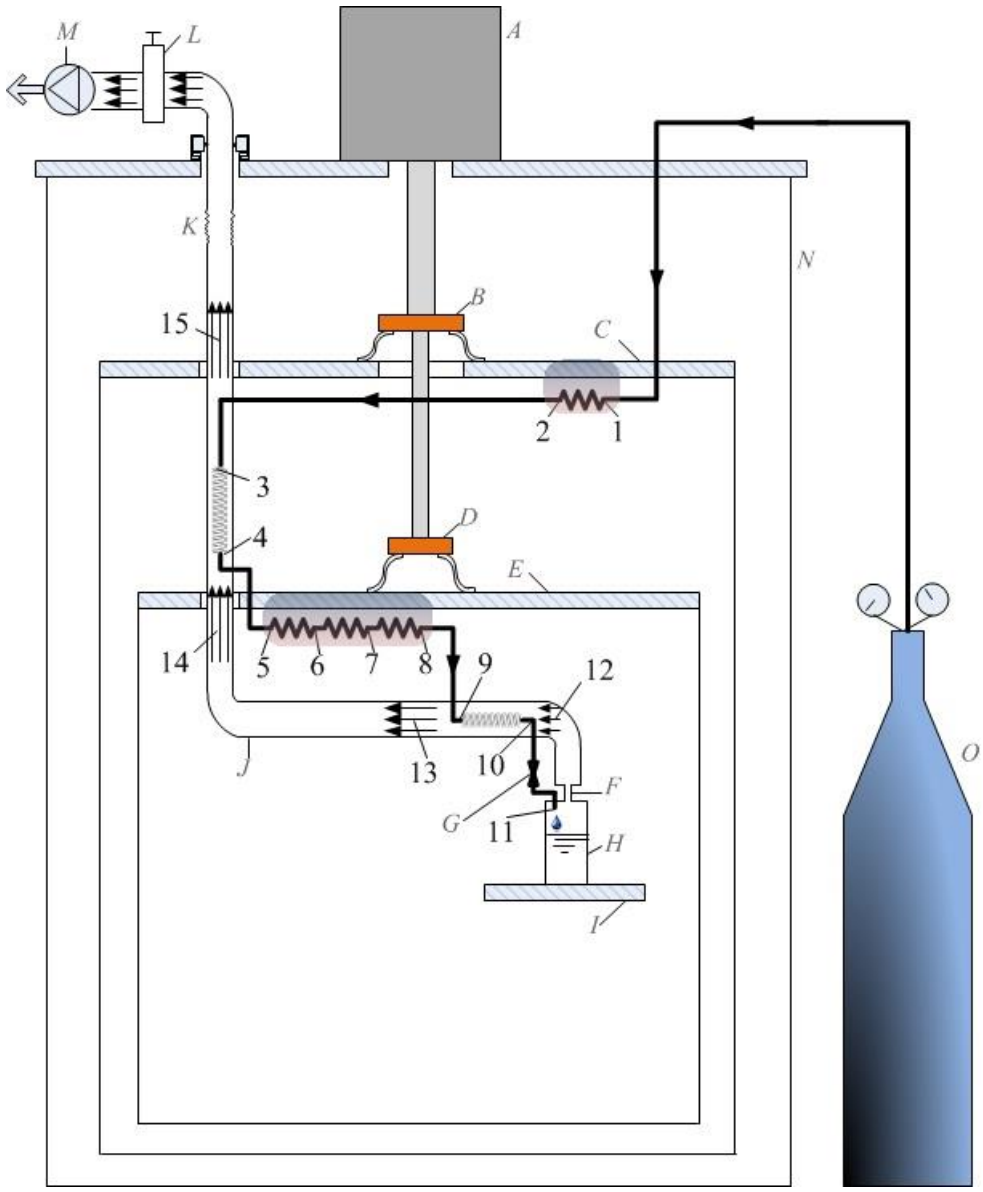

Figure 26. An overall schematic of our 1 Kelvin facility (Helium is traced by numbers, Components are labeled by letters, HX: Heat Exchange(r)); *A*: PT-410 Cryomech cryocooler equipped with vibration isolator, *B*: Cryocooler's 1st stage HX, *C*:1st stage HX platform and shield assembly connected to *B* via heat straps [16], *D*: 2nd stage HX, *E*: 2nd stage HX platform and shield assembly connected to *D* via heat straps, *F*: Superfluid film killer, *G*: Capillary (fixed J-T valve), *H*:Copper 1 Kelvin pot, *I*: 1Kelvin plate, *J*: evacuated exhaust line, *K*: bellows, *L*: Vacuum isolation valve, *M*: SogeVac SV 25-B rotary vane vacuum pump, *N*: Dewar, *O*: Helium reservoir equipped with a 2 stage pressure regulator.

A schematic of the 1 K facility is shown in Figure 26. The 1 K pot uses a series of heat exchangers and recuperators to precool, condense, and sub-cool helium that is released from a room temperature gas bottle. A low temperature of 1.4 K is achieved in the pot once the sub-cooled helium throttles through a Joule-Thomson restrictor resulting in an isenthalpic expansion of the incoming helium before discharging into the pot. A single stage rotary vane pump is used to pull a vacuum on the liquid helium level in the pot. This 1 K pot was able to reach an ultimate low temperature of 1.39 K at no load and provides a cooling power of 150 mW at 1.65 K. More details of this system are provided in a comprehensive paper published by the author (Jahromi 2014). Expanded details of this system can be found in the author's M.S. thesis (Jahromi 2011). Note that previously the 1 K pot was precooled from room temperature to intermediate temperatures using a gas heat switch. The author discovered that by simply using a thin copper thermal strap between the 1 K plate and the second stage heat exchange platform the cool down time was substantially reduced, from about 10 days to 36 hours. A list of the 1 K facility's components and specifications are listed in Table 5. Figure 27 shows an image of the 1 K facility.

Component	Model	Specification
Dewar	Custom – Precision Cryo.	AL-6061 T6 body , 3 shields (outer, 40K, and 4K)
Cryocooler	PT-410	Two stage (30 W @ 40 K) and (1 W @ 4 K) vibration isolated
Compressor	CP 2800	Water cooled (5 GPM)
Turbo Vac. Pump	Pfeiffer – TMH 071	1500 Hz , P < 10^{-7} mbar
Diaphragm pump - roughing	Pfeiffer – MVP 040	Dry, P< 4 mbar
1 K pot vac. Pump	SogeVac 25 B	25 m^3/hr, P< 0.5 mbar
1 K refrigerator	Custom-built at home	0 W @ 1.39 K, 150 mW @ 1.65 K

Table 5. List of some major components in the low temperature facility

Figure 27. An image of the low temperature facility

3.3. Measurement and other lab equipment

Various pieces of equipment were procured in preparation of the experimental setup for the SMP. These includes instruments that acquire temperature, voltage, current, pressure, capacitance, flow rates as well as source meters to supply current to the superconducting magnets. A coil winder was also procured for winding the superconducting magnets. A dual stage vacuum pump was used to aid in the purging of the SMP's closed fluid loop with helium before cooldown.

Two temperature controllers, CryoCon model 44 with 4 thermometry channels each as shown in Figure 28, were used to make temperature measurements. These instruments are also internally equipped with a PID control scheme, enabling the user to control the temperature of a platform/specimen via a 25 or 50 ohm heater. Two types of thermometers were mainly used in the system: 4 Lakeshore Cernox-1030 thermometers insensitive to applied magnetic fields for sensitive temperature measurements and 4 Lakeshore Silicone Diode DT-470 thermometers for non-critical "housekeeping" measurements (i.e., the temperature of the pot return line, the 40 K heat exchanger, etc.).

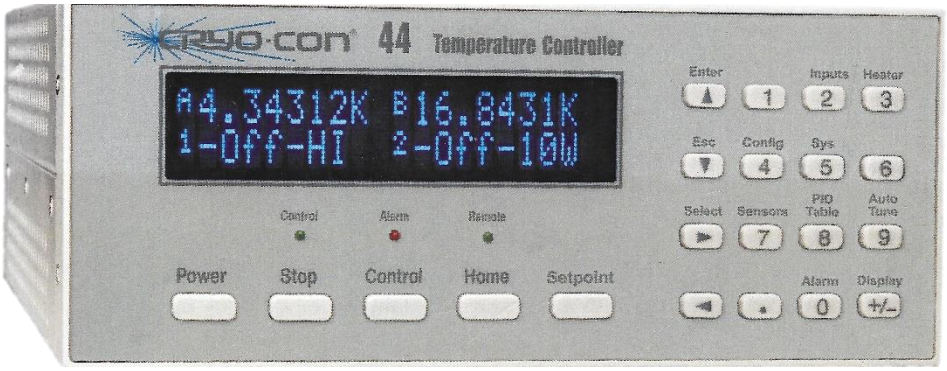

Figure 28. Cryocon model 44 temperature controller

Two programmable current source meters, Keithley model 2440 as shown in Figure 29, capable of supplying a maximum current of 5 Amp and/or potential of 30 Volt were used to energize the superconducting magnetics. These devices provide a 0.012% basic measure accuracy with 5 ½ digit resolution. Two modes of operation are available in these instruments: sourcing current/measuring voltage or sourcing voltage/measuring current via 4 wires. These instruments were used to charge and discharge the superconducting magnets.

Figure 29. Keithley source meter model 2440

A digital multi-meter data acquisition and data-logging system, Keithley model 2700 integrated with a Keithley 7700 multiplexer as shown in Figure 30, with 10 channels capable of providing 6 ½ digit resolution was used to measure various voltage, current, and resistance values throughout the system.

Figure 30. Keithley multimeter model 2700 with multiplexer card

An analog capacitance bridge, General Radio model 1615-A as shown in Figure 31, was used to make capacitance measurements of a dielectric insensitive differential pressure transducer discussed in chapter 6.

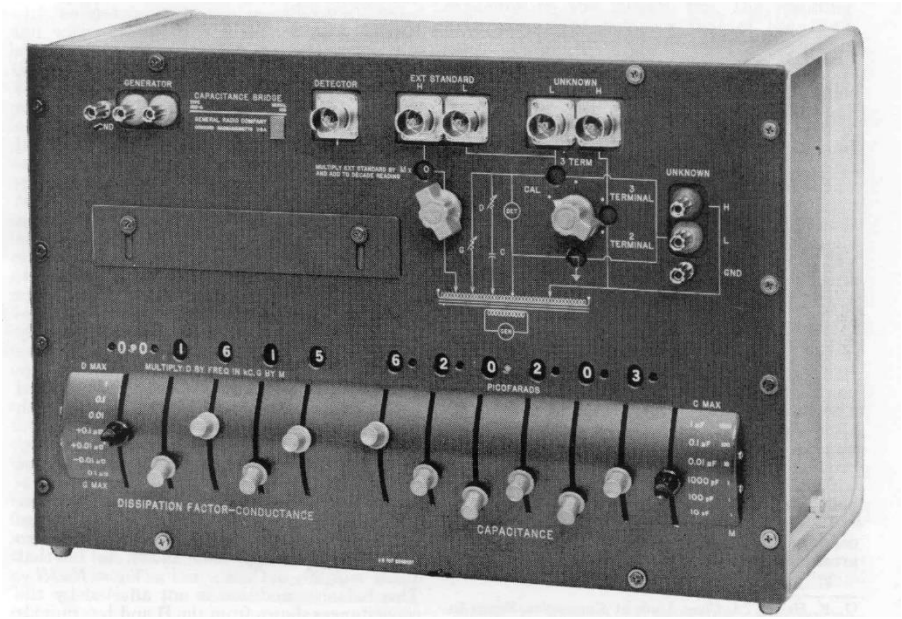

Figure 31. Capacitance bridge GenRad 1615-A

A dual phase lock in amplifier, EG&G model 5210 as shown in Figure 32, was used to find the capacitance value of the pressure transducer via the analog bridge using a nulling technique.

Figure 32. EG&G model 5210 Lock in amplifier

An Alcatel 2021-C dual stage rotary vane pump was used to help purge the SMP fluid line with helium. An absolute pressure transducer, Endres Hausen model Cerebar S PMC71, was used to measure the vacuum level or charge level in the purging line connected to the Alcatel pump.

It was necessary to install a set of two flow meters, OMEGA FMA 1700/1800, one with higher sensitivity that measured flows of up to 500 mL/min of standard N_2 and the other measuring flows up to 2 L/min of standard N_2, in the 1 K pot fluid circuit to accurately measure the mass flow rate of helium in the system in order to diagnose potential blockages in various segments of the fluid path inside the Dewar as a result of impurities, especially the hypodermic capillary used as the J-T restrictor of the 1 K refrigeration system.

A Gorman star winding machine was used to wind the superconducting magnets. This machine was equipped with CNC, enabling the user to program the winder for custom winding conditions and geometries. An image for this winding machine is shown in Figure 33.

Figure 33. Gorman star winder machine

A list of all lab equipment and their usage noted in this section is provided in Table 6.

Equipment	Manufacturer/Model	Purpose
Temperature controller	Cryocon 44 B	Temp monitor/control
Thermometer	Cernox 1030	Temp measurement
Thermometer	DT-470	Temp measurement
Source meter	Keithley 2440	Charging magnets
Multi-meter Multiplexer	Keithley 2700/7700	Various measurements
Capacitance bridge	General Radio 1615-A	Diff. P transducer
Lock in amplifier	EG&G 5210	Nullifying cap. bridge
Vac. Pump	Alcatel 2021-C	Purging exp. Loop
Mass flow meter	OMEGA 1700/1800	1 K pot diagnostic tool
Wire winder	Gorman star winder	SC magnet winding

Table 6. List of measurement and other lab equipment

3.4. References

Jahromi, Amir E., Master's thesis, University of Wisconsin – Madison, 2011

Jahromi, Amir E., and Franklin K. Miller. "Modeling, development, and experimental validation of a Joule–Thompson superfluid refrigerator using a pulse tube cryocooler." *Cryogenics* 61 (2014): 15-24.

4. Modeling of the SMP

An introduction to the SMP is presented in the beginning of this chapter followed by a qualitative description of one cycle operation of the SMP. A model of an ideal SMP is developed and discussed to quantify the pump performance by breaking the cycle into adiabatic and isothermal processes; the two operational limits of the SMP. The model will be able to predict the mass flow rate produced by the SMP under various thermodynamic conditions. Some important loss parameters such as eddy currents within the canister's body, superfluid turbulence in the superleak, and entropy generation due to pressure drop, within the GGG, and heat transfer between GGG and He II are justified to be negligible. Finally the model predictions are provided at the end of this chapter.

4.1. Introduction

Figure 1 shows a simplified schematic of the SMP. This figure shows two SMPs that operate one-half cycle apart from each other. Each SMP consists of a cylindrical stainless steel canister that is surrounded by a low temperature superconducting magnet (Nb-Ti) filled with crushed GGG. He II fills the voids between the GGG particles in each of the canisters. The role of the GGG is to cool or heat the surrounding helium depending on which part of the cycle the SMP is operating. Any other material directly anchored to the canisters would add to the heat capacity of the canisters constituents thus hampering the performance of the SMP. Therefore, the canisters must be thermally isolated from the surroundings. This is accomplished by suspending the canisters from the magnet's mandrel using very thin Kevlar strands. Finally, the two canisters are connected by a superleak. The superleak only allows the superfluid component of ^{4}He to flow from one canister to the other.

4.2. Qualitative description of the SMP's operation during one cycle

The SMP can either act as a displacer (i.e. for an AMRR or a circulator) or a compressor (i.e. for the SPTR) as it approaches either its isothermal or adiabatic limits, respectively. A qualitative description of one cycle operation of the SMP is described in this section. One cycle operation consists of four processes: adiabatic magnetization (process I-II), isothermal magnetization (process II-III), adiabatic demagnetization (process III-IV), and finally isothermal demagnetization (process IV-I).

Consider the LHS-SMP shown in Figure 1. Initially the superconducting magnet of this SMP is either slightly charged or not charged at all; hence, a magnetic field (B_{min}) is applied to the constituents of this canister. He II and the GGG within this canister are in thermal equilibrium at T_{low}. This temperature and applied magnetic field define state I. Then, the applied magnetic field is increased by charging the coil until the temperature of the constituents of the canister reach state II at a new temperature T_{high}. The corresponding applied magnetic field at this time is an intermediate value ($B_{int,II}$). Any further increase of the applied magnetic field (i.e., its rate of rise) is controlled in a way to maintain the temperature of the constituents of the canister at this new temperature, T_{high}. At the end of this process, the applied magnetic field has reached its maximum value at state III, B_{max}. Process II-III continually promotes the transition of some of the superfluid ^{4}He to its normal state. As described earlier in Chapter 2, superfluid ^{4}He flows from the RHS-SMP into the LHS-SMP through the superleak to maintain equal ^{4}He chemical potential across the superleak. This inflow of superfluid ^{4}He displaces some amount of the He II (normal and superfluid) out of the canister through the non-superleak port. Note that no helium is assumed to enter or exit the canister during process I-II because this process occurs at a much faster rate compared to process II-III. The other half of the cycle is operated in reverse order. The applied

magnetic field is decreased until the temperature of the constituents of the canister reach state IV at T_{low}. The corresponding applied magnetic field at this time is a different intermediate value from state II ($B_{int,IV}$). The applied magnetic field is then decreased to its original value at state I. The temperature of the constituents of the canister remain the same during process IV-I. Process IV-I continually demotes some of the normal ^{4}He to superfluid state requiring some normal ^{4}He to replenish the canister via the non superleak port. This concludes the qualitative description of one cycle operation of the SMP.

4.3. Assumptions required for the SMP modeling

This section is divided into five sub sections. Some assumptions along with their justification are presented that help model the ideal SMP cycle. These assumptions include negligible heat generation in the canister body due to eddy currents, minimal or no superfluid turbulence in the superleak, negligible entropy generation due to pressure drop and heat transfer in the bed, and finally negligible entropy generation within the GGG particles.

4.3.1. Eddy currents in the canister body

It is well known that a varying magnetic field in a conductor induces loops of electrical currents due to Faraday's law of induction. These eddy currents flow in closed loops within conductors in planes perpendicular to the magnetic field (Griffiths 2012):

$$\nabla \times \vec{E} = -\frac{\partial \vec{B}}{\partial t} \tag{34}$$

where E is the electrical field, B is the applied magnetic field, and t is time. Note that vectors are shown with an overhead arrow. Eq. (34) can be written in integral form using Stokes theorem:

$$\oint \vec{E} \,.\, d\vec{l} = -\int \frac{\partial \vec{B}}{\partial t} \,.\, d\vec{A} = -\frac{d\phi}{dt} \qquad (35)$$

where *dl* is an infinitesimal vector element of the loop, *dA* is an infinitesimal vector element of the effective surface area, and φ is the magnetic flux. It is straightforward to integrate and apply Ohm's law to Eq. (35) in order to find a relationship between the power dissipated as a result of Eddy currents in a conductor and other variables. The Eddy current dissipation in a cylindrical tube of radius *r*, thickness *th*, and length *L* in the presence of a changing magnetic field $\dot{B}$ is:

$$\dot{Q}_{tube} = \frac{\pi\, L\, \dot{B}^2}{2\, \rho_{el}}\, r^3\, th \qquad (36)$$

where ρ_{el} is the electrical resistivity of the tube. For solid rods of radius r, Eq. (36) can be converted to differential form and integrated over the radius to yield:

$$\dot{Q}_{rod} = \frac{\pi\, L\, \dot{B}^2}{8\, \rho_{el}}\, r^4 \qquad (37)$$

It is now possible to estimate the heat generation due to Eddy currents within the stainless steel 304 canister body by considering the two sealing caps as rods and the main canister as a cylindrical tube. Each tube has a length of 7.5 cm, outer diameter of 3.8 cm, and thickness of 1.6 mm. The caps are 5 mm thick and 3.8 cm in diameter. The maximum field is assumed to be 1 Tesla with an aggressive ramp rate of 5 seconds. Therefore the rates of thermal energy generation in the caps and the tube are estimated to be 160 μW and 100 μW, respectively, for a total of 260 μW. This value of dissipation is deemed negligible when compared to the 10s to 100 mW of power rejected/absorbed by the GGG during one cycle operation of the SMP as demonstrated later in this document.

4.3.2. Superfluid turbulence in the superleak

The flow of He II through a porous element is considered to be in the ideal state as long as the superfluid velocity in the porous media is lower than the critical velocity discussed in Chapter 2. Above the critical velocity, turbulence or vortices are created perpendicular to the flow path inhibiting the flow of superfluid helium by trapping normal helium in such vortices, a mechanism known as the "Gorter-Mellink mutual friction". The goal of this sub section is to characterize this critical velocity, hence arriving at a maximum permissible flow rate through the porous media used in the SMP before experiencing a breakdown of the laminar or "ideal" flow regime.

The critical velocity of superfluid helium through pores with diameters of d is estimated according to a fitted equation with the data taken from Van Sciver (2012):

$$v_{sc} = 0.002812\,(d^{-0.2574}) \tag{38}$$

The type of porous media used for the SMP experiment in this work is a porous glass with the commercial name Vycor 7930®, manufactured by Corning Inc. available in cylindrical rods of various diameters. The average pore size of this type superleak is reported to be 0.004 microns with a porosity of 28% (Corning Inc. 2015). Therefore using Eq. (38) the critical velocity of superfluid through this type superleak is estimated to be 40 cm/s. Murakami et. al. (1992) reports a method for calculating the effective area of porous media used in He II experiments as:

$$A_{eff} = N\,\pi\left(\frac{d}{2}\right)^2 = \frac{\varepsilon\,A_s}{\omega} \tag{39}$$

where N is the number of flow passages, ε is the porosity, ω is the tortuosity, and A_s is the apparent surface area of the superleak perpendicular to flow direction. Brewer et. al (1981) reports the tortuosity of Vycor 7930 to be 0.3. Considering three rods of Vycor in parallel, it is now possible to estimate the maximum mass flow rate through the superleak used in this work. Using 40 cm/s

as the maximum permissible superfluid velocity and using Eq. (39). this value is estimated to be 3.252 g/s. A value much higher than the maximum flow rate predicted by the SMP as discussed later in this document.

4.3.3. Entropy generation due to pressure drop and heat transfer in the bed

Two of the dominant sources of entropy generation in the SMP are that due to pressure drop as a result of He II flow through the packed bed of GGG, and that due to heat transfer across a finite temperature difference between the GGG particles and the surrounding He II. The goal of this section is to quantify these two terms.

The SMP produces flow during an isothermal process. Therefore the entropy generation rate for a differential segment of the packed bed at constant temperature can be expressed as two terms using the chain rule:

$$\left(\frac{\partial \dot{S}_{gen}}{\partial x}\right)_T = \underbrace{\dot{m}\left(\frac{\partial s}{\partial i}\right)_P \left(\frac{\partial i}{\partial x}\right)_T}_{Due\ to\ heat\ transfer} + \underbrace{\dot{m}\left(\frac{\partial s}{\partial P}\right)_i \left(\frac{\partial P}{\partial x}\right)_T}_{Due\ to\ pressure\ drop} \tag{40}$$

where $\dot{s}_{gen}$ is the rate of entropy generation, i is the enthalpy, x is the axial position along the packed bed. The first term on the right hand side of Eq. (40) is the entropy generation rate due to heat transfer and the second term is due to pressure drop as a result of fluid flow. Using derived thermodynamic relations:

$$\left(\frac{\partial s}{\partial i}\right)_P = \frac{1}{\left(\frac{\partial i}{\partial s}\right)_P} = \frac{1}{T} \tag{41}$$

and knowing that the change in enthalpy of the fluid is a result of heat transfer from the GGG particles to the surrounding helium yields:

$$\dot{m}\left(\frac{di}{dx}\right)_T = \dot{Q}' \tag{42}$$

where $\dot{Q}'$ is the heat transfer rate per unit length of the packed bed. After integration the first term on the right hand side of Eq. (40) can be expressed as:

$$\Delta\dot{s}_{gen,\,HT} = \left(\frac{\dot{Q}'}{T} - \frac{\dot{Q}'}{\left(T+\Delta T\right)}\right) \tag{43}$$

the rate of heat transfer between the GGG particles and He II for a differential segment can be expressed as:

$$\dot{Q}' = h\,\alpha\,\Delta T \tag{44}$$

where ΔT is the temperature difference between GGG and He II, h is the heat transfer coefficient and α is the heat transfer area per unit length which can be defined in terms of GGG particle diameter d_p , cross sectional area of the core A_c, and bed porosity ε :

$$\alpha = \frac{\overbrace{\dfrac{4\,\pi\,r^2}{1}}^{Surface\ area\ of\ a\ sphere}}{\underbrace{\dfrac{4\,\pi\,r^3}{3}}_{Volume\ of\ a\ sphere}}\ \underbrace{A_c\,(1-\varepsilon)}_{solid\ occupancy} = \frac{6\,A_c\,(1-\varepsilon)}{d_p} \tag{45}$$

The interfacial thermal boundary conductance which occurs between any two dissimilar materials where electronic transport does not contribute is called Kapitza conductance (Van Sciver 2012). This mode of conductance becomes the dominating factor in determining an appropriate heat transfer coefficient between He II and an adjacent solid. Values of Kapitza resistance in terms

of a heat transfer coefficient is experimentally found between GGG and He II by Hakuraku (1984) as:

$$h_k = \left(0.067\, T_b^3\right)\left\{1 + \frac{3}{2}\left(\frac{\Delta T}{T_b}\right) + \left(\frac{\Delta T}{T_b}\right)^2 + \frac{1}{4}\left(\frac{\Delta T}{T_b}\right)^3\right\} \quad \left[\frac{W}{cm^2 - K}\right] \tag{46}$$

where T_b is the interface temperature. A lower interface temperature provides a more conservative estimate, therefore using the term on the right hand side of Eq. (43) and assuming an interface temperature of 1.4 K, bed porosity of 38%, particle diameter of 1 mm, and a heat transfer rate of 150 mW (as shown later in this document) yields a temperature difference of only 17 μK and 1.3 μW/K of entropy generation due to heat transfer between GGG particles and He II.

Now the second term on the right hand side of Eq. (40) can be expanded by using the fundamental property relation:

$$di = T\, ds + v\, dP \tag{47}$$

where v is the specific volume. The change of entropy with respect to pressure for a constant enthalpy process is derived by setting di to zero in Eq. (47) to yield:

$$\left(\frac{ds}{dP}\right)_i = -\frac{v}{T} \tag{48}$$

by applying Eq. (48) to the second term on the right hand side of Eq. (40) the entropy generation rate due to pressure drop can be expressed as:

$$\frac{d\dot{s}_{gen,\,DP}}{dx} = -\frac{\dot{m}\, v}{T}\left(\frac{dP}{dx}\right)_T = -\frac{\dot{m}}{\rho\, T}\left(\frac{dP}{dx}\right)_T \tag{49}$$

where ρ is the density of the fluid. An extremely conservative estimate of the pressure drop per unit length for He II is found by using the following equation (Nellis 2009):

$$\frac{dP}{dx} = \frac{1}{2}\,\rho\,\bar{v}^2\,\frac{f}{D_h} \tag{50}$$

where $\bar{v}$ is the mean velocity of fluid, f is the Darcy friction factor, and D_h is the hydraulic diameter defined for a packed bed of random spheres as:

$$D_h = \frac{\varepsilon\, d_p}{4\,(1-\varepsilon)} \tag{51}$$

The Reynolds number is needed in order to find the friction factor from graphs provided by London and Kays (1984) for such configurations. The Reynolds number is defined as:

$$Re = \frac{2\,G\,D_h}{\mu} \tag{52}$$

where G is the mass flux defined as:

$$G = \frac{\dot{m}}{\varepsilon\,A_c} \tag{53}$$

Assuming no thermodynamic irreversibilities, the maximum mass flow rate in a He II fountain effect pump can be estimated by applying a simple second law balance on the canister to yield a conservative estimate:

$$\dot{Q} = \dot{m}\,T\,(\underbrace{\cancel{s_{in}} - s_{out}}_{superfluid,\, s=0}) = -\dot{m}\,T\,s \tag{54}$$

Applying a heat of 150 mW at 1.4 K yields a maximum mass flow rate of 810 mg/s. Therefore the friction factor is found to be 0.55 and the pressure drop per unit length of the packed bed is found to be 21.5 Pa/m. Applying this to Eq. (49) yields an entropy generation rate of 6 μW/K due to pressure drop.

The rate at which entropy is being removed from the GGG during the isothermal flow process is estimated to be 100 mW/K. This is the entropy change of the GGG during an isothermal

magnetization process. The total entropy generation due to heat transfer and pressure drop is summed to be 7.3 μW/K. This is 0.007% of the entropy lifted form the GGG therefore entropy generation due to pressure drop and heat transfer between the GGG particles and He II is deemed negligible.

4.3.4. Entropy generation within the GGG particles

The diffusive time constant, (i.e. the time required for a thermal wave to travel from the center of the spherical GGG particles to its surface) is estimated according to (Nellis 2009):

$$\tau_{diff} \approx \frac{L^2}{4\,\alpha} \tag{55}$$

where L is the distance the thermal wave needs to travel and α is the thermal diffusivity defined by:

$$\alpha = \frac{k}{\rho\, c} \tag{56}$$

where k is the thermal conductivity, and c is the specific heat capacity. The diffusive time constant can now be calculated for GGG by considering spherical GGG particles of 1 mm diameter. The diffusive time constant is plotted as a function of applied magnetic field for highest and lowest temperatures in the SMP as shown in Figure 34.

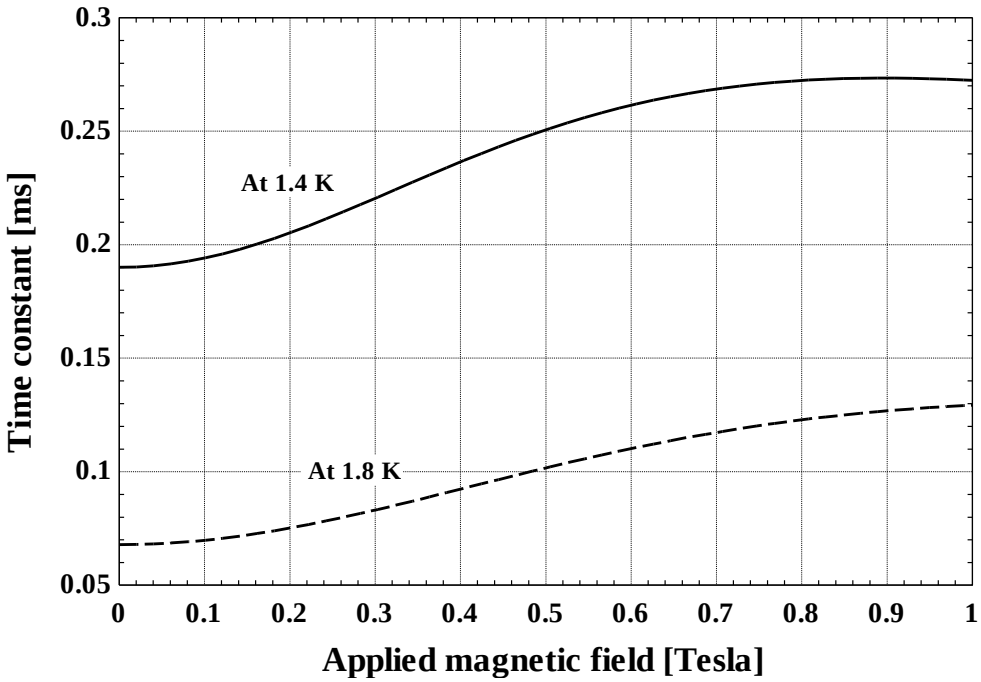

Figure 34. Thermal diffusive time constant for GGG vs applied magnetic field

As can be seen from this plot, the highest diffusive time constant is approximately 0.27 ms which is only 0.0018 % of the fastest time required to ramp the superconducting magnets to peak field for one cycle of the SMP. A low diffusive time constant implies very good internal thermal equilibrium, hence very small finite temperature differences within the material. Any entropy generation within the GGG is safely ignored throughout the model because the diffusive time constant is very short compared to the ramp time of the SMP's superconducting magnet.

4.3.5. Summary of assumptions

A list of assumptions made for the modeling of an ideal cycle of the SMP are listed in Table 7.

Assumption	Reasons
Negligible parasitic heat into canister	Canister suspended via Kevlar strands
Negligible dissipation in canister body due to Eddy currents	Only 260 µW << target 10-150 mW power
No superfluid turbulence in superleak	3.252 g/s threshold >> target design of ~1 g/s
Negligible $\dot{S}_{gen}$ due to pressure drop	6 µW/K (0.006% of total entropy lifted)

Negligible $\dot{S}_{gen}$ due to heat transfer (GGG-He II)	1.3 μW/K (0.0013% of total entropy lifted)
Negligible $\dot{S}_{gen}$ within GGG particles	Low diffusive time constant
Negligible $\dot{S}_{gen}$ within He II	Extremely high effective thermal conductivity due to superfluidity

Table 7. Assumptions made for the model of an ideal SMP cycle

4.4. Ideal cycle; a simple model

A model of an ideal SMP cycle is discussed in this section. It was shown in the previous section that major loss terms can be safely ignored. Chief among them were various major entropy generation terms involved in one cycle operation of the SMP. Unlike mass and energy, entropy is not a conserved quantity. When dealing with thermodynamic analyses of typical systems one can either use mass and energy balances to model a thermodynamic system via the first law or use a combination of first and second laws to find variables of interest such as the rate of entropy generation that could be helpful in exergy or lost work potential analyses. Never can one truly predict a thermodynamic system purely on a second law analysis unless the process is reversible/near reversible, or the rate of entropy generation can be accurately accounted for, the latter being a task often non-trivial. The SMP has the great advantage of operating nearly reversibly. The entropy generation terms are very small due to the unique properties of the superfluid helium. It is now evident how the two subtly remarkable properties of superfluid helium, zero viscosity and entropy, make the SMP unique in that a simple second law analysis can be used to predict the performance of systems of this type.

The SMP has two limits of operation from a thermodynamic perspective: adiabatic and isothermal. Figure 35 shows these two limits on a temperature/applied magnetic field versus time plot. Consider an SMP fluid circuit that shows zero resistance to fluid flow. This results in a purely

isothermal SMP cycle because increasing the applied magnetic field on the constituents of the canister results in a very small increase in temperature of the GGG. This in turn warms the surrounding He II which results in a slight increase of pressure since pressure is only a function of temperature in He II as discussed in chapter 2. Hence helium flows out of the canister with the slightest pressure rise established across the fluid circuit. This is analogous to a piston cylinder apparatus with a wide open outlet valve that operates isobarically upon piston displacement. On the contrary an SMP fluid circuit that shows infinite resistance to fluid flow would behave adiabatically. Increasing the applied magnetic field on the constituents of the canister results in a temperature increase of the GGG and the surrounding He II. Pressure is built up in the He II as magnetization continues because fluid cannot flow out in a highly restrictive fluid circuit and because pressure is once again only a function of temperature in He II. This is analogous to a closed piston cylinder apparatus.

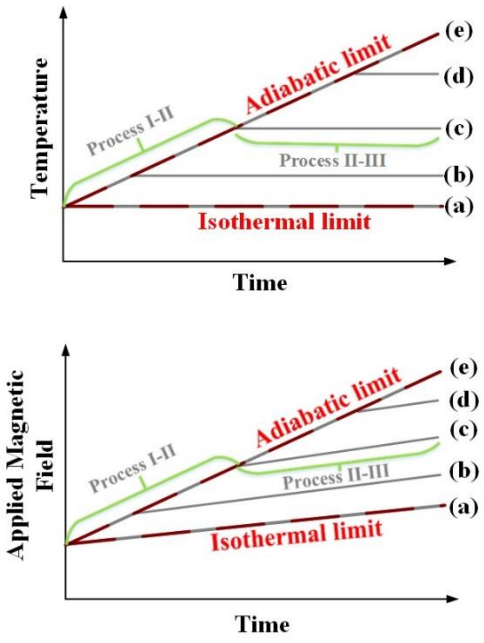

Figure 35. Qualitative plots of temperature and applied magnetic field vs. time in an ideal SMP cycle (a) shows purely isothermal SMP cycle, (e) shows purely adiabatic SMP cycle, and (b) through (d) show combinations of the limits in the SMP operation

It is possible for the SMP to operate between these two thermodynamic limits as shown in cases (b) through (d) of the plots shown in Figure 35. The cycle begins with an adiabatic process. The goal of this process is to build sufficient pressure in the canister to match the pressure difference required to drive the fluid in the circuit. An isothermal process is followed which initiates the flow of mass out of the canister by maintaining the required pressure rise (constant temperature in He II hence constant pressure) needed to continue the flow throughout the circuit as long as the isothermal magnetization process continues. This is because an increase in the field raises the He II temperature via the GGG, promoting some of the superfluid helium to normal state thus requiring some superfluid helium to flow through the canister via the superleak, replenishing the "lost superfluid" fraction within the canister. This displaces some normal and superfluid helium out of the canister through the non superleak port. The goal of the next four sub sections is now clear, to model the SMP cycle using a combination of isothermal and adiabatic processes.

4.4.1. Process I-II (Adiabatic Magnetization)

There is no heat transfer to and from the canister, therefore the process is adiabatic. The canister, the stainless steel body, GGG, and the helium surrounding it are at state I at the beginning of this process. The temperature of state I is (T_{low}) and the applied magnetic field is (B_{min}). The magnetization begins and continues until the constituents of the canister reach (T_{high}) at an intermediate magnetic field ($B_{int,\ I\text{-}II}$) at state II. Thus the goal of this subsection is to find the intermediate magnetic field required to raise the temperature of the canister from (T_{low}) to (T_{high}).

The thermodynamic system is the canister (including the stainless steel body of the canister). During process I-II the entropy of the helium in the canister changes according to:

$$\Delta S_{He,\,I-II} = m_{He}\left(s_{He}\left(T_{high}\right) - s_{He}\left(T_{low}\right)\right) \tag{57}$$

the entropy of GGG changes during this process according to:

$$\Delta S_{GGG,I-II} = m_{GGG}\left(s_{GGG}\left(T_{high}, B_{\text{int},I-II}\right) - s_{GGG}\left(T_{low}, B_{\min}\right)\right) \tag{58}$$

using the relationship for incompressible substances the entropy of the stainless steel body changes according to:

$$\Delta S_{SS,I-II} = m_{SS}\int_{T_{low}}^{T_{high}} \frac{c_{SS}(T)}{T}\,dT \tag{59}$$

no mass of helium enters or leaves the canister during this process therefore an entropy balance for the system yields:

$$\Delta S_{He,I-II} + \Delta S_{GGG,I-II} + \Delta S_{SS,I-II} = 0 \tag{60}$$

This concludes the adiabatic magnetization process.

4.4.2. Process II-III (Isothermal Magnetization)

The temperature of the canister remains constant throughout the isothermal magnetization process. The applied external magnetic field is increased from state II to state III, where the magnetic field has reached (B_{max}). The additional magnetic field during the isothermal magnetization process causes some entropy to leave the canister (He II flowing out). Since the entropy of the incoming superfluid helium is zero, this means that all of the entropy rise in the GGG during this process is equal to that leaving the canister via the non superleak port. The goal of this subsection is to find the displaced mass of helium from the canister.

The entropy of helium in the canister does not change during this process:

$$\Delta S_{He,II-III} = m_{He}\left(s_{He}\left(T_{high}\right) - s_{He}\left(T_{high}\right)\right) = 0 \tag{61}$$

the entropy of GGG changes according to:

$$\Delta S_{GGG,II-III} = m_{GGG}\left(s_{GGG}\left(T_{high}, B_{\max}\right) - s_{GGG}\left(T_{high}, B_{\text{int},I-II}\right)\right) \tag{62}$$

and the entropy of the stainless steel canister does not change:

$$\Delta S_{SS,II-III} = m_{SS}\int_{T_{high}}^{T_{high}} \frac{c_{SS}(T)}{T}\,dT = 0 \tag{63}$$

an entropy balance for this process yields:

$$\underbrace{\cancel{\Delta S_{He,II-III}}}_{0} + \Delta S_{GGG,II-III} + \underbrace{\cancel{\Delta S_{SS,II-III}}}_{0} = -m_{He,out}\; s_{He}\left(T_{high}\right) \tag{64}$$

This concludes the isothermal magnetization process.

4.4.3. Process III-IV (Adiabatic Demagnetization)

The externally applied magnetic field on the canister starts to decrease form state III to an unknown intermediate value ($B_{int,III-IV}$) which is different from the intermediate value found during process I-II. There is no heat transfer to and from the canister, therefore the process is adiabatic. Demagnetization of the GGG particles causes their temperature to drop during this adiabatic process, which in turn causes the surrounding helium to cool. The demagnetization continues until the canister reaches (T_{low}) at state IV.

The change in entropy for helium is found according to:

$$\Delta S_{He,III-IV} = m_{He}\left(s_{He}\left(T_{low}\right) - s_{He}\left(T_{high}\right)\right) \tag{65}$$

the entropy of GGG changes according to:

$$\Delta S_{GGG,III-IV} = m_{GGG}\left(s_{GGG}\left(T_{low}, B_{\text{int},III-IV}\right) - s_{GGG}\left(T_{high}, B_{\max}\right)\right) \tag{66}$$

The entropy of the stainless steel canister changes according to:

$$\Delta S_{SS,III-IV} = m_{SS}\int_{T_{high}}^{T_{low}} \frac{c_{SS}(T)}{T}\,dT \tag{67}$$

an entropy balance on the system yields:

$$\Delta S_{He,III-IV} + \Delta S_{GGG,III-IV} + \Delta S_{SS,III-IV} = 0 \tag{68}$$

This concludes the adiabatic demagnetization process.

4.4.4. Process IV-I (Isothermal Demagnetization)

The temperature of the canister is kept constant during the isothermal demagnetization process. The externally applied magnetic field decreases from state IV and returns to state I (B_{min}). The demagnetization causes some entropy to enter the canister (He II flowing in) at the precooler temperature (T_{pc}). Since the entropy of the outgoing superfluid helium via the superleak is zero, this means that the entropy reduction in the GGG during this process is equal to that entering the canister via the non superleak port. Therefore the mass of helium entering the canister depends on the precooler temperature. The goal of this subsection is to find the mass of helium entering the canister.

The entropy of helium changes according to:

$$\Delta S_{He,IV-I} = m_{He}\left(s_{He}\left(T_{low}\right) - s_{He}\left(T_{low}\right)\right) = 0 \tag{69}$$

The entropy of GGG changes according to:

$$\Delta S_{GGG,IV-I} = m_{GGG}\left(s_{GGG}\left(T_{low}, B_{\min}\right) - s_{GGG}\left(T_{low}, B_{\text{int},III-IV}\right)\right) \tag{70}$$

and the entropy of the stainless steel canister changes according to:

$$\Delta S_{SS,IV-I} = m_{SS}\int_{T_{low}}^{T_{low}} \frac{c_{SS}(T)}{T}\,dT = 0 \tag{71}$$

finally an entropy balance on the system yields:

$$\underbrace{\cancel{\Delta S_{He,IV-I}}}_{0} + \Delta S_{GGG,IV-I} + \underbrace{\cancel{\Delta S_{SS,IV-I}}}_{0} = m_{He,in}\, s_{He}\left(T_{pc}\right) \tag{72}$$

This concludes the modeling of one cycle operation of an ideal SMP.

4.5. Model predictions and results

The four processes involved in one cycle operation of the SMP were modeled in the previous section. Some geometric and thermodynamic values need to be assumed before proceeding with the results. The canister is assumed to be a tube 3.8 cm in outer diameter, 1.6 mm thick wall and 7.5 cm in length. The caps of the canister are cylinders 3.8 cm in diameter and 5 mm in length. The porosity of the bed is assumed to be 0.38. Three values for (T_{low}) are assumed at 1.4, 1.6 and 1.75 K. The maximum applied magnetic field is assumed to be 0.75 Tesla. Note that these values were chosen to closely match with those of the SMP used in the experiment conducted for this work. Figure 36 shows the total mass displaced by the SMP for various values of (T_{low}) as a function of (T_{high}). Note that maximum mass displacement occurs when the values of low and high temperatures match, as expected. These points mark the isothermal limit of operation of the SMP. On the contrary, minimum mass displacement occurs when the SMP operates adiabatically resulting in no flow.

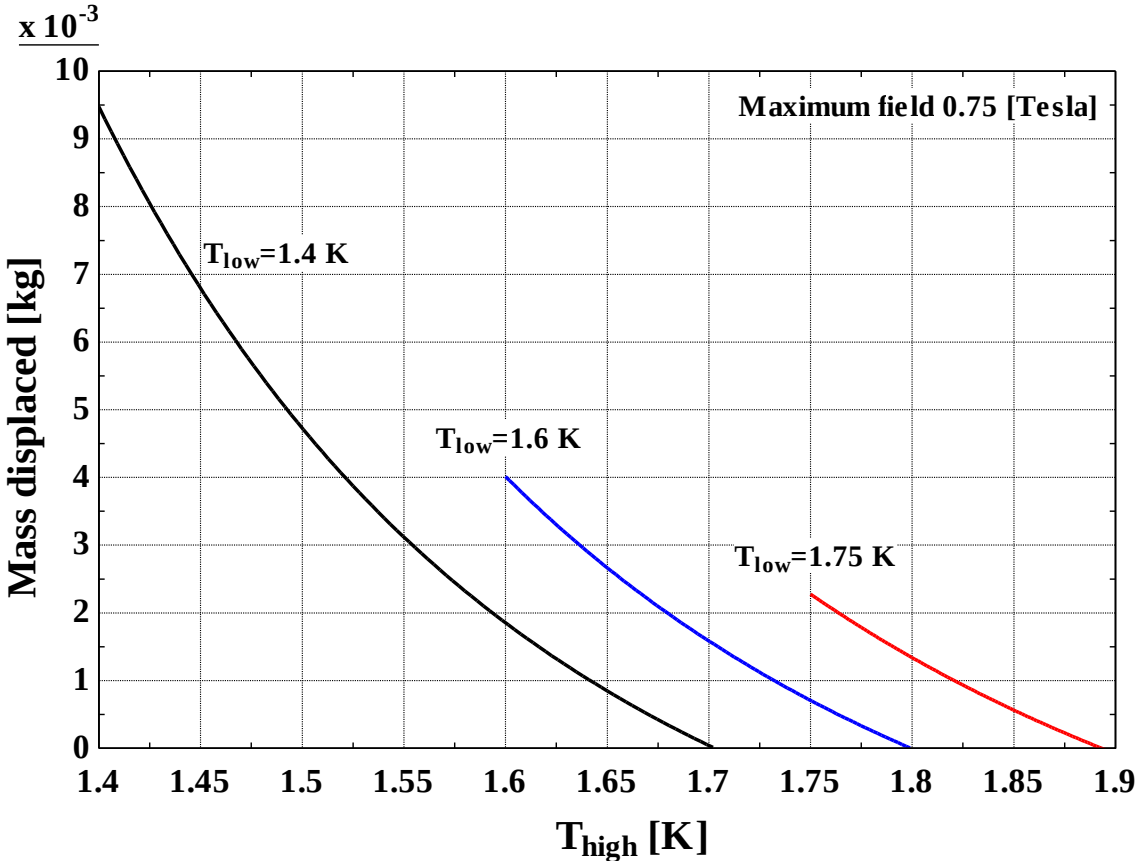

Figure 36. Mass displacement as a function of T_{high} for various values of T_{low} in the SMP

The mass flow rate produced by the SMP can be defined by dividing the total mass displacement by the length of time it takes for process II-III as:

$$\dot{m}_{SMP} = \frac{m_{out}}{\Delta t_{II-III}} \tag{73}$$

and the pump power is defined as the volume flow rate produced by the pump times the pressure difference as a result of the fountain effect as:

$$P = \underbrace{\frac{\dot{m}_{SMP}}{\rho_{He}}}_{\dot{V}_{SMP}} \; dP_{fountain}\Big|_{T_{low}}^{T_{high}} \tag{74}$$

Figure 37 shows a plot of pump power versus (T_{high}) for various values of (T_{low}). As expected, the pump power starts at a minimal value, increases to a maximum value and declines to a minimal value as (T_{high}) gets larger. This is because for low values of (T_{high}) the SMP operates near the isothermal limit representing a system with small fluid flow impedance thus the pressure difference term in Eq. (74) is very small despite $\dot{m}_{SMP}$ being large. At high values of (T_{high}) the power is low because the SMP operates near the adiabatic limit representing a system with large fluid flow impedance thus $\dot{m}_{SMP}$ being very small while the pressure difference is large. An optimum value of power exists between these two limits as shown in Figure 37.

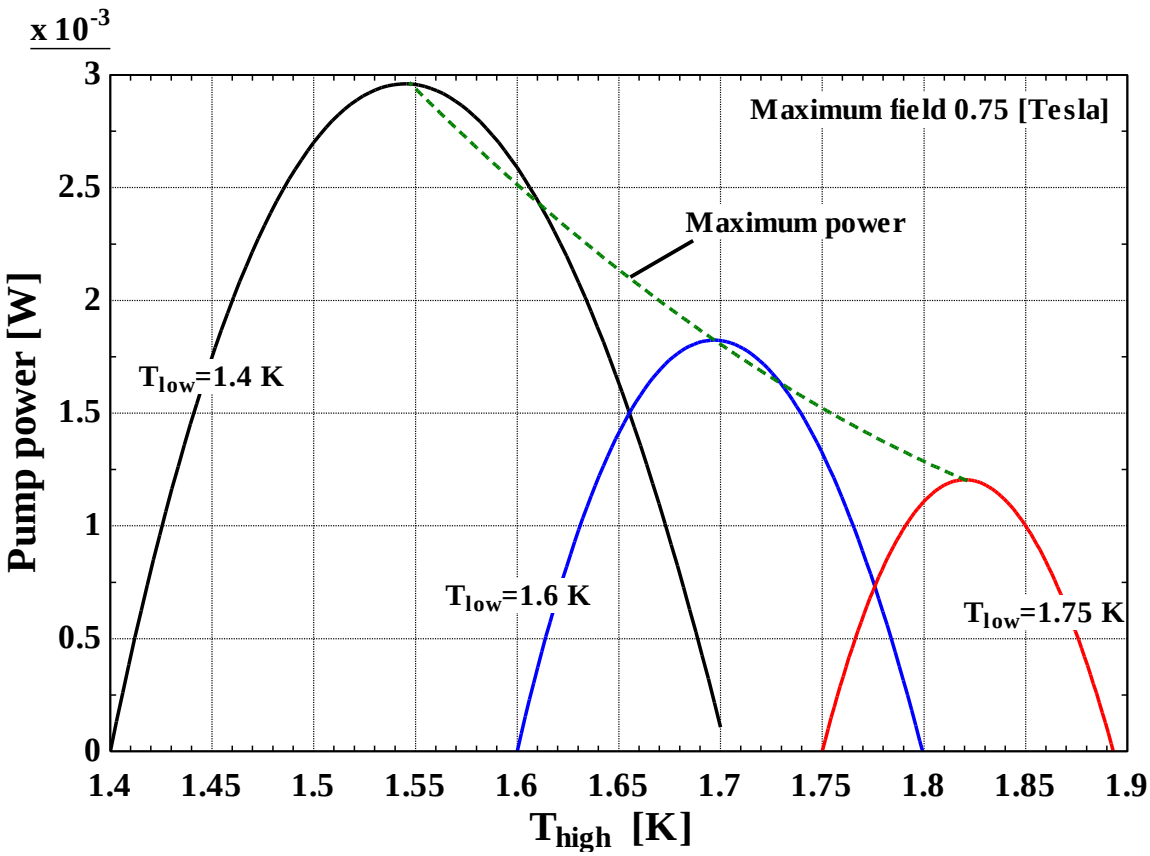

Figure 37. Pump power versus T_{high} for various values of T_{low} . The trend for maximum power is shown by the dashed line.

4.6. References

Brewer, D. F., et al. "Helium-four transition in a restricted geometry below and above the bulk solidification pressure." Physica B+ C 107.1 (1981): 583-584.

Corning Inc., Document for Corning Vycor 7930 Porous Glass, 2015

Griffiths, David Jeffrey, and Reed College. Introduction to electrodynamics. Vol. 3. Upper Saddle River, NJ: prentice Hall, 1999.

Hakuraku, Y. "Kapitza conductance of the gadolinium gallium garnet, Gd 3 Ga 5 O 12 between 1.4 K and 2.1 K." Cryogenics 24.3 (1984): 156-158.

Kays, William Morrow, and Alexander Louis London. "Compact heat exchangers." (1984).

Murakami, M., and T. Hanyu. "Thermomechanical flow of He II through a porous element for a fountain effect pump." Cryogenics 32.4 (1992): 371-378.

Nellis, Gregory., and Sanford A. Klein. Heat Transfer. Cambridge ; New York: Cambridge University Press, 2009.

Van Sciver, Steven W. Helium cryogenics. Springer Science & Business Media, 2012.

5. Numerical model of an AMRR system: an application of the SMP

The main purpose of this chapter is to present a model of a sub Kelvin AMRR that uses the novel SMP as its displacer as a potential application of the SMP. A qualitative description of the AMRR cycle is presented in the beginning of this chapter. It is then necessary to compute the mass of ^{3}He required to circulate in the system based on two design constraints: the cooling power provided by this refrigerator ($\dot{q}_{ref} = 600\ \mu W$) and the low temperature (T_{cc}= 750 mK). The mass of GGG required in the regenerator must be estimated. It is then possible to model each sub component of the AMRR and conclude with a transient cyclic numerical model of the regenerators. Summary of the results for this AMRR is discussed at the end of this chapter.

5.1. Introduction

A typical AMRR system consists of four major components: displacer(s), hot heat exchanger(s), regenerator(s), and cold heat exchanger(s). The role of the displacer is to circulate a particular refrigerant throughout the system. Just like any other refrigerator, an AMRR needs to lift heat from an object (the cold heat exchanger) and reject this heat to a thermal reservoir (the hot heat exchanger). A regenerator can be thought of as a heat exchanger, a refrigerant flows through packed bed of discrete particles: when a hot fluid is forced through the packed bed in a regenerator, it rejects its heat to the particles in the core. This heat is transferred back to the refrigerant when the cold refrigerant is forced back through the packed bed. Hence, a regenerator is a transient device; energy is stored in the packed bed during one-half of the cycle and rejected from the packed bed during the other half of the cycle.

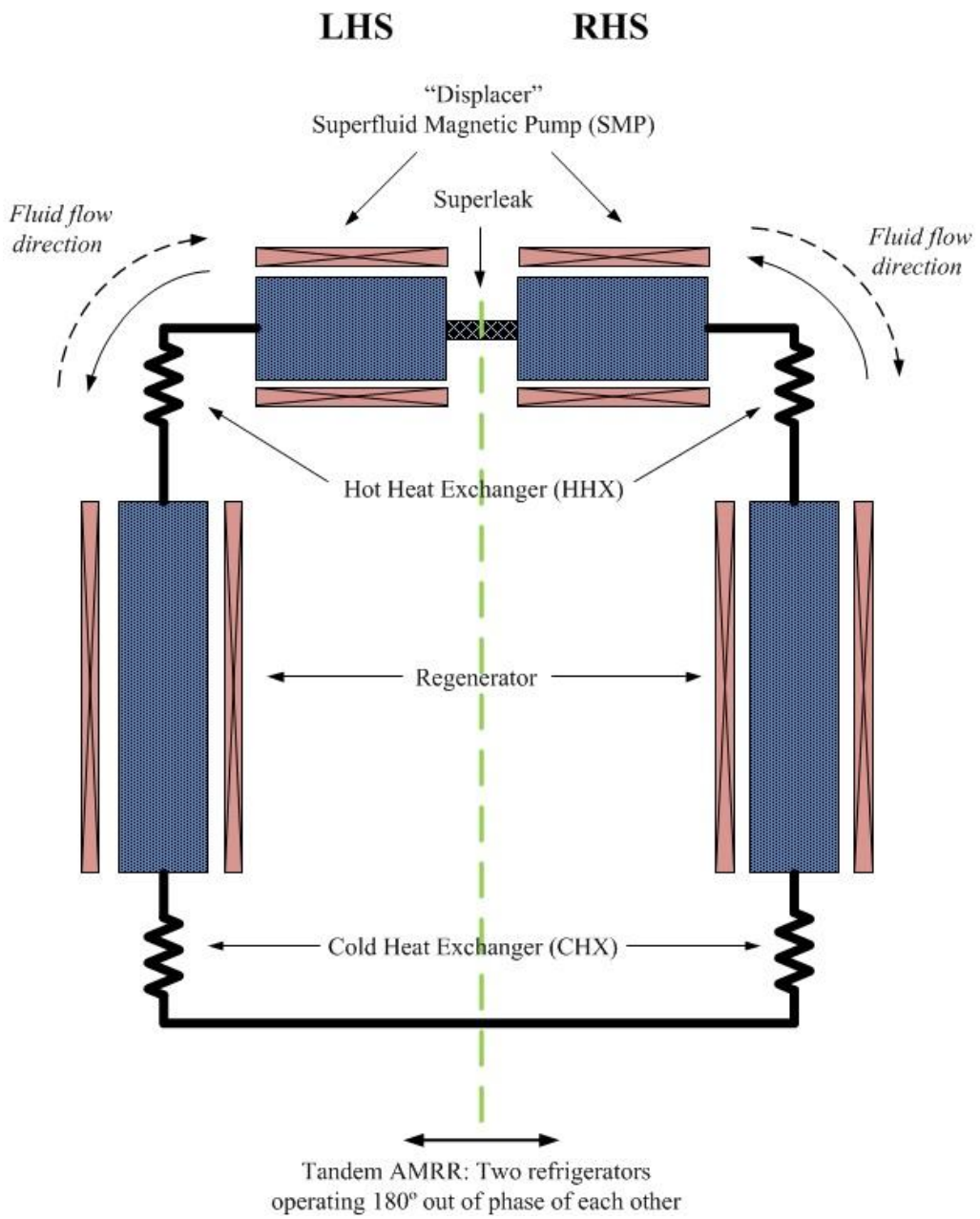

Figure 38. A simplified schematic of the AMRR discussed in this chapter. LHS denotes Left Hand Side and RHS denotes Right Hand Side

5.2. System description

Figure 38 shows a simplified schematic of the AMRR discussed in this chapter. It is a tandem system; two regenerators operate one half-cycle out of phase from each other. The main

advantages of a tandem system for an AMRR are simplified displacer operation and doubling the refrigeration capacity. The system consists of two SMPs, one superleak, two hot heat exchangers, two regenerators, and two cold heat exchangers. The refrigerant used in this system is GGG. ^{3}He-^{4}He is used as a heat transfer fluid in the AMRR system. The SMPs act as displacers in the AMRR system. The advantages of the SMP compared to conventional bellows pistons assemblies are the lack of moving parts, hence higher reliability, and a simplified displacer mechanism that can be activated entirely by changing the voltage on a superconducting solenoid. Both the regenerator and the SMP are identical in their structure. Both comprised of a canister that is surrounded by a low temperature-superconducting magnet (Nb-Ti) which is filled with crushed GGG in which the helium mixture fills the voids between the GGG particles. The only difference comes from their operation. The heat exchangers are made out of tubes that are connected to either the thermal reservoir or the cold temperature platform via solder joints. A qualitative description of one cycle of operation of the AMRR based on the system shown in Figure 38 is described next.

5.3. Cycle operation

For the operation description consider the Left Hand Side (LHS) of the system shown in Figure 38. It is sufficient to consider only one half of the system for modeling purposes for two primary reasons: (1) The two halves operate identically, only one half operates 180 degrees out of phase from the other half, and (2) the superleak and cold heat exchanger are considered as appropriate “breakpoints” for the two halves to be linked. This is because only superfluid ^{4}He can travel through the superleak from one half to the other (superfluid carries no entropy). The model links the two halves via the cold heat exchanger by considering a finite temperature rise as a result of heat exchange in the cold heat exchanger. The low and “promoted” temperature through the

cold heat exchanger set some boundary conditions in the regenerators. One cycle consists of the four following processes, presented chronologically in the next four sub sections.

5.3.1. No-Flow Demagnetization (NFD)

The LHS SMP's temperature and applied field are held constant at $T_{SMP,low}$ and $B_{SMP,low}$ throughout this process; consequently, no flow is produced. The ^{3}He concentration of the mixture in the LHS SMP is at its highest within the SMP system. Initially, a temperature profile exists between the top and bottom of the regenerator (with the bottom being the coldest and the top being the warmest). Demagnetization of the LHS regenerator begins by lowering the applied magnetic field from the peak field, $B_{Reg,peak}$. This process continues until the temperature at the bottom of the regenerator reaches the lowest design temperature $T_{CHX,in}$ at an intermediate magnetic field $B_{Reg,NFD,final}$, thus the temperature profile along the regenerator shifts down during this process. This process is shown in Figure 39-*A*.

5.3.2. Flow Demagnetization (FD)

The LHS SMP's applied field is increased from its minimum value to peak field ($B_{SMP,peak}$) during this process. Doing so raises the temperature of the mixture and promotes the transition of a fraction of the superfluid ^{4}He to normal state. This requires some superfluid ^{4}He to flow from the RHS SMP through the superleak (which only allows superfluid ^{4}He through) and into the LHS SMP in order to maintain constant ^{4}He chemical potential across the superleak. The incoming superfluid ^{4}He displaces some ^{3}He, normal, and superfluid ^{4}He out of the canister via the non-superleak port. The applied field in the LHS regenerator gradually decreases from $B_{Reg,NFD,final}$ until the coil runs out of field while ^{3}He-^{4}He flows down through the regenerator. The change in field is controlled such that the temperature of the mixture exiting at the bottom is equal to $T_{CHX,in}$. Note

that the temperature profile gets distorted rather than shifted during this process. This process is shown in Figure 39-*B*.

5.3.3. No-Flow Magnetization (NFM):

The LHS SMP's temperature and applied field are held constant at $T_{SMP,high}$, and $B_{SMP,high}$ throughout this process; consequently, no flow is produced. The concentration of the mixture in the LHS SMP is at its lowest within the SMP system. Magnetization of the LHS regenerator begins by increasing the applied magnetic field from zero field, $B_{Reg,min}$. This process continues until the temperature at the bottom reaches the design "promoted" temperature of the CHX $T_{CHX,out}$ at an intermediate magnetic field $B_{Reg,NFM,final}$ (different from $B_{Reg,NFD,final}$), thus, the temperature profile along the regenerator shifts up. This process is shown in Figure 39-*C*.

5.3.4. Flow Magnetization (FM):

This process is the opposite of the FD process. The applied field in the LHS regenerator is increased up to $B_{Reg,peak}$. Fluid flows up towards the top of the regenerator and rejects the excess heat to the heat sink. The helium mixture exiting the RHS regenerator is promoted to a temperature of ($T_{CHX,in} + \Delta T$) as a result of some heat accepted by the mixture in the cold heat exchanger. This temperature is designated as $T_{CHX,out}$ and is the temperature of the fluid that enters the LHS regenerator during this process. This process is shown in Figure 39-*D*. The cycle repeats by proceeding with the NFD process. This concludes one cycle of operation of the AMRR.

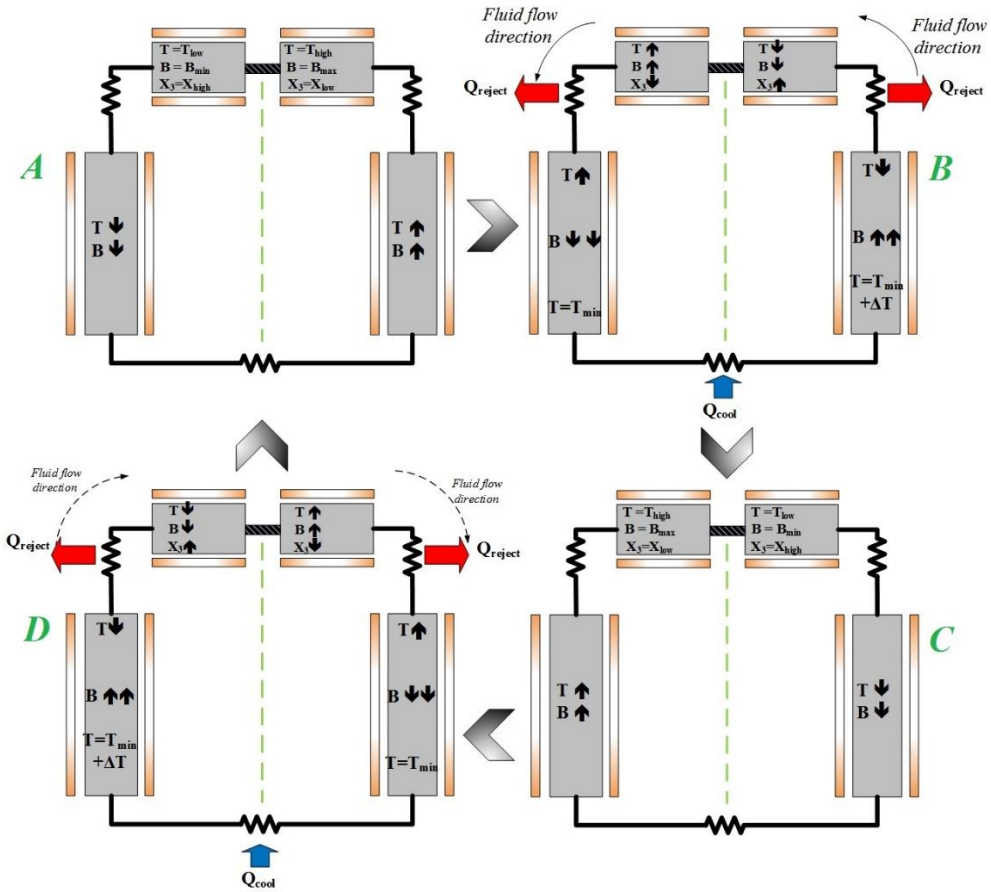

Figure 39. Schematic diagram of the four processes in the AMRR during one cycle operation of the system. Consider Left Hand Side of the system: A) No Flow Demagnetization B) Flow Demagnetization C) No Flow Magnetization D) Flow Magnetization

5.4. Numerical model

Any fluid based refrigeration system consists of a cold heat exchanger where heat is removed from an object, a hot heat exchanger where heat is rejected to a heat sink, and a displacer that reciprocates fluid between the cold and hot heat exchangers. A model of the AMRR system discussed in this chapter is developed first by estimating the power removal required in the cold heat exchanger. Then the details of the regenerators (i.e. mass/moles of refrigerant in the regenerators) is estimated through a first order model. The results from this model are fed into the transient numerical model of the regenerators. The results of this model are used to estimate the

required geometry and thermodynamic operating conditions of the SMP displacer. The goal of this section is to present the methodology and approach used to model the entire AMRR system.

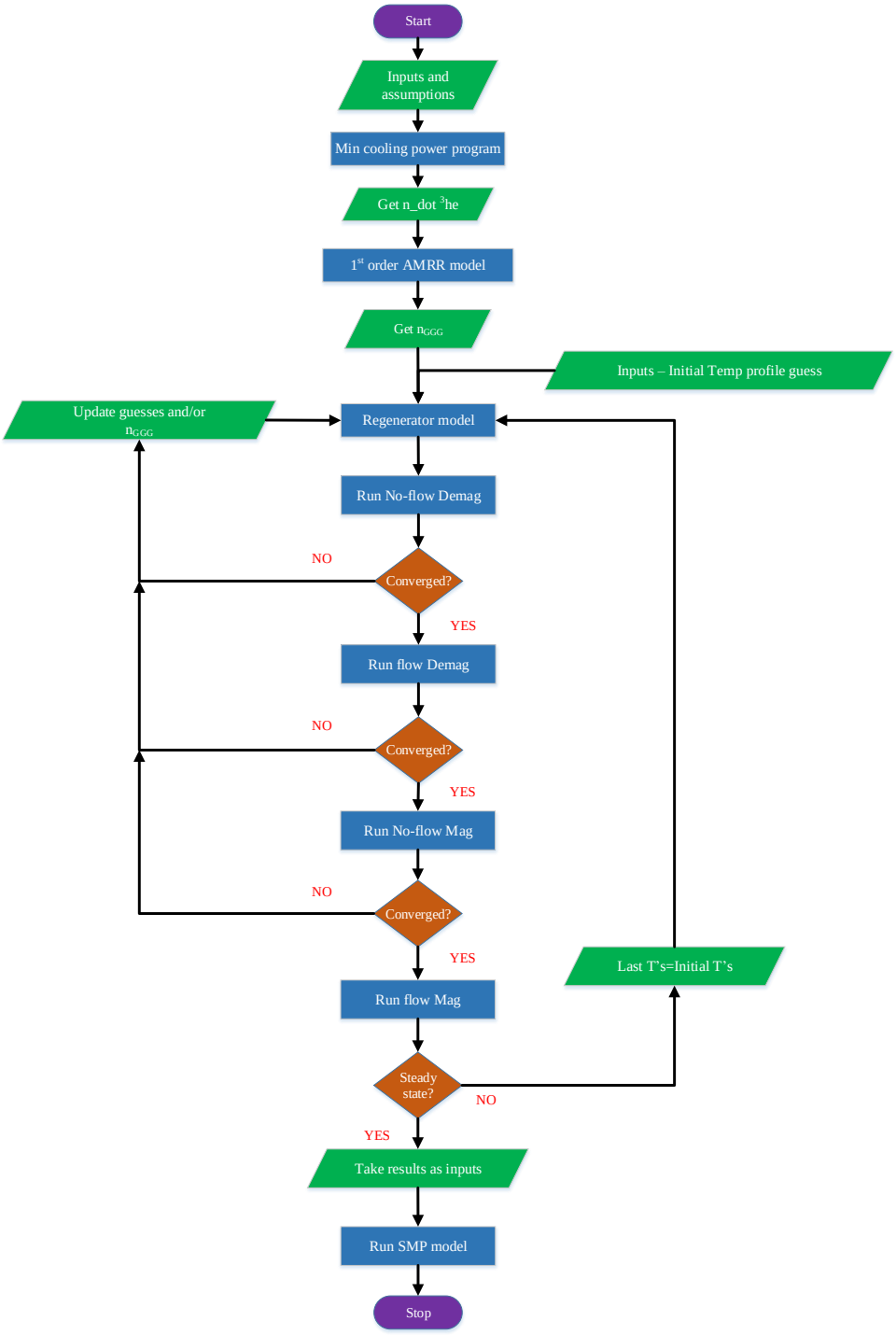

Figure 40. A flowchart diagram of the AMRR model

5.4.1. Cold Heat Exchanger (CHX)

The analysis begins by predicting the heat power leak into the CHX through parasitic losses. These losses include heat generation due to eddy currents, conduction losses, entropy generation due to pressure drop, entropy generation due to finite temperature difference between GGG particles and the liquid mixture, and radiation heat transfer. Margin is added to this power to predefine the operational cooling power. The molar flow rate is predicted by using an energy balance on the CHX. Note that for modeling purposes it is assumed that the ^{4}He chemical potential remains the same throughout the entire system. This is an accurate assumption since superfluid ^{4}He moves unimpeded to remove any gradient in the ^{4}He chemical potential. All thermodynamic properties of the mixture are evaluated at a pressure of 1 bar.

The static bed conduction through each of the regenerators is estimated using the model of Zehner and Schlunder (1970) for a packed bed of irregular particles as presented by Kandula (2011) according to:

$$k_{eff} = k_{fluid}\left(1-\sqrt{1-\psi}+\frac{2\sqrt{1-\psi}}{1-\zeta\,\omega}\left[\frac{(1-\zeta)\omega}{(1-\zeta\omega)^2}\ln\left(\frac{1}{\zeta\omega}\right)-\left(\frac{\omega+1}{2}\right)-\frac{\omega-1}{1-\zeta\omega}\right]\right) \tag{75}$$

where ζ is the ratio of the thermal conductivity of the fluid to the thermal conductivity of the solid material, and the parameters ω and ψ are defined as:

$$\begin{aligned}\psi &= 1-\left[\frac{\omega\left(3-4\omega+\omega^2+2\ln\omega\right)}{(\omega-1)^3}\right]^2\\ \omega &= C\left(\frac{1-\psi}{\psi}\right)^m\end{aligned} \tag{76}$$

in which *C* and *m* are 1.4 and 10/9 for irregular shaped broken particles such as the GGG particles used in the regenerators. Note that this correlation holds true as long as the solid to liquid thermal conductivity ratio stays below 1,300. The maximum thermal conductivity ratio of GGG to liquid mixture experienced throughout the regenerator is less than 800. A 1.5 cm diameter and 14 cm long canister with 0.38 porosity and extreme temperatures of 1.6 K and 750 mK at each end yields a static bed conduction loss of 59 μW for both regenerators. Note that this estimate significantly over-predicts the conduction loss because Zehner and Schlunder's model does not account for phonon mismatch between particles at low temperatures and thus it is used as a conservative value.

The calculation methodology for heat generation due to eddy currents was presented in the previous chapter. Therefore heat generation due to eddy current is estimated in the regenerator's canister wall (SS 304), cap (SS 304), and brazed copper tubing at the CHX by assuming a 3 Tesla field change over the cycle's half-period, which is 80 s. Assuming the regenerator's canister to have a wall thickness of 0.76 mm, the cap to have a thickness of 2 mm, and the tubing to have a length, inner, and outer diameter of 5 cm, 1.56 mm, and 0.76 mm yields a sum of 500 nW in eddy current loss.

The conduction losses along the walls of the canister are estimated as if there is no thermal communication between the contents of the regenerator and the wall using a linear temperature profile assumption from top to bottom. This conduction loss for both regenerators is estimated to be 29 μW. The conduction losses along all Kevlar suspenders, assuming one end to be at the magnet's temperature, 5 K, and the other at 750 mK, are estimated to be 10 μW. The conduction losses along the phosphor bronze thermometer leads attached to both ends of the regenerators are estimated to be 650 nW.

Assuming a conservative emissivity of 0.2 (Flynn 2005) for the SS304 canister walls, the heat transfer from the surroundings to the canisters is estimated to be 100 nW. Other losses including ohmic dissipation, conduction through heater wires mounted on the CHX, and residual helium gas conduction within the Dewar are found to be less than 10 nW.

The entropy generation rate within the regenerator's canisters is estimated by breaking this into two components: one due to pressure drop as a result of fluid flow over the crushed particles, and another due to the finite temperature difference between GGG and the mixture as derived in the previous chapter. These entropy generation rates are applied to the entire length of the regenerators and multiplied by their respective temperature difference to estimate the amount of lost work. The lost work values due to pressure drop and heat transfer are estimated to be 1 nW and 34 μW, respectively.

The sum of all the heat leaks to the CHX is 133 μW. Margin is built into the cooling power to yield a target cooling power of 600 μW. The inlet and outlet conditions of the CHX are designed to be 750 mK and 900 mK respectively. The helium mixture enthalpy can be divided into two components, as described in Chapter 2. An energy balance on the CHX as shown in Figure 41 yields:

$$\dot{q}_{ref}\ \tau = \left(n_{3,CHX-out}\ h^{os}{}_{CHX-out} + n_{4,CHX-out}\ \mu_{4,CHX-out}\right) - \left(n_{3,CHX-in}\ h^{os}{}_{CHX-in} + n_{4,CHX-in}\ \mu_{4,CHX-in}\right) \quad (77)$$

where τ is half the period for one cycle, n is the number of moles, h^{os} is the osmotic enthalpy defined in chapter 2 (previously defined as i^{os}), μ is the chemical potential, and the subscripts 3 and 4 denote ^{3}He and ^{4}He respectively. The number of moles of ^{4}He is related to the number of moles of ^{3}He through the following relation:

$$\frac{1-x}{x} = \frac{n_4}{n_3} \tag{78}$$

Through the justification provided in chapter 2, the pressure and ^{4}He chemical potential are assumed to be the same between the inlet and the outlet of the CHX. Using this assumption and applying Eq. (78) to Eq. (77) yields:

$$\dot{q}_{ref}\ \tau = \left(n_{3,CHX-out}\ h^{os}{}_{CHX-out} + \frac{1-x_{out}}{x_{out}} n_{3,CHX-out}\ \mu_{4,CHX} \right) - \left(n_{3,CHX-in}\ h^{os}{}_{CHX-in} + \frac{1-x_{in}}{x_{in}} n_{3,CHX-in}\ \mu_{4,CHX} \right) \tag{79}$$

the concentration of the mixture entering the CHX is assumed to be 0.2 as a starting point, a value judged appropriate for this AMRR based on the mass of ^{3}He required to charge the system. Using Eq. (79) the required molar flow rate of ^{3}He throughout the system is found to be 80 µmol/s.

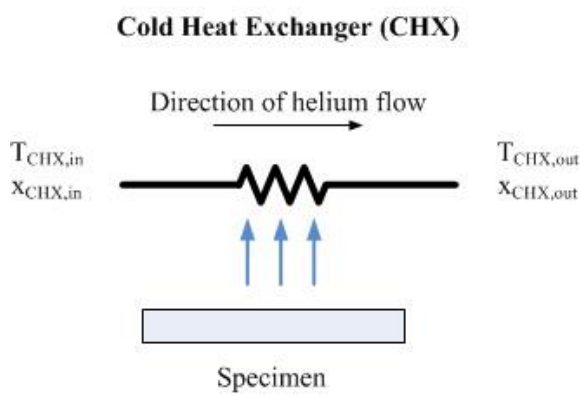

Figure 41. A schematic of the CHX

5.4.2. 1st order AMRR model

The objective of this section is to find an initial estimate of the size of the regenerators needed to provide the necessary cooling in this type refrigerator, primarily the mass of GGG needed in each of the regenerators. The superconducting magnet dimensions will be a function of the regenerator size. For simplicity, the axial temperature profile along the regenerator is assumed to

have a linear profile from high temperature at the top to low temperature at the bottom. The minimum mass of GGG required for each of the regenerators is estimated based on the following 2nd law thermodynamic balance on the regenerator during the demagnetization process:

$$\left(n_{out}\ s_{out} - n_{in}\ s_{in} \right) + \Delta \bar{S}_{GGG} \geq 0 \ \Rightarrow\ n_{GGG} \geq \frac{\left(n_{in}\ s_{in} - n_{out}\ s_{out} \right)}{\Delta \bar{s}_{GGG}} \tag{80}$$

where S and s are the total and specific molar entropy respectively. $\Delta \bar{s}_{GGG}$ is the averaged-molar specific entropy change of GGG during the demagnetization process defined by:

$$\Delta \bar{s}_{GGG} = \frac{\int_{T_{reg,out}}^{T_{reg,in}} s_{GGG}\left(B_{low}, T\right) dT - \int_{T_{reg,out}}^{T_{reg,in}} s_{GGG}\left(B_{high}, T\right) dT}{\left(T_{reg,in} - T_{reg,out}\right)} \tag{81}$$

where the subscripts *reg*, *low*, and *high* refer to regenerator, minimum and maximum applied magnetic field in the regenerator respectively. Note that the mass found via this method is the minimum required mass of GGG for each of the regenerator. Irreversibilities and non-idealities require a larger mass of GGG within the regenerators. The mass of GGG is corrected to its final value through the more accurate model presented in the next section if necessary.

5.4.3. Numerical regenerator model: 1-D transient

Numerical analysis of the regenerator begins by breaking the regenerators into thin discs along the axis. Two separate equations, one for the fluid and another for the refrigerant, are typically used in numerical analyses of regenerators in these types of systems. However if the maximum temperature difference between the GGG particles and surrounding helium mixture experienced locally throughout the regenerator is small then a uniform temperature can be assumed for each of the discs thus eliminating the need to use two separate set of equations. This temperature difference ΔT is estimated by using:

$$\dot{Q}' = h\,\alpha\,\Delta T \tag{82}$$

the heat transfer coefficient between GGG particles and the helium mixture can be estimated by using Gunn's correlation (1977):

$$Nu = (7 - 10\,\varepsilon + 5\,\varepsilon^2)\,(1 + 0.7 Re^{0.2}\ Pr^{\ 1/3}) + (1.33 - 2.4\varepsilon + 1.2\varepsilon^2) Re\ 0.7\ Pr^{1/3} \tag{83}$$

where Pr is the Prandtl number found through graphs for helium mixtures provided by Dobbs (2000) and curve fitted to:

$$Pr_{He,mix} = (0.109\,T^{3.47} + 0.1453) + (x - 0.1)\,1.5 \tag{84}$$

the heat transfer coefficient is found by using:

$$h = \frac{Nu\ k}{D_h} \tag{85}$$

where k is the conductivity of the helium mixture which is only a function of concentration. The conductivity is provided by Miller (2005):

$$k_{He,mix} = 0.001452\ x^{\ -1.16689} \tag{86}$$

thus a porosity of 0.38 for the packed bed, a temperature of 750 mK, concentration of 0.2 and ^{3}He molar flow rate of 80 μmol/s yields a conservative temperature difference of 900 μK between the GGG and the helium mixture. This temperature difference is only 0.12 % of that experienced through the regenerator therefore it is negligible. This justification enables the assumption of uniform temperature throughout each disc, thus solving the energy equation only from the fluid perspective. Figure 42 shows a schematic of the numerical grid system used for this section. The governing equation for each disc becomes:

$$\underbrace{-c_{GGG,disc}\ A_c\ (1-\varepsilon)\,T\left(\left.\frac{\partial s}{\partial B}\right|_T \frac{dB}{dt} + \left.\frac{\partial s}{\partial T}\right|_B \frac{dT}{dt}\right)}_{Heat\ to/\ from\ GGG\ (-Q_{GGG}=Q_{He})} + \underbrace{k_{eff,axial}\ A_c\ \frac{d^2T}{dx^2}}_{Effective\ axial\ cond.} + \underbrace{\dot{n}_{he}\ \frac{di}{dx}}_{Enthalpic\ flow} = \underbrace{c_{he,entrained}\ A_c\ \varepsilon\frac{du}{dt}}_{Stored\ Energy\ in\ fluid} \tag{87}$$

where c is the molar density, A_c is the cross sectional area, t is time, u is the molar specific energy and $k_{eff,axial}$ is the effective axial thermal conductivity defined by Eq. (75).

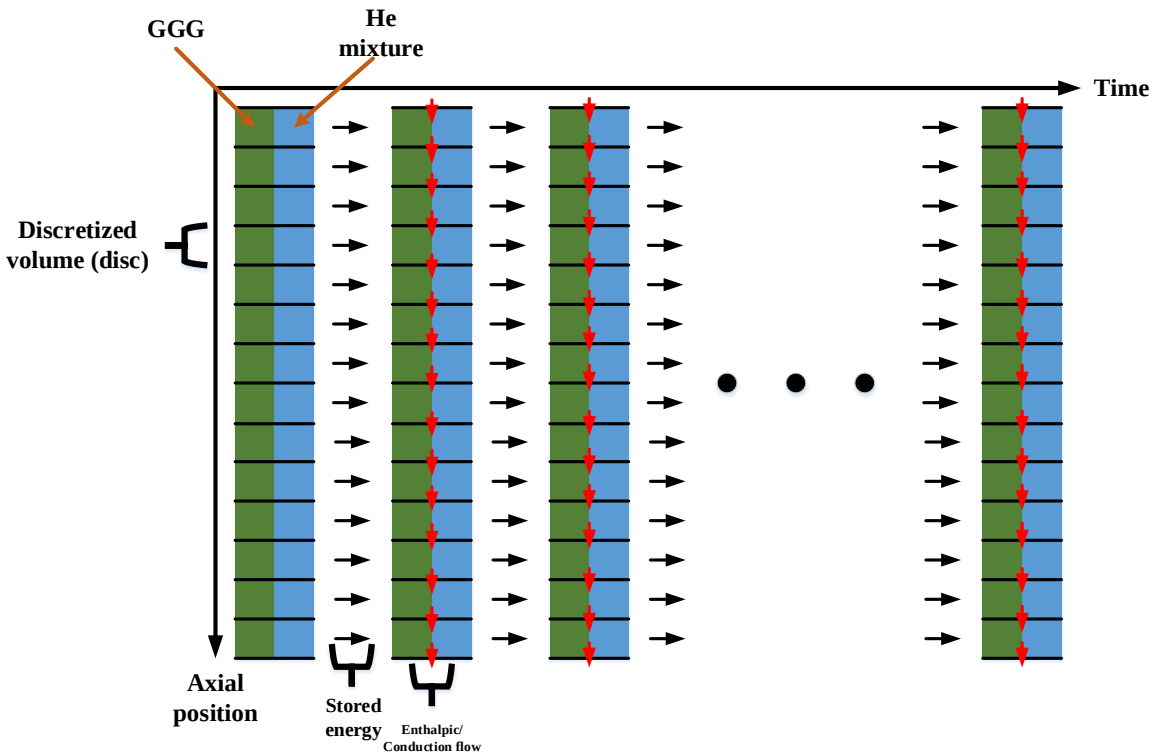

Figure 42. A diagram representing the numerical grid technique used in the AMRR model

A fully implicit method was used and applied to the discretized regenerator in order to analyze each process of the AMRR using Engineering Equation Solver (EES, Klein-Nellis 2014). The approach is to run through each of the processes involved in the AMRR system cyclically until the solution for each process reaches steady state. This was accomplished by using a Macro command in EES. Initially a linear temperature profile was assumed along the length of the regenerator. The Macro would command the file corresponding to the NFD process to open, run and store the last time step values into a text file before saving and closing. Then the Macro commands the file corresponding to the FD process to open, it then imports initial condition values

(i.e. data that was stored at the end of the NFD process), runs the program, saves the last time step values into a text file, saves, and closes. This chain of automated programming continues through all four files each corresponding to the processes involved in the AMRR until convergence is reached within the specified tolerance defined by:

$$\left| \frac{T_{i,j}\big|_{previous\ cycle} - T_{i,j}\big|_{current\ cycle}}{T_{i,j}\big|_{current\ cycle}} \right| < 1.0 \times 10^{-9} \qquad (88)$$

where the indices *i* and *j* denote number of location step and number of time step respectively.

Steady state condition was usually reached after 40 to 50 cycles.

5.4.3.1. NFD process

The analysis begins with the NFD process. The objective of this process is not only predicting the temperature profile but to predict the intermediate field at which the temperature at the bottom of the regenerator reaches 750 mK. The temperature along the regenerator is guessed to be linear between the top and bottom of the regenerator, 1.6 K and 900 mK respectively. Note that this guess is used only once in the very beginning of the cyclic program. As the program goes through successive cycles, the temperature profile changes during each iteration until the model reaches cyclic steady state, that is the temperature at a time t anytime in the cycle is equal to $t + \tau$ where τ is the period of one cycle. The boundary conditions used for this process are listed in Table 8. Note that the first term in the bracket corresponds to location step number and the second term represents the time step number (i.e. T[i,j], i = number of location step and j = number of time step). Location steps run from 1 through *N* and time steps run from 1 through *M*. The steady state temperature profile evolving through this process is shown in Figure 43.

Initial Condition entered once at beginning	$T_{top} - \frac{x}{L_{reg}}\left(T_{top} - T_{bottom}\right)$
Initial Condition after cycle 1	T[i, M] from FM process where i=1..N
BC at top	Adiabatic
BC at bottom	T[N,M]= 750 mK otherwise Adiabatic

Table 8. Initial and boundary condition for NFD process.

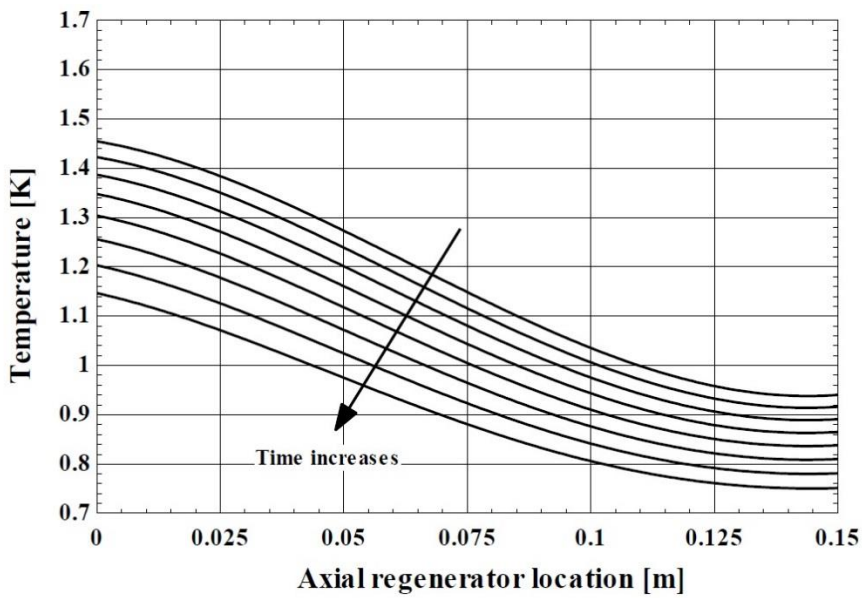

Figure 43. Temperature profile as a function of axial location through the NFD process.

5.4.3.2. FD process

The initial condition for this process is fed from the temperatures obtained through the last time step in the NFD process. The boundary conditions are set such that fluid enters at the HHX temperature, and leaves at $T_{CHX,in}$ = 750 mK. The field change during this process is controlled to keep the outlet temperature at 750 mK until the coil runs out of field. It is during this process where the number of moles of GGG found through the first order model might need adjustment. This could happen if the refrigeration provided by the GGG during this process is not enough to keep the outlet temperature constant at 750 mK. The enthalpic flow is summed through time to yield

the AMRR's average refrigeration power, which must equal 600 μW. Table 9 lists the boundary and initial conditions used for this process. Figure 44 shows the result of the model for the FD process.

Initial Condition	T[i, M] from NFD process where i=1..N
BC at top	Fluid enters at T_{HHX}
BC at bottom	T[N,j+1] = 750 mK where j=1..M-1

Table 9. Initial and boundary conditions for the FD process.

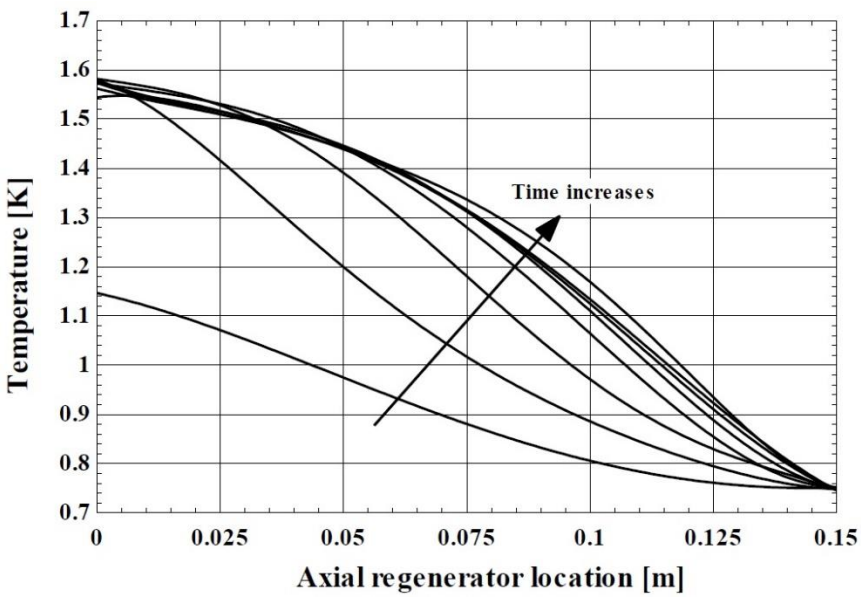

Figure 44. Temperature profile as a function of axial location through the FD process.

5.4.3.3. NFM process

The temperatures obtained in the last time step of the FD process are fed to this process as the initial conditions. The objective of this process is to raise the temperature at the bottom of the regenerator until it matches the temperature at which the CHX outlet is designed to operate, that is $T_{CHX,out}$ = 900 mK. The applied magnetic field increases from zero field until the required intermediate field is found by applying the bottom temperature constraint for the last time step.

Adiabatic conditions are applied to the ends of the regenerator. Table 10 lists the boundary and initial conditions used for the NFM process. Figure 45 shows the temperature profile of the regenerator evolving through time.

Initial Condition	T[i, M] from FD process where i=1..N
BC at top	Adiabatic
BC at bottom	Adiabatic
Constraint to find intermediate field	T[N,M] = T_{CHX_out} = 900 mK otherwise adiabatic

Table 10. Initial and boundary conditions for the NFM process.

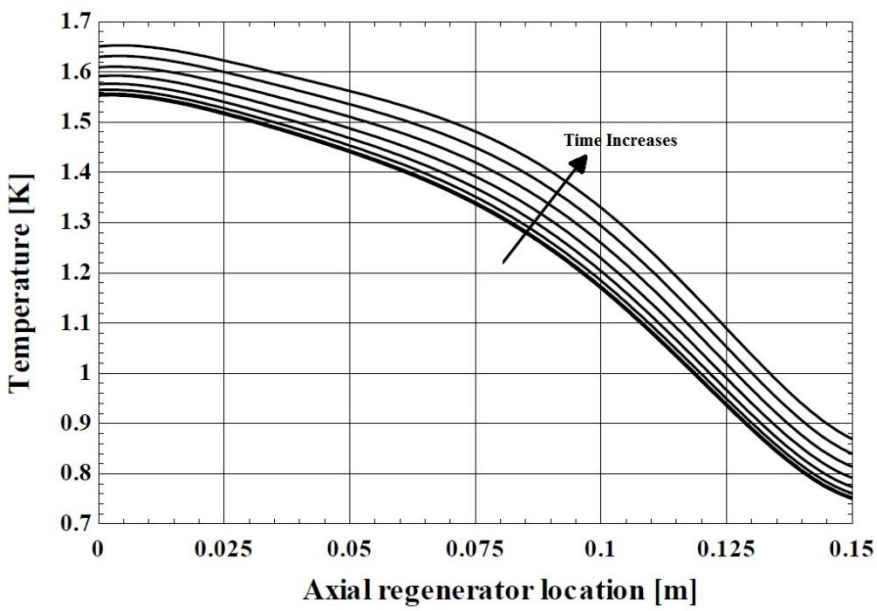

Figure 45. Temperature profile as a function of axial location through the NFM process.

5.4.3.4. FM process

The objective of this process is to return to the beginning of the cycle by rejecting heat to the HHX. The initial conditions for this process are fed from the temperatures obtained in the last time step of the NFM process. The boundary conditions are set such that fluid enters the bottom of the regenerator at CHX outlet's temperature and fluid exits the top at an extrapolated temperature based on the first and second nodes of the regenerator. The heat sink's temperature

will be determined later in this section. Table 11 lists the boundary and initial conditions. Figure 46 shows the temperature profile evolving through time during the FM process.

Initial Condition	T[i, M] from NFM process where i=1..N
BC at top	Fluid exits at $3/2\,T[1, j+1] - 1/2\,T[2, j+1]$ for j=1..M-1
BC at bottom	Fluid enters at $T_{CHX,out}$

Table 11. Initial and boundary conditions for the FM process.

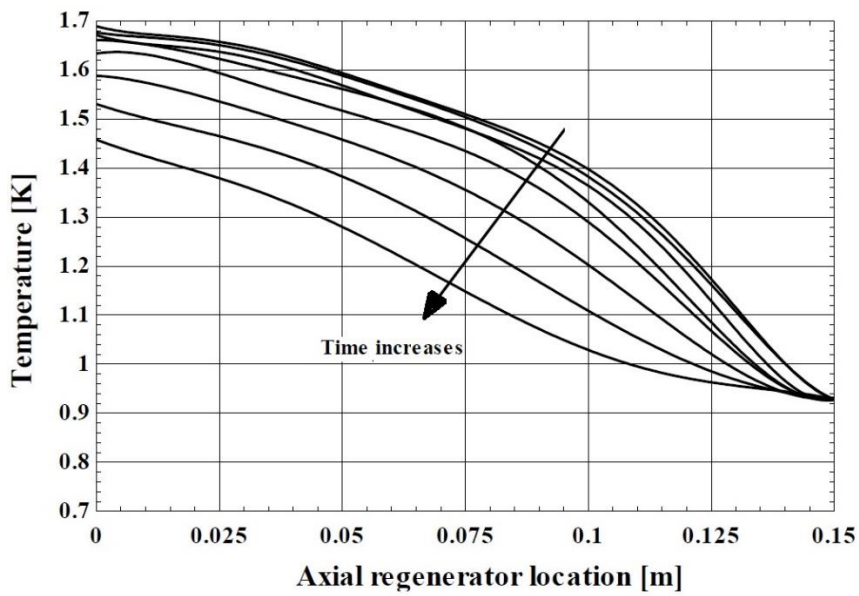

Figure 46. Temperature profile as a function of axial location through the FM process.

5.4.4. SMP

One cycle operation of the SMP in the AMRR system differs significantly from the SMP operation discussed in the previous chapter. This is due to two reasons: a mixture of ^{3}He-^{4}He is used instead of pure ^{4}He, and no significant pressure build up is required by the SMP since the AMRR fluid circuit exhibits minimal impedance to fluid flow. Therefore the SMP operation for an AMRR is simplified and consists of two processes: magnetization and demagnetization as shown in Figure 47. The magnetization process forces some ^{3}He out of the SMP canister and through the entire system. Note that a dynamic equilibrium process exists where ^{3}He moves

throughout the system without affecting the local concentration. Subsequently, the demagnetization process helps the other SMP canister to replenish the ^{4}He leaving that canister by supplying superfluid ^{4}He through the superleak port.

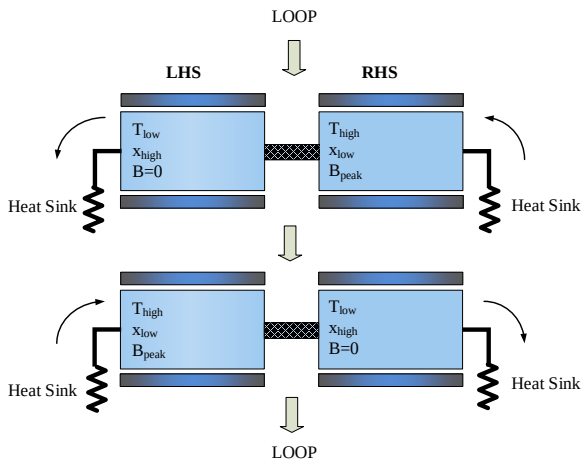

Figure 47. SMP process for one cycle operation of the AMRR

Modeling of the SMP begins by using the results obtained through the CHX and the regenerator analysis. The main input to this program is the required number of moles of ^{3}He needed to shuttle through the regenerator and CHX. Unlike the canisters used in the regenerators, the SMP's canisters are shorter and much wider. The maximum field experienced in the SMP and the temperature swings are much lower than that experienced in the regenerators. Additionally, the temperature of each canister is controlled by regulating the magnetic field change for each canister. These conditions allow the assumption of uniform temperature throughout the SMP's canister at any instant of time. Therefore, the SMP is modeled as a lumped sum changing through time (process). The thermodynamic system is defined to be the helium mixture. The governing equation used for modeling the SMP is:

$$\underbrace{n_{he,trapped}\frac{du_{he}}{dt}}_{stored\ energy} = \underbrace{\frac{dn_{3,displaced}}{dt}(h_{eff,in} - h_{eff,out})}_{Enthalpic\ flow} \underbrace{-T\ n_{GGG}\left(\left.\frac{\partial s}{\partial B}\right|_T \frac{dB}{dt} + \left.\frac{\partial s}{\partial T}\right|_B \frac{dT}{dt}\right)}_{Heat\ to/\ from\ helium\ (Q_{he}=-Q_{GGG})} \tag{89}$$

where $n_{he,trapped}$ is the number of moles of helium entrained in the canister. One of the most important features of the displacer that makes reciprocating flow possible is the superleak that connects the two canisters of the SMP. It is possible to solve for the number of moles of ^{3}He displaced by applying Ebner's model as discussed in chapter 2. The effective enthalpy of fluid entering or leaving the canister through the superleak becomes:

$$n\,h_{eff} = n_4\,\mu_4 = n_3\,\frac{1-x}{x}\,\mu_4 \tag{90}$$

A list of boundary and initial conditions used in the SMP model is listed in Table 12. The model is solved and a plot of applied magnetic field as a function of remaining number of moles of ^{3}He in the canister is shown in Figure 48. According to this solution, the required peak applied magnetic field is 0.65 Tesla.

Magnetization	*Initial condition*	X_{high} & T_{low}
	Inlet BC	Superfluid enters at $\mu_{4,system}$
	Outlet BC	Mixture exits at $T_{canister}$
Demagnetization	*Initial condition*	X_{low} & T_{high}
	Inlet BC	Mixture enters at heat sink T
	Outlet BC	Superfluid leaves at $\mu_{4,system}$

Table 12. Initial and Boundary conditions for the SMP.

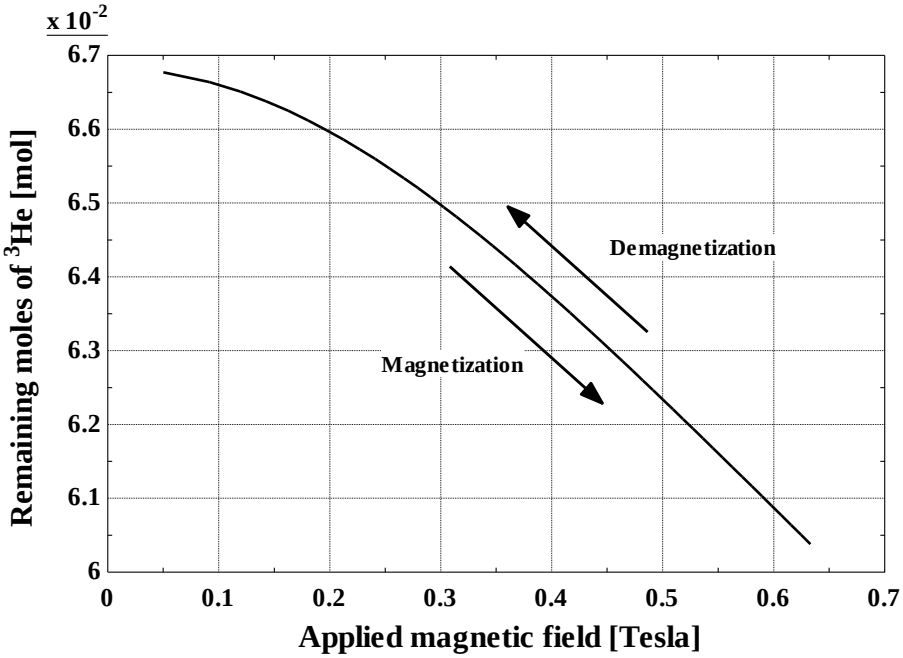

Figure 48. Number of moles of ^{3}He remaining in the canister through the SMP's operation.

5.4.5. Hot Heat Exchanger (HHX)

Finally, the AMRR loop is closed by predicting the temperature at which the heat sink needs to operate. This task is accomplished by summing the internal energy change throughout the entire system for the regenerators and SMP during one cycle operation. The sum of all the internal energy changes for the GGG particles and the helium mixture must be zero:

$$\sum_{cycle} dU_{GGG} + dU_{he,mixture} = 0 \qquad (91)$$

where the change in the internal energy of the GGG is the sum of the work and heat terms. To accomplish this, the initially guessed heat sink temperature is tweaked in the program through trial and error until Eq. (91) becomes negligibly small. The required heat sink temperature is found to be 1.577 K if the molar concentration of the mixture is 0.04 at this temperature. Also, it is now

possible to find the total heat power rejected to the heat sink throughout the entire cycle. This value is found to be 3 mW. The powers are consistent with a thermal efficiency of 20%.

5.5. Potential system losses and limitations

The AMRR discussed in this work has an inherent limitation on both the high and low temperatures experienced throughout the system. The SMPs operate by taking advantage of the superfluid to normal and normal to superfluid conversion of ^{4}He. This requires the SMP (the warmest components of the AMRR system) to run at temperatures lower than the lambda point for ^{4}He. This limitation caps the highest possible temperature of the heat rejection stage to be approximately 2 K. Another inherent limitation of this system appears in the coldest part of the AMRR. As the temperature of the helium mixture is lowered throughout the AMRR system, the ^{3}He concentration increases to maintain the same chemical potential due to ^{4}He. This decrease in temperature may continue until the helium mixture reaches the separation line on the ^{3}He-^{4}He phase diagram. At this point the fluid temperature can no longer be further cooled. For example a system charged at 3% ^{3}He concentration at 1.8 Kelvin may only ultimately provide a minimum cooling temperature of 600 mK. Clever design implementations, such as cascading the regenerators, may enable the user to attain lower temperatures.

5.6. Summary of results

A summary of all the results along with their predefined values are listed in Table 13.

CHX	$T_{CHX,in}$	750 [mK]
	$T_{CHX,out}$	900 [mK]
	Q_c	600 [μW]
Regenerator	d_{reg}	1.5 [cm]
	L_{reg}	14 [cm]
	Porosity	0.38
	m_{GGG}	110 [g]
	$B_{NFD,i}=B_{FM,f}$	3 [Tesla]
	$B_{NFD,f}=B_{FD,i}$	1.2 [Tesla]
	$B_{FD,f}=B_{NFM,i}$	0 [Tesla]
	$B_{NFM,f}=B_{FM,i}$	0.563 [Tesla]
SMP	d_{SMP}	5 [cm]
	L_{SMP}	6.3 [cm]
	Porosity	0.38
	m_{GGG}	540 [g]
	$T_{SMP,high\ T}$	1.627 [K]
	$x_{SMP,high\ T}$	0.03497
	$T_{SMP\ low\ T}$	1.59 [K]
	$x_{SMP\ low\ T}$	0.03871
HHX	$n_{3_shuttle}$	6.396 [mmol]
	$T_{heat\ sink}$	1.577 [K]
	Q_h	3 mW
System	Cycle period	180 [s]
	NFD period	10 [s]
	FD period	80 [s]
	NFM period	10 [s]
	FM period	80 [s]

Table 13. Summary of the AMRR model results

5.7. References

Dobbs, Roland. *Helium Three*. No. 108. Oxford University Press, 2000.

Flynn, Thomas M. *Cryogenic engineering*. Vol. 1. 2005.

Gunn, D. J. "Transfer of heat or mass to particles in fixed and fluidised beds."*International Journal of Heat and Mass Transfer* 21.4 (1978): 467-476.

Kandula, Max. "On the effective thermal conductivity of porous packed beds with uniform spherical particles." *Journal of Porous Media* 14.10 (2011).

Klein, S.A., Nellis, G. F., Engineering Equation Solver, Ver 9.772. 2014

Miller, F. K., PhD thesis, Massachusetts Institute of Technology, 2005

Zehner, P., and E. U. Schlunder. "On the effective heat conductivity in packed beds with flowing fluid at medium and high temperatures." *Chem. Ing. Tech* 42 (1970): 933-941.

6. Construction and assembly

Various pieces of equipment were designed and constructed for the SMP experiment discussed in this work. These include superconducting magnets, canister with crushed GGG, superleak, superfluid helium shutoff valve, Venturi flow meter, and a dielectric insensitive differential pressure transducer. The goal of this chapter is to discuss the design (if necessary) as well as techniques used in the construction of these equipment.

6.1. Introduction

Typical experiments are often modular; a commercially available sub assembly can be used to fit the needs of a particular experimental setup. Many of the tools and measurement equipment that are commercially available for typical experiments cannot be used in low temperature experiments especially those involving superfluid ^{4}He. Lack of qualification for use at extremely cold test environments, superfluid ^{4}He seal tightness, and lack of availability due to low demand as a result of limited and specialized applications are among chief reasons. Design and fabrication of components for experiments conducted at very low temperatures, especially those involving superfluid ^{4}He require a great deal of meticulous planning, technical knowledge, and skill set. Many sensitive design issues, and techniques used in the construction of these devices or tools are discussed in this chapter.

6.2. Superconducting magnets

The superconducting magnets discussed in this work are electromagnets made from solenoidal coils of superconducting wire. One of the primary advantages of electromagnets as opposed to permanent magnets (i.e. Neodymium magnets) are their ability to increase or decrease

the applied magnetic field by increasing or decreasing the current in the coil respectively, while remaining stationary. To accomplish this with an ordinary magnet, one must physically move an object in and out of the magnetic field (i.e. via a rotary disc). Design and construction of a superconducting magnet is discussed in this section.

The design of a superconducting magnet is constrained by the geometric compatibility as well as the electrical requirements. For instance the superconducting magnet of the SMP is designed to provide a maximum field of 1.5 Tesla at 4.7 Amp. The bore must accommodate a 12 cm long and 3.8 cm diameter canister. The design begins by specifying the winding configuration. Then hoop stress in the wire must be computed and checked against the maximum allowable stress for the wire material. Various loss parameters such as eddy current losses, and A.C. losses must be summed to determine whether the total loss is acceptable or not. The flow chart in Figure 49 shows the processes involved in the design of a superconducting magnet.

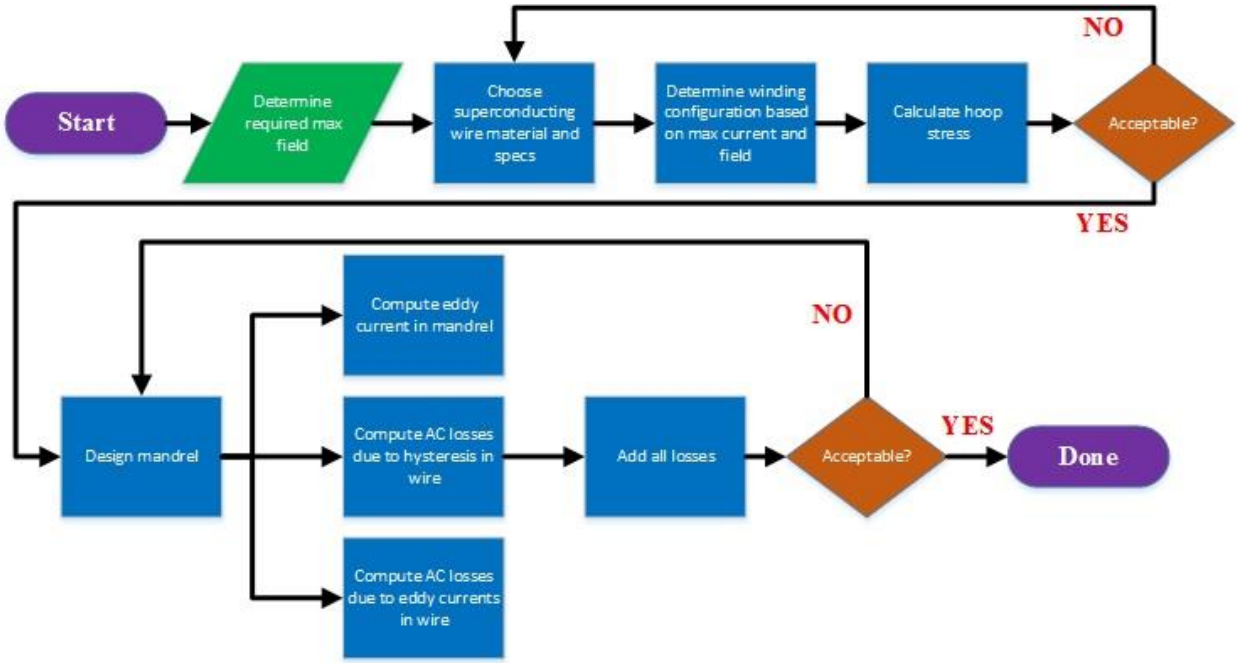

Figure 49. Processes involved in the design of a superconducting magnet.

6.2.1. Niobium-Titanium (Nb-Ti) superconducting wire

One of the most important parameters in the design of any superconducting magnet is the material used in the superconductor. A superconductor is a material in which its electrical resistivity drops to zero below a certain temperature known as the transition temperature (T_0) in the absence of any externally applied magnetic field. The critical current density (J_{cr}), temperature (T_{cr}), and field (B_{cr}) are defined as values above which the superconducting material becomes normal or resistive. For further reading refer to "Superconducting magnets" by Wilson (1985). For reading on the theoretical details of the BCS theory refer to Bardeen et. al. (1957).

Niobium-Titanium is chosen as the wire material for the magnets in this work because it is commercially available in very small diameters (as small as 30 micron). Their high critical current density at low temperatures and superior mechanical properties relative to other superconductors makes this material an excellent candidate for use in superconducting magnets at low temperatures. Nb-Ti's transition temperature at zero magnetic field is 9.2 K. It is a type II superconductor; there is a lower critical field at which the transition to normal state commences and an upper critical field at which the transition terminates (Barron 1985). Figure 50 shows the three-dimensional plot of the dependence of critical-current density on magnetic field and temperature for two common superconductors, Nb-Ti and Nb_3Sn.

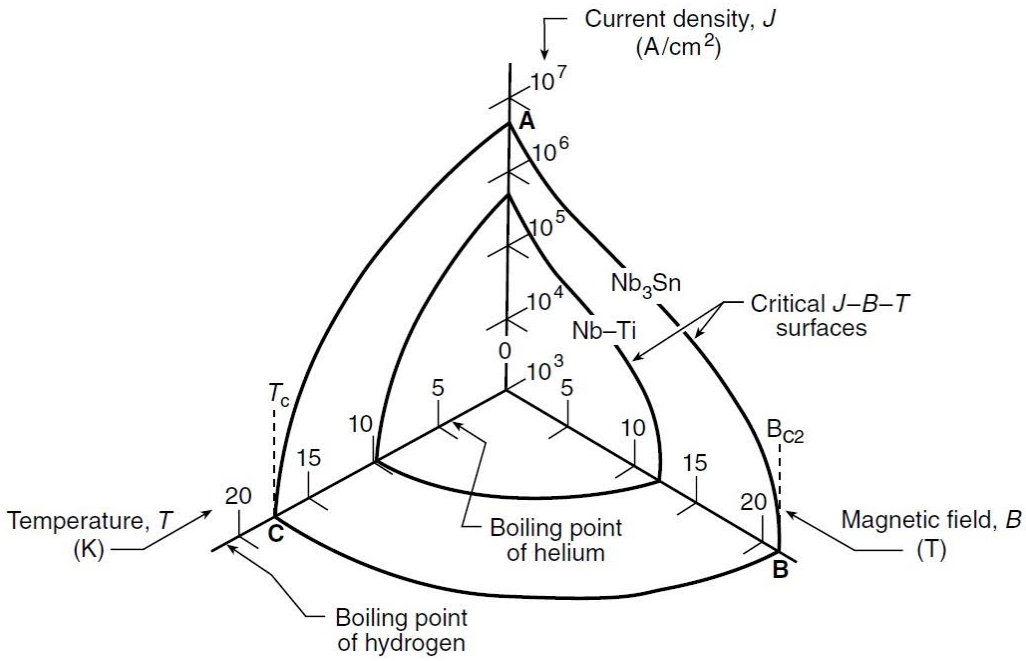

Figure 50. Critical current density of two commercial low temperature superconductors as a function of magnetic field and temperature (Ekin 2006).

The Nb-Ti wires used for the magnets in this work are in the form of filamentary composites as shown in Figure 51. The advantage of using multi filament wire versus single filament is lower AC losses during changes of the applied magnetic field. Every wire consists of small superconducting filaments embedded in a matrix of non-superconducting material (typically copper). The primary purpose of the non-superconducting material is to provide thermal stability since a superconducting material is very resistive and generates a lot of heat in its normal state. Electrical current will flow in the path of least resistance, therefore when below the transition temperature, current flows in the superconductor. In the case of an undesired quench, a state where the superconductors' temperature is inadvertently raised above its transition temperature, the current will flow in the copper matrix since its electrical resistivity is much lower than that of the

superconducting material just above its transition temperature. This prevents the magnet from a burnout situation.

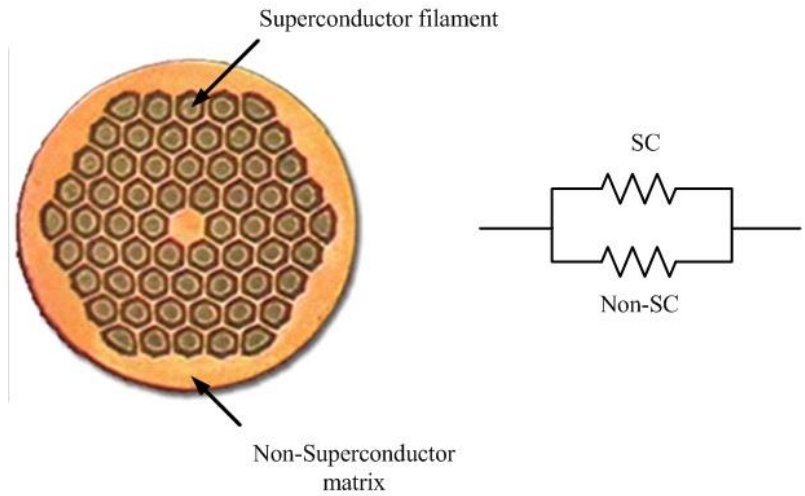

Figure 51. Cross sectional view of a typical multi filamentary superconducting wire with a resistance network shown along the length of the wire.

6.2.2. Axial magnetic field of a solenoid

The magnetic field at any point along the axis of a tightly wound solenoid consisting of *n* turns per unit length wrapped around a cylindrical tube (mandrel) must be calculated in order to determine the geometrical parameters of the superconducting magnets. The author of this work has derived an expression for the axial magnetic field inside a solenoid based on the Biot-Savart law. Proof of this lengthy derivation is provided in the appendix in order to avoid distraction from the main subject. For points on the axis within the solenoid:

$$B_{axis,inside} = \frac{\mu_0\, n\, I}{2}\left[\frac{x_2}{\sqrt{x_2^2 + R_{coil}{}^2}} + \frac{L_{coil} - x_2}{\sqrt{\left(L_{coil} - x_2\right)^2 + R_{coil}{}^2}}\right] \qquad (92)$$

where μ_0 is the permeability of free space (4π x 10^{-7} N/A^2), I is the current, L_{coil} is the total length of the coil, x_2 is the distance measured from the left edge of the coil to the point of interest, and R_{coil} is determined according to:

$$R_{coil} = R_{mandrel} + d_{sc,wire}\left(\frac{1}{2}\right)\left(\overbrace{\frac{\left(\frac{N_{total}}{1}\right)}{\underbrace{\left(\frac{L_{coil}}{d_{sc,wire}}\right)}_{\substack{Number\ of\ turns \\ in\ 1\ single\ layer}}}}^{Number\ of\ layers}\right) \tag{93}$$

where $R_{mandrel}$ is the outer radius of the mandrel, $d_{sc,wire}$ is the diameter of the superconducting wire (including insulation), and N_{total} is the total number of windings. A superconducting magnet made with Supercon wire type 54S43-7 with a diameter of 102 micron, coil length of 12 cm, mandrel diameter of 5 cm, and 34,000 turns would produce a maximum magnetic field of 1.5 Tesla at 4.7 Amp.

6.2.3. Hoop stress

Any magnetic field exerts a force on a current carrying conductor. This force, calculated by the Lorentz force law, for magnetostatic conditions is:

$$\vec{F}_{mag} = I\int d\vec{l} \times \vec{B} \tag{94}$$

where dl is a vector along the current carrying conductor. Since the magnetic field in a solenoid is axial and the wires run circumferentially, the two vectors dl and B are perpendicular to one another. Therefore according to Eq. (94) the magnetic force on the wire for the case of a solenoid is in the radial direction. This is analogous to a cylinder that is charged with gas at a high pressure, in this case the cylinder is the coil and the high pressure gas is the magnetic field.

The simplest calculation of hoop stress is based on the assumption that each turn acts independently of its neighbors. Within the winding of a solenoid, the variation of axial field with radius may usually be approximated to a fair accuracy by a linear fall-off from B_a at the inner radius a to B_b at the outer radius b (Wilson 1985):

$$B = \frac{(b-r)B_a + (r-a)B_b}{(b-a)} = \frac{(\alpha-\varepsilon)B_a + (\varepsilon-1)B_b}{(\alpha-1)} \tag{95}$$

where variable r is the radius, $\varepsilon=r/a$, and $\alpha=b/a$. Hoop stress calculation for an infinite solenoid provides a conservative estimate as compared to a finite solenoid due to the lack of fringing effect at the ends. Therefore for the special case of an infinite solenoid B_b=0 and $B_a=\mu_0 J (b-a)$ (Wilson 1985):

$$\sigma_\theta = B\ J\ r = \frac{B_a^2}{2\mu_0}\frac{2(\alpha-\varepsilon)\ \varepsilon}{(\alpha-1)^2} \tag{96}$$

where J is the current density. Note that the first fraction on the right hand side of Eq. (96) is the stored energy density in the magnetic field (a scaling factor). It is clear from this equation that ε changes with r. A conservative estimate of the hoop stress can be obtained by taking the derivative of Eq. (96) with respect to ε and setting it to zero to find the maximum value of σ_θ:

$$\sigma_\theta = \frac{B_a^2}{2\mu_0}\frac{2\left(\frac{\alpha}{2}\right)\left(\frac{\alpha}{2}\right)}{(\alpha-1)^2} = \frac{B_a^2}{4\mu_0}\frac{\alpha^2}{(\alpha-1)^2} \tag{97}$$

the hoop stress for the SMP coil with inner and outer radius of 2.54 and 2.89 cm respectively is found to be 30 MPa, a value much lower than the working maximum allowable stress for Nb-Ti which is 500 MPa.

6.2.4. Heat generation due to eddy currents in mandrel

An equation for the rate of heat generation in a tube was earlier presented in Eq. (36). The mandrel is a tube made out of Aluminum 6061-T6 for two reasons: it provides good structural support, and it provides good thermal stability due to its relatively high thermal conductivity at low temperatures. The bore of the SMP magnet's mandrel is 4.44 cm in diameter and the outer diameter is 5.08 cm. Therefore a high ramp rate of 0.1 Tesla/s would yield a heat generation rate of 6 mW in the mandrel due to eddy currents.

6.2.5. A.C. losses

A.C. losses are resistive losses occurring in the magnet due to A.C. fields. The changing magnetic field generates an electromotive force within the superconductor, which locally drives the current density beyond its critical value. Therefore care must be taken to avoid excessive A.C. losses in a superconducting magnet.

6.2.5.1. A.C. losses due to hysteresis

A.C. losses due to hysteresis in the superconductor filaments of a wire are very complicated phenomenon and calculations for these type losses are not straightforward and must be obtained from semi empirical relationships. Wilson (1985) presents an equation to estimate heat generation due to hysteretic A.C. losses per cycle per unit volume of superconducting material in the wire (note that this is not power):

$$Q_{AC,hys,specific} = \frac{8}{3\pi} d_f \; J_{c0} \; B_0 \left[\frac{B_m + B_0}{B_m} \ln\left(\frac{B_m + B_0}{B_0} \right) - 1 \right] \qquad (98)$$

where d_f is the filament diameter, J_{c0} and B_0 are constants presented in Kim and Andersons model (1962, and 1963) (i.e $J_c(B)=J_{c0} \cdot B_0/(B+B_0)$, B_m is the maximum applied magnetic field. Note that

despite the transient nature of this loss, it does not depend on the cycle time. The heat generation for a specific length of a superconducting wire in units of Watts is:

$$Q_{AC,hys} = Q_{AC,hys,specific}\ \lambda_{SC}\ \mathcal{V}_{SC} \tag{99}$$

where λ_{SC} is the fraction of Nb-Ti in the wire, and $\mathcal{V}_{SC}$ is the total volume of the wire. The filaments have a diameter of 7 micron. Using a value of 2 x 10^{10} Amp/m^2 and 0.15 Tesla for J_{c0} and B_0 respectively yields 11.6 mW of power dissipated due to A.C. hysteretic loss averaged over 15 s.

6.2.5.2. A.C. losses due to eddy currents in the wire

The last type of loss in superconducting magnets to consider is A.C. losses due to eddy currents. This loss is due to eddy current associated with the current coupling phenomenon in superconductor-normal conductor geometry and is not a straightforward task to calculate. Wilson (1985) presents an equation to estimate this type of loss per cycle per unit volume of the superconducting wire:

$$\dot{Q}_{AC,Eddy,specific} = \frac{B_{ml}^2}{2\,\mu_0}\frac{8\,\tau}{t_m} \tag{100}$$

where B_{ml} is the local field amplitude which must be averaged over the winding section ($B_{ml}^2=1/3\ B_m^2$), t_m is the time for the magnetic field to rise from its lowest value to its peak (B_m), and τ is the natural time constant of the eddy current system (note that this loss, unlike hysteresis loss depends on the cycle time):

$$\tau = \frac{\mu_0}{2\,\rho_{eff}}\left(\frac{L_{pitch}}{2\,\pi}\right)^2 \tag{101}$$

where L_{pitch} is the twist pitch of the superconducting filaments, and ρ_{eff} is the effective resistivity of the matrix defined by:

$$\rho_{eff} = \rho_m \frac{1+\lambda_{SC}}{1-\lambda_{SC}} \tag{102}$$

note that Eq. (100) is valid only if t_m is much larger than τ. Once again, the following relationship is used to obtain the heat generation in units of Watts as:

$$\dot{Q}_{AC,Eddy} = \dot{Q}_{AC,Eddy,specific}\ \lambda_{SC}\ \forall_{SC} \tag{103}$$

the twist pitch for the superconducting wire used in the SMP magnet is 12.7 mm. The A.C. loss due to eddy currents is estimated to be 2.5 mW.

6.2.6. Maximum temperature rise in mandrel

All of the losses found in the previous sub sections are summed to 20.1 mW rejecting all of this to the second stage heat exchange platform. A conservative estimate of the maximum temperature rise within the mandrel can be obtained by applying all the summed power to the mid-section of the mandrel thus taking half this power to travel in either direction and towards the edges of the mandrel. The mandrel flanges are thermally anchored to the second stage heat exchange platform therefore the temperature at these ends are kept at approximately 4 K. Applying the entire heat to the mid-section results in a maximum temperature rise of 230 mK in the mandrel. This value is acceptable since a temperature of 4.25 K is still far below the critical temperature of the superconducting coil at 1.5 Tesla.

6.2.7. Summary of model parameters

A summary of important specifications and design parameters are provided in Table 14. The applied magnetic field as a function of axial location within the solenoid is shown in Figure 52.

Superconducting wire	Type	Supercon 54S43
	Number of filaments	54
	Filament diameter	7 micron
	Cu: SC ratio	1.3:1
	Bare wire diameter	79 micron
	Insulated wire diameter	102 micron
	Critical current @ 3 Tesla & 4.2 K	5 Amp
	Twist pitch	12.7 mm
Mandrel	Material	Al-6061-T6
	Outer diameter	5.08 cm
	Inner diameter	4.44 cm
	Length	12 cm
Coil	Heat dis. due to eddy currents	6 mW
	Number of windings	34,000
	Heat dis. due to A.C. hysteresis	11.6 mW
	Heat dis. due to A.C. eddy currents	2.5 mW
	Maximum field	1.5 Tesla

Table 14. Design parameters for the SMP superconducting magnet.

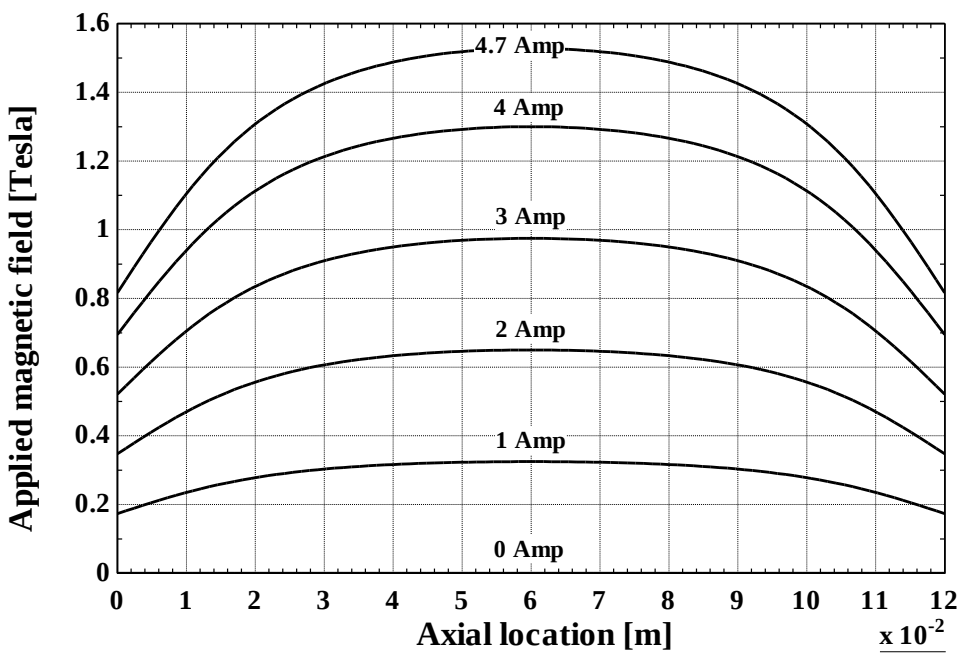

Figure 52. Applied magnetic field as a function of axial location.

6.2.8. Superconducting magnet construction

The procedure involved in the construction of the superconducting magnets is listed in chronological order:

1) The mandrel is machined out of a thick tubing of Aluminum 6061-T6; after cutting the tubing to the correct length a lathe was used to turn the mandrel to the specified outer diameter (inner diameter was left untouched). A flange was formed at either side for two purposes: to contain the coil, and to allow for mounting to the cold temperature platform. A diode pocket was machined into the side of one of the flanges of the mandrel using CNC mill. A channel was created between the pocket and the winding area to allow the superconducting wire to pass through once at the beginning of the winding process and once at the end. The mandrel is shown in Figure 53.

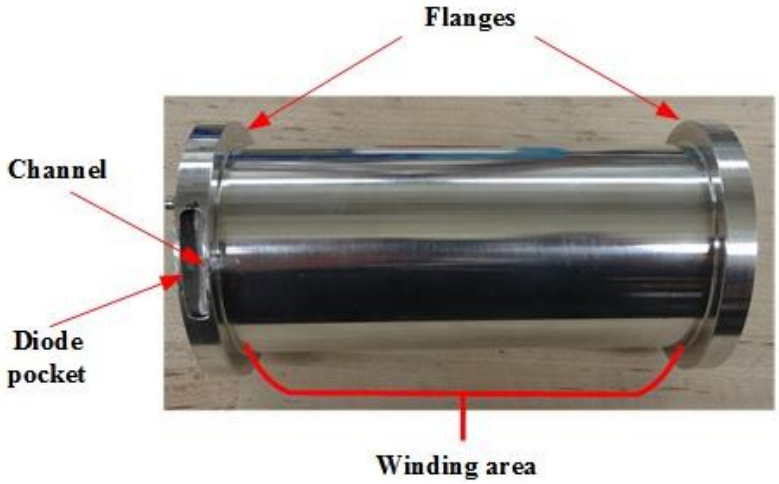

Figure 53. Image of the mandrel after machining operation is complete.

2) The mandrel was carefully polished to a fine finish using 3M's 281Q and 481Q polishing papers. The mandrel was secured on the lathe and a speed of 5 to 10 RPM was selected before commencing the polishing operation by starting with the 30 micron paper and progressively using finer polishing papers all the way down to 1 micron.

3) The mandrel was extensively cleaned by using Acetone to remove any grease or oil residue left from the machining operation. After that Methanol was used to clean any Acetone residue (white streaks) from the surfaces.

4) A 0.025 mm thick Kapton tape was used to cover the winding area and inner surfaces of both flanges. This very thin tape protects the coil against shorts to the mandrel in case there is a defect in the wire's electrical insulation. Care must be taken to avoid any air bubbles forming underneath the tape upon application. Tape overlaps must be kept to a minimum to prevent unnecessary increase in thermal resistance between the mandrel and the wires.

5) The CNC must be set up on the coil winding machine. Winding parameters such as speed, start position, stop position, braking option, pitch, and direction may be configured at this time.

6) The tension of the superconducting wire must be adjusted to an appropriate level. Tension can be controlled by adjusting the wire gripper shown in Figure 54. The author found this by tying one end of the wire to a mass weighting 180 g and adjusting the wire gripper tightness until the mass was dropping vertically at a constant velocity. Note that the required tension will be different for different sizes of wire.

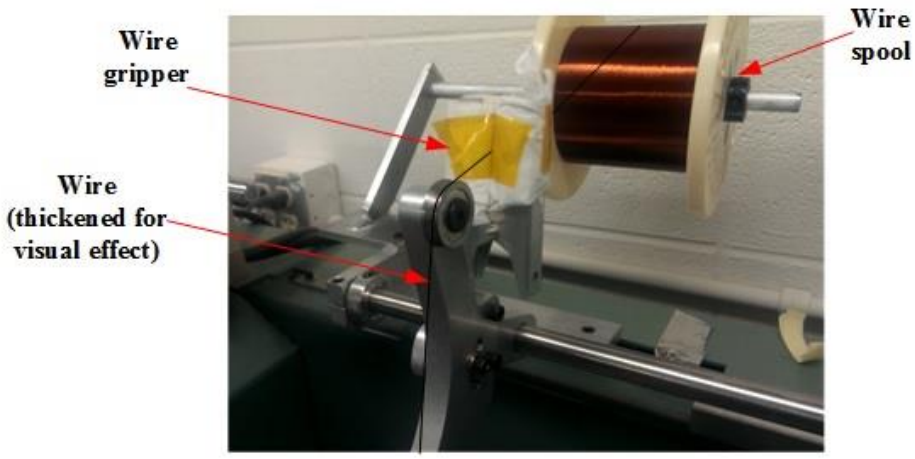

Figure 54. Wire spool configuration (wire is highlighted for enhanced visual effect).

7) Two plates were prepared and bolted on to either of the mandrel's flanges. These plates act as a securing interface between the mandrel and the winding machine's tailstock and center as shown in Figure 55. The mandrel is secured on the machine and tested for minimal eccentricity before commencing the winding operation.

8) The wire is fed through the pulleys and their height is adjusted such that the lower pulley is closest to the mandrel. The wire is wrapped several times around the flange and temporarily secured by tapes to allow for some free length of lead at one terminal. The wire is carefully fed through the channel and into the winding area.

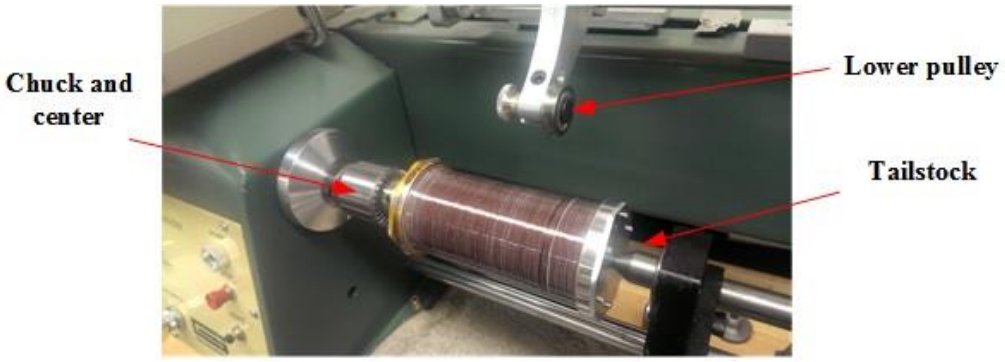

Figure 55. An image taken at a random time during the winding process.

9) A special epoxy, CTD-A521, is used for potting of the coil during the winding operation. The potting is necessary because it allows for good thermal communication between the mandrel and the coil once the epoxy is cured. It also keeps the wires in place during magnetization and demagnetization of the coil minimizing heat generation due to friction between individual loops of wires. The CTD-A521 epoxy needs to be degassed by a vacuum jar that is connected to a vacuum pump. This operation ensures the epoxy is free of air bubbles which could potentially create undesired voids in the epoxy once cured. A

moderate amount of epoxy must be continuously applied via a brush throughout the entire winding operation. No pauses can be made in the winding process otherwise the epoxy will harden. Figure 55 also shows an image at a random time during the winding operation.

10) After finishing the winding operation the solenoid will need to be continuously rotated at low speeds (2-5 RPM) for 2 days. This is necessary to keep the epoxy uniform around the coil and to prevent the wet epoxy from drooping. The solenoid needs to be left untouched for an additional 5 days because CTD-A521 has a complete curing time of 7 days.

11) The wire lead that was temporarily taped to the flange prior to winding must be carefully unwrapped at this point. Each end of the lead must be carefully stripped from its electrical insulation close to the coil. The stripping length must be kept short to about 2 cm. Various techniques exist for stripping off the insulation depending on the insulation material. For Formvar insulations either Formic acid or a commercial product called Insulstrip can be used. For tougher insulations such as ISOMID or ML a small pot of molten salt can be used to strip the insulation off the wires. <u>It should be emphasized that ultimate care must be taken in the insulation-stripping process. Inadvertent damage to the wire as a result of the stripping process can render the entire solenoid useless.</u>

12) It is best practice to fortify a superconducting magnet against undesired quenches by using either passive or active protection mechanisms. The author used passive protection due to its ease of implementation and superior performance. This protection mechanism is formed by using two back to back diodes, type 1N4001, in parallel with the coil circuit as shown in Figure 56. The two back to back diodes help eliminating the need to track the terminal signs. In the case of a quench, the coil's electrical resistance raises significantly causing a voltage to appear between the leads which usually exceeds the voltage set at the source.

When this occurs the voltage across the leads are higher than the forward voltage in the diodes. This allows the electrical current to flow through the diodes. The diodes then protect the magnet by gradually dissipating the heat as the current loops around the closed diode-coil circuit. Therefore for this step the stripped wires must be soldered to the 2 diode leads.

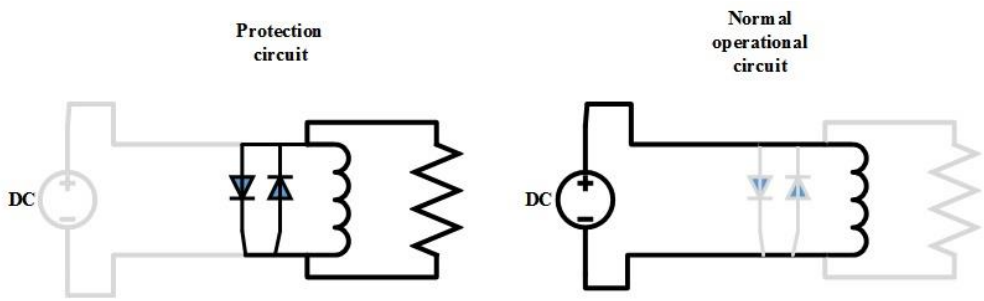

Figure 56. Demonstration of protection vs. normal operation circuit.

13) The diodes need to be thermally anchored at low temperatures otherwise the heat generated in the diodes could potentially damage them. To accomplish this the diodes are carefully inserted into the diode pocket made into the flange surface before pouring degassed CTD-A521 epoxy into the pocket to fill the entire pocket. Allow some strain relief mechanism for the leads in order to protect the wires against the sharp edges of the hardened epoxy. This can be done by inserting a piece of heat shrink tubing into each of the outgoing leads as shown in Figure 57.

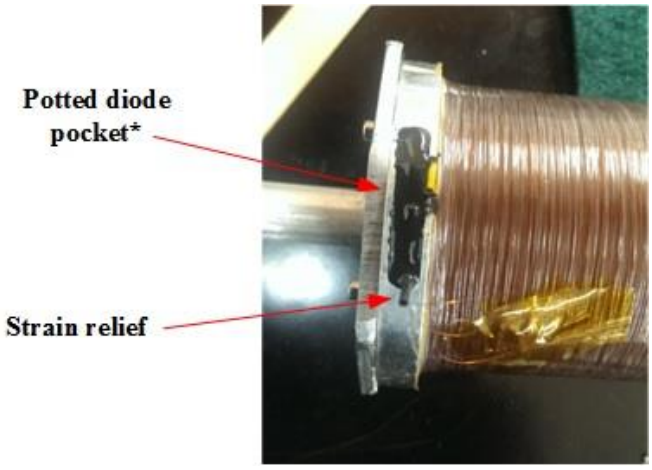

Figure 57. Potted diode pocket. NOTE: *CTD-A521 is white, see excerpt at end of section.

14) The magnet can be tested now. The electrical resistance of the solenoid can be checked before cooldown to verify electrical continuity. The value of the electrical resistance can be compared to its nominal value. If a higher than expected resistance is observed it could be indicative of the wire being stretched too much under tension during the winding process. If the resistance is smaller than expected it could be indicative of a wire-wire or wire-mandrel short. It is recommended that the coil be cooled down to 4 K at least twice prior to initial charging of the magnet to ensure loops of wire have settled inside the coil as a result of thermal contractions and expansions.

This concludes the winding procedure for a superconducting magnet. Two superconducting magnets are needed for the full SMP experiment. The construction of these superconducting magnets require a high level of experience and skillset. In fact construction of these superconducting magnets by a novice has a 50% chance of success according to a skilled NASA technician with 30 years of experience (Hait 2014). Unsurprisingly yet unfortunately out of the two superconducting magnets, one failed to operate shortly before the SMP experiment.

However it should be noted that this failed superconducting magnet operated nominally during the six prior cooldowns. Thus the design and skillset used in the winding of this superconducting magnet is judged to be appropriate except for one design flaw that was later discovered through a private communication with NASA Goddard Space Flight Center: the diode pocket should not be potted with epoxy other than that used in the coil itself. This is because the two dissimilar materials, in this case the two adjacent epoxies, can put enough strain on the wire upon thermal contractions and expansions, ultimately resulting in a detachment of the wire tunneled between the two epoxies. The finished products are shown in Figure 58.

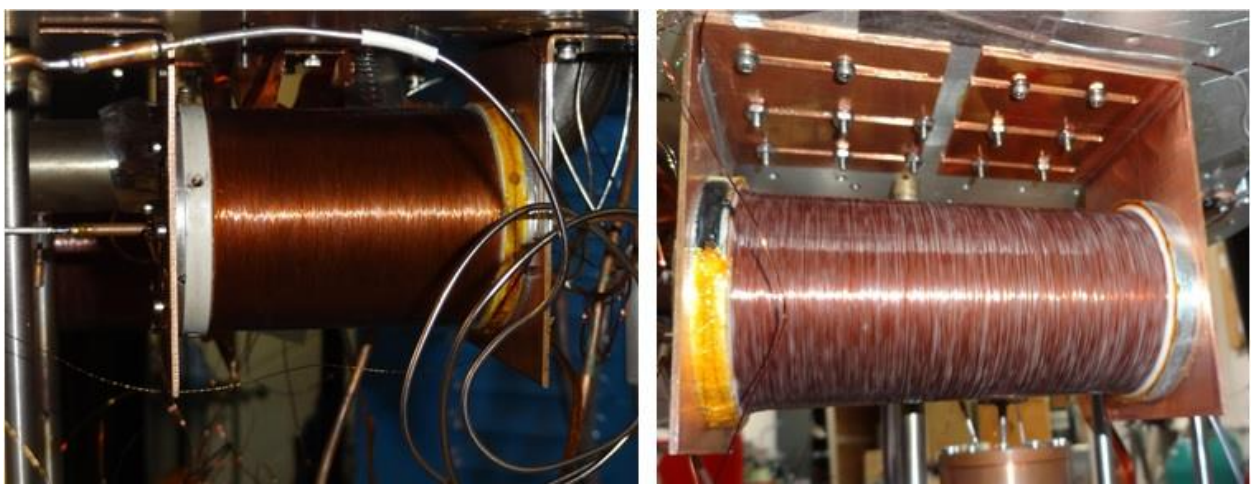

Figure 58. An image of the finished products.

6.3. GGG canisters

One of the canisters for the SMP was premade so the other canister had to be constructed. This section describes the construction of the latter canister. As discussed earlier the GGG canisters are stainless steel tubes that contain crushed GGG that is sealed against superfluid ^{4}He via two lids at the ends. Construction of these canisters involved four stages: manufacturing the canister,

crushing the GGG, packing the canister with crushed GGG particles, and sealing the canister via two lids.

The manufacturing of the canister begins by selecting a thick walled stainless steel 304 tubing. The construction procedure for the canister is identical to the mandrel used in the superconducting magnet, only the canister lacks the diode pocket as it is irrelevant for this application. Two lids are machined out of a round stock of stainless steel 304 to seal either end of the canister.

The procured GGG was shipped in the form of large irregularly shaped chunks. These chunks needed to be crushed to particles roughly 1 mm in diameter or lower before packing into the canister. Due to its expensiveness, the GGG was not crushed until the crushing procedure was perfected by practicing on glass. Glass particles crush in a manner similar to GGG and are much less expensive. The custom made crushing apparatus consisted of a thick walled cylinder that was welded to a base plate made out of steel. A steel piston was machined in a manner to fit relatively snug inside the cylinder bore. A grade 8 steel bolt was used and torqued into the tapped blind hole of the piston. This allowed the impact from the hammer to transmit to the piston. Figure 59 shows an image of this apparatus.

Figure 59. An image of the custom made crushing apparatus.

Usually two to three moderate hammer blows was sufficient to crush the GGG particles into finer particles. Then the crushed particles were sifted through a sieve with openings of 1.2 mm. Particles still remaining in the sieve were kept and later re-crushed. Particles that fell though the 1.2 mm sieve were sifted once more through a finer sieve with openings of 0.2 mm. Those particles that pass through the latter sieve were rejected and the particles that did not make through were kept in a pile to be used. Figure 60 shows a flowchart demonstrating the sequence used in the crushing operation.

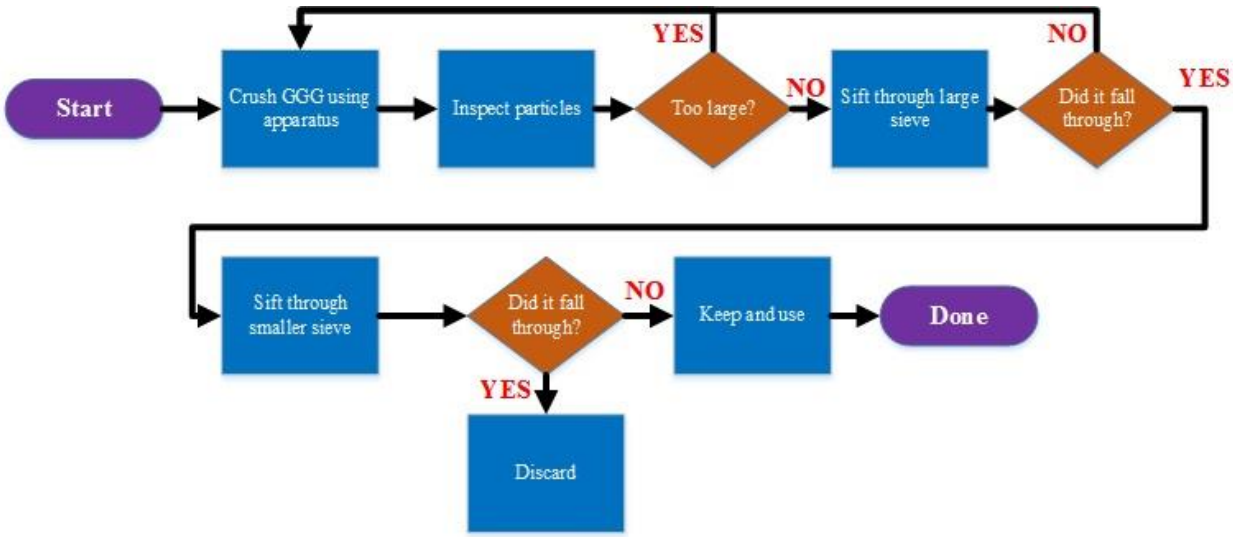

Figure 60. A flowchart of the crushing procedure.

The canister was thoroughly cleaned with Acetone and Methanol prior to packing. One side of the canister was sealed prior to packing of the canister. The sealing procedure will be discussed later in this section. A palm sander was used to shake the canister while pouring the crushed GGG particles inside the tube. Doing so ensured efficient packing of the particles as a result of active mixing and settling of the particles inside the canister. Packing continued until there was no looseness among the particles upon sealing the second lid against the canister.

Figure 61 shows a schematic of the canister lid. The lids have a hole drilled off center to allow fluid to pass through during the SMP operation. Copper tubing is brazed to one side of this hole and a tapped hole with a flat bottom surface is made to accommodate a stack of screens and a washer on the opposite side of the hole. A hollow set screw is used to secure the washer and the screens against the flat bottom. The purpose of this configuration is to contain the particles within the canister and prevent the small particles from escaping the canister. The set of screens are selected such that the opening is much smaller than the smallest particles in the canister (0.1 mm).

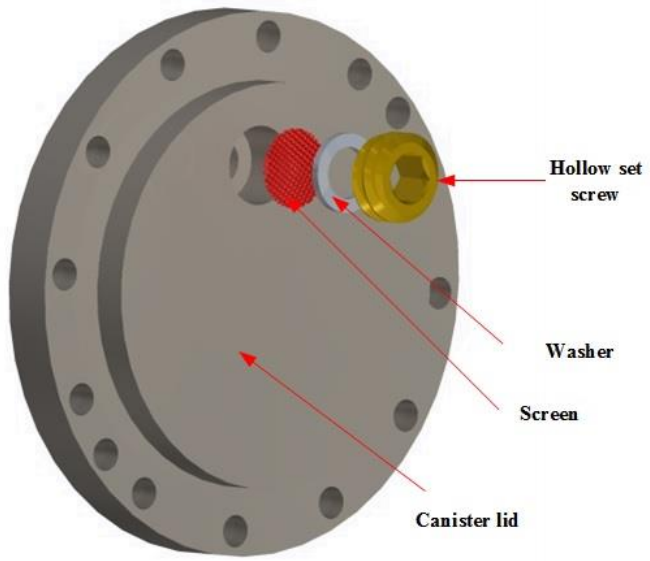

Figure 61. Schematic of the canister lid.

The lid is sealed against the canister's flange by forming an O-ring out of a piece of Indium wire, crossing the ends once and tightening the bolts until the Indium O-ring has been significantly compressed. It is well known to the low temperature community that Indium creeps in seals of this type. It is necessary to revisit and tighten the bolts over time. The author chose to retighten the bolts for a total number of 4 times 8 hours apart from each other. The canister seal was checked with a ^{4}He leak detector at room temperature and the integrity of the joint was verified.

Lastly, the canister needed to be suspended within the superconducting bore. To accomplish this a large ring and a small disc were machined out of Aluminum. Four slits and a cross were cut into the large ring and the small disc respectively. Two pieces of Kevlar string were used to constrain the ring and the disc by epoxying the string in the grooves as shown in Figure 62. Note the "T" shaped cuts in the ring, this is to prevent the epoxy from slipping out of the groove. Finally the disc is bolted on to the two canister lids and the ring is bolted on to the superconducting magnet flanges in order to suspend the canisters in the magnet's bore.

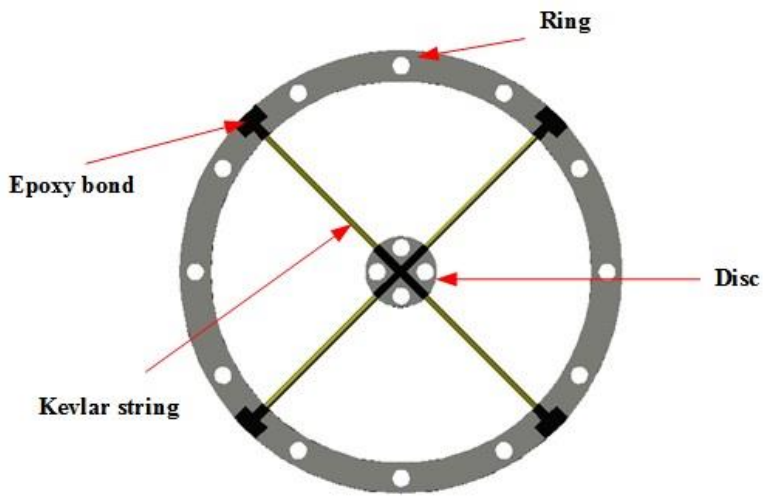

Figure 62. Suspender mechanism for the canisters.

Figure 63 shows an image of the finished canisters.

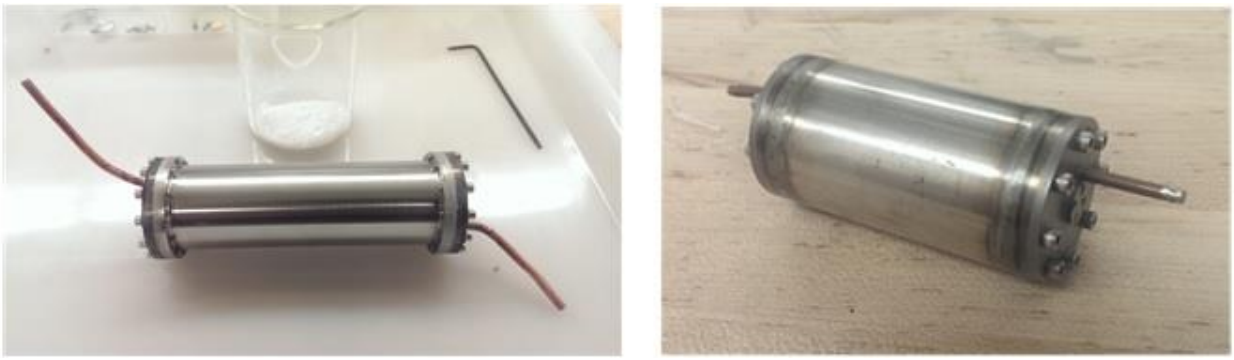

Figure 63. An image of the finished canisters. Right image is the premade canister and left canister is the one constructed for this work.

6.4. Superleak

The superleak consist of 4 major components as shown in Figure 64: three cylindrical pieces of Vycor glass, sleeve, case, and a cap. Brass was chosen as the material used for the latter three components due to its ease of machinability. The case has a flange lip that accommodates 8 tapped holes for this specific design. Enough spacing is left between the tapped holes and the inner diameter of the flange to allow for an Indium O-ring to be used as a sealing medium. Referring to Figure 64, a pocket is created inside the case and a shoulder is machined towards the right end of the pocket to act as a barrier for the sleeve when slid inside to allow for a small dead space between the right face of the sleeve and the bottom of the case. A hole is drilled at the far right of the case to allow for a tubing to be brazed or soft soldered for fluid flow.

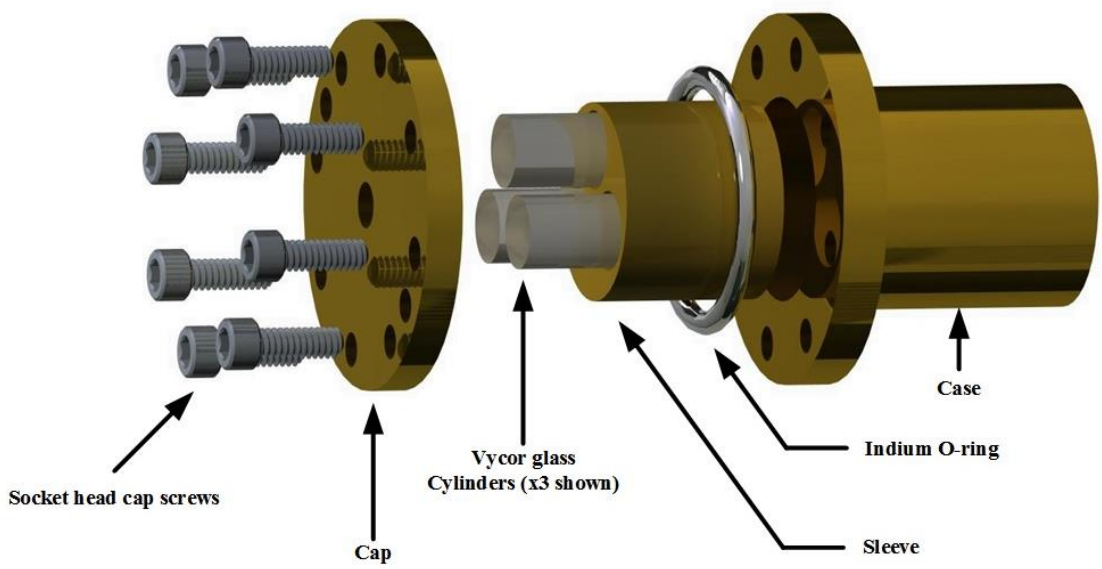

Figure 64. An exploded view of the superleak assembly.

The sleeve has three holes to house three Vycor rods each with a diameter and length of 0.5 and 1.4 cm respectively. It is important to leave a gap of about 0.2 mm between the outer diameter of the sleeve and the inner diameter of the case to allow for proper epoxy bondage.

The cap has a mating flange with 8 clearance holes and two tapped service holes if disassembly is required. A hole is drilled in the center of the cap to allow for a tubing to be mounted. Note that a small dead volume is also intentionally created between the cap and the sleeve at this end.

It is imperative that the mating surfaces at the flange site be adequately prepared for a reliable Indium seal joint. This can be accomplished by leaving the surfaces untouched after facing the mating surfaces on a lathe. These concentric ridges left by the facing tool traps the Indium material very effectively in between the mating surfaces once compressed. If the mating surfaces have any defect by inspection under a microscope, particularly radial scratches or grooves, it becomes important to lap polish the mating surfaces to a mirror finish by using 3M's 281Q and 481Q polishing paper set (1, 2, 3, 9, 15, and 30 microns) progressively starting from the most coarse to the finest polishing paper.

Stycast 1266 is an excellent candidate for use in seals that require a superfluid tight joint. The lack of resin in this clear epoxy prevents the formation of pockets, or pores in the hardened epoxy. The epoxy was degassed by placing the mixed sample inside a glass jar and pulling a vacuum until foaming and bubbling stopped inside the mix. Figure 65 shows a semi-sectional view of the superleak assembly. Epoxy was applied to the outer surfaces of the Vycor rods before inserting them into the three corresponding holes of the sleeve. Care was taken to have the three rods flush against a hard surface during epoxy curing. Four strips of AWG 34 copper wire were used around the outside of the rods longitudinally and 90 degrees apart from each other to ensure

a uniform gap was present between the outer surface of the rods and the inner surface of the sleeve holes for a reliable epoxy joint. Note that 1.3 mm of the rod was sticking out beyond the sleeve at either end. This was to ensure that the rods can be properly cleaned from any epoxy residue. Once the epoxy was cured, the face of the Vycor rods were lap polished at both end and the surface was examined under a microscope until no leftover epoxy was found blocking the surface of the rods as this could decrease the effective surface area available for superfluid flow.

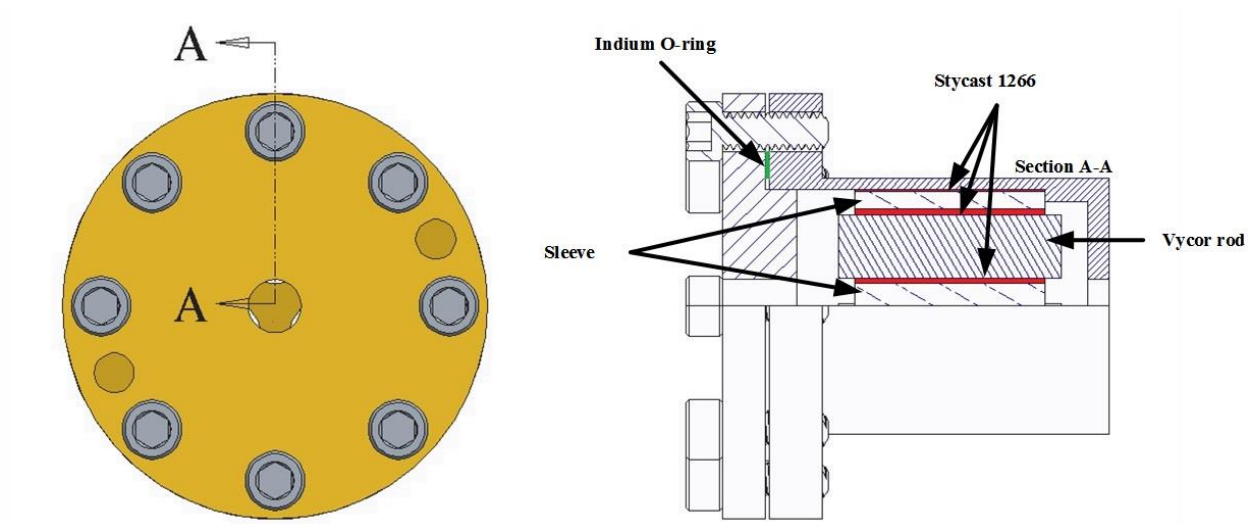

Figure 65. A semi-sectional view of the superleak assembly.

The assembly can be easily taken apart with minimal damage to the components of the superleak if disassembly is required (i.e. if one of the Vycor rods is cracked, damaged, or inadvertently saturated with water). The lid can be removed by inserting two screws into the tapped service holes and torqueing them evenly until the lid pops off. A thin scalpel or razor blade can be used to gently remove the residual Indium adhered to the mating surfaces. Note that re-polishing of the mating surfaces is required prior to reassembly as slight damage to the mating surfaces is expected when removing the Indium residue. Then the case sub-assembly can be heated up to 100 degrees Celsius until the cured Stycast 1266 softens and turns into gel consistency. The parts can

be carefully removed by a pair of tweezers and serviced or replaced for reuse before reassembly. An image of the finished product is shown in Figure 66.

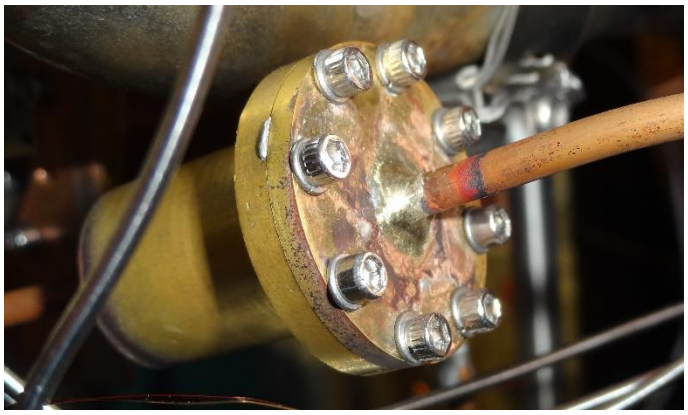

Figure 66. An image of the finished product.

6.5. Superfluid shut-off valve

Helium is fed into the SMP experimental loop via a helium tank at room temperature. The incoming helium is precooled, condensed, and sub-cooled by exchanging heat with the first and second stage heat exchange platforms as well as the 1 K platform. The sub-cooling of helium ceases once the temperature reaches the lambda point. The extremely high thermal transport properties of helium prevents this fluid from reaching sub-lambda temperatures if the fluid circuit is internally left exposed to higher temperatures. To fix this, a valve must be used in close proximity to the experimental loop that is capable of sealing against superfluid helium. A commercially available valve by Swagelok, model SS-4BW-TW, is used for this application. This stainless steel valve is bellows-sealed welded preventing any leakage from the fluid loop to the outer environment. This valve comes with a spherical stem tip that is stationary relative to the stem; its tip does not rotate upon closing and opening of the valve. This property allows the valve to be repeatable upon repeated sealing as the mating interface is always identical. Each time the

valve is shut the sharp edged shoulder “chews” the spherical tip which in turn forms a reliable seal against superfluid helium hence no internal leakage occurs. Figure 67 shows a schematic of this valve created by Swagelok (2015).

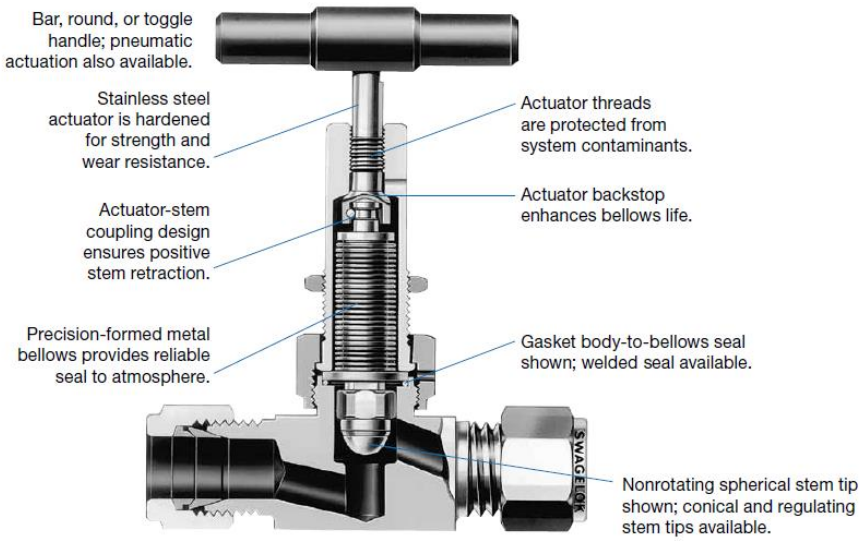

Figure 67. Schematic of the SS-4BW-TW valve used to seal against superfluid helium (Swagelok 2015)

The valve had to be retrofitted in order to be compatible with the Dewar configuration. This meant removing the manufacturer’s handle and custom building an interface that would allow a long driving shaft to operate the valve from outside the Dewar. For this purpose a long thin walled stainless steel tubing 9.5 mm in outer diameter and wall thickness of 0.25 mm was used. This tubing extends from outside the Dewar to the stem of the valve which is installed on an extender plate attached to the 1 K heat exchange platform. An adapter was made out of a brass ring and brazed onto the bottom end of the drive shaft. Three holes were drilled and tapped on the outside of the ring to allow three 4-40 bolts to grab the stem of the valve. A brass plug was brazed on the opposite side of the drive shaft in order to maintain a high vacuum seal for the Dewar. This end passes through a quick connect fitting, making a high vacuum seal between the drive shaft and

the connector via a small rubber gasket. Figure 68 shows an image and layout of the valve and the drive shaft.

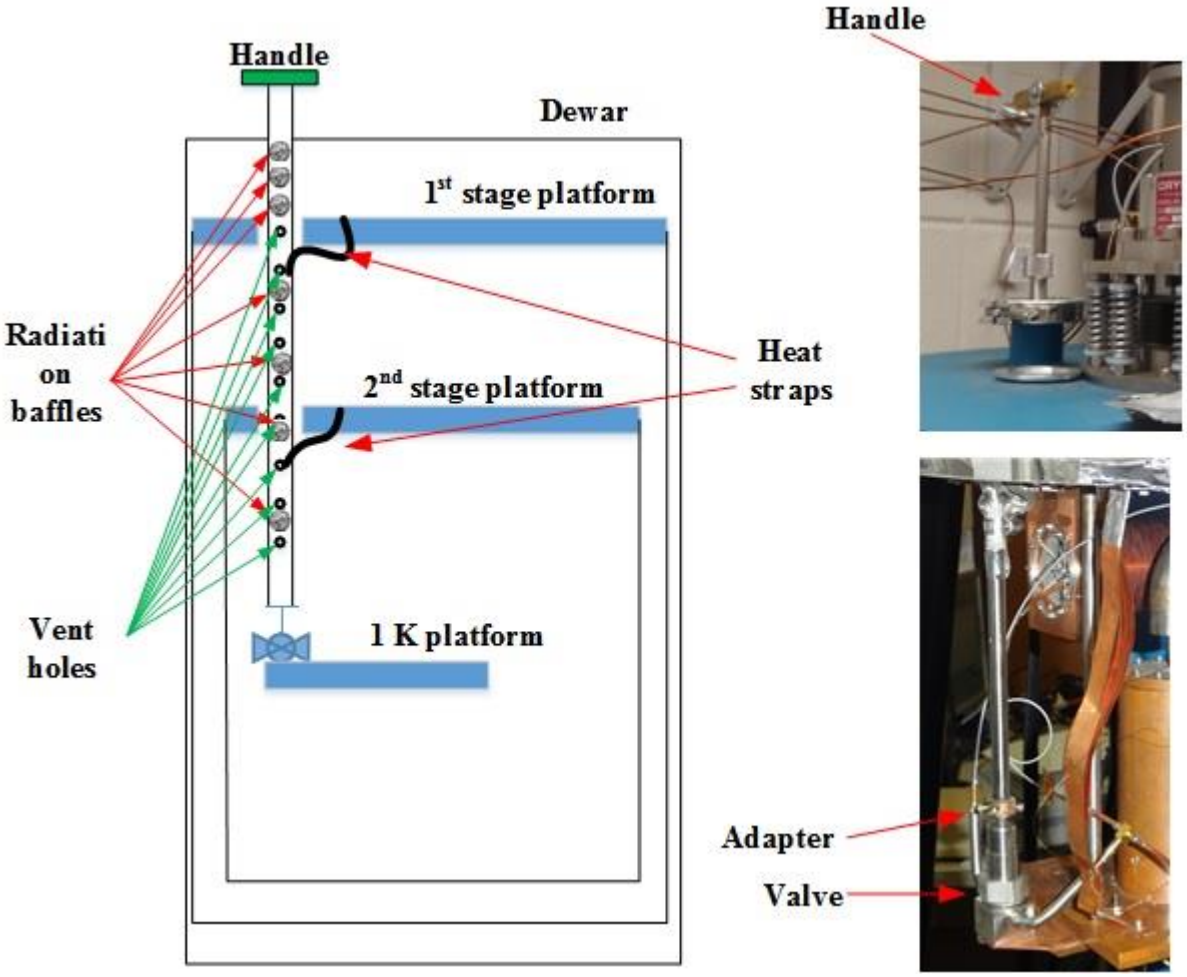

Figure 68. An image of the superfluid shut-off valve along with a representing schematic.

The outside of the drive shaft was polished to a mirror finish in order to reduce its radiative emissivity. Several holes were drilled on the outside of the drive shaft to allow for proper venting upon creating a high vacuum inside the Dewar. Several radiation baffles were made by simply wrinkling some MLI and forming it into “balls” and inserting them inside the shaft at appropriate levels to reduce periscopic radiation from room temperature onto the valve. Finally some tinned-copper braided cables were used to thermally anchor two sections of the drive shaft to the first and

second stage heat exchange platforms via hose clamps in order minimize parasitic conduction into the experiment.

6.6. Venturi flow meter

One of the goals of the SMP experiment is to measure the mass flow rate produced by the pump. There are a variety of flowmeters that base their operation on the Bernoulli's principle: as fluid accelerates through a narrow restriction the static pressure decreases to compensate for an increase in dynamic pressure. Examples of these type flowmeters are venturi, orifice, and flow nozzles. A venturi flow meter has the advantage of offering minimal pressure loss, and extremely high discharge coefficients: a parameter used to measure how close to ideal a flow meter operates, the higher the discharge coefficient the closer to ideal the flowmeter operates. He II flowmetering with venturis have been experimentally demonstrated in the past with discharge coefficients ranging between 0.99 and 1.00 (Van Sciver 1990). The relationship between mass flow rate and pressure drop between the pressure taps of a venturi is easily derived from the Bernoulli's equation:

$$\dot{m} = A_{throat} \sqrt{\frac{2\,\rho\,\Delta P}{\left(1-\left(\frac{d_{throat}}{d_{inlet}}\right)^4\right)}} \qquad (104)$$

where d_{thorat} and d_{inlet} are the throat and inlet diameters respectively, and A_{throat} is the cross sectional area of the throat. The venturi flow meter was custom built. It is made from a round stock of brass. Details of the venturi flow meter along with the finished product is shown in Figure 69. This design produces a maximum pressure difference of approximately 13 kPa between the two ports. This value corresponds to a He II mass flow rate of 1 g/s.

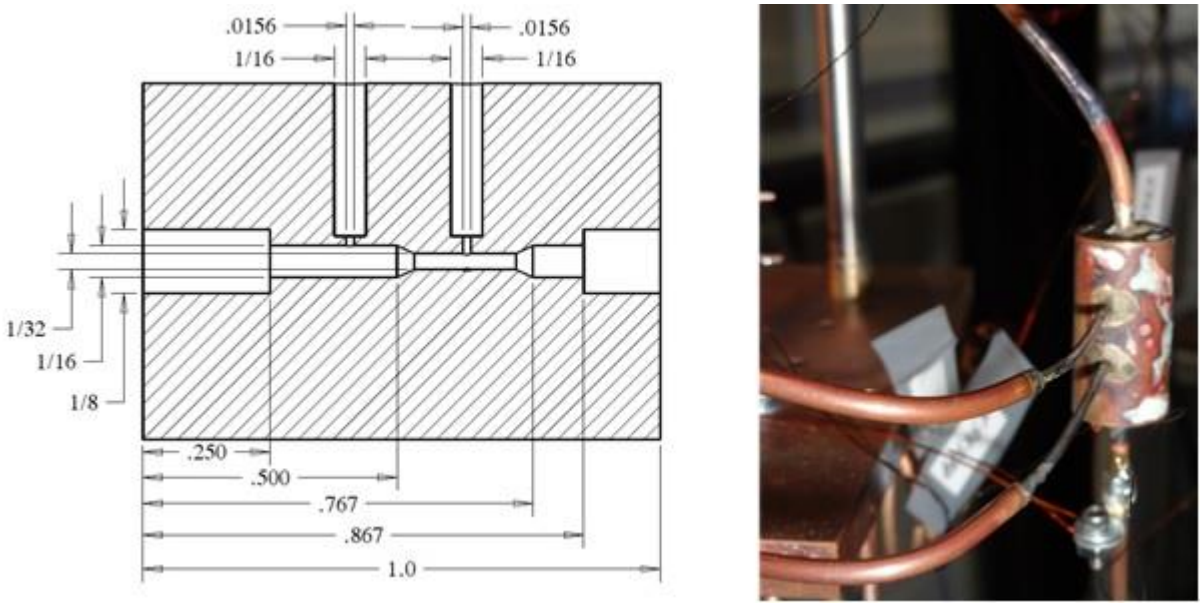

Figure 69. A drawing and image of the venturi flowmeter

6.7. Differential Pressure gauge

A differential pressure gauge is required to be mounted to the two pressure taps of the venturi flowmeter in order to measure the flow rate produced by the SMP. Vast majority of the commercially available differential pressure transducers cannot be used at low temperatures, especially with He II. One well-known pressure transducer with excellent accuracy and repeatability for use in He II was the Siemens KPY-12 pressure transducers (Maddocks 1987). Unfortunately this product has been discontinued due to its limited demand. An alternative was considered and implemented by custom building a dielectric insensitive differential pressure transducer that was first developed by Brisson and Talbot (1998).

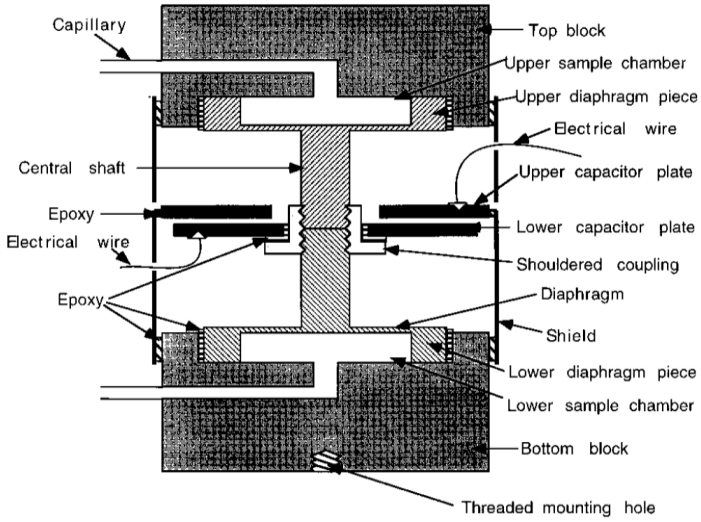

Figure 70. Diagram of the dielectric insensitive differential pressure transducer (Talbot 1998)

This transducer has two sample chambers. The lower sample chamber has a thin walled diaphragm that is connected by a central shaft to a thin walled diaphragm in the upper sample chamber. The central shaft of the upper and lower diaphragms meet via a shouldered coupling. An annular capacitor plate (lower), electrically isolated by an epoxy layer and pieces of Kapton tape, is mounted onto the shouldered coupling. The other annular capacitor plate (upper) is electrically isolated by mounting it to the shield using epoxy. The shield serves several purposes: First, it sets the relative positions of the top and bottom blocks, as well as the upper capacitor plate. Second, it electrically shields the capacitor plates from the environment, reducing stray capacitance.

Each of the sample chambers is pressurized through capillaries soldered to the top and bottom blocks. The displacement of the central shaft is proportional to the pressure difference between the chambers. The displacement changes the gap between the capacitor plates hence the

capacitance of the gauge. If the pressure in each sample chamber is the same then no displacement occurs hence no change in capacitance. Construction procedure and details of the model for this pressure transducer is thoroughly discussed in a paper published by Brisson and Talbot (1998).

Figure 71. Pressure transducer, finished product.

The two limits of operation for the pressure transducer are low and high differential pressure. Depending on the instrumentation, low pressure differentials might require the pressure transducer to be assembled in such a way to increase the sensitivity of the gauge in this range. This is accomplished by purposefully setting the distance between the upper and lower capacitor plates very small during assembly. In this case a small displacement of either capacitor plates would produce a big change in the capacitance value. However the caveat to this is the limited operational range of the transducer. In this case if high differences in pressure is produced, permanent damage to the transducer might occur as a result of interference between the upper and lower capacitor plates. Thus it is safe practice to connect the higher pressure port to the upper chamber in order to

bias the lower plate away from the upper plate hence avoiding interference of the plates in such configurations. Figure 71 shows the final product built by the author. The capacitance was measured to be 534 pF with no pressure difference at 1.4 K. It should be noted that the relationship between pressure difference and change in capacitance is very close to linear for the pressure range between 0 to 13 kPa as shown in Figure 72.

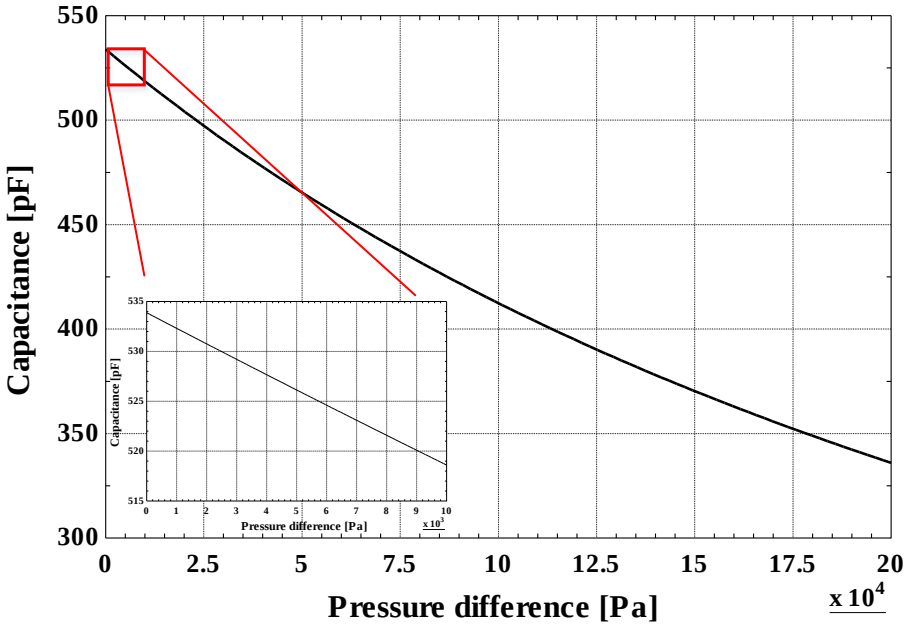

Figure 72. Change in capacitance as a function of differential pressure for the pressure gauge.

Note that every part involved in the pressure transducer were made out of brass except for the two diaphragms. These diaphragms were chosen to be made out of Beryllium-Copper because this alloy provides superior performance as opposed to brass. This is because unlike brass, Beryllium-Copper does not microyield during operation. Microyielding could cause some instabilities in the measurement.

6.8. References

Anderson, P_W. "Theory of flux creep in hard superconductors." Physical Review Letters 9.7 (1962): 309.

Bardeen, John, Leon N. Cooper, and J. Robert Schrieffer. "Theory of superconductivity." Physical Review 108.5 (1957): 1175.

Barron, Randall F. Cryogenic systems. Clarendon Press, 1985.

Ekin, Jack. Experimental Techniques for Low-Temperature Measurements: Cryostat Design, Material Properties and Superconductor Critical-Current Testing: Cryostat Design, Material Properties and Superconductor Critical-Current Testing. Oxford University Press, 2006.

Hait, Thomas. Private communication NASA-Goddard Space Flight Center (GSFC), 2014

Kim, Y. B., C. F. Hempstead, and A. R. Strnad. "Critical persistent currents in hard superconductors." Physical Review Letters 9.7 (1962): 306.

Kim, Y. B., C. F. Hempstead, and A. R. Strnad. "Flux creep in hard superconductors." Physical Review 131.6 (1963): 2486.

Swagelok Company catalog 2015

Talbot, Tokeem, and J. G. Brisson. "Dielectric-insensitive capacitive differential pressure gauge for use at low temperature." Review of scientific instruments 70.4 (1999): 2161-2165.

Van Sciver, S. W., et al. "He II flowmetering." Cryogenics 31.2 (1991): 75-86.

Walstrom, P. L., and J. R. Maddocks. "Use of Siemens KPY pressure sensors at liquid helium temperatures." Cryogenics 27.8 (1987): 439-441.

Wilson, Martin N. "Superconducting magnets." (1983).

7. Experimental results

This chapter is divided into four sections: The experiment design and layout is provided as a framework for understanding how the various pieces of equipment interact with one another. The procedure of running the experiment is described next followed by the results of the test runs. Finally the results are analyzed. The most important results are summarized in a table at the end of this chapter.

7.1. SMP experiment design

The goal of this section is to familiarize the reader with the setup used for the experiment conducted in this work. Figure 73 shows a diagram of the SMP experimental configuration. Two separate and independent ^{4}He fluid circuits can be recognized from this diagram: The open loop connected to (Tank A) is the circuit used to run the 1 K refrigerator, and the closed loop connected to (Tank B) is the main circuit used for the SMP experiment. Various valves and pieces of equipment were used throughout each of these circuits for fluid management. Description of the assembly for each of these fluid circuits is described next.

A dual stage pressure regulator is installed on Tank A (at room temperature) to control the pressure of helium required to run the 1 K refrigerator. The Three Way Valve (TWV) labeled number 1, is used to either direct helium to the 1 K refrigerator's line or to evacuate this line via a diaphragm pump. The evacuation is necessary in order to purge the line with ^{4}He prior to operating the system otherwise impurities can block the line upon cooldown. Two mass flow meters are installed in-line to verify the flow of helium against that observed during a successful run of the 1 K refrigerator. This is because the 1 K refrigerator has shown to be susceptible to inadvertent blockages during cooldowns. FM 1 is a flow meter with a lower full scale reading and higher

resolution, and FM 2 is a flow meter with a higher full scale reading and lower resolution. After the flow rate is measured by these flow meters, helium enters the Dewar and begins precooling to approximately 40 K by exchanging heat with the first stage heat exchange platform via Heat Exchanger 4 (HX 4). Then it continues to further precool to approximately 10 K by exchanging heat with the cold helium vapor in the exhaust line via the first stage recuperator labeled HX 5. The incoming helium continues to precool, condense, and subcool to approximately 4 K by exchanging heat with the second stage heat exchange platform in HX 6 before further subcooling to approximately 2.2 K in the second stage recuperator labeled HX 7. The temperature of this subcooled helium drops to approximately 1 K after an isenthalpic expansion process through the J-T restrictor. Liquid helium is accumulated in the 1 K pot at this stage. Any heat (parasitic or planned) results in the evaporation of a fraction of the pot's liquid helium. This exhausted helium vapor is used in recuperators HX 7 and HX 5 before being released to atmospheric conditions via a rotary vane pump.

Just like Tank A, Tank B is equipped with a dual stage pressure regulator. This pressure regulator is used to charge the SMP experiment loop to an appropriate pressure. Several Ball Valves (BV) are used for fluid management. BV 1 is used as the main helium shut off valve. BV 2 allows evacuation of the line for two reasons: to purge the line with helium before the experiment begins, and to evacuate the helium from the line after the experiment is completed. BV 3 was only open when the line had a positive pressure. This is because the pressure transducer was believed to leak air into the line upon evacuating the tubes.

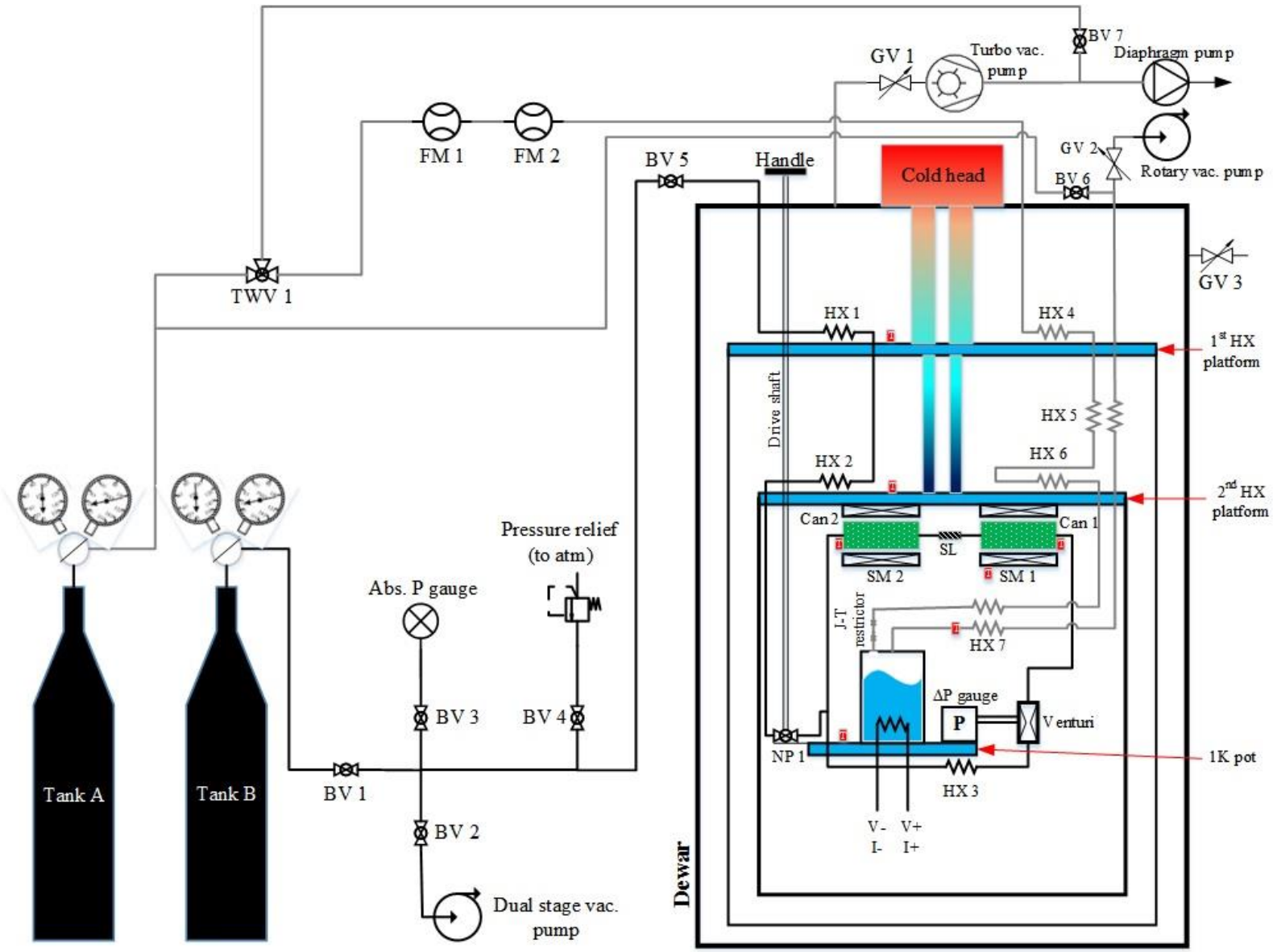

Figure 73. A diagram of the SMP experimental setup.

Once cooled down to sufficiently low temperatures BV 5 and Nupro Valve (NP 1) are opened to allow helium to fill the experimental loop by exchanging heat with the first and second stage heat exchange platforms in HX 1 and 2 respectively. Helium begins to precool, condense, and subcool in the closed SMP loop. Continual supervision of the apparatus is not possible because this process takes a relatively long amount of time (at least 48 hours). For this reason a pressure relief valve is installed on the loop and outside the Dewar to relieve any pressure build up in the closed loop as a result of a cryocooler shut down or any other refrigerator malfunction. This prevents line rupture and the subsequent severe damage. Thus BV 4 is closed once the charging of the experimental loop terminates.

The superconducting magnets are thermally anchored to the second stage heat exchange platform via thin copper plates that are pre-bent to form an “L” bracket. The GGG canisters are suspended inside the magnets’ bores via Kevlar. The superleak connects the two canisters via solder joints. The differential pressure transducer is mounted to a small thick copper plate before mounting this plate onto the 1 K heat exchange platform. The two ports of the pressure gauge are soldered to the two taps of the venturi flow meter via slip joints. A heat exchanger, HX 3, is formed by soldering a length of copper tubing to a copper plate before bolting it onto the 1 K heat exchange platform.

A total of seven thermometers were mounted in the experiment. A thermometer was mounted onto each of the canisters. A third thermometer was installed on the superconducting magnet to ensure that the coil operated below the critical temperature of Nb-Ti. The remaining thermometers were installed on the 1 K heat exchange platform, 1 K exhaust line, second stage and first stage heat exchange platforms for housekeeping purposes. A heater was installed on the

1 K heat exchange platform to allow the user to raise the temperature of the 1 K pot to appropriate levels if needed.

7.2. SMP experiment procedure

This section describes the experimental procedure which is used each time the apparatus is run. This procedure is divided into four parts: the preparation phase before cooldown, cooldown, experimental run, and warm up. Refer to Figure 73 for the references made in the procedure.

Note: To eliminate any sort of confusion close all valves (BV 1 through BV 7, TWV 1, GV 1 and 2, and NP 1) prior to following these procedures.

Preparation of the 1 K pot:

1) Turn on the rotary vacuum pump, let it warm up for 15 minutes. Read the vacuum gauge, pressure should be less than 600 mTorr. If it is not less than 600 mTorr then inspect pump (Pump might be due for an oil change).
2) Turn on the diaphragm pump. Wait until the corresponding pressure gauge reads -25 inHg or less.
3) Open BV 7 and turn TWV 1 knob's arrow towards the vacuum sign. Evacuate the forward line of the 1 K pot for about 2 hours before proceeding to next step.
4) Slowly open GV 2, evacuate the 1 K exhaust line and wait until the gauge reads a pressure less than 600 mTorr.
5) Close GV 2. Adjust the pressure regulator on Tank A to read 30 psig. Slowly open BV 6. Let helium backfill the 1 K pot. Do not allow the bellows hose connected to the rotary vacuum pump to over expand during this process. Close BV 6 after backfill is complete. Wait for 3 minutes.

6) Repeat steps 4 and 5 for a total of five times.

7) Open GV 2 and leave open for the remainder of the procedure.

8) Turn on FM 1 and FM 2, wait for 10 minutes until units are warmed up. Display should show zero at no flow, if this is not the case then adjust the knob until displays show zero.

9) Record the value displayed by the pressure gauge connected to the rotary vacuum pump.

10) Turn TWV 1's knob towards the helium sign. The lower range flowmeter must display a value higher than 2 mL/min and lower than 20 mL/min of standard N_2. If the display shows a value lower than 2 mL/min then the line is clogged somewhere, inspection and repair is required before proceeding any further. If a value higher than 20 mL/min is displayed then a leak in the line is suspected, leak check the line by tracing it from the tank to the 1 K pot with a sniffer probe. Leaks must be fixed before proceeding any further.

11) Read the value displayed by the pressure gauge connected to the rotary vacuum pump. Compare this value to that recorded in step 9. Proceed if the new value is higher than the old value. If not re-inspect the line with an emphasis on the J-T restrictor.

12) Turn TVW 1's knob towards the vacuum sign. Wait for 1 hour before proceeding any further.

13) Turn TVW 1's knob towards the helium sign. Wait for about 5 minutes.

14) Repeat steps 12 and 13 for a total of five times.

15) Leave TVW 1's knob towards the helium sign. The 1 K pot line needs to be completely flushed with helium before cooling down. Record the mass flow rate of helium measured by FM 1 and FM 2 in LabVIEW during this time. Continue waiting until the mass flow rate reaches a plateau over time, approximately 24-48 hours.

Preparation of the SMP's experimental loop:

1) Turn on the dual stage vacuum pump, wait until unit is warmed up for 15 minutes.
2) Slowly open BV 2, BV 5, and NP 1. Leave them open until the line is evacuated. Wait for about 10 minutes.
3) Adjust the pressure regulator on tank B to read 10 psig. Close BV 2 and slowly open BV 1.
4) Thoroughly leak check the line with a helium leak detector via a sniffer probe. If leaks are detected, the suspect joint or area must be repaired before proceeding any further. Proceed to the next step if no leaks are detected.
5) Close BV 1 and open BV 2 while the dual stage vacuum pump is running. Wait for 1 hour.
6) Open BV 1 and close BV 2. Fill the line with helium. Wait for about 10 minutes.
7) Repeat steps 5 and 6 for a total of 10 times.
8) Close BV 1 and open BV 2, wait for about 1 hour.
9) Shut NP 1 tight by applying a moderate amount of torque on the handle. Note: do not over torque, this could result in damaging the adapter or the valve stem.
10) Close BV 5 and BV 2. Turn off the dual stage vacuum pump at this time.
11) Immediately open BV 1. Let the line be under positive pressure from the tank up to BV 5.
12) BV 3 may now be opened and the absolute pressure gauge may be turned on.
13) Check all electrical connections (thermometers, gauges, heaters, etc.) and the superconducting magnets for any shorts or discontinuities.

Cool down:

1) Close up the Dewar by bolting on the second stage shield first, being extremely careful to not pinch any of the wires or thermometers in between the flange. Bolt on the first stage shield next. Finally bolt on the Dewar body to the upper rim.

2) Make sure that the Dewar's vent valve, GV 3, is tightly closed after closing up the Dewar.

3) Close BV 7 and turn on the diaphragm pump. Make sure GV 1 is open at this time. Allow the diaphragm pump to pump on the Dewar until the pump goes quiet (an indication that the pressure in the Dewar matches the ultimate low pressure of the diaphragm pump). This usually takes about 30-45 minutes.

4) Turn on the Pfeiffer turbo molecular pump. Monitor the turbo pump speed by reading the rotation speed displayed on the controller box; it should achieve an ultimate speed of 1500 Hz within 45 minutes. Do NOT turn off the diaphragm pump, this pump will need to pump on the backside of the turbo pump.

5) Allow the Dewar to be further evacuated by the turbo pump overnight. The pressure in the Dewar must be lower than (2×10^{-5}) mbar.

6) The cryocooler's compressor unit uses water as a coolant. City water is used to circulate water in the compressor. Make sure the water filter is not clogged. Open the water valve and observe the water flow into the drain. The compressor needs a cooling water flow rate of 5 gpm.

7) Turn the lever of the 3 phase breaker box for the cryocooler's compressor to the "ON" position. Flip the two main breaker switches on the compressor before pushing the green button on the compressor to turn the unit on. The cryocooler is now on and cool down has begun. Refer to the manual for CryoMech PT-410 for any issues related to the cold head or the compressor unit.

8) Start recording all temperatures, voltages, and currents necessary by activating the LabVIEW program for cooldowns.

9) Note that it is normal for FM 1 and FM 2 readings to initially increase, drop and oscillate before rapidly increasing to high values once the 1 K pot reaches nominal operation.

Experimental run:

1) Gently open NP 1 one and a half turns once the 1 K pot's temperature reaches approximately 1.4 K.

2) Observe the displays on FM 1 and FM 2 during this step. Lower the regulator pressure to 1-2 psig. Send a shot of helium down to the experimental loop by quickly opening and closing BV 5. Watch the values displayed by FM 1 and FM 2. Do NOT allow these values to drop below 0.1 L/min or 100 mL/min, shut BV 5 quickly once the value drops to the specified values. Despite the two fluid circuits being independent this drop in helium mass flow through the 1 K refrigerator is normal as the warm incoming helium results in a rapid evaporation of liquid helium in the 1 K pot which causes a temporary pressure increase in the incoming line.

3) Continue sending small batches of helium down to the SMP loop until the flow rate displayed by FM 1 and FM 2 no longer drop rapidly. BV 5 may be partially opened, with caution, to allow continuous charging of the SMP loop at this time.

4) Close GV 4 at this time to prevent inadvertent damage to the turbo molecular pump in case the pressurized line inside the Dewar ruptures into the vacuum space.

5) Open BV 4 to allow for the SMP loop to relieve its pressure in the case of an emergency. This passive protection system also relieves the operator from the burden of continual

supervision of the apparatus while the helium condenses and subcools in the SMP loop. Make sure the variable knob is adjusted to the desired pressure set on the relief valve.

6) Check to see if the condensation has completed in the SMP loop by one of the following methods: 1) Check the temperature of the canisters and compare those values with that of the saturation temperature that corresponds to the charge pressure; condensation has completed if the actual temperature is lower than the saturation temperature. 2) Close BV 1 and observe the pressure reading on the absolute pressure gauge. If the reading is dropping actively condensation is still in progress, if not condensation has completed.

7) Carefully close NP 1 tightly once the temperature of the 1 K pot and canisters approach 2.2 K. Note that breaking the drive shaft by over torqueing the valve can result in a catastrophic situation. The operator no longer has access to the valve stem and there is no option but to let the loop to rupture upon a warmup. Note that the pressure relief valve at this time is ineffective, close supervision is necessary until NP 1 is reopened.

8) Turn on the dual stage vacuum pump and allow to warm up for 15 minutes.

9) Open BV 2 and pump on the backside of NP 1 to allow evaporation of the liquid helium column formed behind NP 1's port.

10) Wait until the temperatures of the canisters and the 1 K pot reach an equilibrium at approximately 1.4 to 1.5 K. The core experiment can now begin.

11) Control the temperature of the canisters and the 1 K pot via the heater anchored to the 1 K heat exchange platform by using the PID control loop on the temperature controllers.

Shut down and warmup:

1) Slowly and carefully open NP 1. Make sure the dual stage vacuum is still on and BV 2 is open while BV 1 is closed.

2) Occasionally send moderate pulses of current into the 1 K pot's heater in order to boil off the liquid helium in the SMP loop and the 1 K pot. Doing so should result in the 1 K pot's temperature to increase from its base value to approximately 2.5 to 3 K. Repeat this 5 times.

3) Turn off the compressor by pressing the black button on the unit.

4) Wait for 1 minute before shutting of the cooling water. Flip the main breaker switches to off.

5) Monitor the pressure regulator of Tank A. Pressure starts building up on the forward side of the 1 K pot as the system begins warming up by absorbing the parasitic heat. Relieve some of the pressure to ambient once the pressure reaches 60 to 70 psig.

6) Let the dual stage vacuum pump operate with BV 2, BV 5 and, NP 1 open until a gargling noise is heard from the pump. True boil off of liquid helium in the SMP loop has now begun. This usually starts an hour and a half to two hours after cryocooler shut down. Allow the pump to catch the boiled off helium until the liquid level is depleted (this can be checked by observing the display on the absolute pressure gauge while BV 2 is temporarily closed. Boil off is still continuing if the pressure reading rises rapidly).

7) <u>Make sure GV 1 is closed and the turbo molecular pump is shut off before conducting this step.</u> Wait until the coldest temperature in the Dewar reaches 25 K. Take a large bag and purge it with N_2 Before filling with pure Nitrogen. Carefully place the bag's mount on the opening of GV 3 and quickly open and close this valve to allow some exchange gas in the Dewar. This speeds up the warm up of the components in the Dewar. Wait until all the temperatures in the Dewar are above the dew point of water given the conditions in the lab.

7.3. Preparatory steps towards the SMP experiment

This section details the preparatory steps taken towards the SMP experiment. The section is divided into two subsections. The first subsection describes the pre-checks performed prior to the experiment, a step necessary to ensure all components were functional. The second subsection describes steps taken to prepare the flow metering device.

7.3.1. Pre-checks

The various pieces of equipment and components involved in the SMP loop were checked prior to full experimentation once the liquid helium in the SMP loop had subcooled to temperatures near that of the 1 K pot (1.44 K). The Cernox thermometers mounted on the two canisters and the 1 K heat exchange platform all matched in their value once the loop reached thermal equilibrium at 1.44 K. This step verified the temperature controller's operation and calibration of all thermometers. Next the two superconducting magnets were checked using the model 2440 Keithley source meters by implementing a 4-wire technique (two leads used for sourcing voltage, and two leads to measure current). The current compliance was set to a low value for this pre-check step (100 mA). A linear relationship between the supplied voltage (V) and rate of rise of current (di/dt) was observed for SM 1 as expected according to:

$$V = L\frac{di}{dt} \tag{105}$$

where L is the inductance of the superconducting magnet obtained through a prior successful experiment (L_{SM1} = 5 H). Note that Eq. (105) holds true as long as a circuit is purely inductive.

Unfortunately, SM 2 was discovered to have an open circuit before running this experiment. As will be discussed later, the SMP is still fully capable of operating nominally with

only one active superconducting magnet and canister. The author chose to keep the second canister in place despite it not being able to actively participate in the cycle for two primary reasons: The entire loop was proven to be superfluid tight in prior experiments so the joints were left undisturbed for continued joint integrity, and to use the second canister as a thermal reservoir (adding considerable heat capacity due to GGG particles). In other words, the temperature difference across the superleak would quickly diminish in the absence of a second canister.

Note that Can 1 is referred to as the "active canister" and Can 2 as the "passive canister" for the rest of this document.

7.3.2. Preparation

The only component that required an extensive amount of preparation was the flow metering device. As discussed earlier, the venturi flow meter is the main device used to measure the mass flow rate produced by the SMP. Its pressure taps are connected to the ports of a custom built capacitive differential pressure transducer. A fully automated high precision capacitance bridge capable of actively measuring the capacitance was not available, so the author had to rely on the use of an analog capacitance bridge via a lock in amplifier.

The lock in amplifier can generate an AC signal with a specified frequency and voltage amplitude via its internal signal generator. The frequency and amplitude were set to 1 kHz and a maximum value of 1.99 V respectively. The output of the lock in amplifier was connected to the input of the GenRad 1615-A capacitance bridge. The leads of the differential pressure transducer were connected to the "unknown 3-terminal" port of the capacitance bridge. The output port of the capacitance bridge was connected to the input port of the lock in amplifier. The capacitance bridge is equipped with two series of knobs: six digital knobs each representing a digit for the capacitance

and four digital knobs for the dissipation factor as seen in Figure 31. These knobs are manipulated through an iterative process qualitatively shown on a phasor diagram in Figure 74 until balance is achieved (nulling the lock in amplifier). The procedure for this process is described next.

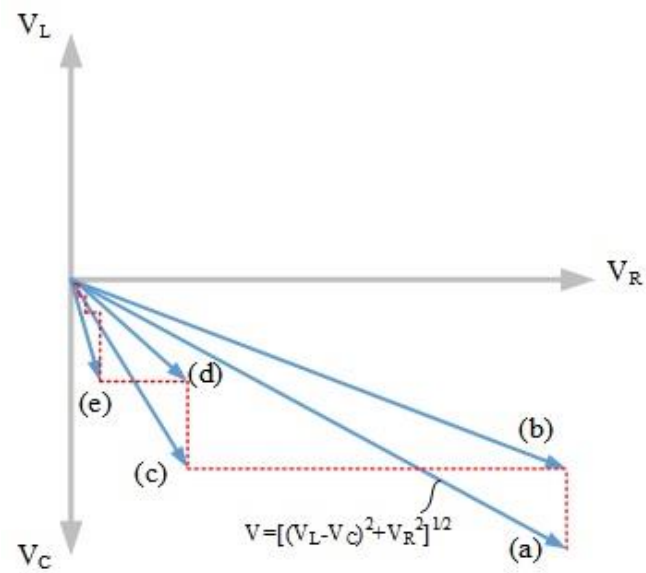

Figure 74. Phasor diagram representing the balancing procedure for the capacitance bridge. Dotted line shows the path to balancing the bridge.

Bridge Balance procedure:

1) Set all capacitance and dissipation dials to “0” on the capacitance bridge. Select “Auto measure” twice on the lock in amplifier. This will adjust the phase, amplitude, and time constant of the measured signal. Note that at this time the bridge is completely out of balance. A mismatch between the circuit’s true dissipation (resistance) and that set by the capacitance bridge appears on the real axis of the phasor diagram in Figure 74. Also a mismatch between the circuit’s capacitance and the capacitance set on the bridge appears on the imaginary axis of the phasor diagram. The resultant of these vectors is represented by (a) in Figure 74 at this time.

2) Move “C MAX” control to a setting slightly in excess of the approximate value of the capacitor being measured.

3) Set “D MAX” switch to 0.01.

4) Adjust the phase on the lock in amplifier until the signal is at its peak amplitude.

5) Adjust the left-most capacitance dial first for minimum deflection of signal on the lock in amplifier. Continue positioning the remaining capacitance dials one by one from left to right for minimum deflection of the signal on the lock in amplifier. Adjust the phase on the lock in amplifier if necessary. The capacitance mismatch between the circuit and the bridge should decrease during this step leading to the vector represented by (b) in Figure 74.

6) Manipulate the dissipation factor dials starting with right-most to refine balance further. This step decreases the mismatch between the resistance of the circuit and the bridge resulting in a vector represented by (c) in Figure 74. Adjusting the phase on the lock in amplifier might be necessary.

7) Alternate manipulating the capacitance dials followed by the dissipation factor dials until final null is accomplished on the lock in amplifier. Note that an increase in “D MAX” setting may be required if null is not achieved. The path of this alternate manipulation is shown by a dotted line in Figure 74. The goal is now clear: to reduce the resultant signal until the amplitude of this vector is significantly diminished thus achieving a null.

7.4. SMP experimental results

The SMP experiment was conducted at three different base temperatures of 1.44, 1.61, and 1.76 K. This was achieved by controlling the temperature of the 1 K heat exchange platform via the PID controller and allowing the SMP fluid loop to reach thermal equilibrium with the 1 K pot at each of the three base temperatures. Unfortunately the helium supply for the 1 K refrigeration

system was running low during this experiment, so the author chose to use six ramp rates for the superconducting magnet only at the base temperature of 1.44 K and three ramp rates for the other base temperatures in order to make the data acquisition efficient given the limited time available. Using six ramp rates at 1.44 K enabled the author to confirm the relationship between ramp rate and mass flow rate produced by the pump at a constant base temperature more accurately. For consistency only the three primary ramp rates are studied in this section. Results for all runs are detailed in the data analysis section. Table 15 lists all the runs conducted for the SMP experiment.

Run number	Base temperature (K)	Ramp rate (mTesla/s)
1	1.44	5
2*	1.44	10
3*	1.44	15
4*	1.44	20
5	1.44	25
6	1.44	50
7	1.61	5
8	1.61	25
9	1.61	50
10	1.76	5
11	1.76	25
12	1.76	50

Table 15. List of experimental runs for SMP. *Denotes runs not discussed in this subsection for consistency.

Three different ramp rates were primarily used for the superconducting magnet by sourcing a voltage of 1, 0.5, and 0.1 V. Using Eq. (105) and an inductance of 5 H for the superconducting magnet yields a current ramp rate of 0.2, 0.1, and 0.02 A/s respectively. The maximum current for the entire set of experiments was set to 3 A. The superconducting magnet produces a magnetic field of 0.75 Tesla at this current. Thus the three ramp rates correspond to a rate of rise in the magnetic field of 50, 25, and 5 mTesla/s respectively.

The temperature of the active canister, passive canister, and the applied magnetic field are plotted as a function of time for the three base temperatures using three primary ramp rates at each base temperature as shown in the plots on pages 166, 167, and 168. The goal of the remainder of this section is to qualitatively describe the trends observed in these plots.

Each experimental run consists of two processes: Flow magnetization and isomagnetic flow. Flow magnetization commences upon raising the applied magnetic field, and terminates once the magnetic field reaches its peak value. The canisters were allowed to thermally equilibrate with the 1 K heat exchange platform during the isomagnetic flow process before being demagnetized to reach initial state at zero field.

7.4.1. General trend

Flow magnetization process:

The temperature of the GGG particles rise as the constituents of the active canister are magnetized. This rise in the GGG's temperature raises the temperature of the surrounding helium. The passive canister's temperature also rises during this process. This occurs because some superfluid helium leaves the passive canister with no entropy while an equivalent mass of normal and superfluid helium enter the passive canister (a net increase of entropy in the constituents of the passive canister). Contrary to the original claim, one might expect the temperature of the active canister to fall because superfluid helium enters via the superleak with no entropy while an equivalent mass of normal and superfluid helium leave the active canister via the non superleak port. However this is not true because the magnetization process deposits a much higher amount of energy into the helium via the GGG compared to the amount of energy carried away by the flow

of helium during this process (a net increase in entropy in the constituents of the active canister). The expected results are seen in all the runs.

Isomagnetic flow process:

The applied magnetic field is held constant once it reaches its peak value. The temperature of the active canister immediately starts falling after magnetization is complete because the GGG particles are no longer actively heated via the magnetic field. Superfluid helium enters the active canister through the superleak while some normal and superfluid helium are displaced from the canister via the non-superleak port (a net decrease of entropy in the constituents of the active canister). However, the temperature of the passive canister does not immediately drop after the magnetization process is complete. In fact, the temperature of the passive canister continues rising for a little longer before falling back down. This lag is expected because the temperature of the active canister is much higher than that of the passive canister at the beginning of the isomagnetic flow process. Helium exiting the active canister is cooled by exchanging heat with the 1 K heat exchange platform as flow continues. A reduction in the temperature of the active canister over time during the isomagnetic flow process implies a reduction in the temperature of the helium exiting the 1 K heat exchanger. Therefore the temperature of the passive canister only begins dropping once the temperature of helium going into this canister is sufficiently low.

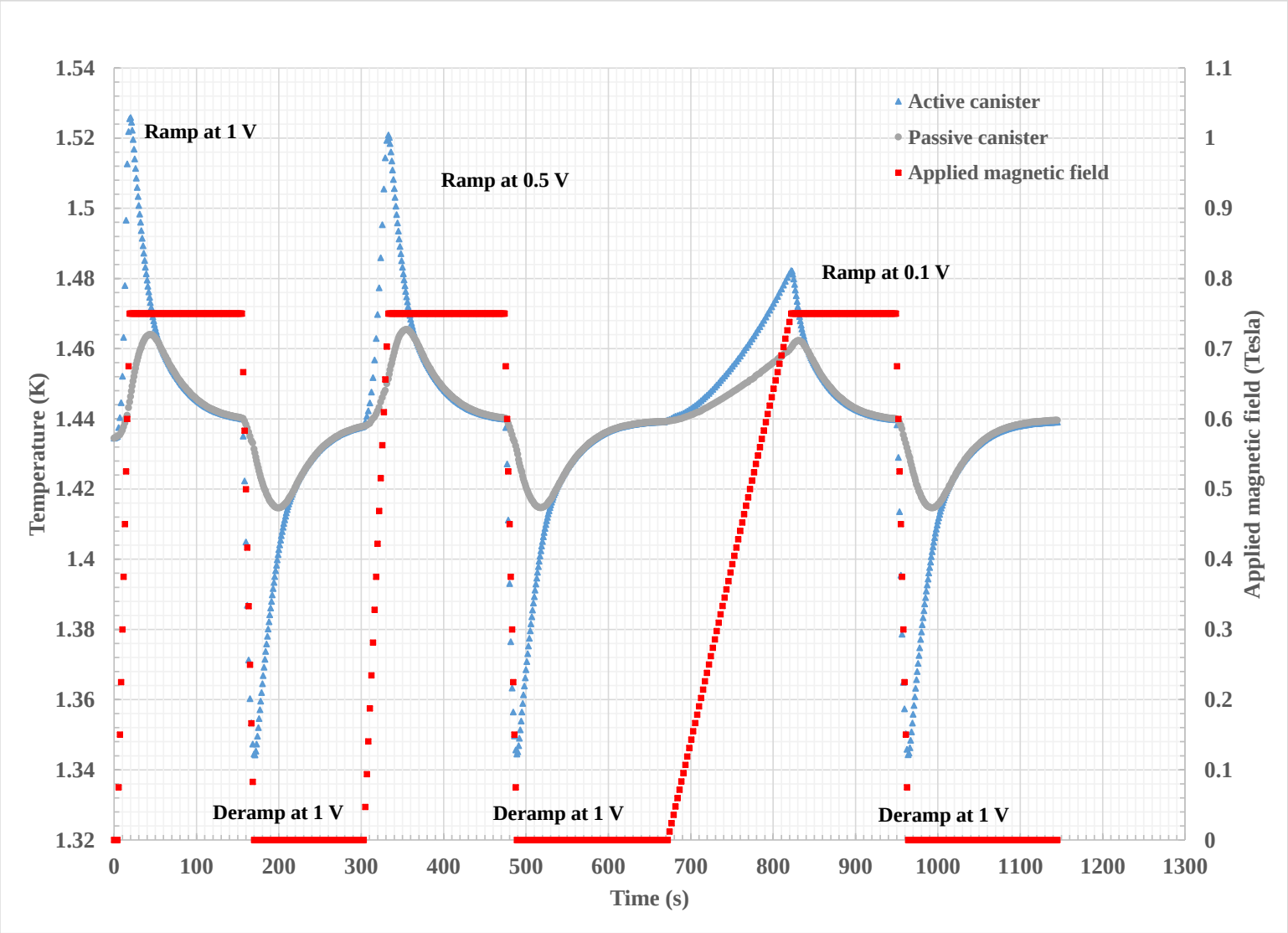

Figure 75. Experimental data for SMP experiment at base temperature of 1.44 K

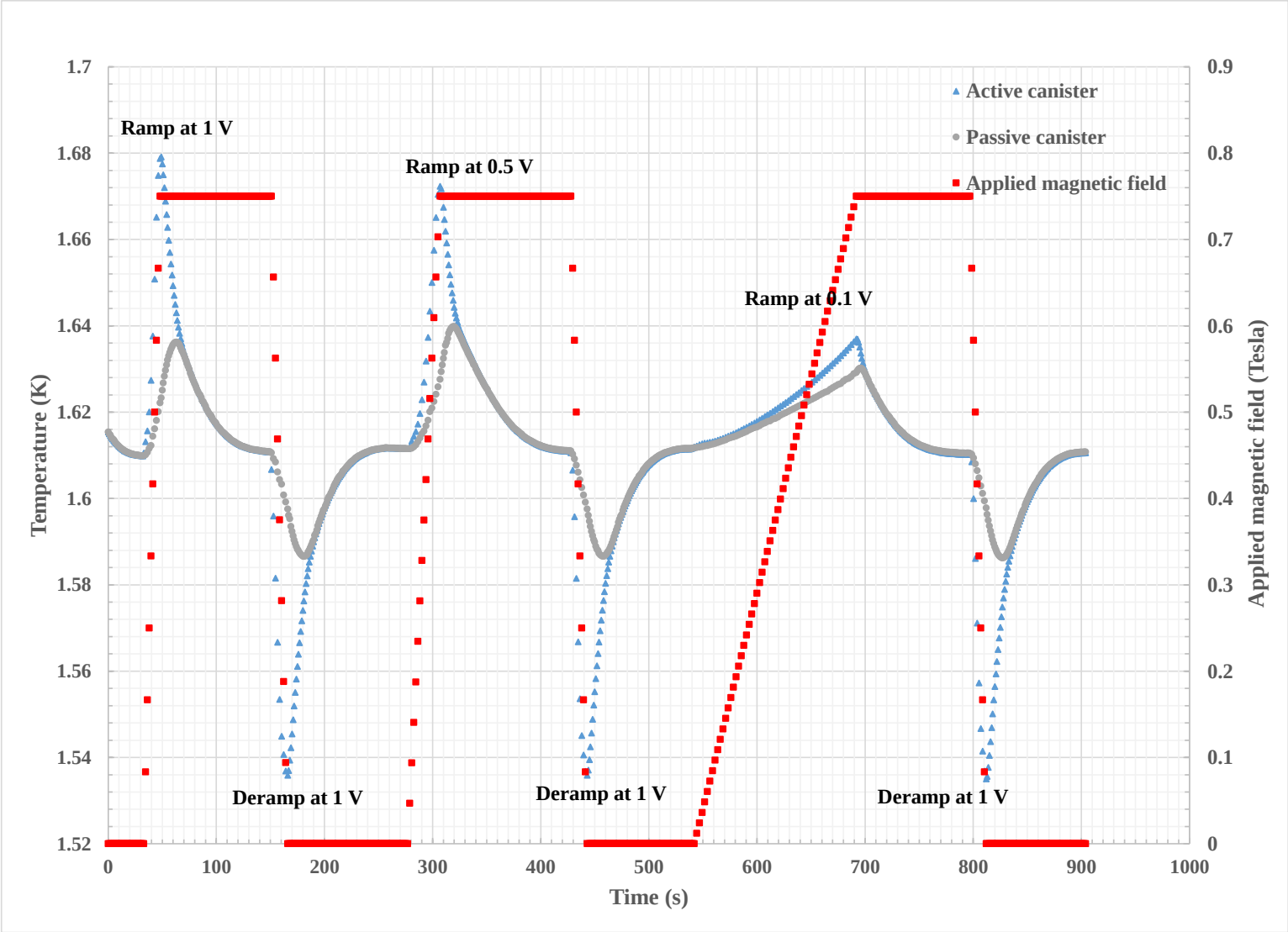

Figure 76. Experimental data for SMP experiment at base temperature of 1.61 K

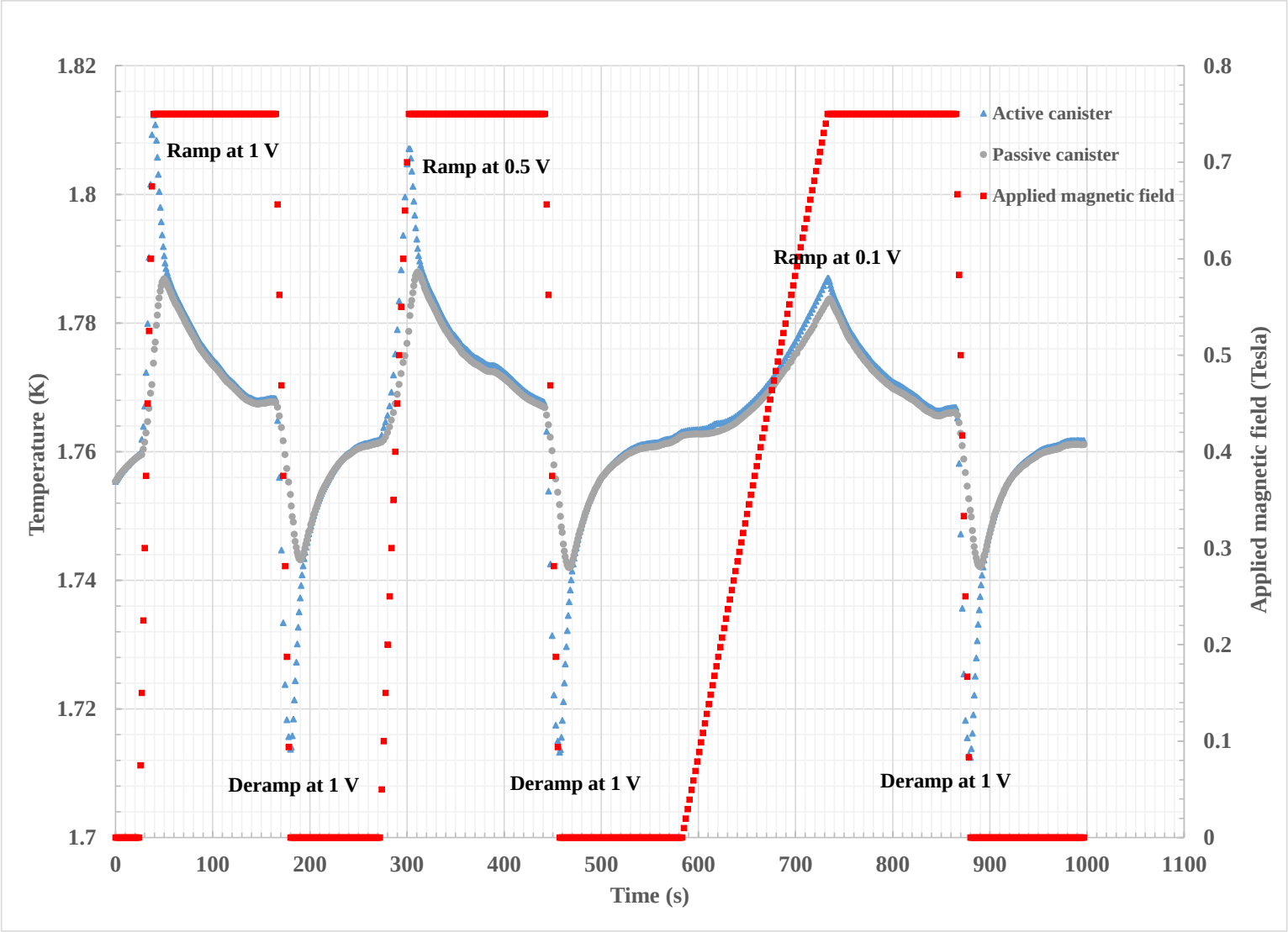

Figure 77. Experimental data for SMP experiment at base temperature of 1.76 K

7.4.2. Temperature amplitude vs. ramp rate

For each run at a particular base temperature, the temperature amplitude was found to decrease as the ramp rate decreased. This indicates that the SMP successfully produced a flow of helium in the circuit. If this were not the case, the temperature amplitude in the canister would be the same regardless of the rate of rise of the applied magnetic field. This is better understood by considering a thought experiment where a thermally isolated canister is closed on both ends. Raising the applied magnetic field on the constituents of the canister at different rates would produce the same temperature amplitude because the added energy is not being carried to other areas due to the canister's thermal isolation.

7.4.3. Canister temperatures vs. base temperature

The temperature between the active and passive canisters appear to approach one another faster for similar ramp rates at higher base temperatures. As discussed earlier in chapter 2, the effective thermal conductivity of He II is a strong function of temperature. At very low temperatures (~ 1 K) the fraction of superfluid well exceeds the normal component. Superfluid cannot carry heat, therefore the effective thermal conductivity of He II is low at low temperatures. This is also true at temperatures close to the lambda point for the opposite reason: the fraction of normal helium well exceeds the superfluid component, thus the scarcity of superfluid helium in this region causes He II to behave more similar to an ordinary fluid from a thermal transport perspective. The highest effective thermal conductivity appears when the fraction of normal and superfluid components are equal. This is because the normal component can carry heat and the superfluid component moves unimpeded to dampen any temperature gradient within He II. This

occurs at approximately 1.9 K. Therefore, the closer a base temperature is to this threshold, the faster the temperature of the two canisters approach one another.

7.5. SMP experiment data analysis

This section describes how the data in the previous section is interpreted to yield meaningful results. This section is divided into five sub sections. The first sub section shows that the SMP met its primary objective of providing flow within the circuit. The second subsection analyzes the data obtained to quantify the mass flow rate produced by the SMP via a simple thermodynamic model. The author also attempts to compare the calibrated mass flow rate data obtained via the venturi flow meter with that obtained through the thermodynamic model. The third subsection details the trends observed between mass flow rate, base temperature, and ramp rates. The fourth subsection presents a pump curve that is useful to comparing the experimental results with the analytical model presented in chapter 4. Finally, the fifth subsection provides an energy-based efficiency for the SMP experimented for this work.

7.5.1. Proof of flow in the SMP circuit

Proof of flow in the SMP circuit was qualitatively and partially discussed in subsection 7.4.2. Another proof of flow can be shown by presenting data from a previous experiment where the active canister was capped on one end and open to the superfluid shut off valve. This setup was identical to the one used for the SMP experiment, except the ports were capped on both sides. Helium was condensed and subcooled to 1.4 K, then the superconducting magnet was charged and the constituents of the canister were magnetized. After magnetization was complete the applied magnetic field was held constant at peak value. As shown in Figure 78, unlike the trends observed in the figures shown on pages 166 through 168, the canister's temperature did not drop rapidly but

rather very slowly over time. This is a confirmation that the temperature drop observed during the isomagnetic flow processes are indicative of flow in the SMP loop.

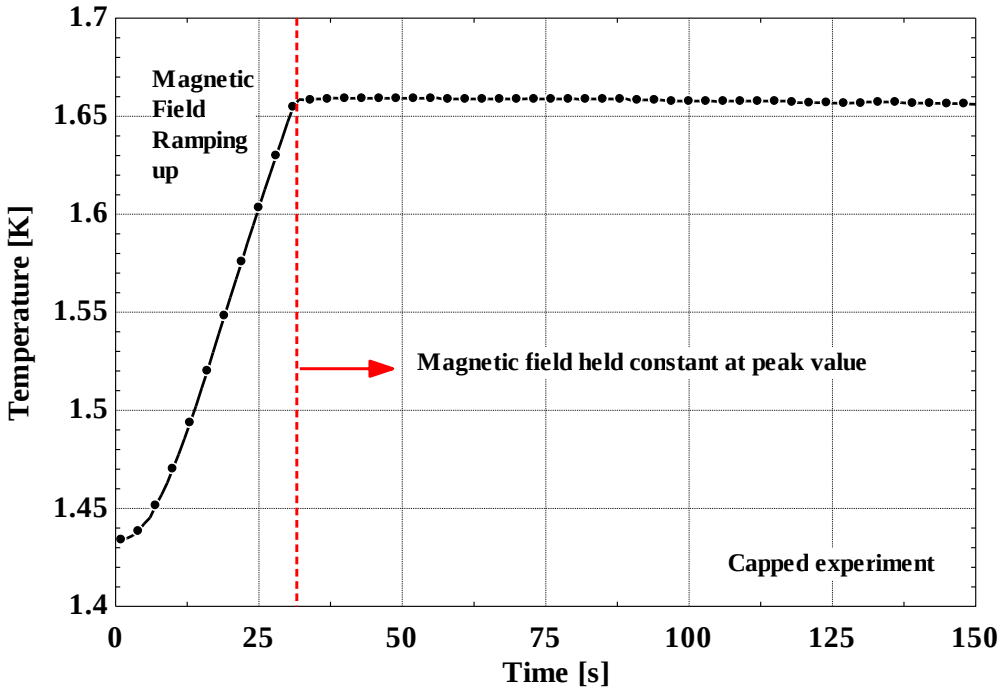

Figure 78. Temperature of the active canister vs. time during a capped experiment.

The author attempted prove that helium must be below the lambda point in order to see a pumping effect in the SMP experiment by raising the temperature of the 1 K heat exchange platform to approximately 3.55 K at the conclusion of the SMP experiment and allowing the canisters to thermally equilibrate with the 1 K pot. Then magnetic field was applied to the constituents of the active canister only to receive to deviation of signal coming from the capacitive pressure transducer as shown in Figure 79: a confirmation that the SMP configuration does not work above the lambda point as expected.

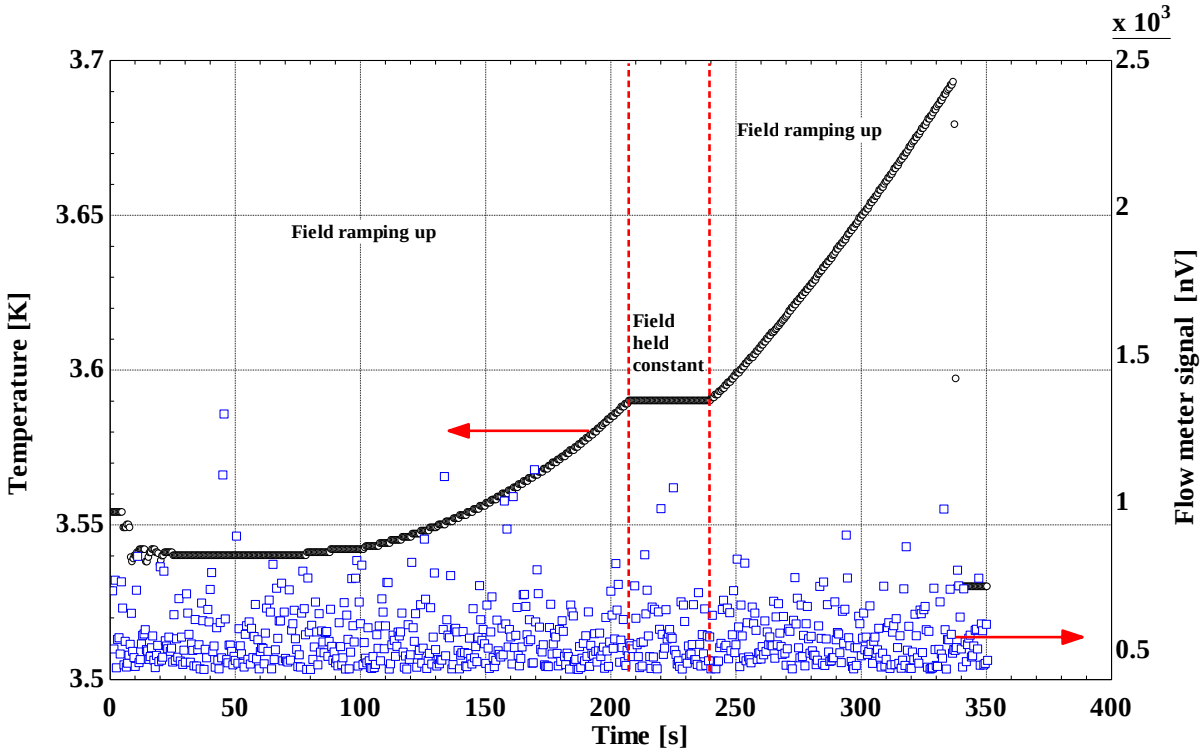

Figure 79. Temperature of the active canister vs. time above the lambda point.

7.5.2. Mass flow rate produced by the SMP

The mass flow rate of helium produced by the SMP can be calculated via a method similar to the one presented in chapter 4. This model uses an entropy balance for the magnetization and isomagnetic flow processes to find the mass displaced from the active canister by using:

$$m_{He,canister}\left(s_{He}\left(T_{j+1}\right)-s_{He}\left(T_j\right)\right)+m_{GGG}\left(s_{GGG}\left(T_{j+1},B_{j+1}\right)-s_{GGG}\left(T_j,B_j\right)\right)+\ldots$$
$$\ldots m_{SS}\int_{T_j}^{T_{j+1}}\frac{c_{SS}\left(T\right)}{T}dT=m_{in}\underbrace{s_{He}}_{=0\ (superfluid)}-m_{out}\,s_{He}\left(\frac{T_{j+1}+T_j}{2}\right) \qquad (106)$$

where $m_{He,canister}$, m_{GGG}, and m_{SS} are the mass of helium entrained in the canister, GGG, and the stainless steel body of the canister respectively, s_{He} and s_{GGG} are the entropy of helium and GGG respectively, and subscript $j+1$ and j denote the final and initial time step respectively. The entropy

of helium leaving the canister is evaluated at an average temperature between the beginning and end of the time step. The entrained masses of helium and GGG as well as the canister are easily determined by knowing the geometrical and packing properties of the active canister. The values for the applied magnetic field and temperatures are directly taken from the raw experimental data. The only unknown left in Eq. (106) is the mass pushed out of the active canister for each time step which is easily calculated by using this equation. The mass flow rate is calculated by dividing the mass pushed out during each step by the time it took for the same step. The mass flow rates obtained via this method are presented in plots shown on pages 175 through 177 for the three base temperatures.

Despite not having a prior calibration for the venturi flow meter, it is possible to analyze the signal obtained from the differential pressure transducer and translate this signal into meaningful data. This was accomplished using a semi-empirical technique: the signal received from the pressure transducer is sorted and processed, then the processed data is mathematically manipulated to match with the mass flow rate obtained via the thermodynamic model discussed earlier in this subsection. The two mass flow rates will be qualitatively compared and if they closely agree with one another then the venturi flow meter is considered to be calibrated for use in similar future experiments.

It was shown earlier in chapter 6 that the relationship between the change in capacitance and a change in the pressure difference follows a linear relationship within the range of the SMP's operation:

$$\Delta P \propto \Delta C \tag{107}$$

The relationship between the change in the pressure transducer's signal on the lock in amplifier and the capacitance is also linear within the range of operation of the SMP:

$$\Delta V \propto \Delta C \tag{108}$$

The density of helium does not change over the range of operation of the SMP thus inspection of Eq. (104) reveals that the mass flow rate in a venturi flow meter is proportional to the square root of the pressure difference:

$$\dot{m} = o\sqrt{o\,\Delta P} = o'\sqrt{\Delta P} \propto \sqrt{\Delta P} \tag{109}$$

where the constants in Eq. (104) are lumped into o .

Combining Eq. (107) and (108) and applying to Eq. (109) yields:

$$\dot{m} = o''\sqrt{\Delta V} \tag{110}$$

where o'' is the constant of calibration determined by dividing the mass flow rate found via the thermodynamic model by the processed data obtained from the venturi flowmeter. The mass flow rates obtained via this semi-empirical calibration method are presented in the plots on pages 175 through 177 for the three base temperatures.

Finally the total mass of helium pushed out of the active canister during each run can be calculated by finding the area under each run's mass flow rate curve. Comparing the total mass pushed out for different runs at the same base temperatures yields the same amount. This is not surprising at all given that the active canister was very well thermally isolated from its surroundings. Note that higher ramp rates yield higher peak values for mass flow rate as expected.

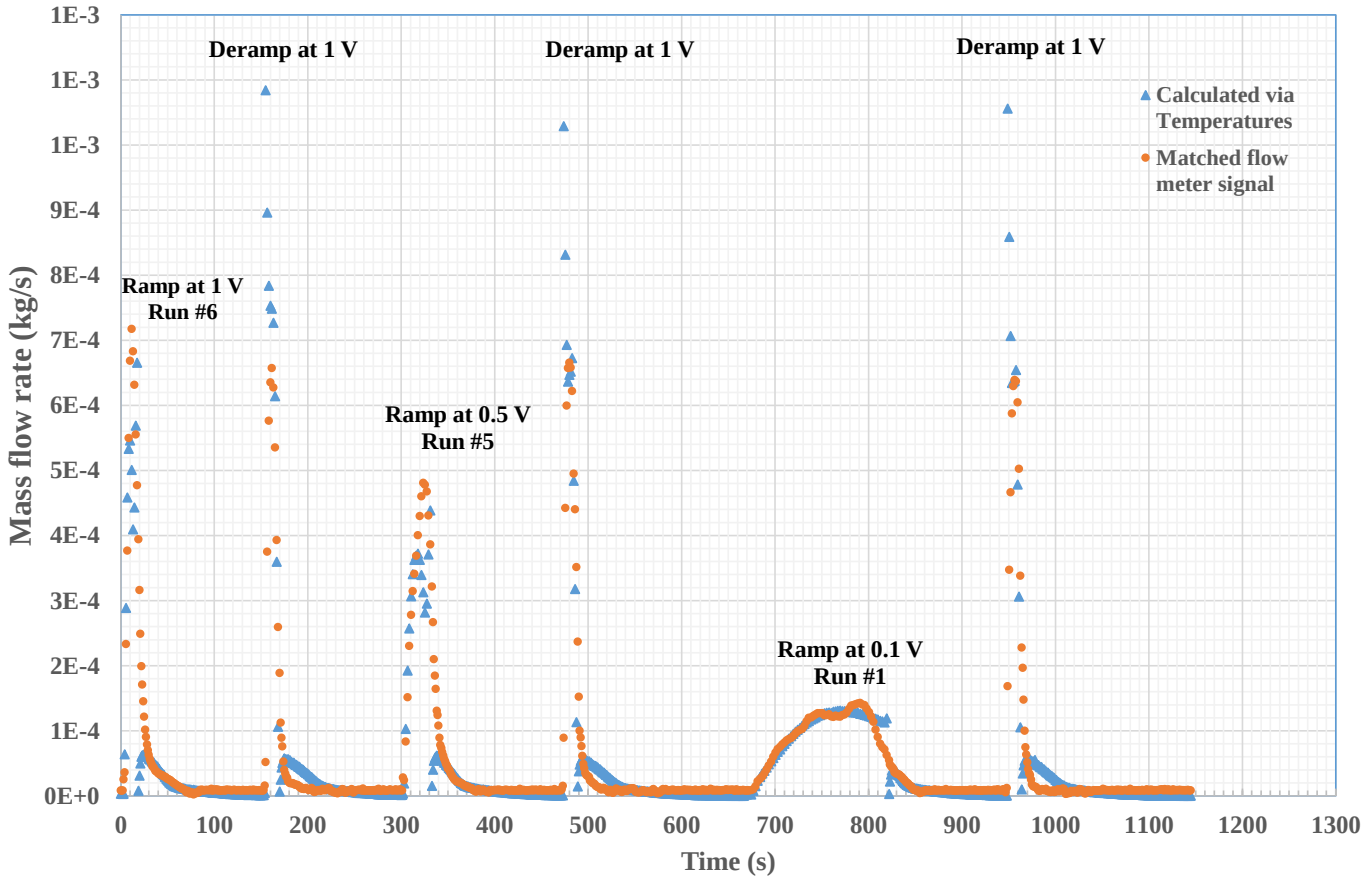

Figure 80. Mass flow rate vs. time for the SMP experiment at base temperature of 1.44 K

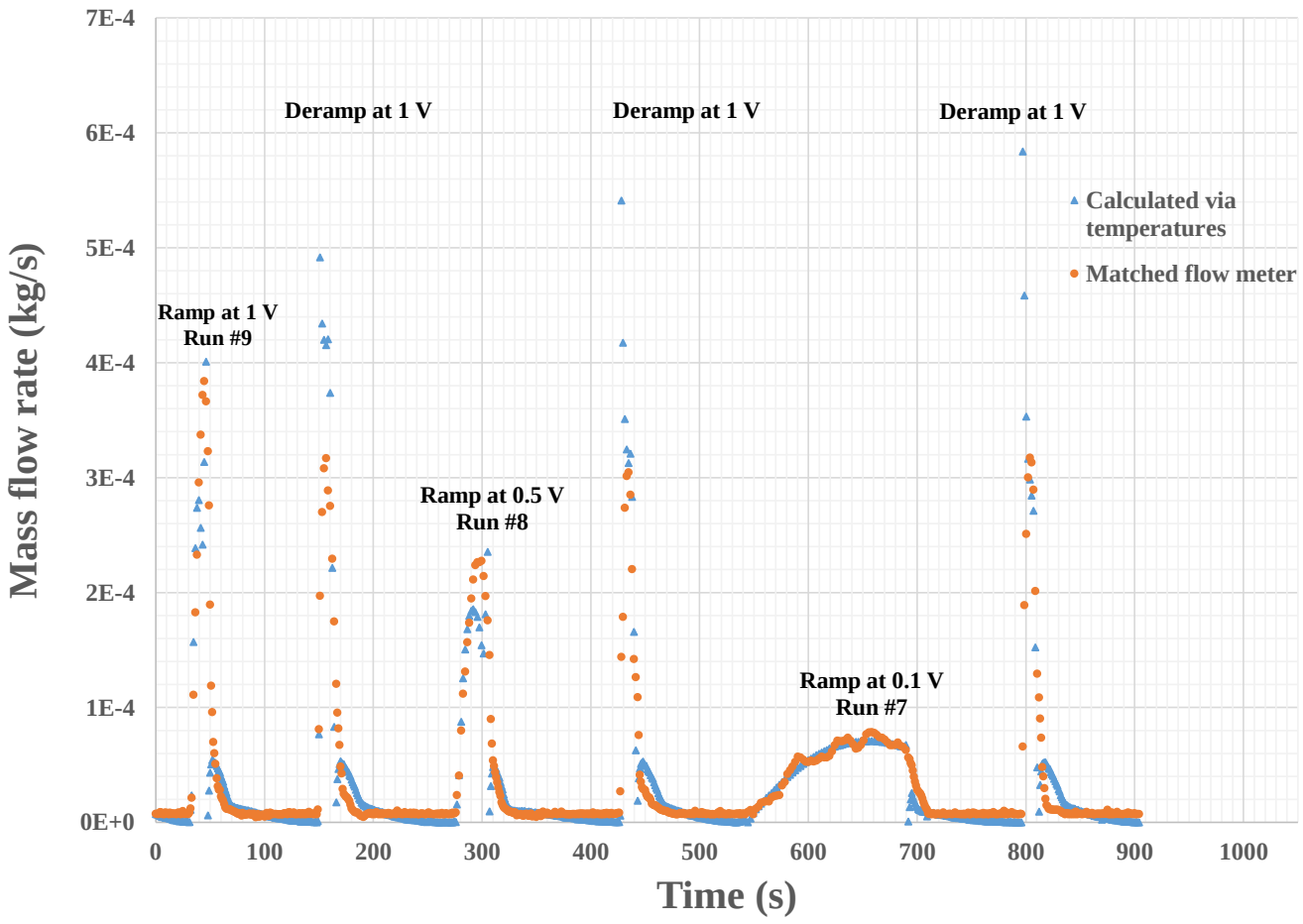

Figure 81. Mass flow rate vs. time for the SMP experiment at base temperature of 1.61 K

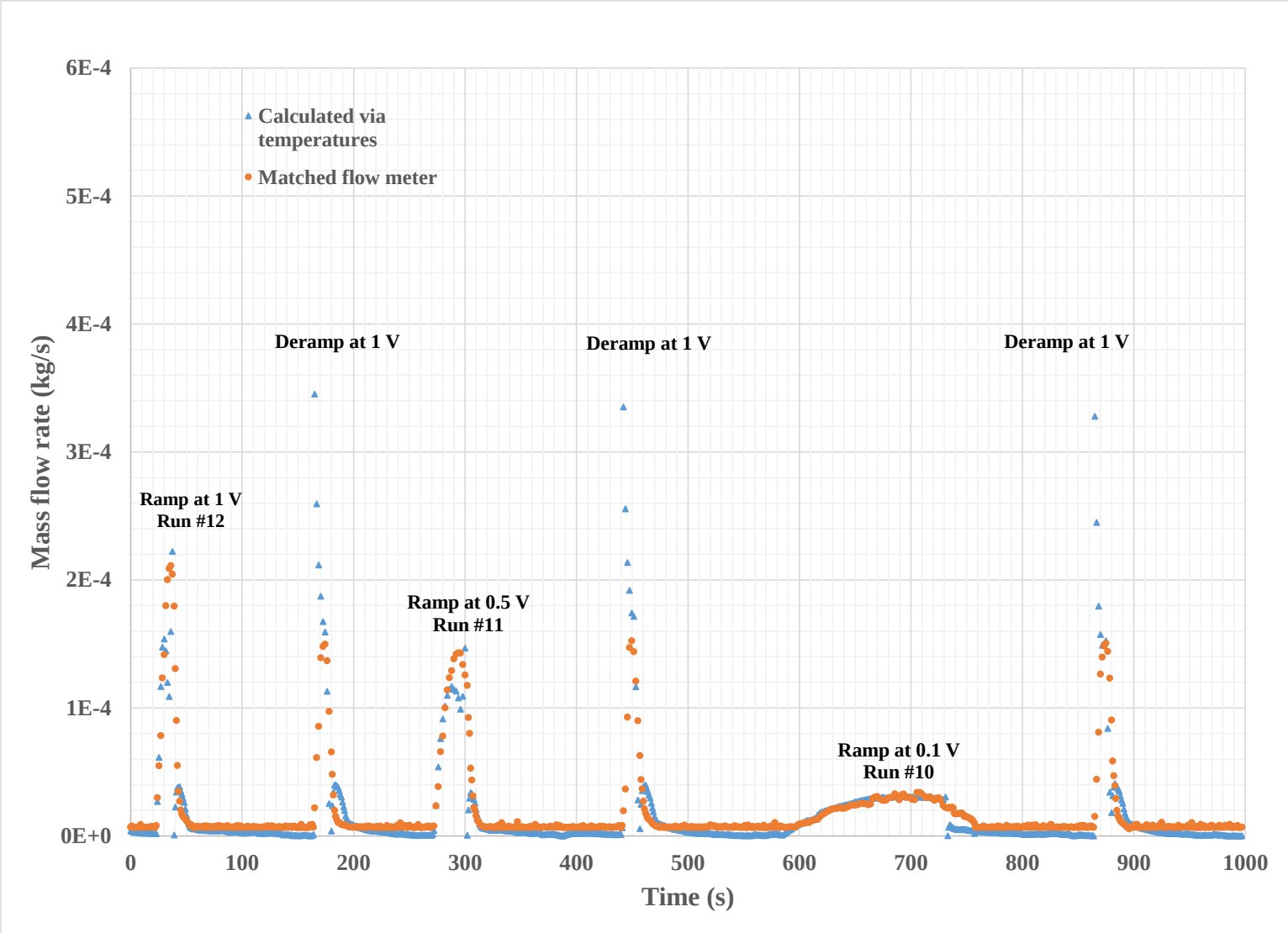

Figure 82. Mass flow rate vs. time for the SMP experiment at base temperature of 1.76 K

7.5.3. Mass flow rate versus ramp rate

The average mass flow rate produced during each run is obtained by integrating the mass flow rate over time and dividing it by the time it took for the flow to stop. Figure 83 shows the experimental results of the averaged mass flow rate as a function of the ramp rate used at three different base temperatures. An obvious trend is observed immediately: the relationship between the mass flow rate produced by the SMP ($\dot{m}_{SMP}$) and the ramp rate (the thermal power generated by the GGG, $\dot{Q}_{GGG}$) is completely linear for each base temperature (T_{base}). This is expected because the superleak was sized to avoid superfluid turbulence within the range of operation of the SMP. Using a traditional thermomechanical pump, Nakai et. al. (1996) experimentally verified that the relationship between mass flow rate and heater input is completely linear and matches with theoretical predictions presented by Eq. (54) for lower heat inputs while data points deviated from this behavior at higher values of heat input due to the creation of superfluid vortices in the superleak as a result of higher mass flow rates produced by the pump.

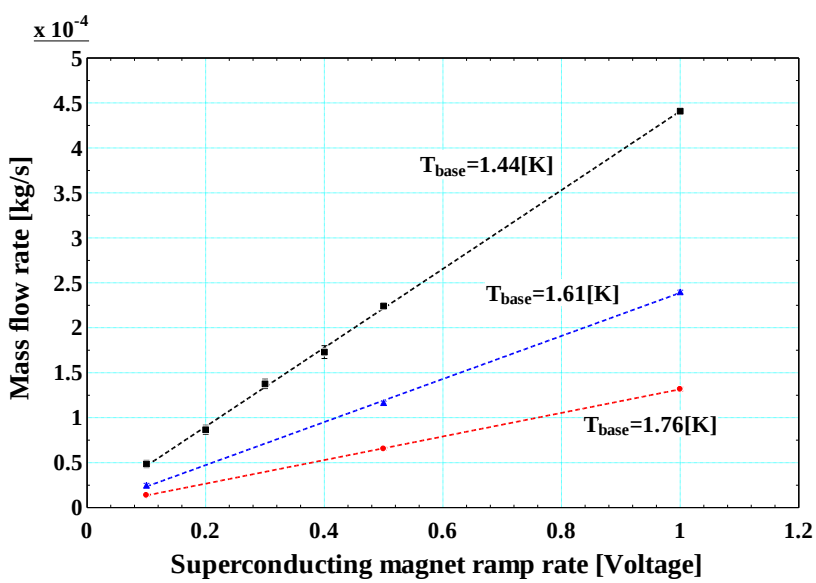

Figure 83. Mass flow rate produced by the SMP as a function of superconducting magnet ramp rates for three base temperatures. Note: error bars are very small.

The data from Figure 83 is fitted to a third degree polynomial to yield a correlation for the mass flow rate produced by the SMP:

$$\dot{m}_{SMP} = V_{scm}\left(0.001316\,T_{base}{}^{3} - 0.004928\,T_{base}{}^{2} + 0.004673\,T_{base}\right) \tag{111}$$

where V_{SCM} is the sourced voltage for the superconducting magnet and T_{base} is the base temperature. Note that this correlation only applies to the specific SMP and fluid circuit used for this work. Reconfiguring or changing any components of the SMP loop will yield a different correlation. Thus this correlation can only be used as an approximate guide to scaling for other systems using the SMP technology. The merit of this correlation is investigated next.

The heat transfer from GGG particles into the helium can be found by using the experimental data and applying the following equation to each time step:

$$Q_{GGG,step} = m_{GGG}\left(\left.\frac{\partial s}{\partial B}\right|_{\frac{T_{j+1}+T_j}{2}}\left(B_{j+1}-B_j\right) + \left.\frac{\partial s}{\partial T}\right|_{\frac{B_{j+1}+B_j}{2}}\left(T_{j+1}-T_j\right)\right)\frac{T_{j+1}+T_j}{2} \tag{112}$$

The heat transfer is summed and averaged over the run time to yield the averaged heater power for each run:

$$\dot{Q}_{GGG} = \frac{Q_{GGG}}{\Delta t_{run}} \tag{113}$$

Using Eq. (54) for an ideal fountain effect pump and approximating the temperature of helium leaving the active canister as the base temperature yields:

$$\underset{\propto ramp\ rate}{\dot{Q}_{GGG}} = \dot{m}_{SMP}\ s\left(T_{out}\right)T_{out} \cong \dot{m}_{SMP}\ s\left(T_{base}\right)T_{base} \tag{114}$$

It is now possible to test the merit of the correlation presented by Eq. (111) by applying the averaged heat transfer rate from GGG to helium found experimentally and calculating the mass flow rate produced by the SMP. The calculated mass flow rate and the experimental results are compared in Figure 84. This plot shows that the correlation deviates from experimental results at lower base temperatures and higher ramp rates. This is because the assumption that helium leaves the active canister at the base temperature is not very accurate as the temperature rise in the active canister increases at lower base temperatures and higher ramp rates.

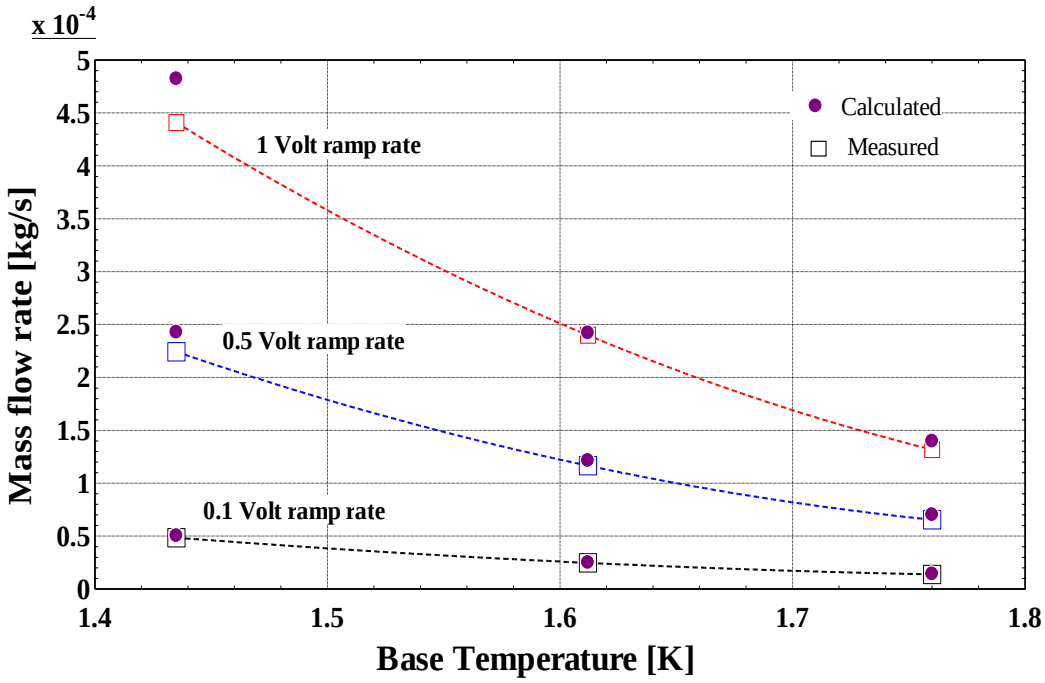

Figure 84. Mass flow rate produced by the SMP as a function of base temperature for three ramp rates.

Naturally higher ramp rates yield higher mass flow rates produced by the SMP because the heat transfer rate is higher. The mass flow rate increases as the base temperature decreases. This behavior is expected since the entropy of helium decreases as base temperature decreases.

Inspection of Eq. (114) reveals that mass flow rate must increase to compensate for a decrease in the helium's entropy and temperature at similar heat transfer rates.

7.5.4. Pump curves for the SMP

Typically the proper pump for a particular application is selected by utilizing the system curve and pump performance curve. A system curve is unique to every individual fluid circuit: it describes the head (pressure) required to maintain fluid flow in a pipe system due to static, minor, and major losses. A pump performance curve is unique to every individual pump: it describes the head it can produce to meet a certain fluid flow rate. The intersection of these curves on a head vs. flow rate diagram determines the operating point of a particular pump-circuit system.

Unfortunately determining a system curve for a fluid loop with He II is not a straightforward task. However a pump performance curve for an SMP can be generated by using the concepts presented in chapter 4 and the operating points are overlaid using the data obtained through the SMP experiment.

Using an ideal SMP, the difference in temperature between the base level and the temperature at the end of the adiabatic magnetization process results in a rise in the fountain pressure. This pressure difference is used to generate the pump performance curves seen in Figure 85 through Figure 87. The operating points are those obtained through the actual experiment. The fountain pressure difference between the active and passive canisters is calculated from the experimental data. The experimental pressure difference and mass flow rate for every individual run is overlaid on the pump performance curve. Note that the SMP is analogous to a variable speed pump, different ramp rates produce different curves on the pressure difference vs. mass flow rate plots. Also unlike traditional pumps, the SMP pump curves vary for different base temperatures.

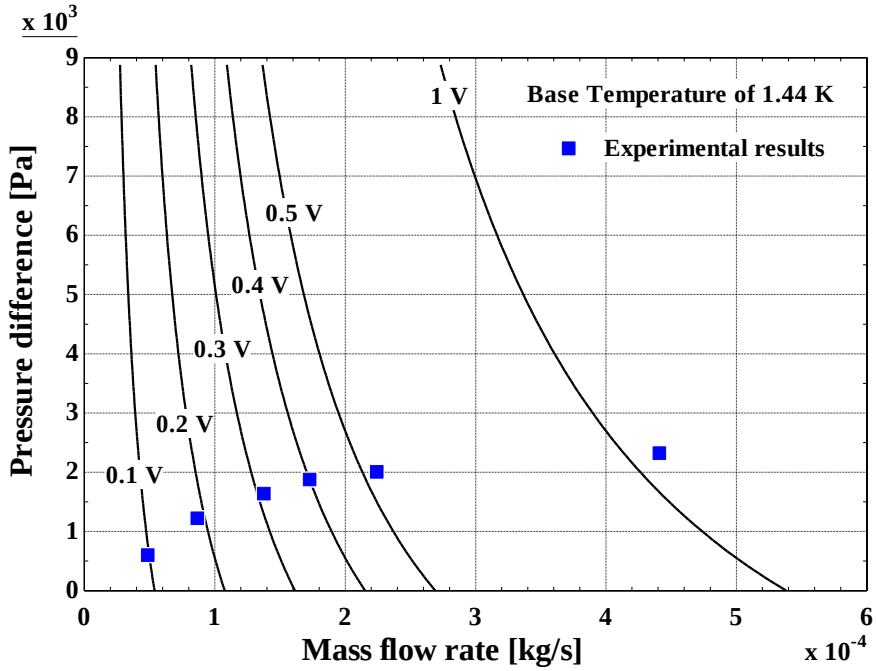

Figure 85. SMP pump curve at a base temperature of 1.44 K

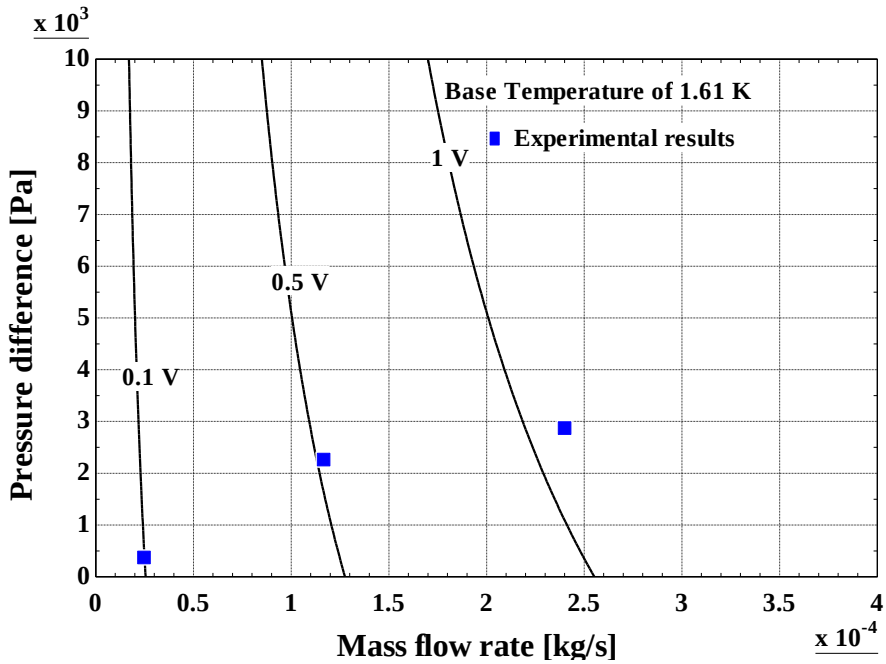

Figure 86. SMP pump curve at a base temperature of 1.61 K

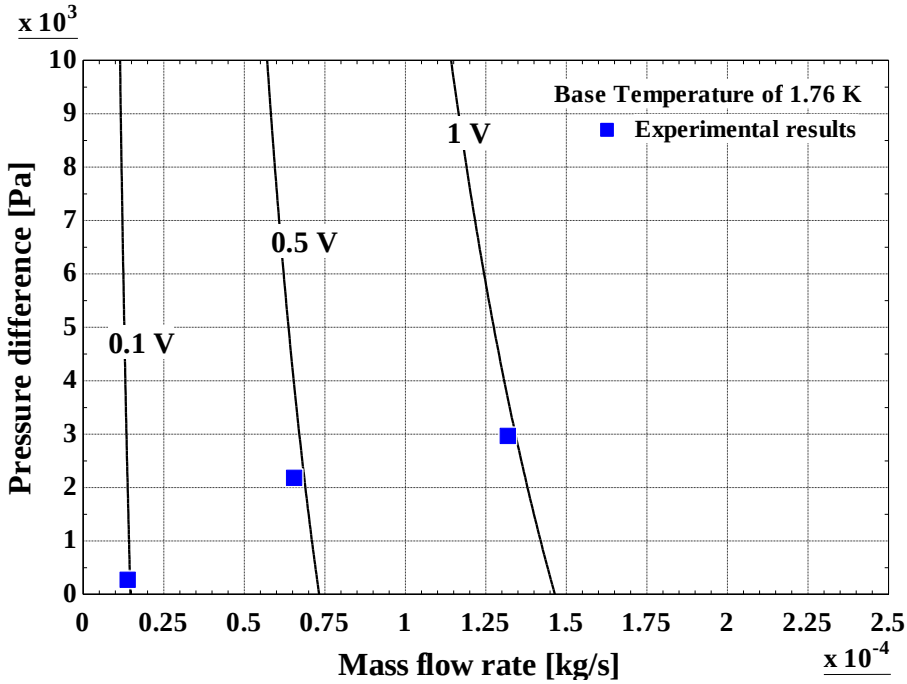

Figure 87. SMP pump curve at a base temperature of 1.76 K

7.5.5. SMP's energy efficiency

An energy efficiency is defined for pumps operating based on the fountain effect by Rivetti (1993) and Van Sciver (1990) by dividing the fluid power the pump produces by the heat transfer rate into He II as:

$$\eta_{FEP} = \frac{\overbrace{\dfrac{\dot{m}\,\Delta P}{\rho}}^{Energy\ out}}{\underbrace{\dot{Q}}_{Energy\ in}} \tag{115}$$

Experimental values of energy efficiency for the SMP are shown in Figure 88. This figure shows that higher ramp rates and lower temperatures resulted in highest energy efficiencies, while lower ramp rates and higher temperatures produced the opposite. This is expected because higher ramp rates produced a higher mass flow rate and pressure difference while lower ramp rates produced small mass flow rates and low pressure differences between the two canisters. As can be seen from

the plot, the energy efficiency is expected to reach a plateau at higher ramp rates. In fact at very high ramp rates, not shown in the plots, the efficiency is expected to drop as a result of the mass flow rate deviating from the ideal state due to superfluid turbulence in the superleak.

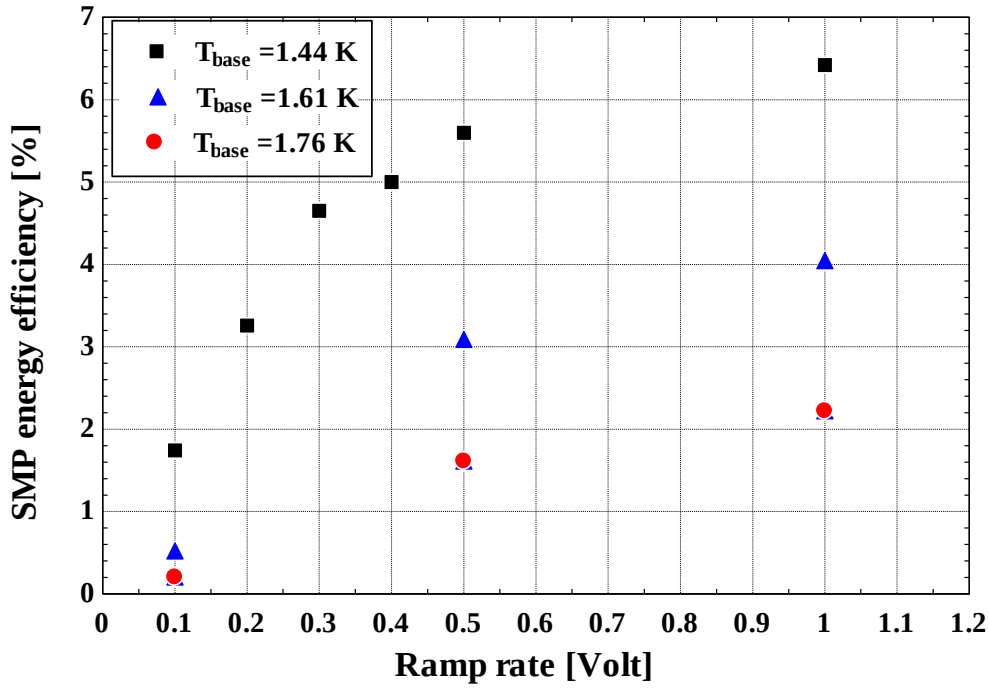

Figure 88. Energy efficiency of the SMP as a function of ramp rate at three base temperatures.

7.6. Summary of results

Experimental results from the previous sections show that the SMP operated successfully and its performance was close to ideal. The most important results from the SMP experiment are listed in Table 16.

Run number	Base temperature (K)	Ramp rate (mTesla/s)	Mass flow rate (mg/s)	Fountain pressure (Pa)	Heat transfer rate (mW)	Efficiency (%)
1	1.44	5	48.52	600	11.36	1.743
2	1.44	10	86.55	1221	22.06	3.259
3	1.44	15	137.6	1638	32.96	4.651
4	1.44	20	173.0	1876	44.15	5.001
5	1.44	25	224.2	2006	54.64	5.598
6	1.44	50	440.9	2323	108.5	6.421
7	1.61	5	24.7	374	12.02	0.5528
8	1.61	25	116.6	2265	58.15	3.09
9	1.61	50	239.9	2872	115.8	4.047
10	1.76	5	13.78	271	12.24	0.2075
11	1.76	25	65.47	2181	60.14	1.615
12	1.76	50	131.8	2968	119.6	2.225

Table 16. Summary of SMP experimental results

7.7. References

Maytal, B., J. A. Nissen, and S. W. Van Sciver. "Interaction of He II transfer line and fountain effect pump." *Cryogenics* 30.11 (1990): 930-934.

Nakai, Hirotaka, et al. "Superfluid helium flow through porous media."*Cryogenics* 36.9 (1996): 667-673.

Rivetti, A., et al. "Testing methods and performance of IMGC fountain effect pump." *Cryogenics* 33.4 (1993): 443-448.

8. Conclusions and future work

This chapter presents the main conclusions drawn from this work. It then summarizes a list of potential future work and improvements that could be made for future SMP experiments. Finally the application of the SMP in a much larger scope is presented as future potential work.

8.1. Summary/conclusions

This work detailed the modeling, development, and experimental validation of a proof of concept Superfluid Magnetic Pump with no mechanical moving parts that could potentially be used in various sub Kelvin refrigerators that operate with a mixture of ^{3}He-^{4}He as their refrigerant. The SMP could also be used as a circulator of He II for applications where temperature uniformity of objects/surfaces is necessary. Examples of the latter include cooling of large superconducting magnets, cooling of radiation shields, and cooling of sensitive detectors that operate in sub Lambda temperatures.

The SMP presented in this work is the first device to use the thermodynamic coupling which exists in a paramagnetic material and a liquid at sub Lambda temperature simultaneously. This was achieved by exploiting some of the remarkable properties of He II, specifically those pertinent to the superfluid helium component such as zero entropy and zero viscosity. A paramagnetic material was used to heat and cool the surrounding liquid helium in the canisters via the application of a magnetic field. This elevation of temperature in He II results in an increase of the pressure due to the fountain effect. Once a potential gradient is established in the fluid loop (pressure difference) flow of He II commences. This enables the SMP to be free of any moving mechanical parts.

The operation of the pump was described through a simple thermodynamic model. This model allowed the author to gain a significant insight into the design and implementation of the actual SMP experiment. It detailed the two limits of operation of the SMP making this device suitable for use either as a pure circulator or as a compressor.

An application of the SMP was considered by describing a sub Kelvin Active Magnetic Regenerative Refrigerator that uses a mixture of ^{3}He-^{4}He as its refrigerant. A qualitative description of one cycle operation of this refrigerator was presented followed by a detailed model of such refrigeration system that could lift 600 μW of heat at 850 mK. A 1 dimensional transient numerical model was primarily used to predict the regenerator's performance, as the heart of the system, for this type refrigerator. Thus an SMP was theoretically put to test and validated for use in a sub Kelvin refrigerator via this model.

The construction and assembly of various components involved in the SMP experiment were also described. This discussion included the design and construction of superconducting magnets, a very delicate task that required the author several trials at various stages of construction to succeed. IT detailed the construction procedure for the canisters, the superleak, superfluid shut-off valve assembly, and flow metering device for He II at low temperatures. Many valuable lessons were learnt by the author. The goal was to convey these techniques to readers that are involved in the continuation of this project.

Finally the SMP was put to test. The components were built and assembled. The experiment was designed and the system was cooled down and tested to prove that it can provide a flow of He II. The author successfully demonstrated that not only did the SMP qualitatively and adequately operate, but it proved to work very close to ideal when compared to theoretical models presented in chapter 4.

Some of the important highlights and conclusions are listed below:

- A simple model was used to predict the performance of the SMP. This model uses the application of the second law of thermodynamics by considering entropy generation rates to be negligible for the system described in this work. Thus the SMP system was theoretically proven to operate nearly reversibly.
- A model for a sub Kelvin AMRR was developed and theoretically proved that replacing traditional bellows-piston compressors with the SMP could in fact help the refrigerator to provide very low temperatures.
- The superconducting magnet leads must be anchored thermally very well otherwise any free length of the superconducting lead that is not thermally sunk could potentially cause the leads to burn out due to a rapid lead quench.
- The superconducting magnet construction proved to require patience, meticulosity, and detailed panning. The techniques used in constructing the second superconducting magnet proved to be extremely valuable. The magnet in fact worked for several times but unfortunately the author was only later informed from colleagues that the diodes must be potted using the same epoxy as that used in the windings of the magnet.
- A differential pressure transducer was originally built with brass diaphragms. Brass was shown to be susceptible to microyielding at low temperatures. Advice was taken form Prof. Brisson at MIT to use Beryllium-Copper diaphragms instead. The latter type transducer proved to work reliably at low temperatures.
- Calibration of the venturi flow meter in an open system proved to be a difficult task. The open system did not allow for a stable reading of the mass flow rate resulting from constant liquid percolations, and coalescing at low temperatures. Thus a closed system would be

necessary to accurately calibrate the flow metering system prior its use. However the author attempted to use a semi-empirical technique to calibrate the flow meter during the SMP experiment.

- The SMP proved to work ideally and its performance matched with theory. Some expected trends were observed from the experimental data which included higher mass flow production at higher ramp rates and lower temperatures.
- The SMP experiment showed that the relationship between ramp rate and mass flow rate at constant base temperatures was linear. This proved that no superfluid turbulence was detected in the superleak, thus allowing the SMP to work ideally as designed.
- A series of pump curves were generated for the SMP and experimental results were compared to locate the operating points on these curves.
- The SMP's energy efficiency was calculated via the experimental results. As expected, a higher ramp rate and lower temperature resulted in the highest values for efficiency.
- One of the greatest advantages of the SMP as opposed to traditional fountain effect pumps is its ability to heat and cool He II by magnetizing and demagnetizing the GGG-filled canisters. This capability allows the SMP to operate nearly reversible.

8.2. Future work

The last section of this document is divided into three brief subsections. The first subsection suggests an experiment where the second canister also participates in the operation of the SMP. The second subsection suggests using a mixture of ^{3}He-^{4}He as the fluid for a future SMP experiment. Finally the third subsection proposes the use of the SMP in sub Kelvin refrigerators.

8.2.1. Second canister and superconducting magnet

It was noted earlier that due to an unfortunate and unforeseen error in the construction of the second superconducting magnet, it failed to operate prior to the actual SMP experiment for this work. The author suggests going through the construction procedure for a superconducting magnet presented in this document and building a new magnet. It is of great importance and benefit to design the second magnet in such a way to minimize its inductance in order to match its performance with the first superconducting magnet. Then the combination of the first and second canisters can be used in a future SMP experiment to validate the performance of the tandem SMP and to get it one step closer to its potential use in a sub Kelvin refrigeration system. The experiment can be design to include two absolute pressure transducers, each connected to a pressure tap close to the non superleak port of the canisters to experimentally measure the pressure difference between the two canisters. This method will provide a more accurate mapping of the pump curve for the SMP. Finally the system can run under various operational conditions with pure ^{4}He including symmetrical and asymmetrical ramping of the two superconducting magnets.

8.2.2. ^{3}He-^{4}He test

Another important step towards the SMP's validation for use in ^{3}He-^{4}He based sub Kelvin refrigerators is to experimentally verify its performance with a mixture of helium. Due to its limited national supply He is not only very costly to procure but it also requires obtaining an approval from the U.S. Department of Energy. The author helped coordinating and planning the procurement of a limited supply of ^{3}He. This He supply could enable students to test the SMP with a mixture of ^{3}He and ^{4}He. The SMP cycle can run under various conditions including but not limited to using different concentrations of ^{3}He through the system. An extensive performance

map for the SMP can be obtained via this method that could prove to be of great value for use in the design of helium mixture based sub Kelvin refrigeration systems that use the SMP as its circulator/compressor.

8.2.3. AMRR, SPTR, and CCDR

Three primary sub Kelvin refrigerators, each with a unique design, are selected to use the SMP as their circulator/compressor: An Active Magnetic Regenerative Refrigerator (AMRR), Superfluid Pulse Tube Refrigerator (SPTR), and Cold Cycle Dilution Refrigerator (CCDR).

The AMRR will use the SMP as a circulator; No significant pressure rise is required to drive the fluid around the loop. A model of the AMRR was provided in this work as the primary example of a system that could greatly benefit from the SMP's use. One potential issue with systems of this type however, is the existence of a lower limit of minimum temperature this system can achieve. This is because the refrigerator halts once the concentration and temperature coincide with the separation line. This issue can be potentially remedied by cascading the regenerator and coupling two or three regenerators that use slightly different concentration of ^{3}He. Doing so could extend the range of operation of the AMRR to lower temperatures (staircase approach to raising concentration and lowering temperatures).

The SPTR is less straightforward to theoretically model when compared to the AMRR. However an SPTR that uses a bellows-piston compressor on the warm side of the refrigerator has been previously successfully demonstrated at MIT and Los Alamos National Labs (LANL). Systems of this type proved to operate at temperatures as low as 250 mK. Thus replacing the existing compressor in this system with the SMP will free up the entire system from any mechanical moving parts, making it an attractive choice for use in space science missions.

Lastly, the CCDR is of great interest to the space science detector community because it has the ability to provide the lowest temperatures, in fact temperatures lower than existing ADRs (5 to 7 mK). This type refrigerator uses a closed cycle to circulate ^{3}He in an inert background of superfluid ^{4}He. This system has been successfully modeled by Bryant Mueller and it theoretically showed to work well with the SMP as its circulator. However this system will need to use a series of check valves to make the fluid flow produced by the SMP unidirectional. This could add to the complexity of this type refrigerator and unfortunately a check valve capable of delivering the needs of the CCDR has not yet been successfully tested.

Appendix

Appendix A

Derivation of the magnetic field for any point along the axis of a solenoid:

The magnetic field at any point along the axis of a tightly wound solenoid (helical coil) consisting of *n* turns per unit length wrapped around a cylindrical tube (mandrel) is calculated for the superconducting magnet in this subsection. The analysis begins by finding the magnetic field along the axis of a single loop of wire and then using the principle of superposition to generalize this field to a tightly wound solenoid.

The magnetic field a distance *h* above the center of a single circular loop of radius *R* is derived by applying the Biot-Savart law to the schematic shown in Figure 0-1:

$$d\vec{B}(h) = \frac{\mu_0 \, I}{4\,\pi} \frac{d\vec{l} \times \lambda}{\lambda^2} \tag{A1}$$

where μ_0 is the permeability of free space (4π x 10^{-7} N/A^2), *I* is the current in the circular loop, λ and λ are the unit vector along the direction and magnitude of the vector $\vec{\lambda}$ respectively. The vectors λ and $d\vec{l}$ are always perpendicular to one another along the circular loop therefore the magnitude of the cross product of these two vectors is:

$$\left|d\vec{l} \times \lambda\right| = \left|d\vec{l}\right|\left|\lambda\right|\sin\left(\frac{\pi}{2}\right) = \left|d\vec{l}\right| = dl \tag{A2}$$

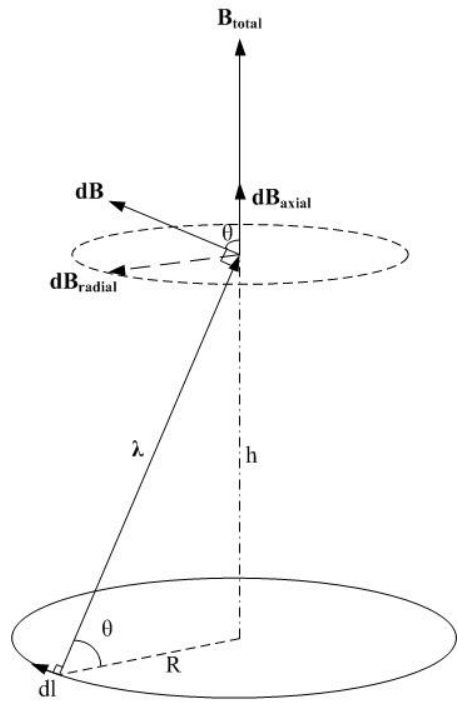

Figure 0-1 Magnetic field a distance h above the center of a single circular loop carrying current *I*

Each point along the circular loop contributes a differential element to the total magnetic field at a distance *h* above the center of the circular loop. It can be seen from Figure 0-1 that radial contributions of magnetic field from all the points on the ring cancel due to symmetry and all there is remained are the axial components of magnetic field from each point. Therefore the total magnetic field is:

$$\vec{B}_{total} = \int_{along\ loop} d\vec{B} \cos\theta \tag{A3}$$

applying Eqs. (A3) and (A2) to Eq. (A1) yields:

$$B_{total} = \frac{\mu_0\ I}{4\ \pi} \int \frac{dl \cos\theta}{\lambda^2}\ h \tag{A4}$$

where h is a unit vector along the direction of vector h. The λ^2 and the cosine terms are constants in this case therefore Eq. (A4) is rewritten as:

$$B_{total} = \frac{\mu_0 I}{4\pi} \frac{\cos\theta}{\lambda^2} \int dl\, h = \frac{\mu_0 I}{4\pi} \frac{\cos\theta}{\lambda^2} 2\pi R\, h = \frac{\mu_0 I}{2} \frac{R^2}{\left(R^2 + h^2\right)^{3/2}} h \tag{A5}$$

Now consider a tightly wound solenoid with n turns of wire per unit length as shown in Figure 0-2:

$$n = \frac{N_{turns}}{L} \tag{A6}$$

where N_{turns} is the number of total turns, and L is the axial length of the solenoid.

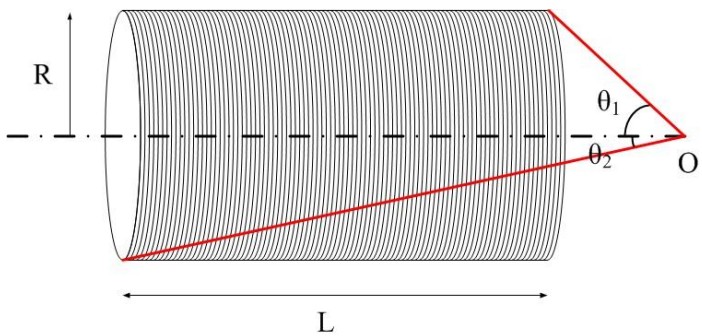

Figure 0-2 A tightly wound solenoid with *n* turns per unit length, magnetic field is calculated along the axis of the solenoid at arbitrary points

A solenoid is the product of superimposing single circular loops along their axes. Therefore the magnetic field at any point along the axis of the solenoid can be found by considering a differential segment of the solenoid dz as shown in Figure 0-3 and applying the result found in Eq. (A5) where I is replaced by ($n.I.dz$):

$$dB = \frac{\mu_0 \left(n\, I\, dz\right)}{2} \frac{R^2}{\left(R^2 + z^2\right)^{3/2}} \hat{z} \tag{A7}$$

This equation can be written in integral form as:

$$B = \frac{\mu_0\, n\, I}{2} \int \frac{R^2}{\left(R^2 + z^2\right)^{3/2}}\, dz\, \hat{z} \tag{A8}$$

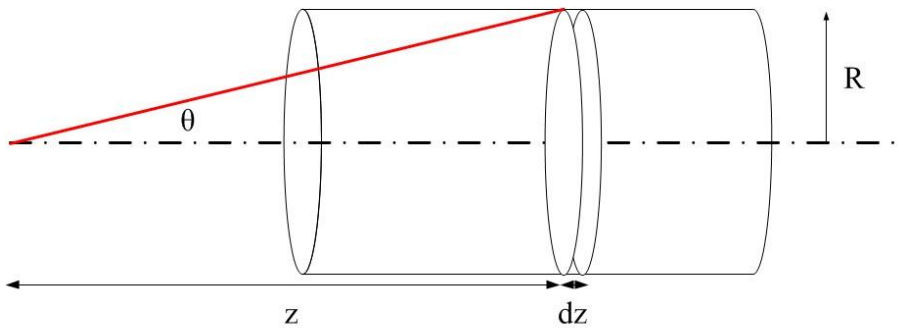

Figure 0-3 Differential segment of the solenoid

realizing that:

$$z = R\frac{\cos\theta}{\sin\theta} = R\cot\theta \tag{A9}$$

differentiation of variable z with respect to angle θ yields:

$$dz = -\frac{R^2}{\sin^2\theta}\, d\theta \tag{A10}$$

applying the result of Eq. (A10) to Eq. (A8) yields:

$$B = \frac{\mu_0\, n\, I}{2} \int_{\theta_1}^{\theta_2} (-R) \frac{R^2 \sin^3\theta}{R^3 \sin^2\theta}\, d\theta\, \hat{z} = -\frac{\mu_0\, n\, I}{2} \int_{\theta_1}^{\theta_2} \sin\theta\, d\theta\, \hat{z} = \frac{\mu_0\, n\, I}{2} \left(\cos\theta_2 - \cos\theta_1\right) \hat{z} \tag{A11}$$

according to the diagram shown in Figure 0-4 if the point along the axis of the solenoid is within the solenoid then the cosine terms of Eq. (A11) can be written as:

$$\cos\theta_1 = -\sin(\theta_1 - \frac{\pi}{2}) = -\frac{x_1}{\sqrt{x_1^{\,2} + R^2}} \tag{A12}$$

and,

$$\cos\theta_2 = \frac{x_2}{\sqrt{x_2^2 + R^2}} \tag{A13}$$

where,

$$L_{coil} = x_1 + x_2 \tag{A14}$$

and if the point is outside the solenoid then:

$$\cos\theta_1 = \frac{x_1}{\sqrt{x_1^2 + R^2}} \tag{A15}$$

and,

$$\cos\theta_2 = \frac{x_2}{\sqrt{x_2^2 + R^2}} \tag{A16}$$

Where,

$$\begin{cases} L_{coil} = x_2 - x_1 & if\ outside\ of\ solenoid\ and\ to\ the\ right \\ L_{coil} = x_1 - x_2 & if\ outside\ of\ solenoid\ and\ to\ the\ left \end{cases} \tag{A17}$$

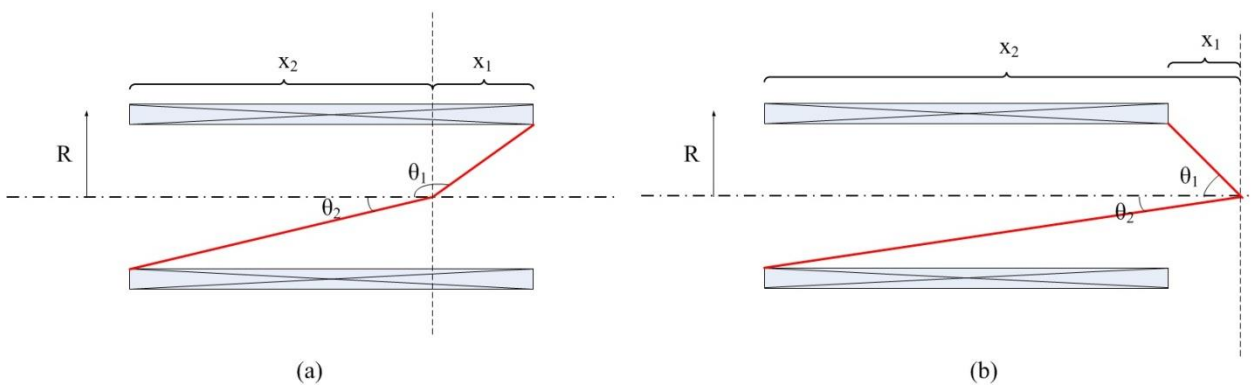

Figure 0-4 Diagram of solenoid in two situations (a) the point along the axis of the solenoid is within the solenoid (b) the point along the axis is outside the solenoid

An expression for the magnetic field along the axis of a solenoid can be obtained by using the result of Eq. (A11) and combining Eqs. (A12), (A13), and (A14) for points within the solenoid:

$$\boxed{B_{axis,inside} = \frac{\mu_0\ n\ I}{2}\left[\frac{x_2}{\sqrt{x_2^2+R^2}} + \frac{L_{coil}-x_2}{\sqrt{\left(L_{coil}-x_2\right)^2+R^2}}\right]} \tag{A18}$$

An expression for the magnetic field along the axis of a solenoid is obtained for points outside of the solenoid by using the result of Eq. (A11) and combining Eqs. (A15), (A16), and (A17):

$$\boxed{B_{axis,outside} = \frac{\mu_0\ n\ I}{2}\left[\frac{x_2}{\sqrt{x_2^2+R^2}} - \frac{x_2 \pm L_{coil}}{\sqrt{\left(x_2 \pm L_{coil}\right)^2+R^2}}\right] \quad where \begin{cases} + & for\ left\ side \\ - & for\ right\ side \end{cases}} \tag{A19}$$

The effective radius of each coil during calculation of the magnetic field must be determined. The number of turns for one layer of winding is obtained by:

$$\frac{L_{coil}}{d_{SC,wire}} = N_{turns,1\,layer} - 1 \cong N_{turns,1\,layer} \qquad because\ N_{turns,1\,layer} >> 1 \tag{A20}$$

where $d_{SC,wire}$ is the diameter of the wire. The number of layers stacked on top of each other in a coil is obtained by:

$$N_{layers} = \frac{N_{total}}{N_{turns,1\,layer}} \tag{A21}$$

where N_{total} is the total number of turns for a coil. The thickness of the coil is computed according to:

$$th_{coil} = d_{SC,wire}\ N_{layers} \tag{A22}$$

therefore the effective radius during calculation of magnetic fields for a coil can be taken to be:

$$R_{coil} = R_{mandrel} + \frac{th_{coil}}{2} \tag{A23}$$

where R_{coil} is the average radius of the coil between the most inner and outer layers.

Appendix B

Estimating the CHX requirement

```
$TABSTOPS 0.2 0.4 0.6 1
"!Amir Jahromi"

"!This code calculates the minimum cooling power required for the AMRR to operate based on various
different loss mechanisms which are listed here"

"!1. Losses due to static conduction through the regenerator bed from T_top to T_bottom"
"!2. Entropy generation due to pressure drop as a result of flow and finite heat transfer between the
mixture and the GGG"
"!3. Heat generation due to Eddy currents in the canister wall material axially, and through the end caps
and tube at the CHX"
"!4. Heat introduced form the thermometer leads at the CHX"
"!5. Leads for the heater to measure the cooling power of the CHX"
"!6. Radiation form surrounding"
"!7. Residual gas conduction in the Dewar as a result of remaining gas --> ignore, because of cold temp
platform gettering and future incorporation of zeolite getter on the 4K platform"
"!8. Conduction along canister wall"
"!9. Conduction through the Kevlar suspenders"

"!Dependent variables"

"Constants and knowns"
N_reg=2[-] "Number of regenerators"
MW_GGG=1.01235[kg/mol]        "Molar mass of GGG"
rho_GGG=7080[kg/m3]    "Density of GGG"

"SMP parameters"
T_SMP_lowT=1.59[K]      "Lowest temp of SMP - highest concentration - reference point"
x_SMP_lowT=0.03871[-]  "Corresponding concentration"
n_3_shuttle=0.006395[mol]        "Number of Helium 3 needed to shuttle - found this earlier - enetered
later"
tau_half=80[s]      "Half-cycle period"

"Regenerator parameters"
T_reg_top=1.6[K]  "Top regenerator mean temperature"
T_reg_bot=0.78[K] "Bottom regenerator mean temp - conservative"
L_reg=14[cm]*convert(cm,m)       "Length of regenerator"
d_reg=1.5[cm]*convert(cm,m)      "Diameter of regenerator - this is ID"
por_reg=0.38       "Porosity in regenerator"
d_particle=0.001[m]        "Diameter of crushed GGG particles"
B_reg_high=1.5[Tesla]      "High field during the flow Demag process"
B_reg_low=0[Tesla]         "Low field during the flow Demag process"
dB_reg=3[Tesla]   "Field swing for Eddy current calculations"
L_CHX_tube=2[in]*convert(in,m)  "Length of the Cold Heat EXchanger tubing sticking out"
od_CHX_tube=1[in]/16*convert(in,m)       "OD of CHX tubing"
th_cap=2[mm]*convert(mm,m)      "Cap thickness"
d_cap=1.5[cm]*Convert(cm,m)     "Diameter of cap"
th_reg_wall=1[in]/32*convert(in,m)"Regenerator wall thickness"
```

```
"Calculated pump parameters"
mu_system=mu4(T_SMP_lowT,x_SMP_lowT)     "Finding the chem-4 throughout the system"
x_reg_avg=(x_reg_top+x_reg_bot)/2        "Average concentration throughout regenerator"
n_total_shuttle=n_3_shuttle/x_reg_avg    "ESTIMATED total number of moles shuttling in the
regenerator"
n_dot_reg=n_total_shuttle/tau_half       "Total molar flow rate through regenerator"
m_dot_reg=n_dot_reg*MW_avg(x_reg_avg)    "MAss flow rate through regenerator"

"!1. Static bed conduction"
mu_system=mu4(T_reg_top, x_reg_top)  "Finding the concentration for top of Reg"
mu_system=mu4(T_reg_bot, x_reg_bot)  "Finding concentration for bot of Reg"

k_G_avg=INTEGRAL(k_G(T_int1),T_int1, T_reg_bot,T_reg_top)/(T_reg_top-T_reg_bot) "Averaged GGG
conductivity"
k_he_mix_avg=INTEGRAL(k_he_mix(x_int1), x_int1, x_reg_top, x_reg_bot)/(x_reg_bot-x_reg_top)
    "Averaged he mixture conductivity"

CALL k_effective(por_reg, k_G_avg, k_he_mix_avg: k_eff, a_Warning$) "Finding effective conductivity"
A_c_reg=pi#*d_reg^2/4            "Cross sectional area of Reg"

q_dot_static_bed=k_eff*A_c_reg*(T_reg_top-T_Reg_bot)/L_reg*N_reg   "Static bed conduction for both
regenerators"


"!2. S_gen calculation"

"2.1 S_gen due to pressure drop"
rho_avg=rho_mix(T_reg_avg,x_reg_avg)  "Average density of mixture through Reg"
m_dot_reg=rho_avg*u_d*A_c_reg         "Mass flow rate through Reg"
dP\dx/(rho_avg*u_d^2)*d_particle*(por_reg^3/(1-por_reg))=180*(1-por_reg)/Re_avg+4   "Finding dP/dx
for each Reg. Kaviany 1999"
Re_avg=rho_avg*u_d*d_particle/viscosity_mix(T_reg_avg)        "Averaged Reynolds number based on
Kaviany's definition"

s_gen_p_drop=m_dot_reg/(rho_avg*T_reg_avg)*dP\dx*L_reg*T_reg_avg          "Derived, s_gen due to
pressure drop based on ds=dh/T-v/T*dP"

"2.2 S_gen due to heat transfer"

s_integral_high=INTEGRAL(S_G(T_int3, B_reg_high), T_int3, T_reg_top,T_reg_bot)/MW_GGG
    "Integrated high field entropy - assuming linear temp profile for estimate"
s_integral_low=INTEGRAL(S_G(T_int4, B_reg_low), T_int4, T_reg_top,T_reg_bot)/MW_GGG
    "Integrated low field entropy - assuming linear temp profile for estimate"
dS_G_dot=(s_integral_high-s_integral_low)/((T_reg_top-T_reg_bot)*tau_half)     "Change in s during
Flow Demag, divided by half cycle period to get W/kg-K"

hc_reg=hc_mix(por_reg, Re_avg, Pr_avg, d_particle, k_he_mix_avg)      "Finding the heat transfer
coefficient between mixture and GGG"
Pr_avg=Pr_mix(T_reg_avg,x_reg_avg)          "Prandtl number of mixture"
alpha=6*A_c_reg*(1-por_reg)/d_particle      "Heat transfer surface area for packed bed per unit
length"

s_gen_ht=dS_G_dot^2*A_c_reg^2*rho_GGG^2*(1-
por_reg)^2/((hc_reg*alpha)+(dS_G_dot*A_c_reg*rho_GGG*(1-por_reg))  )*(T_reg_top-T_reg_bot)*L_reg
    "Derived, s_gen due to finite temperature heat transfer between GGG and mixture"
```

```
"!3. Eddy Current heat generation"
"3.1 In the canister wall"

B_dot=dB_reg/tau_half                "Change of field - full field"
T_reg_avg=(T_reg_top+T_reg_bot)/2                "Averaged Reg. temperature"
rho_el_wall=ElectricalResistivity('Stainless_AISI304', T=T_reg_avg)        "Electrical resistivity of wall
material"
q_dot_eddy_Wall=pi#*L_reg*B_dot^2*(d_reg/2)^3*th_reg_wall/(2*rho_el_wall)*N_reg      "Derived, heat
generation due to Eddy currents, both Reg."

"3.2 In the bottom cap"

q_dot_eddy_cap=pi#*th_cap*B_dot^2*(d_cap/2)^4/(8*rho_el_cap)          "Derived, heat generation due to
Eddy currents both Reg."
rho_el_cap=ElectricalResistivity('Stainless_AISI304', T=1[K])*N_reg        "Electrical resistivity of cap"

"3.3 CHX tube sticking out - conservative estimate for simplicity sake"

q_dot_eddy_CHX_tube=pi#*L_CHX_tube*B_dot^2*(od_CHX_tube/2)^4/(8*rho_el_CHX_tube)*N_reg
     "Heat generation due to Eddy currents in the CHX tubing sticking out"
rho_el_CHX_tube=rho_el_cu(T_reg_bot, 20)                "Electrical resistivity of CHX tubing"

"!4. Thermometer leads"
k_phb=3[W/m-K]              "Thermal conductivity for Phosphor Bronze- thermometer leads"
L_leads=0.3[m]              "Free length of leads"
dT_leads=4[K]               "Temp difference in leads between 4K plate and CHX - Conservative"
d_lead=0.002[in]*convert(in,m)              "Diameter of the thermometer leads"
N_leads=8           "Number of leads"
A_c_leads=pi#*d_lead^2/4*N_leads                "Cross sectional area of each lead"
q_dot_th_leads=k_phb*A_c_leads*dT_leads/L_leads                "Conduction loss through leads - NOTE:
Ohmix diss. is negligible"

"!5. Heater leads"
"NEGLIGIBLE estimated 5 microW for 1mA of current d_wire=0.003[in]"

"!6. Radiation from surroundings"
q_dot_rad=eps_SS*sigma#*A_s_canister*(T_magnet^4-T_reg_bot^4)*N_reg      "Radiation heat tranfer to
the regenerator - Assume F_mag_Reg=1, all to T_reg_bottom - Conservative"
A_s_Canister=pi#*d_reg*L_reg+pi#*d_cap^2/4*2          "Surface area of the regenerator canister"
eps_SS=0.02[-]              "Flynn conservative estimate for SS emmissivity"
T_magnet=5[K]               "Conservative magnet temp"

"!7. Residual gas conduction"
"IGNORED, only helium is the residual gas, even with helium the estimated conduction is much less than
1 nW -- Note: Add coconut charcoal or zeolite to the cold stage to avoid any residual conduction issues"

"!8. Conduction along canister wall"
k_wall_eff=INTEGRAL(k_SS304(T_int_wall), T_int_Wall, T_reg_bot, T_reg_top) "Integrated conductivity
along Reg. wall"
q_dot_wall=k_wall_eff*A_c_Wall/L_reg*N_reg                "Heat leak due to conduction along Reg. wall"
od_reg=d_reg+2*th_reg_wall                "OD of Reg canister"
A_c_wall=pi#*(od_reg^2-d_reg^2)/4                "Cross sectional area of canister wall"


"!9. Conduction through KEvlar suspenders"
N_kevlar=4[-]               "Number of Kevlar strands for each Reg to suspend canister at the bottom"
```

```
A_C_kevlar=pi#*D_kevlar^2/4                "Cross sectional area of Kevlar string"
L_kevlar=1[cm]*convert(cm,m)               "Length of each Kevlar string"
D_kevlar=0.02[in]*convert(in,m)            "Diameter of Kevlar strings"
q_dot_kevlar=INTEGRAL(k_Kevlar(T_int6), T_int6, T_reg_bot,
T_magnet)*A_c_kevlar/L_kevlar*N_reg*N_kevlar "Conduction leak through Kevlar strings"

"!Summing all the losses to determine minimum cooling power required for no load"
q_dot_sum=q_dot_static_bed+s_gen_p_drop+s_gen_ht+q_dot_eddy_wall+q_dot_eddy_cap+q_dot_eddy
_CHX_tube+q_dot_th_leads+q_dot_rad+q_dot_wall+q_dot_kevlar

"!Building safety factor into the cooling power"
q_dot_ref_target=4.5*q_dot_sum  "Use a 4.5X factor for safety - 4.5 to match the already modeled
regnerator"

"!Determining the flow of he3 required to promote from 780mK to 900mK"
T_CHX_in=T_reg_bot       "CHX inlet temp"
x_CHX_in=x_reg_bot       "CHX inlet concentration"
T_CHX_out=0.9[K]         "CHX outlet temp"
mu_system=mu4(T_CHX_out, x_CHX_out)        "Finding CHX outlet concentration"
q_dot_ref_target=n_dot_3_target*(h_os(T_CHX_out, x_CHX_out, mu_system)-h_os(T_CHX_in,
x_CHX_in, mu_system))+(n_dot_3_target*(1-x_CHX_out)/x_CHX_out*mu_system-n_dot_3_target*(1-
x_CHX_in)/x_CHX_in*mu_system)          "Finding the required number of moles for 3He to shuttle"
n_3_target=n_dot_3_target*tau_half       "Total number of moles of 3He required during Flow Demag - or
Flow Mag due to mass conservation"
```

EES code for 1st order AMRR model

```
$TABSTOPS   0.2 0.4  0.8 1 in

"!Amir E Jahromi"

"!first order model of the AMRR system operating between 780 mK and 1.6K"

"!Fixed properties"

rho_GGG=7080[kg/m^3]    "Density of GGG"
MW_GGG=1.012[kg/mol]  "Molar mass of GGG"

"Second law used to find the MINIMUM mass of GGG required in the regenerator"

"===================reserve variables here==================="
T_hhx_out=1.577[K]
x_hhx_out=x_reg_top
mu_system=mu4(T_hhx_out, x_hhx_out)
mu_system=mu4(T_SMP_lowT, x_SMP_lowT)
T_SMP_lowT=1.5902[K]
x_SMP_lowT=0.03871[-]
"==========================================================="

"!Design parameters"
q_dot_ref=600[microW]*convert(microW,W)          "Refrigeration power at 0.78-0.9K/ Cold HX"
```

```
half_period=80[s]        "1/2 period for the (de)/magnetization of the regenerator"


"!Finding the moles of He-3 required to shuttle in the Cold HX in half-period"

q_ref_total=q_dot_ref*half_period  "Total heat lifted in the cold HX"

"Known inlet and outlet states"
T_chx_in=0.78[K]  "Inlet CHX temperature"
mu_system=mu4(T_chx_in, x_chx_in)
T_chx_out=0.9[K]  "Outlet CHX temperature"
mu_system=mu4(T_chx_out, x_chx_out)


"Calculated inlet and outlet properties"
h_os_chx_in=h_os(T_chx_in,x_chx_in,mu_system)     "Inlet osmotic enthalpy"

h_os_chx_out=h_os(T_chx_out,x_chx_out,mu_system)       "Outlet osmotic enthalpy"


"Solve for the mole of He3 needed to shuttle by applying an energy balance"
(n_3*h_os_chx_in+(1-x_chx_in)/x_chx_in*n_3*mu_system)-(n_3*h_os_chx_out+(1-
x_chx_out)/x_chx_out*n_3*mu_system)+q_ref_total=Err_chx
Err_chx=0       "Set error to 0 to solve"


"!Finding the mass of GGG required in each of the regenerators"

"Regenerator design parameters"
reg_porosity=0.38 "Porosity in regenerator, V_void/V_total. 0.38 commonly used -- Nellis (2009),
McAdams (1954), Londong and Kays (1964), McCabe (1985), Perry (2007)"
d_reg=0.015[m]     "Regenerator diameter, a reasonable diameter considering magnet bore"
B_reg_low=0[Tesla]     "Lowest B in regenerator throughout the AMRR cycle"
B_reg_high=1.5[Tesla]"Highest B in regenerator during FM - AMRR cycle"

"Known inlet and outlet states"
T_reg_bot=T_chx_in   "Outlet temp"
x_reg_bot=x_chx_in    "Outlet conc."
T_reg_top=T_hhx_out "Inlet temp"


"Calculated inlet and outlet properties"
s_3_reg_bot=s_he(T_reg_bot, x_reg_bot)/x_reg_bot                "Outlet reg entropy per mole of 3He"
h_os_reg_bot=h_os(T_reg_bot,x_reg_bot, mu_system)                    "Outlet osmotic enthalpy"

s_3_reg_top=s_he(T_reg_top, x_reg_top)/x_reg_top                "Inlet reg entropy per mole of 3He"
h_os_reg_top=h_os(T_reg_top,x_reg_top, mu_system)                    "Inlet osmotic enthalpy"

"Finding the MINIMUM mass/mole of GGG required in the regenerator by applying an entropy balance"
S_gen_HT=0.0034[J/K]     "Feed from min cooling power program"
dS_GGG_reg=n_GGG_reg*(S_GGG_reg_final-S_GGG_reg_initial)
    "Final and initial state of S_GGG NOTE: this is purely averaged out over the regenerator, temp
distribution is assumed linear between top and bottom of regenerator"
    S_GGG_reg_final=INTEGRAL(S_G(T_int_f, B_reg_low),T_int_f,T_reg_bot,T_reg_top)/(T_reg_top-
T_reg_bot)          "INTEGRAL-AVG of the entropy of GGG at the end of demagnetization"
```

```
    S_GGG_reg_initial=INTEGRAL(S_G(T_int_i,B_reg_high),T_int_i,T_reg_bot, T_reg_top)/(T_reg_top-
T_reg_bot)     "INTEGRAL-AVG of the entropy of GGG at the beginning of demagnetization"
"Entropy balance on the regenerator"
n_3*(s_3_reg_top-s_3_reg_bot)=dS_GGG_reg+S_Gen_HT
m_GGG_reg=n_GGG_reg*MW_GGG       "Minimum mass of GGG is calculated here"

"Finding length of regenerator with initially assumed reg diameter"
rho_GGG=m_GGG_reg/V_GGG_reg        "Finding MINIMUM volume of GGG required"
V_reg=V_GGG_reg/(1-reg_porosity)        "Finding MINIMUM regenerator total volume"
V_reg=pi#*d_reg^2/4*l_reg                        "Finding MINIMUM length of regenerator"
```

EES code for Regenerator model

NFD process:

```
"!Amir E Jahromi"

$Import  'C:\Users\Amir\Documents\CYCLE ANALYSIS - experiment2\buffer_data4.txt' /skiplines=11
buffer4[1..10]

"!NO FLOW DEMAG"
$TABSTOPS 0.2 0.4 0.8 1
"This program solves for the temperature profile along the length of the regenerator"

"Inputs"

"Known information"
por_reg=0.38[-]     "porosity"
A_c_reg=pi#*d_reg^2/4     "X-sectional area of Reg"
mu_system=mu4(T_pc, x_pc)  "Chem potential - 4"
T_chx_in=0.78[K]  "CHX inlet"
t_sim=10[s]     "Simulation time"
rho_GGG=7080[kg/m3]     "Density of GGG"
MW_GGG=1.01235[kg/mol]     "Molar weight of GGG"
B_high=3[Tesla]         "Highest field - peak"
{B_low=1.7[Tesla]}"Comment out after updating guesses"


"GGG mass and vol"
vol_sub_reg=A_c_reg*DELTAx
V_he_sub=vol_sub_reg*(por_reg)
vol_sub_GGG=vol_sub_reg*(1-por_reg)
m_sub_GGG=n_sub_GGG*MW_GGG
n_sub_GGG=rho_GGG*vol_sub_GGG/MW_GGG

"Setup spatial nodes"
N=10
DELTAx=L_reg/(N-1)

Duplicate i=1,N
    reg_loc[i]=(i-1)*DELTAx
    T[i,1]=buffer4[i]      "T_pc-reg_loc[i]/L_reg*(T_pc-T_CHX_in)"
end
```

```
"Setup time step nodes"
M=8
DELTAt=t_sim/(M-1)

Duplicate j=1,M
    time_step[j]=(j-1)*DELTAt
    B[j]=B_high-time_step[j]/t_sim*(B_high-B_low)
end

Duplicate j=1,M-1
    B_avg[j]=(B[j]+B[j+1])/2
end

"!NODE 1 could play with DELTAx in the q_dot_top equation"

Duplicate j=1, M-1
    n_he3_sub[1,j]=v_he_sub/v_he(T[1,j],x[1,j])*x[1,j]
    x[1,j]=x_he(T[1,j], mu_system)
    -n_sub_GGG/(2*DELTAt) * ( T[1,j] + T[1,j+1])/2 * (dsdb( ( T[1,j] + T[1,j+1])/2 , (B[j+1] + B[j])/2 ) *
(B[j+1] - B[j]) + dsdT( ( T[1,j] + T[1,j+1])/2 , (B[j+1] + B[j])/2 ) * (T[1,j+1] - T[1,j]))+ k_he_mix_top[1,j+1] *
A_c_reg * (T_pc - T[1,j+1])/(DELTAx) + k_he_mix_bot[1,j+1] * A_c_reg * (T[2,j+1] - T[1,j+1])/DELTAx =
n_he3_sub[1,j]/(2*DELTAt) * ( u_he3(T[1,j+1], x_he(T[1,j+1], mu_system))-u_he3(T[1,j], x[1,j]))

    k_GGG_top[1,j+1]=k_G((T[1,j+1]+T_pc)/2)
    k_he_mix_top[1,j+1]=k_he_mix((x_he(T[1,j+1], mu_system)+x_pc)/2)
    CALL k_effective(por_reg, k_GGG_top[1,j+1], k_he_mix_top[1,j+1]: k_eff_top[1,j+1],
a_Warning_top$[1,j+1])

    k_GGG_bot[1,j+1]=k_G((T[1,j+1]+T[2,j+1])/2)
    k_he_mix_bot[1,j+1]=k_he_mix(  (x_he(T[1,j+1], mu_system)+x_he(T[2,j+1], mu_system))/2)
    CALL k_effective(por_reg, k_GGG_bot[1,j+1], k_he_mix_bot[1,j+1]: k_eff_bot[1,j+1],
a_Warning_bot$[1,j+1])

"!===FOR CLOSING CYCLE"
dW_G[1,j+1]=m_sub_GGG/2*(B[j+1]+B[j])/2*(vM(T[1,j+1], B[j+1])-vM(T[1,j], B[j]))
dQ_G[1,j+1]=n_sub_GGG/(2) * ( T[1,j] + T[1,j+1])/2 * (dsdb( ( T[1,j] + T[1,j+1])/2 , (B[j+1] + B[j])/2 ) *
(B[j+1] - B[j]) + dsdT( ( T[1,j] + T[1,j+1])/2 , (B[j+1] + B[j])/2 ) * (T[1,j+1] - T[1,j]))
dU_he[1,j+1]= n_he3_sub[1,j]/(2) * ( u_he3(T[1,j+1], x_he(T[1,j+1], mu_system))-u_he3(T[1,j], x[1,j]))
"!====END==============="
end


"Node N"
T[N,M]=T_CHX_in      "Last node last time step Condition"
Duplicate j=1, M-1
    n_he3_sub[N,j]=v_he_sub/v_he(T[N,j],x[N,j])*x[N,j]
    x[N,j]=x_he(T[N,j], mu_system)
    -n_sub_GGG/(2*DELTAt) * ( T[N,j] + T[N,j+1])/2 * (dsdb( ( T[N,j] + T[N,j+1])/2 , (B[j+1] + B[j])/2 ) *
(B[j+1] - B[j]) + dsdT( ( T[N,j] + T[N,j+1])/2 , (B[j+1] + B[j])/2 ) * (T[N,j+1] - T[N,j])) + k_he_mix_top[N,j+1] *
A_c_reg * (T[N-1,j+1] - T[N,j+1])/(DELTAx)  = n_he3_sub[N,j]/(2*DELTAt) * ( u_he3(T[N,j+1],
x_he(T[N,j+1], mu_system))-u_he3(T[N,j], x[N,j]))

    k_GGG_top[N,j+1]=k_G((T[N,j+1]+T[N-1,j+1])/2)
    k_he_mix_top[N,j+1]=k_he_mix((x_he(T[N,j+1], mu_system)+x_he(T[N-1,j+1], mu_system))/2)
```

```
    CALL k_effective(por_reg, k_GGG_top[N,j+1], k_he_mix_top[N,j+1]: k_eff_top[N,j+1],
a_Warning_top$[N,j+1])

"!===FOR CLOSING CYCLE"
dW_G[N,j+1]=m_sub_GGG/2*(B[j+1]+B[j])/2*(vM(T[N,j+1], B[j+1])-vM(T[N,j], B[j]))
dQ_G[N,j+1]=n_sub_GGG/(2) * ( T[N,j] + T[N,j+1])/2 * (dsdb( ( T[N,j] + T[N,j+1])/2 , (B[j+1] + B[j])/2 ) *
(B[j+1] - B[j]) + dsdT( ( T[N,j] + T[N,j+1])/2 , (B[j+1] + B[j])/2 ) * (T[N,j+1] - T[N,j]))
dU_he[N,j+1]= n_he3_sub[N,j]/(2) * ( u_he3(T[N,j+1], x_he(T[N,j+1], mu_system))-u_he3(T[N,j], x[N,j]))
"!====END=============="


end

Duplicate j=1,M-1
    Duplicate i=2,N-1
    n_he3_sub[i,j]=v_he_sub/v_he(T[i,j],x[i,j])*x[i,j]
    x[i,j]=x_he(T[i,j], mu_system)
    -n_sub_GGG/(DELTAt) * ( T[i,j] + T[i,j+1])/2 * (dsdb( ( T[i,j] + T[i,j+1])/2 , (B[j+1] + B[j])/2 ) * (B[j+1] -
B[j]) + dsdT( ( T[i,j] + T[i,j+1])/2 , (B[j+1] + B[j])/2 ) * (T[i,j+1] - T[i,j])) + k_he_mix_top[i,j+1] * A_c_reg * (T[i-
1,j+1] - T[i,j+1])/(DELTAx) + k_he_mix_bot[i,j+1] * A_c_reg * (T[i+1,j+1] - T[i,j+1])/DELTAx =
n_he3_sub[i,j]/(DELTAt) * ( u_he3(T[i,j+1], x_he(T[i,j+1], mu_system))-u_he3(T[i,j], x[i,j]))

    k_GGG_top[i,j+1]=k_G((T[i,j+1]+T[i-1,j+1])/2)
    k_he_mix_top[i,j+1]=k_he_mix(   (x_he(T[i,j+1], mu_system)+x_he(T[i-1,j+1], mu_system))/2   )
    CALL k_effective(por_reg, k_GGG_top[i,j+1], k_he_mix_top[i,j+1]: k_eff_top[i,j+1],
a_Warning_top$[i,j+1])

    k_GGG_bot[i,j+1]=k_G((T[i,j+1]+T[i+1,j+1])/2)
    k_he_mix_bot[i,j+1]=k_he_mix(  (x_he(T[i,j+1], mu_system)+x_he(T[i+1,j+1], mu_system))/2)
    CALL k_effective(por_reg, k_GGG_bot[i,j+1], k_he_mix_bot[i,j+1]: k_eff_bot[i,j+1],
a_Warning_bot$[i,j+1])

"!===FOR CLOSING CYCLE"
dW_G[i,j+1]=m_sub_GGG*(B[j+1]+B[j])/2*(vM(T[i,j+1], B[j+1])-vM(T[i,j], B[j]))
dQ_G[i,j+1]=n_sub_GGG * ( T[i,j] + T[i,j+1])/2 * (dsdb( ( T[i,j] + T[i,j+1])/2 , (B[j+1] + B[j])/2 ) * (B[j+1] - B[j])
+ dsdT( ( T[i,j] + T[i,j+1])/2 , (B[j+1] + B[j])/2 ) * (T[i,j+1] - T[i,j]))
dU_he[i,j+1]= n_he3_sub[i,j] * ( u_he3(T[i,j+1], x_he(T[i,j+1], mu_system))-u_he3(T[i,j], x[i,j]))
"!====END=============="

    end
end

"Placing work terms in a 1D array for SUM calculation"
Duplicate i=1,N
    WW1[i]=dW_G[i,2]
    WW2[i]=dW_G[i,2]
    WW3[i]=dW_G[i,3]
    WW4[i]=dW_G[i,4]
    WW5[i]=dW_G[i,5]
    WW6[i]=dW_G[i,6]
    WW7[i]=dW_G[i,7]
    WW8[i]=dW_G[i,8]
end

"Placing Q terms in a 1D array for SUM calculation"
Duplicate i=1,N
```

```
    QQ1[i]=dQ_G[i,2]
    QQ2[i]=dQ_G[i,2]
    QQ3[i]=dQ_G[i,3]
    QQ4[i]=dQ_G[i,4]
    QQ5[i]=dQ_G[i,5]
    QQ6[i]=dQ_G[i,6]
    QQ7[i]=dQ_G[i,7]
    QQ8[i]=dQ_G[i,8]
end

"Placing u terms in a 1D array for SUM calculation"
Duplicate i=1,N
    UU1[i]=dU_he[i,2]
    UU2[i]=dU_he[i,2]
    UU3[i]=dU_he[i,3]
    UU4[i]=dU_he[i,4]
    UU5[i]=dU_he[i,5]
    UU6[i]=dU_he[i,6]
    UU7[i]=dU_he[i,7]
    UU8[i]=dU_He[i,8]
end

"Finding SUM of work, u_GGG and, u_he"
W_SUM=SUM(WW1[i], i=1,N)+SUM(WW8[i], i=1,N)+SUM(WW2[i], i=1,N)+SUM(WW3[i],
i=1,N)+SUM(WW4[i], i=1,N)+SUM(WW5[i], i=1,N)+SUM(WW6[i], i=1,N)+SUM(WW7[i], i=1,N)
Q_SUM=SUM(QQ1[i], i=1,N)+SUM(QQ8[i], i=1,N)+SUM(QQ2[i], i=1,N)+SUM(QQ3[i],
i=1,N)+SUM(QQ4[i], i=1,N)+SUM(QQ5[i], i=1,N)+SUM(QQ6[i], i=1,N)+SUM(QQ7[i], i=1,N)
U_he_SUM=SUM(UU1[i], i=1,N)+SUM(UU8[i], i=1,N)+SUM(UU2[i], i=1,N)+SUM(UU3[i],
i=1,N)+SUM(UU4[i], i=1,N)+SUM(UU5[i], i=1,N)+SUM(UU6[i], i=1,N)+SUM(UU7[i], i=1,N)

Duplicate i=1,N
    T[i,M]=buffer[i]
end

B_low1=B[M]

$Export 'C:\Users\Amir\Documents\CYCLE ANALYSIS - experiment2\buffer_data1.txt' buffer[1..N]
B_low1
```

FM process:

```
"!Amir E Jahromi"

$Import  'C:\Users\Amir\Documents\CYCLE ANALYSIS - experiment2\buffer_data1.txt' /skiplines=12
buffer1[1..10] B_low1

"!FLOW DEMAG"

$TABSTOPS 0.2 0.4 0.8 1
"This program solves for the temperature profile along the length of the regenerator"

"Inputs"
```

```
"Known information"
por_reg=0.38[-]
A_c_reg=pi#*d_reg^2/4
mu_system=mu4(T_pc, x_pc)
T_chx=0.9[K]
T_chx_in=0.78[K]
t_sim=80[s]
rho_GGG=7080[kg/m3]
MW_GGG=1.01235[kg/mol]
B_low=0[Tesla]
{n_3_shuttle=0.0058[mol]} "COMMET out after updating guess"
n_dot_3=n_3_shuttle/t_sim
B[1]=B_low1    "First node field"
B[M]=B_low     "Last mode field"

"Finding mass and vol of GGG"
vol_sub_reg=A_c_reg*DELTAx
V_he_sub=vol_sub_reg*(por_reg)
vol_sub_GGG=vol_sub_reg*(1-por_reg)
m_sub_GGG=n_sub_GGG*MW_GGG
n_sub_GGG=rho_GGG*vol_sub_GGG/MW_GGG


"Setup spatial node"
N=10
DELTAx=L_reg/(N-1)

Duplicate i=1,N
    reg_loc[i]=(i-1)*DELTAx
    T[i,1]=buffer1[i]      "T_pc-reg_loc[i]/L_reg*(T_pc-T_CHX_in)"
end

"Setup time step nodes"
M=8
DELTAt=t_sim/(M-1)

Duplicate j=1,M
    time_step[j]=(j-1)*DELTAt
    //B[j]=B_high-time_step[j]/t_sim*(B_high-B_low)
end

Duplicate j=1,M-1
    B_avg[j]=(B[j]+B[j+1])/2
end

"!NODE 1 could play with DELTAx in the q_dot_top equation"


Duplicate j=1, M-1
    n_he3_sub[1,j]=v_he_sub/v_he(T[1,j],x[1,j])*x[1,j]
    x[1,j]=x_he(T[1,j], mu_system)
    -n_sub_GGG/(2*DELTAt) * ( T[1,j] + T[1,j+1])/2 * (dsdb( ( T[1,j] + T[1,j+1])/2 , (B[j+1] + B[j])/2 ) *
(B[j+1] - B[j]) + dsdT( ( T[1,j] + T[1,j+1])/2 , (B[j+1] + B[j])/2 ) * (T[1,j+1] - T[1,j])) +
k_he_mix_bot[1,j+1]*A_c_reg * (T[2, j+1]-T[1,j+1])/(DELTAx) + n_dot_3 * h_os( (T[1,j+1]+T_pc)/2,
x_he((T[1,j+1]+T_pc)/2, mu_system), mu_system) +  n_dot_3*mu_system* ( (1- x_he((T[1,j+1]+T_pc)/2,
mu_system))/x_he((T[1,j+1]+T_pc)/2, mu_system))          -n_dot_3 * h_os( (T[2,j+1]+T[1,j+1])/2,
```

```
x_he((T[2,j+1]+T[1,j+1])/2, mu_system), mu_system)    -    n_dot_3*mu_system* ( (1- x_he(
(T[2,j+1]+T[1,j+1])/2      , mu_system))/x_he((T[2,j+1]+T[1,j+1])/2, mu_system))       =
n_he3_sub[1,j]/(2*DELTAt) * ( u_he3(T[1,j+1], x_he(T[1,j+1], mu_system))-u_he3(T[1,j], x[1,j]))

    k_GGG_bot[1,j+1]=k_G((T[1,j+1]+T[2,j+1])/2)
    k_he_mix_bot[1,j+1]=k_he_mix(  (x_he(T[1,j+1], mu_system)+x_he(T[2,j+1], mu_system))/2)
    CALL k_effective(por_reg, k_GGG_bot[1,j+1], k_he_mix_bot[1,j+1]: k_eff_bot[1,j+1],
a_Warning_bot$[1,j+1])

dW_G[1,j+1]=m_sub_GGG/2*(B[j+1]+B[j])/2*(vM(T[1,j+1], B[j+1])-vM(T[1,j], B[j]))
dQ_G[1,j+1]=n_sub_GGG/(2) * ( T[1,j] + T[1,j+1])/2 * (dsdb( ( T[1,j] + T[1,j+1])/2 , (B[j+1] + B[j])/2 ) *
(B[j+1] - B[j]) + dsdT( ( T[1,j] + T[1,j+1])/2 , (B[j+1] + B[j])/2 ) * (T[1,j+1] - T[1,j]))
dU_he[1,j+1]=n_he3_sub[1,j]/(2) * ( u_he3(T[1,j+1], x_he(T[1,j+1], mu_system))-u_he3(T[1,j], x[1,j]))
end


"!Node N"

Duplicate j=1, M-1
    T[N,j+1]=T_chx_in "BC at node N"
    n_he3_sub[N,j]=v_he_sub/v_he(T[N,j],x[N,j])*x[N,j]
    x[N,j]=x_he(T[N,j], mu_system)
    -n_sub_GGG/(2*DELTAt) * ( T[N,j] + T[N,j+1])/2 * (dsdb( ( T[N,j] + T[N,j+1])/2 , (B[j+1] + B[j])/2 ) *
(B[j+1] - B[j]) + dsdT( ( T[N,j] + T[N,j+1])/2 , (B[j+1] + B[j])/2 ) * (T[N,j+1] - T[N,j])) + k_he_mix_top[N,j+1] *
A_c_reg * (T[N-1,j+1] - T[N,j+1])/(DELTAx) + n_dot_3 * h_os( (T[N,j+1]+T[N-1,j+1])/2, x_he((T[N,j+1]+T[N-
1,j+1])/2, mu_system), mu_system) +  n_dot_3*mu_system* ( (1- x_he((T[N,j+1]+T[N-1,j+1])/2,
mu_system))/x_he((T[N,j+1]+T[N-1,j+1])/2, mu_system))          -n_dot_3 * h_os( 3/2*T[N,j+1]-1/2*T[N-
1,j+1], x_he(3/2*T[N,j+1]-1/2*T[N-1,j+1], mu_system), mu_system)    -    n_dot_3*mu_system* ( (1- x_he(
3/2*T[N,j+1]-1/2*T[N-1,j+1]      , mu_system))/x_he(3/2*T[N,j+1]-1/2*T[N-1,j+1], mu_system))       =
n_he3_sub[N,j]/(2*DELTAt) * ( u_he3(T[N,j+1], x_he(T[N,j+1], mu_system))-u_he3(T[N,j], x[N,j]))


DELTAt*(n_dot_3 * h_os( T[N,j+1], x_he(T[N,j+1], mu_system), mu_system)    +    n_dot_3*mu_system* (
(1- x_he(   T[N,j+1]      , mu_system))/x_he((T[N,j+1]), mu_system)))  -   DELTAt*(n_dot_3 * h_os(
T_CHX, x_he(T_CHX, mu_system), mu_system)    +    n_dot_3*mu_system* ( (1- x_he( T_CHX       ,
mu_system))/x_he(T_CHX, mu_system)))    =Q_ref[N,j+1]

    k_GGG_top[N,j+1]=k_G((T[N,j+1]+T[N-1,j+1])/2)
    k_he_mix_top[N,j+1]=k_he_mix((x_he(T[N,j+1], mu_system)+x_he(T[N-1,j+1], mu_system))/2)
    CALL k_effective(por_reg, k_GGG_top[N,j+1], k_he_mix_top[N,j+1]: k_eff_top[N,j+1],
a_Warning_top$[N,j+1])

dW_G[N,j+1]=m_sub_GGG/2*(B[j+1]+B[j])/2*(vM(T[N,j+1], B[j+1])-vM(T[N,j], B[j]))
dQ_G[N,j+1]=n_sub_GGG/(2) * ( T[N,j] + T[N,j+1])/2 * (dsdb( ( T[N,j] + T[N,j+1])/2 , (B[j+1] + B[j])/2 ) *
(B[j+1] - B[j]) + dsdT( ( T[N,j] + T[N,j+1])/2 , (B[j+1] + B[j])/2 ) * (T[N,j+1] - T[N,j]))
dU_he[N,j+1]=n_he3_sub[N,j]/(2) * ( u_he3(T[N,j+1], x_he(T[N,j+1], mu_system))-u_he3(T[N,j], x[N,j]))
end


"!Nodes i=2..N-1"
Duplicate j=1,M-1
    Duplicate i=2,N-1
    n_he3_sub[i,j]=v_he_sub/v_he(T[i,j],x[i,j])*x[i,j]
    x[i,j]=x_he(T[i,j], mu_system)
```

```
    -n_sub_GGG/(DELTAt) * ( T[i,j] + T[i,j+1])/2 * (dsdb( ( T[i,j] + T[i,j+1])/2 , (B[j+1] + B[j])/2 ) * (B[j+1] -
B[j]) + dsdT( ( T[i,j] + T[i,j+1])/2 , (B[j+1] + B[j])/2 ) * (T[i,j+1] - T[i,j])) + k_he_mix_top[i,j+1] * A_c_reg * (T[i-
1,j+1] - T[i,j+1])/(DELTAx) + k_he_mix_bot[i,j+1] * A_c_reg * (T[i+1,j+1] - T[i,j+1])/DELTAx +  n_dot_3 *
h_os( (T[i-1,j+1]+T[i,j+1])/2, x_he((T[i,j+1]+T[i-1,j+1])/2, mu_system), mu_system)       +
n_dot_3*mu_system* ( (1- x_he((T[i,j+1]+T[i-1,j+1])/2, mu_system))/x_he((T[i,j+1]+T[i-1,j+1])/2,
mu_system))     - n_dot_3 * h_os( (T[i+1,j+1]+T[i,j+1])/2, x_he((T[i,j+1]+T[i+1,j+1])/2, mu_system),
mu_system)  -  n_dot_3*mu_system* ( (1- x_he((T[i,j+1]+T[i+1,j+1])/2,
mu_system))/x_he((T[i,j+1]+T[i+1,j+1])/2, mu_system)) = n_he3_sub[i,j]/(DELTAt) * ( u_he3(T[i,j+1],
x_he(T[i,j+1], mu_system))-u_he3(T[i,j], x[i,j]))

    k_GGG_top[i,j+1]=k_G((T[i,j+1]+T[i-1,j+1])/2)
    k_he_mix_top[i,j+1]=k_he_mix(   (x_he(T[i,j+1], mu_system)+x_he(T[i-1,j+1], mu_system))/2   )
    CALL k_effective(por_reg, k_GGG_top[i,j+1], k_he_mix_top[i,j+1]: k_eff_top[i,j+1],
a_Warning_top$[i,j+1])

    k_GGG_bot[i,j+1]=k_G((T[i,j+1]+T[i+1,j+1])/2)
    k_he_mix_bot[i,j+1]=k_he_mix(  (x_he(T[i,j+1], mu_system)+x_he(T[i+1,j+1], mu_system))/2)
    CALL k_effective(por_reg, k_GGG_bot[i,j+1], k_he_mix_bot[i,j+1]: k_eff_bot[i,j+1],
a_Warning_bot$[i,j+1])

dW_G[i,j+1]=m_sub_GGG*(B[j+1]+B[j])/2*(vM(T[i,j+1], B[j+1])-vM(T[i,j], B[j]))
dQ_G[i,j+1]=n_sub_GGG * ( T[i,j] + T[i,j+1])/2 * (dsdb( ( T[i,j] + T[i,j+1])/2 , (B[j+1] + B[j])/2 ) * (B[j+1] - B[j])
+ dsdT( ( T[i,j] + T[i,j+1])/2 , (B[j+1] + B[j])/2 ) * (T[i,j+1] - T[i,j]))
dU_he[i,j+1]=n_he3_sub[i,j] * ( u_he3(T[i,j+1], x_he(T[i,j+1], mu_system))-u_he3(T[i,j], x[i,j]))
    end
end

Q_ref_sum=SUM(Q_ref[N,j],j=2,M)/t_sim


Duplicate i=1,N
    WW1[i]=dW_G[i,2]
    WW2[i]=dW_G[i,2]
    WW3[i]=dW_G[i,3]
    WW4[i]=dW_G[i,4]
    WW5[i]=dW_G[i,5]
    WW6[i]=dW_G[i,6]
    WW7[i]=dW_G[i,7]
    WW8[i]=dW_G[i,8]
end

Duplicate i=1,N
    QQ1[i]=dQ_G[i,2]
    QQ2[i]=dQ_G[i,2]
    QQ3[i]=dQ_G[i,3]
    QQ4[i]=dQ_G[i,4]
    QQ5[i]=dQ_G[i,5]
    QQ6[i]=dQ_G[i,6]
    QQ7[i]=dQ_G[i,7]
    QQ8[i]=dQ_G[i,8]
end

Duplicate i=1,N
    UU1[i]=dU_he[i,2]
    UU2[i]=dU_he[i,2]
    UU3[i]=dU_he[i,3]
```

```
    UU4[i]=dU_he[i,4]
    UU5[i]=dU_he[i,5]
    UU6[i]=dU_he[i,6]
    UU7[i]=dU_he[i,7]
    UU8[i]=dU_He[i,8]
end


W_SUM=SUM(WW1[i], i=1,N)+SUM(WW8[i], i=1,N)+SUM(WW2[i], i=1,N)+SUM(WW3[i],
i=1,N)+SUM(WW4[i], i=1,N)+SUM(WW5[i], i=1,N)+SUM(WW6[i], i=1,N)+SUM(WW7[i], i=1,N)
Q_SUM=SUM(QQ1[i], i=1,N)+SUM(QQ8[i], i=1,N)+SUM(QQ2[i], i=1,N)+SUM(QQ3[i],
i=1,N)+SUM(QQ4[i], i=1,N)+SUM(QQ5[i], i=1,N)+SUM(QQ6[i], i=1,N)+SUM(QQ7[i], i=1,N)
U_he_SUM=SUM(UU1[i], i=1,N)+SUM(UU8[i], i=1,N)+SUM(UU2[i], i=1,N)+SUM(UU3[i],
i=1,N)+SUM(UU4[i], i=1,N)+SUM(UU5[i], i=1,N)+SUM(UU6[i], i=1,N)+SUM(UU7[i], i=1,N)

Duplicate i=1,N
    T[i,M]=buffer[i]
end

$Export 'C:\Users\Amir\Documents\CYCLE ANALYSIS - experiment2\buffer_data2.txt' buffer[1..N]
n_3_shuttle
```

NFM process:

```
"!Amir E Jahromi"
$Import  'C:\Users\Amir\Documents\CYCLE ANALYSIS - experiment2\buffer_data2.txt' /skiplines=12
buffer2[1..10] n_3_shuttle

"!NOFLOW MAG"

$TABSTOPS 0.2 0.4 0.8 1
"This program solves for the temperature profile along the length of the regenerator"

"Inputs"

"Known information"
por_reg=0.38[-]
A_c_reg=pi#*d_reg^2/4
mu_system=mu4(T_pc, x_pc)
T_chx_in=0.78[K]
T_chx_out=0.9[K]
t_sim=5[s]
rho_GGG=7080[kg/m3]
MW_GGG=1.01235[kg/mol]
B_low=0[Tesla]
B_high3=B[M]


vol_sub_reg=A_c_reg*DELTAx
V_he_sub=vol_sub_reg*(por_reg)
vol_sub_GGG=vol_sub_reg*(1-por_reg)
m_sub_GGG=n_sub_GGG*MW_GGG
n_sub_GGG=rho_GGG*vol_sub_GGG/MW_GGG
```

```
N=10
DELTAx=L_reg/(N-1)



Duplicate i=1,N
    reg_loc[i]=(i-1)*DELTAx
    T[i,1]=buffer2[i]      "T_pc-reg_loc[i]/L_reg*(T_pc-T_CHX_in)"
end

M=8
DELTAt=t_sim/(M-1)


Duplicate j=1,M
    time_step[j]=(j-1)*DELTAt
    B[j]=B_low+time_step[j]/t_sim*(B_high-B_low)
end

Duplicate j=1,M-1
    B_avg[j]=(B[j]+B[j+1])/2
end

"!NODE 1 could play with DELTAx in the q_dot_top equation"

Duplicate j=1, M-1
    n_he3_sub[1,j]=v_he_sub/v_he(T[1,j],x[1,j])*x[1,j]
    x[1,j]=x_he(T[1,j], mu_system)
    -n_sub_GGG/(2*DELTAt) * ( T[1,j] + T[1,j+1])/2 * (dsdb( ( T[1,j] + T[1,j+1])/2 , (B[j+1] + B[j])/2 ) *
(B[j+1] - B[j]) + dsdT( ( T[1,j] + T[1,j+1])/2 , (B[j+1] + B[j])/2 ) * (T[1,j+1] - T[1,j])) + k_he_mix_top[1,j+1] *
A_c_reg * (T_pc - T[1,j+1])/(DELTAx) + k_he_mix_bot[1,j+1] * A_c_reg * (T[2,j+1] - T[1,j+1])/DELTAx =
n_he3_sub[1,j]/(2*DELTAt) * ( u_he3(T[1,j+1], x_he(T[1,j+1], mu_system))-u_he3(T[1,j], x[1,j]))

    k_GGG_top[1,j+1]=k_G((T[1,j+1]+T_pc)/2)
    k_he_mix_top[1,j+1]=k_he_mix((x_he(T[1,j+1], mu_system)+x_pc)/2)
    CALL k_effective(por_reg, k_GGG_top[1,j+1], k_he_mix_top[1,j+1]: k_eff_top[1,j+1],
a_Warning_top$[1,j+1])

    k_GGG_bot[1,j+1]=k_G((T[1,j+1]+T[2,j+1])/2)
    k_he_mix_bot[1,j+1]=k_he_mix(  (x_he(T[1,j+1], mu_system)+x_he(T[2,j+1], mu_system))/2)
    CALL k_effective(por_reg, k_GGG_bot[1,j+1], k_he_mix_bot[1,j+1]: k_eff_bot[1,j+1],
a_Warning_bot$[1,j+1])

dW_G[1,j+1]=m_sub_GGG/2*(B[j+1]+B[j])/2*(vM(T[1,j+1], B[j+1])-vM(T[1,j], B[j]))
dQ_G[1,j+1]=n_sub_GGG/(2) * ( T[1,j] + T[1,j+1])/2 * (dsdb( ( T[1,j] + T[1,j+1])/2 , (B[j+1] + B[j])/2 ) *
(B[j+1] - B[j]) + dsdT( ( T[1,j] + T[1,j+1])/2 , (B[j+1] + B[j])/2 ) * (T[1,j+1] - T[1,j]))
dU_he[1,j+1]= n_he3_sub[1,j]/(2) * ( u_he3(T[1,j+1], x_he(T[1,j+1], mu_system))-u_he3(T[1,j], x[1,j]))
end


"Node N"
T[N,M]=T_chx_out
Duplicate j=1, M-1
    n_he3_sub[N,j]=v_he_sub/v_he(T[N,j],x[N,j])*x[N,j]
    x[N,j]=x_he(T[N,j], mu_system)
```

```
    -n_sub_GGG/(2*DELTAt) * ( T[N,j] + T[N,j+1])/2 * (dsdb( ( T[N,j] + T[N,j+1])/2 , (B[j+1] + B[j])/2 ) *
(B[j+1] - B[j]) + dsdT( ( T[N,j] + T[N,j+1])/2 , (B[j+1] + B[j])/2 ) * (T[N,j+1] - T[N,j])) + k_he_mix_top[N,j+1] *
A_c_reg * (T[N-1,j+1] - T[N,j+1])/(DELTAx)  = n_he3_sub[N,j]/(2*DELTAt) * ( u_he3(T[N,j+1],
x_he(T[N,j+1], mu_system))-u_he3(T[N,j], x[N,j]))

    k_GGG_top[N,j+1]=k_G((T[N,j+1]+T[N-1,j+1])/2)
    k_he_mix_top[N,j+1]=k_he_mix((x_he(T[N,j+1], mu_system)+x_he(T[N-1,j+1], mu_system))/2)
    CALL k_effective(por_reg, k_GGG_top[N,j+1], k_he_mix_top[N,j+1]: k_eff_top[N,j+1],
a_Warning_top$[N,j+1])

dW_G[N,j+1]=m_sub_GGG/2*(B[j+1]+B[j])/2*(vM(T[N,j+1], B[j+1])-vM(T[N,j], B[j]))
dQ_G[N,j+1]=n_sub_GGG/(2) * ( T[N,j] + T[N,j+1])/2 * (dsdb( ( T[N,j] + T[N,j+1])/2 , (B[j+1] + B[j])/2 ) *
(B[j+1] - B[j]) + dsdT( ( T[N,j] + T[N,j+1])/2 , (B[j+1] + B[j])/2 ) * (T[N ,j+1] - T[N,j]))
dU_he[N,j+1]=n_he3_sub[N,j]/(2) * ( u_he3(T[N,j+1], x_he(T[N,j+1], mu_system))-u_he3(T[N,j], x[N,j]))
end

Duplicate j=1,M-1
    Duplicate i=2,N-1
    n_he3_sub[i,j]=v_he_sub/v_he(T[i,j],x[i,j])*x[i,j]
    x[i,j]=x_he(T[i,j], mu_system)
    -n_sub_GGG/(DELTAt) * ( T[i,j] + T[i,j+1])/2 * (dsdb( ( T[i,j] + T[i,j+1])/2 , (B[j+1] + B[j])/2 ) * (B[j+1] -
B[j]) + dsdT( ( T[i,j] + T[i,j+1])/2 , (B[j+1] + B[j])/2 ) * (T[i,j+1] - T[i,j])) + k_he_mix_top[i,j+1] * A_c_reg * (T[i-
1,j+1] - T[i,j+1])/(DELTAx) + k_he_mix_bot[i,j+1] * A_c_reg * (T[i+1,j+1] - T[i,j+1])/DELTAx =
n_he3_sub[i,j]/(DELTAt) * ( u_he3(T[i,j+1], x_he(T[i,j+1], mu_system))-u_he3(T[i,j], x[i,j]))

    k_GGG_top[i,j+1]=k_G((T[i,j+1]+T[i-1,j+1])/2)
    k_he_mix_top[i,j+1]=k_he_mix(   (x_he(T[i,j+1], mu_system)+x_he(T[i-1,j+1], mu_system))/2   )
    CALL k_effective(por_reg, k_GGG_top[i,j+1], k_he_mix_top[i,j+1]: k_eff_top[i,j+1],
a_Warning_top$[i,j+1])

    k_GGG_bot[i,j+1]=k_G((T[i,j+1]+T[i+1,j+1])/2)
    k_he_mix_bot[i,j+1]=k_he_mix(  (x_he(T[i,j+1], mu_system)+x_he(T[i+1,j+1], mu_system))/2)
    CALL k_effective(por_reg, k_GGG_bot[i,j+1], k_he_mix_bot[i,j+1]: k_eff_bot[i,j+1],
a_Warning_bot$[i,j+1])

dW_G[i,j+1]=(m_sub_GGG*(B[j+1]+B[j])/2*(vM(T[i,j+1], B[j+1])-vM(T[i,j], B[j])))
dQ_G[i,j+1]=n_sub_GGG * ( T[i,j] + T[i,j+1])/2 * (dsdb( ( T[i,j] + T[i,j+1])/2 , (B[j+1] + B[j])/2 ) * (B[j+1] - B[j])
+ dsdT( ( T[i,j] + T[i,j+1])/2 , (B[j+1] + B[j])/2 ) * (T[i,j+1] - T[i,j]))
dU_he[i,j+1]=n_he3_sub[i,j] * ( u_he3(T[i,j+1], x_he(T[i,j+1], mu_system))-u_he3(T[i,j], x[i,j]))
    end
end


Duplicate i=1,N
    WW1[i]=dW_G[i,2]
    WW2[i]=dW_G[i,2]
    WW3[i]=dW_G[i,3]
    WW4[i]=dW_G[i,4]
    WW5[i]=dW_G[i,5]
    WW6[i]=dW_G[i,6]
    WW7[i]=dW_G[i,7]
    WW8[i]=dW_G[i,8]
end

Duplicate i=1,N
    QQ1[i]=dQ_G[i,2]
```

```
    QQ2[i]=dQ_G[i,2]
    QQ3[i]=dQ_G[i,3]
    QQ4[i]=dQ_G[i,4]
    QQ5[i]=dQ_G[i,5]
    QQ6[i]=dQ_G[i,6]
    QQ7[i]=dQ_G[i,7]
    QQ8[i]=dQ_G[i,8]
end

Duplicate i=1,N
    UU1[i]=dU_he[i,2]
    UU2[i]=dU_he[i,2]
    UU3[i]=dU_he[i,3]
    UU4[i]=dU_he[i,4]
    UU5[i]=dU_he[i,5]
    UU6[i]=dU_he[i,6]
    UU7[i]=dU_he[i,7]
    UU8[i]=dU_He[i,8]
end

W_SUM=SUM(WW1[i], i=1,N)+SUM(WW8[i], i=1,N)+SUM(WW2[i], i=1,N)+SUM(WW3[i],
i=1,N)+SUM(WW4[i], i=1,N)+SUM(WW5[i], i=1,N)+SUM(WW6[i], i=1,N)+SUM(WW7[i], i=1,N)
Q_SUM=SUM(QQ1[i], i=1,N)+SUM(QQ8[i], i=1,N)+SUM(QQ2[i], i=1,N)+SUM(QQ3[i],
i=1,N)+SUM(QQ4[i], i=1,N)+SUM(QQ5[i], i=1,N)+SUM(QQ6[i], i=1,N)+SUM(QQ7[i], i=1,N)
U_he_SUM=SUM(UU1[i], i=1,N)+SUM(UU8[i], i=1,N)+SUM(UU2[i], i=1,N)+SUM(UU3[i],
i=1,N)+SUM(UU4[i], i=1,N)+SUM(UU5[i], i=1,N)+SUM(UU6[i], i=1,N)+SUM(UU7[i], i=1,N)

Duplicate i=1,N
    T[i,M]=buffer[i]
end

$Export 'C:\Users\Amir\Documents\CYCLE ANALYSIS - experiment2\buffer_data3.txt' buffer[1..N]
n_3_shuttle B_high3
```

FM process:

```
"!Amir E Jahromi"

$Import  'C:\Users\Amir\Documents\CYCLE ANALYSIS - experiment2\buffer_data3.txt' /skiplines=13
buffer3[1..10] n_3_shuttle4 B_low4

"!FLOW MAG"

$TABSTOPS 0.2 0.4 0.8 1
"This program solves for the temperature profile along the length of the regenerator"

"Inputs"

"Known information"
por_reg=0.38[-]
A_c_reg=pi#*d_reg^2/4
mu_system=mu4(T_pc, x_pc)
T_chx=0.95[K]
t_sim=80[s]
```

```
rho_GGG=7080[kg/m3]
MW_GGG=1.01235[kg/mol]
B_high=3[Tesla]
{B_low=0.45[Tesla]}
n_3_shuttle= - n_3_shuttle4
n_dot_3=n_3_shuttle/t_sim
B[1]=B_low4

vol_sub_reg=A_c_reg*DELTAx
V_he_sub=vol_sub_reg*(por_reg)
vol_sub_GGG=vol_sub_reg*(1-por_reg)
m_sub_GGG=n_sub_GGG*MW_GGG
n_sub_GGG=rho_GGG*vol_sub_GGG/MW_GGG


N=10
DELTAx=L_reg/(N-1)


"INITIAL GUESS FOR TEMP PROFILE - LINEAR"
Duplicate i=1,N
    reg_loc[i]=(i-1)*DELTAx
    T[i,1]=buffer3[i]      "T_pc-reg_loc[i]/L_reg*(T_pc-T_CHX)"
end

M=8
DELTAt=t_sim/(M-1)


Duplicate j=1,M
    time_step[j]=(j-1)*DELTAt
    B[j]=B_low+time_step[j]/t_sim*(B_high-B_low)
end

Duplicate j=1,M-1
    B_avg[j]=(B[j]+B[j+1])/2
end

"!NODE 1 could play with DELTAx in the q_dot_top equation"


Duplicate j=1, M-1
    n_he3_sub[1,j]=v_he_sub/v_he(T[1,j],x[1,j])*x[1,j]
    x[1,j]=x_he(T[1,j], mu_system)

-n_sub_GGG/(2*DELTAt) * ( T[1,j] + T[1,j+1])/2 * (dsdb( ( T[1,j] + T[1,j+1])/2 , (B[2] + B[1])/2 ) * (B[2] -
B[1]) + dsdT( ( T[1,j] + T[1,j+1])/2 , (B[2] + B[1])/2 ) * (T[1,j+1] - T[1,j])) + k_he_mix_bot[1,j+1] * A_c_reg *
(T[2,j+1] - T[1,j+1])/(DELTAx)+ n_dot_3 *h_os( 3/2*T[1,j+1]-1/2*T[2,j+1], x_he(3/2*T[1,j+1]-1/2*T[2,j+1],
mu_system), mu_system)+n_dot_3*mu_system* ( (1- x_he(3/2*T[1,j+1]-1/2*T[2,j+1],
mu_system))/x_he(3/2*T[1,j+1]-1/2*T[2,j+1], mu_system))-n_dot_3 * h_os( (T[1,j+1]+T[2,j+1])/2,
x_he((T[1,j+1]+T[2,j+1])/2, mu_system), mu_system)-    n_dot_3*mu_system* ( (1- x_he(
(T[1,j+1]+T[2,j+1])/2      , mu_system))/x_he((T[1,j+1]+T[2,j+1])/2,
mu_system))=n_he3_sub[N,j]/(2*DELTAt) * ( u_he3(T[N,j+1], x_he(T[N,j+1], mu_system))-u_he3(T[N,j],
x[N,j]))
```

```
DELTAt*(n_dot_3 * h_os( T_pc, x_he(T_pc, mu_system), mu_system)    +    n_dot_3*mu_system* ( (1-
x_he(   T_pc      , mu_system))/x_he((T_pc), mu_system)))  -   DELTAt*(n_dot_3 * h_os( T[1,j+1],
x_he(T[1,j+1], mu_system), mu_system)    +    n_dot_3*mu_system* ( (1- x_he( T[1,j+1]       ,
mu_system))/x_he(T[1,j+1], mu_system)))    =Q_rej[1,j+1]

     k_GGG_bot[1,j+1]=k_G((T[1,j+1]+T[2,j+1])/2)
     k_he_mix_bot[1,j+1]=k_he_mix(  (x_he(T[1,j+1], mu_system)+x_he(T[2,j+1], mu_system))/2)
     CALL k_effective(por_reg, k_GGG_bot[1,j+1], k_he_mix_bot[1,j+1]: k_eff_bot[1,j+1],
a_Warning_bot$[1,j+1])

dW_G[1,j+1]=(m_sub_GGG/2*(B[j+1]+B[j])/2*(vM(T[1,j+1], B[j+1])-vM(T[1,j], B[j])))
dQ_G[1,j+1]=n_sub_GGG/(2) * ( T[1,j] + T[1,j+1])/2 * (dsdb( ( T[1,j] + T[1,j+1])/2 , (B[2] + B[1])/2 ) * (B[2] -
B[1]) + dsdT( ( T[1,j] + T[1,j+1])/2 , (B[2] + B[1])/2 ) * (T[1,j+1] - T[1,j]))
dU_he[1,j+1]=n_he3_sub[N,j]/(2) * ( u_he3(T[N,j+1], x_he(T[N,j+1], mu_system))-u_he3(T[N,j], x[N,j]))
end


"!Node N"

Duplicate j=1, M-1
     n_he3_sub[N,j]=v_he_sub/v_he(T[N,j],x[N,j])*x[N,j]
     x[N,j]=x_he(T[N,j], mu_system)

-n_sub_GGG/(2*DELTAt) * ( T[N,j] + T[N,j+1])/2 * (dsdb( ( T[N,j] + T[N,j+1])/2 , (B[j+1] + B[j])/2 ) * (B[j+1]  -
B[j]) + dsdT( ( T[N,j] + T[N,j+1])/2 , (B[j+1] + B[j])/2 ) * (T[N,j+1] - T[N,j])) + "k_he_mix_top[N,j+1]*A_c_reg
* (T[N-1, j+1]-T[N,j+1])/(DELTAx) +" n_dot_3 * h_os( (T[N-1,j+1]+T[N,j+1])/2, x_he((T[N-1,j+1]+T[N,j+1])/2,
mu_system), mu_system) +  n_dot_3*mu_system* ( (1- x_he((T[N,j+1]+T[N-1,j+1])/2,
mu_system))/x_he((T[N,j+1]+T[N-1,j+1])/2, mu_system))          -n_dot_3 * h_os( (T[N,j+1]+T_CHX)/2,
x_he((T[N,j+1]+T_CHX)/2, mu_system), mu_system)    -    n_dot_3*mu_system* ( (1- x_he(
(T[N,j+1]+T_CHX)/2      , mu_system))/x_he((T[N,j+1]+T_CHX)/2, mu_system))       =
n_he3_sub[N,j]/(2*DELTAt) * ( u_he3(T[N,j+1], x_he(T[N,j+1], mu_system))-u_he3(T[N,j], x[N,j]))

     k_GGG_top[N,j+1]=k_G((T[N,j+1]+T[N-1,j+1])/2)
     k_he_mix_top[N,j+1]=k_he_mix((x_he(T[N,j+1], mu_system)+x_he(T[N-1,j+1], mu_system))/2)
     CALL k_effective(por_reg, k_GGG_top[N,j+1], k_he_mix_top[N,j+1]: k_eff_top[N,j+1],
a_Warning_top$[N,j+1])

dW_G[N,j+1]=(m_sub_GGG/2*(B[j+1]+B[j])/2*(vM(T[N,j+1], B[j+1])-vM(T[N,j], B[j])))
dQ_G[N,j+1]=n_sub_GGG/(2) * ( T[N,j] + T[N,j+1])/2 * (dsdb( ( T[N,j] + T[N,j+1])/2 , (B[j+1] + B[j])/2 ) *
(B[j+1] - B[j]) + dsdT( ( T[N,j] + T[N,j+1])/2 , (B[j+1] + B[j])/2 ) * (T[N,j+1] - T[N,j]))
dU_he[N,j+1]=n_he3_sub[N,j]/(2) * ( u_he3(T[N,j+1], x_he(T[N,j+1], mu_system))-u_he3(T[N,j], x[N,j]))
end

"!Nodes i=2..N-1"
Duplicate j=1,M-1
     Duplicate i=2,N-1
     n_he3_sub[i,j]=v_he_sub/v_he(T[i,j],x[i,j])*x[i,j]
     x[i,j]=x_he(T[i,j], mu_system)
     -n_sub_GGG/(DELTAt) * ( T[i,j] + T[i,j+1])/2 * (dsdb( ( T[i,j] + T[i,j+1])/2 , (B[j+1] + B[j])/2 ) * (B[j+1] -
B[j]) + dsdT( ( T[i,j] + T[i,j+1])/2 , (B[j+1] + B[j])/2 ) * (T[i,j+1] - T[i,j])) + k_he_mix_top[i,j+1] * A_c_reg * (T[i-
1,j+1] - T[i,j+1])/(DELTAx) + k_he_mix_bot[i,j+1] * A_c_reg * (T[i+1,j+1] - T[i,j+1])/DELTAx          +  n_dot_3
* h_os( (T[i-1,j+1]+T[i,j+1])/2, x_he((T[i,j+1]+T[i-1,j+1])/2, mu_system), mu_system)       +
n_dot_3*mu_system* ( (1- x_he((T[i,j+1]+T[i-1,j+1])/2, mu_system))/x_he((T[i,j+1]+T[i-1,j+1])/2,
mu_system))     - n_dot_3 * h_os( (T[i+1,j+1]+T[i,j+1])/2, x_he((T[i,j+1]+T[i+1,j+1])/2, mu_system),
mu_system)  -  n_dot_3*mu_system* ( (1- x_he((T[i,j+1]+T[i+1,j+1])/2,
```

```
mu_system))/x_he((T[i,j+1]+T[i+1,j+1])/2, mu_system)) = n_he3_sub[i,j]/(DELTAt) * ( u_he3(T[i,j+1],
x_he(T[i,j+1], mu_system))-u_he3(T[i,j], x[i,j]))

    k_GGG_top[i,j+1]=k_G((T[i,j+1]+T[i-1,j+1])/2)
    k_he_mix_top[i,j+1]=k_he_mix(   (x_he(T[i,j+1], mu_system)+x_he(T[i-1,j+1], mu_system))/2   )
    CALL k_effective(por_reg, k_GGG_top[i,j+1], k_he_mix_top[i,j+1]: k_eff_top[i,j+1],
a_Warning_top$[i,j+1])

    k_GGG_bot[i,j+1]=k_G((T[i,j+1]+T[i+1,j+1])/2)
    k_he_mix_bot[i,j+1]=k_he_mix(  (x_he(T[i,j+1], mu_system)+x_he(T[i+1,j+1], mu_system))/2)
    CALL k_effective(por_reg, k_GGG_bot[i,j+1], k_he_mix_bot[i,j+1]: k_eff_bot[i,j+1],
a_Warning_bot$[i,j+1])

dW_G[i,j+1]=(m_sub_GGG*(B[j+1]+B[j])/2*(vM(T[i,j+1], B[j+1])-vM(T[i,j], B[j])))
dQ_G[i,j+1]=n_sub_GGG * ( T[i,j] + T[i,j+1])/2 * (dsdb( ( T[i,j] + T[i,j+1])/2 , (B[j+1] + B[j])/2 ) * (B[j+1]  - B[j])
+ dsdT( ( T[i,j] + T[i,j+1])/2 , (B[j+1] + B[j])/2 ) * (T[i,j+1]  - T[i,j]))
dU_he[i,j+1]=n_he3_sub[i,j] * ( u_he3(T[i,j+1], x_he(T[i,j+1], mu_system))-u_he3(T[i,j], x[i,j]))
    end
end


Q_rej_sum=SUM(Q_rej[1,j], j=2,M)/t_sim


Duplicate i=1,N
    WW1[i]=dW_G[i,2]
    WW2[i]=dW_G[i,2]
    WW3[i]=dW_G[i,3]
    WW4[i]=dW_G[i,4]
    WW5[i]=dW_G[i,5]
    WW6[i]=dW_G[i,6]
    WW7[i]=dW_G[i,7]
    WW8[i]=dW_G[i,8]
end

Duplicate i=1,N
    QQ1[i]=dQ_G[i,2]
    QQ2[i]=dQ_G[i,2]
    QQ3[i]=dQ_G[i,3]
    QQ4[i]=dQ_G[i,4]
    QQ5[i]=dQ_G[i,5]
    QQ6[i]=dQ_G[i,6]
    QQ7[i]=dQ_G[i,7]
    QQ8[i]=dQ_G[i,8]
end

Duplicate i=1,N
    UU1[i]=dU_he[i,2]
    UU2[i]=dU_he[i,2]
    UU3[i]=dU_he[i,3]
    UU4[i]=dU_he[i,4]
    UU5[i]=dU_he[i,5]
    UU6[i]=dU_he[i,6]
    UU7[i]=dU_he[i,7]
    UU8[i]=dU_He[i,8]
end
```

```
W_SUM=SUM(WW1[i], i=1,N)+SUM(WW8[i], i=1,N)+SUM(WW2[i], i=1,N)+SUM(WW3[i],
i=1,N)+SUM(WW4[i], i=1,N)+SUM(WW5[i], i=1,N)+SUM(WW6[i], i=1,N)+SUM(WW7[i], i=1,N)
Q_SUM=SUM(QQ1[i], i=1,N)+SUM(QQ8[i], i=1,N)+SUM(QQ2[i], i=1,N)+SUM(QQ3[i],
i=1,N)+SUM(QQ4[i], i=1,N)+SUM(QQ5[i], i=1,N)+SUM(QQ6[i], i=1,N)+SUM(QQ7[i], i=1,N)
U_he_SUM=SUM(UU1[i], i=1,N)+SUM(UU8[i], i=1,N)+SUM(UU2[i], i=1,N)+SUM(UU3[i],
i=1,N)+SUM(UU4[i], i=1,N)+SUM(UU5[i], i=1,N)+SUM(UU6[i], i=1,N)+SUM(UU7[i], i=1,N)

cache=T[1,M]

Duplicate i=1,N
    T[i,M]=buffer[i]
end

$Export 'C:\Users\Amir\Documents\CYCLE ANALYSIS - experiment2\cache.txt' cache
$Export 'C:\Users\Amir\Documents\CYCLE ANALYSIS - experiment2\buffer_data4.txt' buffer[1..N]
```

EES code for the SMP model

```
"!Pump sizing"
"==========================================================================
==========="
V_canister=pi#*d_canister^2/4*l_canister        "Solving for design variable of canister - either length or
diameter"
V_canister=125[cm^3]*convert(cm^3,m^3)          "Assumed canister volume Vol=void+GGG"
    d_canister=0.05[m]                          "Diameter of canister"
    {l_canister=0.11[m]}                        "Length of canister"

"!Fixed properties"

rho_GGG=7080[kg/m^3]            "Density of GGG"
MW_GGG=1.01235[kg/mol]          "Molar weight of GGG"

"!mole of GGG"

rho_GGG=m_GGG/V_GGG             "Finding mass of GGG"
n_GGG=m_GGG/MW_GGG                      "Finding mole of GGG"

"!Volumes of GGG and helium in canister"

porosity=0.38                   "Porosity in SMP, V_void/V_total. 0.38 commonly used -- Nellis
(2009), McAdams (1954), London and Kays (1964), McCabe (1985), Perry (2007)"
V_he=V_canister*porosity        "Finding volume of helium in canister"
V_GGG=V_canister*(1-porosity)   "Finding volume of GGG in canister"

"!Known properties a--> T_low, b--> T_high"

T_a=1.5902[K]           "Low T beginning of adiabatic magnetization"
T_b=1.6274[K]           "High T end of adiabatic magnetization/ during isothermal magnetization"
B_a=0.05[Tesla]         "Lowest magnetic field"
//x_a=0.03              "High conc. this is before pumping out"
mu_4=mu4(T_a, x_a)
```

```
x_b=x_he(T_b,mu_4)
v_sp_a=v_he(T_a,x_a)
v_sp_b=v_he(T_b,x_b)
n_3_displaced=n_3_a-n_3_b
n_3_a=V_he*x_a/v_sp_a
n_3_b=V_he*x_b/v_sp_b

T_pc_regenerator=1.577[K] "FEED from regenerator analysis"
x_pc_regenerator=0.04
mu_4=mu4(T_pc_regenerator,x_pc_regenerator)

{T_pc=1.6
n_3_displaced=0.0055}

"!Magnetization process -- going from T_low to T_high"

"Properties"

"Set up numerical solution"
N=50                        "Number of NODES, N-1 is number of steps"
dx=(x_a-x_b)/(N-1)          "Defining concentration steps; because of the superleak, only 3He exits and
does NOT enter during pump out process, subsequently concentration changes as 3He is pushed out"

"!Setting up first node parameters"
x_mag[1]=x_a                "Conc. first node"
T_mag[1]=T_a
n_3_mag[1]=n_3_a            "Number moles of 3He for first node"
Vol[1]=v_he(T_a,x_a)                                "Spec. molar volume first node"

"!Property - The following parameters are all NODE property"
Duplicate i=1,N-1
      x_mag[i+1]=x_mag[i]-dx          "Conc. for each node"
      mu_4=mu4(T_mag[i+1],x_mag[i+1])         "Temp step"
      n_3_mag[i+1]=V_he*x_mag[i+1]/Vol[i+1]   "Number of 3He remaining in the canister"
      Vol[i+1]=v_he(T_mag[i+1],x_mag[i+1])    "Molar spec. vol in the canister"
end

"!Setting up first node parameters"
B_mag[1]=B_a                "Magnetic field for first node - fed from previoud part"
u_he3[1]=u_he3(T_a, x_a)    "Internal energy per mole of 3He first node"
total_mole[1]=n_3_mag[1]/x_mag[1]                   "Total mole of helium mixture in the canister first
node"

Duplicate j=1,N-1
    total_mole[j+1]=n_3_mag[j+1]/x_mag[j+1]         "Total mole of helium mixture in the canister"
    u_he3[j+1]=u_he3(T_mag[j+1], x_mag[j+1])        "Int specific energy per 3He mole for each node"
    dU_he3[j]=(n_3_mag[j+1]*u_he3[j+1])-(n_3_mag[j]*u_he3[j])
    h_os[j]=h_os(T_mag[j],x_avg[j],mu_4)            "Osmotic
enthalpy"
     x_avg[j]=(x_mag[j]+x_mag[j+1])/2"Average conc. for each process"
    //h[j]=h_mix(T_mag[j], x_avg[j])                "Mixture enthalpy"
    dh_flow_out[j]=(n_3_mag[j]-n_3_mag[j+1])*h_os[j] +  ((1-x_mag[j])/x_mag[j]*n_3_mag[j]-(1-
x_mag[j+1])/x_mag[j+1]* n_3_mag[j+1])*mu_4
    dh_flow_in[j]=ABS((n_3_mag[j+1]-n_3_mag[j]))*mu_4+(total_mole[j+1]-total_mole[j])*mu_4
    dQ_G[j]=n_GGG*(T_bar_g[j]*(dsdT(T_bar_g[j],B_bar[j])*(T_mag[j+1]-T_mag[j])   +
dsdB(T_bar_g[j],B_bar[j])*(B_mag[j+1]-B_mag[j])))
```

```
    T_bar_g[j]=(T_mag[j+1]+T_mag[j])/2
    B_bar[j]=(B_mag[j+1]+B_mag[j])/2
    dQ_G[j]+dU_he3[j]=dh_flow_in[j]-dh_flow_out[j]
    dB_mag[j]=ABS(B_mag[j+1]-B_mag[j])
    dN_mag[j+1]=n_3_mag[j]-n_3_mag[j+1]

    h_os_hhx_in[j]=h_os(T_pc_regenerator, x_avg[j], mu_4)
    dQ_reject[j]=(n_3_mag[j+1]-n_3_mag[j])*(h_os[j] - h_os_hhx_in[j])
end

Q_rej_sum=SUM(dQ_reject[j], j=1,N-1)


x_demag[1]=x_b                "Conc. first node"
T_demag[1]=T_b
n_3_demag[1]=n_3_b            "Number moles of 3He for first node"
Vol_de[1]=v_he(T_b,x_b)                                   "Spec. molar volume first node"

"!Property - The following parameters are all NODE property"
Duplicate i=1,N-1
      x_demag[i+1]=x_demag[i]+dx      "Conc. for each node"
      mu_4=mu4(T_demag[i+1],x_demag[i+1])   "Temp step"
      n_3_demag[i+1]=V_he*x_demag[i+1]/Vol_de[i+1]     "Number of 3He remaining in the canister"
      Vol_de[i+1]=v_he(T_demag[i+1],x_demag[i+1])       "Molar spec. vol in the canister"
end

"!Setting up first node parameters"
B_demag[1]=B_mag[N]       "Magnetic field for first node - fed from previoud part"
u_he3_de[1]=u_he3(T_b, x_b)           "Internal energy per mole of 3He first node"
total_mole_de[1]=n_3_demag[1]/x_demag[1]                  "Total mole of helium mixture in the canister first
node"


Duplicate j=1,N-1
    total_mole_de[j+1]=n_3_demag[j+1]/x_demag[j+1]     "Total mole of helium mixture in the canister"
    u_he3_de[j+1]=u_he3(T_demag[j+1], x_demag[j+1])  "Int specific energy per 3He mole for each node"
    dU_he3_de[j]=(n_3_demag[j+1]*u_he3_de[j+1])-(n_3_demag[j]*u_he3_de[j])
    h_os_de[j]=h_os(T_PC,x_avg_de[j],mu_4)                "Osmotic
enthalpy"
     x_avg_de[j]=(x_demag[j]+x_demag[j+1])/2  "Average conc. for each process"
    //h_de[j]=h_mix(T_PC, x_avg_de[j])                    "Mixture enthalpy"
    dh_flow_out_de[j]=ABS((n_3_demag[j+1]-n_3_demag[j]))*mu_4+(total_mole_de[j+1]-
total_mole_de[j])*mu_4
    dh_flow_in_de[j]= (n_3_demag[j+1]-n_3_demag[j])*h_os_de[j]    +    ((1-
x_mag[j+1])/x_mag[j+1]*n_3_mag[j+1]-(1-x_mag[j])/x_mag[j]* n_3_mag[j])*mu_4
    dQ_G_de[j]=n_GGG*(T_bar_g_de[j]*(dsdT(T_bar_g_de[j],B_bar_de[j])*(T_demag[j+1]-T_demag[j])   +
dsdB(T_bar_g_de[j],B_bar_de[j])*(B_demag[j+1]-B_demag[j])))
    T_bar_g_de[j]=(T_demag[j+1]+T_demag[j])/2
    B_bar_de[j]=(B_demag[j+1]+B_demag[j])/2
    dQ_G_de[j]+dU_he3_de[j]=dh_flow_in_de[j]-dh_flow_out_de[j]
    dB_demag[j]=ABS(B_demag[j+1]-B_demag[j])
    dN_demag[j+1]=n_3_demag[j]-n_3_demag[j+1]
end

B_demag[N]=B_a
```